Time of Formation of Earth and Mars Constrained by Siderophile Element Geochemistry and the 182Hf-182W Isotope System

HARVARD UNIVERSITY
Graduate School of Arts and Sciences

DISSERTATION ACCEPTANCE CERTIFICATE

The undersigned, appointed by the

Department of Earth and Planetary Sciences

have examined a dissertation entitled
"Time of Formation of Earth and Mars Constrained by Siderophile Element Geochemistry and the ^{182}Hf-^{182}W Isotope System"

presented by Gang Yu

candidate for the degree of Doctor of Philosophy and hereby certify that it is worthy of acceptance.

Signature _____

Typed name: Prof. Stein Jacobsen

Signature _____

Typed name: Assoc. Prof. Sujoy Mukhopadhyay

Signature _____

Typed name: Prof. Richard J. O'Connell

Signature _____

Typed name: Prof. Dimitar Sasselov

Date: April 25, 2012

Time of Formation of Earth and Mars Constrained by Siderophile Element Geochemistry and the ^{182}Hf-^{182}W Isotope System

A dissertation presented

by

Gang Yu

to

The Department of Earth and Planetary Sciences

in partial fulfillment of the requirements

for the degree of

Doctor of Philosophy

in the subject of

Earth and Planetary Sciences

Harvard University
Cambridge, Massachusetts

April, 2012

Dissertation Advisor: Professor Stein B. Jacobsen Gang Yu

Time of Formation of Earth and Mars Constrained by Siderophile Element Geochemistry and the ^{182}Hf-^{182}W Isotope System

Abstract

^{182}Hf-^{182}W chronometry is considered the most powerful tool to determine the formation timescale of the terrestrial planets. However, previous work employed oversimplified accretion and core formation models. The accretion and core formation models presented here for the ^{182}W isotopic evolution in the mantles of the accreting Earth and Mars, can incorporate the core formation conditions constrained by siderophile element geochemistry and can be successfully applied to constrain the formation timescale of Earth and Mars.

Elemental abundance analyses of the Allende meteorite and two martian meteorites lead to new estimates of core-mantle concentration ratios of Si, V, Cr and Mn for Earth and two distinct mantle Hf/W ratios for Mars respectively, and provide better constraints on the models. It is concluded that formation of the proto-Earth (~87% of its present mass) has to complete rapidly in 10.7 ± 2.5 Myr after the onset of the Solar

System for a late (≥ 52 Myr) Moon-forming giant impact. The mean time of Mars' accretion is determined to be 3.6 ± 0.1 Myr, meaning that Mars accretes to 95% of its present mass in 10.8 ± 0.3 Myr after the formation of the Solar System. Therefore, Mars is not a planetary embryo, and Mars and proto-Earth may be formed on a similar timescale if a late Moon-forming giant impact is assumed. In contrast, if the Moon formed early at ~30 Myr then it takes about 3 times longer to form the proto-Earth compared to Mars.

A stochastic mantle stirring and sampling model was developed to investigate the evolution of W isotope heterogeneities in the mantles of Earth and Mars after accretion and core formation. Our results confirm the mantle stirring rate of ~ 500 Myr constrained by the long-lived isotope systems in Earth and suggest that the mantle stirring rate in Mars is much slower (~2 Ga).

A new concept is developed: the core formation memory of a siderophile element. Siderophile elements are shown to have different capabilities in recording core formation history, a very important fact to consider in any core formation modeling.

Contents

List of Tables

List of Figures

Acknowledgements

The completion of my dissertation and subsequent Ph.D. has been a long journey. Looking back, I am surprised and very grateful for all I have received these years. It certainly helped shape me as a person and lead me to where I am standing today. I am so fortunate to have my Ph.D. studies full of those gifts.

First and foremost I must thank my advisor Professor Stein B. Jacobsen. Since the first day I joined his research group, he has taught me, consciously and unconsciously, how to become an excellent geochemist in the day-to-day interactions. I really appreciate his great contributions of time, thoughts and funding to make my Ph.D. studies productive and stimulating. Especially he provided his unselfish support when I needed it most, without which it is impossible to have this dissertation today. Professor Jacobsen is always very serious and strict when dealing with teaching, research and publications, but he is obviously one of the most easy-going professors at EPS at Harvard. I always feel comfortable and encouraged to express my ideas freely in front of him. He has set and will always be my role model on how to be a successful scientist, an enlightening mentor and most importantly a kind gentleman.

The other members of Jacobsen Group have contributed a lot to my personal and professional development at Harvard. We exchanged research ideas, performed experiments together and discussed the topics of interest. The group is a source of friendship as well as good advice and collaborations. It is truly my pleasure to work with the current and past Jacobsen group members: Dr. Michail I. Petaev, Dr. Shichun Huang, Dr. Rama Chakrabarti, Dr. Juraj Farkaš, Dr. Nataliya Krestina, Maria Peto, Rita Parai, Mike C. Ranen and Steven Jaret.

I am also very thankful for my Ph.D. committee members Professor Richard J. O'Connell, Professor Dimitar D. Sasselov and Professor Sujoy Mukhopadhyay. They have provided enormous amount of constructive advice and support during my studies and preparation of the dissertation. In addition, I have benefited a lot from many other professors of EPS at Harvard through various ways, including classroom learning, discussions and even casual conversations. I would like to thank Professor Daniel Schrag, Professor Charles H. Langmuir and Professor Sarah T. Stewart-Mukhopadhyay for their mentoring, help and support in the past few years. The administration of EPS also worked hard to create a harmonious research environment, so that I could fully focus on my studies and research. I especially appreciate the support from Chenoweth Moffatt, Sarah Colgan, Cindy Marsh, Ganna Savostyanova, Maryorie Grande and Bridget Mastandrea.

I always feel very lucky to have the chance to pursue my Ph.D. degree with so many talented and motivated fellow graduate students at Harvard. We learned a lot from each other, shared the stress, comforted one another for failure, and most importantly enjoyed the happiness and success together. A few names are worth special mentioning: Atreyee Bhattacharya, Maria Peto, Rita Parai, Allison Gale, Phoebe Robinson, Jonathan Tucker and Stephen Turner. Without you, my life cannot be so joyful and colorful.

Lastly, my gratitude must go to my dear parents and twin brother Qiang who are thousands of miles away in China. In all my life, they are my most supportive fans who always have faith in me, no matter what I do and where I am. My dear friends around me are also my source of power and confidence. Thank you all!

Chapter 1

Introduction

Isotope and trace element geochemistry aims to study the transport and distribution of elements and their isotopes within the Earth and understand the mechanisms behind it. Since Earth is a member of the rocky body family in the Solar System, application of isotope and trace element geochemistry could extend beyond the Earth to encompass the entire Solar System and even other solar systems. The subject is called Cosmochemistry.

Victor Goldschmidt is widely considered as the father of modern geochemistry. In a series of publications in 1920s-1930s (Goldschmidt, 1923, 1937), he, for the first time, systematically studied the geochemical behavior of elements and grouped them according to their preferred host phase into four categories: lithophile (rock-loving), siderophile (metal-loving), chalcophile (ore-loving or chalcogen-loving) and atmophile (gas-loving) elements. In the meantime, after discovery of radioactive decays, isotope geochemistry was developed to solve the long lasting debate about the age of the Earth. In 1907, Bertram Boltwood, an American chemist,

published the first 'radiometric age' of the Earth. He determined the Pb concentrations in three samples of pitchblende, a uranium ore, and found their ages ranging from 410 to 535 million years - the evidence favoring an older Earth than previously thought (~ 99 million years based on ocean salinity). Since 1940, marked by the wide application of mass spectrometry, isotope geochemistry has expanded its territory from merely providing the precise ages of geologic events (e.g. age of the Solar System ~4.567 Ga (Amelin et al., 2010)) to tracing the geologic processes and providing critical information on the rates and pathways of geologic evolutions.

Today with this powerful tool of isotope and trace element geochemistry, we can determine the origins of elements and isotopes and understand the formation and evolution of stars and planets. We can study the condensation and evaporation processes in the solar nebula and understand the chemical evolution of the solar nebula disk. We can estimate the formation timescale of planets, moons and other rocky materials in the Solar System and understand the formation and evolution of the planetary system. We can constrain how and when the planetary core, mantle, crust and atmosphere were formed. We can recognize mantle plumes, know that sediments can be subducted in the mantle and investigate how the Earth's mantle convects. We can understand how and in what rate mountains rose and then was eroded

by weathering. We can quantify the geological timescale, study the occurrence and evolution of early life and the human history beyond the records. We can address environmental issues like acid rain, the ozone hole, global warming and water pollution. We can study the formation of most non-renewable natural resources like metal ore, natural gas and oil deposits. Clearly, the mature trace element geochemistry and the powerful isotope geochemistry together play an indispensable role assisting human beings to understand the history and future of our Earth, other planets in the Solar System and beyond.

This presented work will focus on the application of isotope and trace element geochemistry on constraining the time of formation of the Earth-Moon system and Mars in order to understand formation of terrestrial planets in the Solar System. The big picture for terrestrial planet formation is (from the widely accepted standard model -- the planetesimal hypothesis, Chambers (2004)): (1) The young Sun is surrounded by a disk of gas and dust and then dust grains stick together to form km-sized planetesimals. (2) Collisions of planetesimals produce a few tens of Moon-to-Mars-sized planetary embryos in a rapid "runaway" growth phase followed by a slowed-down "oligarchic" growth phase (approximately 0.1-1 million years after the onset of the Solar System at 1 AU). (3) Finally planetary embryos suffer giant impacts, leading to full size planets like Earth in 10-100 million years. In order to test the

planetesimal hypothesis, a few related timescale questions will be addressed in the dissertation, such as "what is the relationship between formation timescale of proto-Earth and the timing of Moon-forming event?" and "whether Mars was formed during a "runaway" growth phase (< 1 Myr) as a leftover planetary embryo or it had an Earth-like accretion history simply as a smaller planet?".

Isotope systems can only date the event that can significantly fractionate the elemental ratios of their parent and daughter isotopes. As we know, the characteristic differentiation event for formation of terrestrial planets has to be the core formation. All terrestrial planets in the Solar System have a big Fe metallic core, which accounts for ~20-65% of its total mass. So core formation process -- separation of a bulk planet into the distinct metal and silicate phases, is the most important differentiation event in a planet's history. It is widely believed that core formation processes (metal segregation < 10^3 year (e.g. Rubie et al., 2003; Li et al., 2011)) generally are faster than accretion processes (~1-100 million years (e.g. Wetherill, 1986; Yin et al., 2002)). So the timescale of accretion of terrestrial planets can be inferred from the timescale of formation of their metallic cores.

The ^{182}Hf-^{182}W short-lived radiogenic system with a half-life of 8.9 Myr (Vockenhuber et al., 2004) is the most powerful tool to date core formation of terrestrial planets because of its three characteristics: (1) Its

half-life is comparable to the timescale of formation of planetary cores (Rubie et al., 2007). (2) Both Hf and W are refractory elements and their concentrations in planetary mantles can be estimated with some certainty compared to other isotopic systems (e.g. U-Pb and Pd-Ag). Those isotopic systems suffer from the fact that one or both parent and daughter elements is more or less volatile during accretion and their volatile loss is still difficult to determine (McDonough and Sun, 1995). (3) W is moderately siderophile (metal-loving) and Hf is lithophile (silicate-loving). Thus metal segregation during core formation would significantly fractionate Hf/W ratio in planetary mantles and then result in a significant ^{182}W anomaly after millions of years (cf. Harper and Jacobsen, 1996).

Using ^{182}Hf-^{182}W system to constrain the timescale of formation of a terrestrial planet requires knowledge about the W isotopic composition in the planetary mantle and its accretion and core formation process. So far, we can only access samples from two terrestrial planets -- Earth and Mars. Young terrestrial rocks that have been reported show a homogeneous W isotopic composition ($\varepsilon_{W(CHUR)}$ = 1.9 ± 0.2 (Kleine et al., 2002; Yin et al., 2002)). Rock samples from Mars are believed to be represented by shergottites, nakhlites and chassignite (SNC) meteorites (McSween, 2003). In contrast to terrestrial rocks, martian meteorites present a range of W isotope compositions: shergottites have an $\varepsilon_{W(CHUR)}$ of

2.0-3.0 and nakhlites + chassignite have an $\varepsilon_{W(CHUR)}$ of 4.65-5.65 (Foley et al., 2005).

The simplest model for planetary accretion and core formation process is a two-stage model, which assumes that the undifferentiated planet has a chondritic composition at stage I (before the core formation) and then the whole core suddenly segregated from the planetery mantle at a certain time (t_{2stage}). During stage II (after core formation till today) the planetary mantle has the current mantle's Hf/W ratio and develops the ^{182}W excess. The calculation equations for two-stage model age (t_{2stage}) are first introduced by Harper and Jacobsen (1996). The first accurate two-stage model age of the Earth was reported by Yin et al. (2002) as t_{2stage} = 29.5 ± 1.5 Myr after the formation of the Solar System.

A more realistic model – the continuous accretion and core formation model with a global magma ocean has been developed and employed by Harper and Jacobsen (1996) and Jacobsen (2005) to interpret the W isotopic composition of terrestrial rocks. In the model, they employed an exponentially decreasing accretion rate for terrestrial planets inferred by simulations (Wetherill, 1986) and defined the mean age to indicate the formation timescale of a terrestrial planet (the mean age is the time needed to build ~63% of the planet's mass). Their work gives a mean age of ~10 Myr for Earth formation, which is equivalent to ~33 Myr when the Earth reaches 95% of its present mass. Although the result is

undistinguishable from the two-stage model age within uncertainty, as pointed by Jacobsen (2005), the similar ages from the two models are just coincident because the Earth's mantle happens to have a Hf/W ratio corresponding to $f^{Hf/W}$=12 ± 2. If a planet's mantle has an $f^{Hf/W}$ < ~9 (e.g. Mars might has an $f^{Hf/W}$ < 6), the two model ages will be very different from each other.

The limitation in those previous models is their assumption for core formation processes. They assumed that during accretion and core formation, the planet's mantle always has a global magma ocean with a constant Hf/W ratio as the current mantle, which is inconsistent with what is known about core formation processes from siderophile element geochemistry. In addition, those models cannot explain the W isotope signature of martian meteorites and then it is difficulties to use them to date Mars. Previous work that applied this isotope system to date Mars had to assume that the martian mantle has a shergottites-like W isotopic composition (ignoring nakhlites and chassignite). They obtained Hf-W ages for Mars that varied from 0 to 15Myr (Kleine et al., 2004; Foley et al., 2005; Nimmo and Kleine, 2007; Kleine et al., 2009; Dauphas and Pourmand, 2011). Since they ignored nakhlites and chassignite with more radiogenic ^{182}W, the relationship of their reported ages to the Mars' age is not clear. The wide range of the ages comes from the poorly constrained Hf/W ratio in martian mantle due to the limited ICP-MS data of martian

meteorites. Two important martian meteorites – Zagami and Nakhla representing shergottite and nakhlite respectively, have no published ICP-MS data yet. In Chapter 4, we measured trace element concentrations of the two martian meteorites by ICP-MS. The results combined with recent published ICP-MS data for other martian meteorites lead to precise estimates of distinct Hf/W ratios in mantle sources of shergottites and nakhlites + chassignite.

Siderophile (metal-loving) elements in planetary mantles partition into the cores during core formation. However, the observed mantle abundances of siderophile elements in the Earth are mostly higher than what would be expected based on low-pressure (1 bar) metal-silicate partitioning experiments (e.g. Drake and Righter, 2002). This discrepancy has been known as the 'excess siderophile' problem. Several possible explanations have been proposed: (1) Inefficient core formation (Jones and Drake, 1986): This is a disequilibrium core formation model in which core separation was incomplete and left some fraction of metal in the mantle. Later this metal was re-oxidized and then re-mixed within the mantle and led to the observed elevated mantle concentrations of siderophile elements. Although this model can fit many of the elemental abundances, it cannot explain depletions of the slightly siderophile elements (V and Cr) in the mantle. In addition, re-oxidization of the 'retained' metal requires enormous amounts of water, equivalent to about 15 times of the current

mass of the hydrosphere (Wood et al., 2006). (2) Heterogeneous accretion (Wänke and Gold, 1981; O'Neill, 1991): This model proposes an increasing oxidation state in the mantle during accretion and core formation. The conditions of core segregation changed from reducing at the beginning of accretion to more oxidizing towards the end. At the very reducing beginning condition, some fractions of the slightly siderophile elements such as Nb, Si, V and Cr would have been extracted to the core together with all the moderately and highly siderophile elements. Then conditions gradually became more oxidizing towards the end of accretion, and core extraction of siderophile elements would have ceased accordingly, from the slightly to the more strongly siderophile elements. In the final stage, core formation ceased completely and then a 'late veneer' of about 0.5% of chondritic material was added. The added chondritic material raised the mantle concentrations of highly siderophile elements to their present levels. This model can solve the 'excess siderophile' problem, but it is too difficult to test. (3) High pressure core formation with a deep magma ocean (Stevenson, 1990; Li and Agee, 1996): Since this testable model is able to explain the 'excess siderophile' problem with results from metal-silicate partitioning experiments, it has become the leading theory for core formation in terrestrial planets. Li and Agee (1996) demonstrated that partition coefficients of Ni and Co converge at high pressures (~28 GPa) by carrying out a series of experiments from 2 GPa to 20 GPa and

they concluded that the similar depletions of the two elements in Earth's mantle could be produced in a deep peridotite magma ocean at 28 GPa with a depth of 750-1,100 km.

Wood et al. (2005; 2006; 2008; 2008) further developed this deep magma ocean model by employing a more realistic, continuous core formation model and new experimental data on slightly siderophile elements (Si, Nb, V, Cr and Mn). By matching the observed siderophile element abundances in Earth's mantle today, they suggest a deep magma ocean model, which has a magma ocean with a thickness of approximately 35% of the depth to the core-mantle boundary in the accreting Earth and considers the increasing oxidation state in Earth mantle, which requires the oxidized Fe content in mantle to increase from 0.5–1.0% to the current level of 6.26%. In fact, the new result about the oxidation state of Earth's mantle during core formation came mainly from their new constraints for slightly siderophile elements (Si, Nb, V, Cr and Mn).

Since the slightly siderophile elements (e.g. V) started to play an important role in determining core formation conditions of Earth, we need to investigate how well we know their small depletions in Earth's mantle. These depletions are calculated from their abundances in bulk silicate mantle and bulk Earth. Siderophile element abundances of the bulk mantle are generally determined from measurements of mantle peridotites

(e.g. McDonough, 2003; Palme and O'Neill, 2003), and implicit in any mantle concentration estimate is the assumption that the mantle is well mixed and the deep mantle has the same composition as the upper mantle represented by mantle peridotites. Siderophile element abundances of the bulk Earth are estimated based on the compositions of CI chondrites, which are thought to be representative of the undifferentiated early Solar System material with a mean composition of the Solar System (Anders and Grevesse, 1989). Adjustments are made to the compositions of CI chondrites to account for the relative depletion of the bulk Earth in volatile elements. The correction for volatile losses is the most difficult and important step in estimating the concentrations of siderophile elements in bulk terrestrial planets.

One approach to correct volatile losses of siderophile elements and estimate their bulk Earth concentrations is to construct a volatility trend in the plot of elemental abundances of bulk silicate planets vs. condensation temperature of elements (McDonough, 2003). The trend is determined by the volatile lithophile elements in the plot. Then, the bulk mantle abundance of siderophile elements can be determined from this volatility trend given their condensation temperatures. Alternatively, Allègre et al. (1995) constructed a different volatility trend defined by different types of chondritic meteorites in plots of two element ratios -- two different volatile elements divided by the same refractory element.

The volatility trend has better linearity because of involving fewer elements and can lead to more precise estimation. However, bulk Earth abundances of some slightly siderophile elements have not been estimated in this way because of lacking good data (Allègre et al., 1995). In Chapter 2, we report new elemental abundances for some elements in Allende CV chondrite. We use this new data to construct the volatile trends for slightly siderophile elements (V, Cr, Si and Mn). The result leads to more precise estimates for the bulk Earth abundances of the elements and their new core-mantle partition coefficients. In Chapter 2, we also report the trace element data of three CAIs from Allende. It is a collaboration work with Dr. Juraj FarkaŠ and Dr. Shichun Huang in the Jacobsen group, who conducted Ca isotope measurements on the same CAIs. The results advance our understanding of condensation and evaporation processes related to formation of CAIs in the early Solar System.

In Chapter 3, we construct an accretion and core formation model for the Hf-W system in Earth, which can incorporate core formation constraints from the siderophile element geochemistry and the timing of the Moon-forming event inferred from isotope studies on lunar rocks. The model leads to a new constraint for the formation timescale of the Earth and Moon system and provides a new way to evaluate the probabilities of different formation scenarios.

Similar to the Earth, in terms of siderophile element abundances in martian mantle, Righter and Drake (1997) and Righter and Chabot (2011) suggest a "deep magma ocean" core formation model for Mars. The deep magma ocean has a depth corresponding to about ~14 GPa (approximately ~760 km deep). In Chapter 4, we modeled the evolution of W isotopic composition in the "deep magma ocean" core formation model. The model can match the two groups of Hf/W ratios and W isotope composition of martian meteorites simultaneously and results in a more precise estimate on timescale of formation of Mars.

Application of the Hf-W system in the "deep magma ocean" core formation model to the Earth faces a problem. There is no observation of non-homogeneous W isotopic composition in Earth today as for martian rocks. Therefore, in Chapter 5, we built a stochastic mixing and sampling model for formation of basalts on Earth and Mars, which can successfully explain the homogeneous W isotopic composition in young terrestrial basalts as a result of active convection in Earth's mantle. Convection in the Earth reduce the early W isotope heterogeneity scale to a much smaller scale than the sampling scale of terrestrial igneous rocks. Mars still shows the W isotopic heterogeneity because of its slower mantle convection rate.

There are small limitations and questionable assumptions in previous core formation studies based on siderophile element geochemistry

(Wade and Wood, 2005; Wood et al., 2008). For example, the division of different stages of the continuous core formation with different oxidation states is arbitrary and leads to a non-unique solution. In Chapter 6, we address such issues and investigate the distinct ability of a specific siderophile element on recording the core formation history. We define and quantify a new concept -- "core formation memory" to demonstrate the ability. The results not only provide a basis to interpret the conditions inferred from core-mantle partitioning of siderophile elements, but also further facilitate application of multiple siderophile elements on constraining the continuous core formation.

In summary, this dissertation applies a combination of the ^{182}Hf-^{182}W isotope system and siderophile element geochemistry to study and understand W isotope evolution in the mantles of Earth and Mars during accretion and core formation processes and constrain the time of formation of Earth and Mars. While each chapter focuses on a singular topic, the work comes together in a big picture about when Earth and Mars were formed. The presented work overall has advanced our understanding of core formation, early mantle convection and planet formation in the Solar System.

Chapter 2

Elemental Abundances of Allende Chondrite and its Calcium-Aluminum-rich Inclusions: Implications to Bulk Earth Abundances of Some Slightly Siderophile Elements and Evaporation and Condensation Processes in the Early Solar System

Part of this chapter has been presented at the 2009 40th Lunar and Planetary Science Conference and published in Huang et al., (2012) Geochimica et Cosmochimica Acta 77, 252–265

2.1 Introduction

The Allende meteorite is the largest carbonaceous chondrite ever found on the surface of Earth. It fell over the Mexican state of Chihuahua on February 8, 1969. It is notable as a heterogeneous meteorite for possessing abundant, large calcium-aluminum-rich inclusions (CAIs), which are the oldest objects in the Solar System (Gray et al., 1973; Amelin et al., 2002; Amelin et al., 2010). Those CAIs have shown very large mass-dependent isotopic fractionations in Mg, Si, Ca and O isotopes, pointing to the important roles of evaporation and condensation

in the formation and evolution of refractory inclusions (Clayton et al., 1973; Lee et al., 1979; Jungck et al., 1984; Niederer and Papanastassiou, 1984; Grossman et al., 2008; Krot et al., 2008; MacPherson et al., 2008; Lee et al., 2011). Among the previous refractory inclusions studied on Mg, Si and Ca isotopes, many exhibit correlated enrichments in heavy Mg and Si isotopes relative to the composition of the bulk silicate Earth, but they generally have lighter Ca isotopes, which are uncorrelated with Mg or Si isotopic effects (Niederer and Papanastassiou, 1984; Clayton et al., 1988). Hence, the observed heavier Mg and Si isotopes and lighter Ca isotopes in refractory inclusions cannot be explained by a single-stage evaporation or condensation process. On the contrary, this implies that the fractionation of Mg, Si and Ca isotopes occurred at different stages of refractory inclusion evolution (Niederer and Papanastassiou, 1984).

Several types of Rare Earth Element (REE) patterns have been observed in refractory inclusions and believed to be important indicators for the formation and evolution of refractory inclusions (Figure 2.1) (e.g. Tanaka and Masuda, 1973; Mason and Taylor, 1982; Ireland and Fegley, 2000; MacPherson, 2003). The Group I REE pattern (including Group I, III, V and VI in Mason and Taylor, (1982)) is essentially flat at ~10-20 folds enrichment level relative to the CI chondrites, with various enrichments or depletions on the multi-valence REEs (Ce, Eu and Yb).

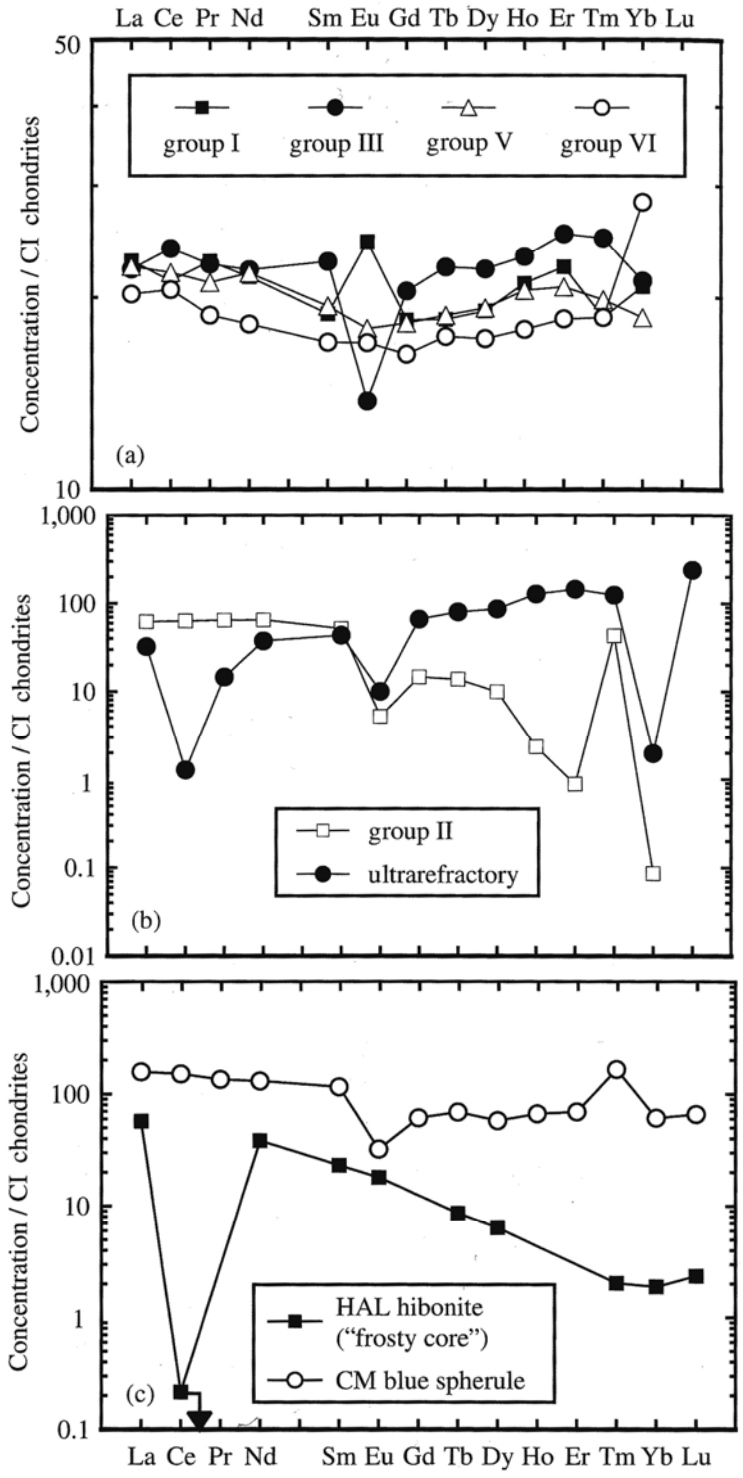

Figure 2.1 Examples of typical REE patterns observed in CAIs from MacPherson (2003). Data sources: Mason and Taylor (1982); Ireland et al. (1988) and Davis et al. (1982).

The Group II REE pattern is characterized by a flat light REE pattern and a positive Tm anomaly. It is depleted in both the most volatile (Eu and Yb) and most refractory (heavy REEs except for Tm and Yb) REEs. The third pattern, the ultra-refractory REE pattern, is characterized by the enrichment in the super-refractory REEs, and is roughly complementary to the Group II REE pattern. This type of REE pattern has been identified in several minerals, CAIs and ultra-refractory nodules, such as platy hibonite crystals and CAIs (MH-115, HIB-11) from CM2 Murchison (Boynton et al., 1980; Ireland et al., 1988; Simon et al., 1996; Simon et al., 2002), a CAI from CV3 Efremovka (El Goresy et al., 2002), and an ultra-refractory nodule from CV3 Allende (Hiyagon et al., 2003).

The distinctive Group II REE pattern was first recognized in an Allende CAI (Tanaka and Masuda, 1973). The first theoretical interpretation of the Group II REE pattern using the thermodynamic data available at that time was published in Boynton (1975) and more follow-up work was done by Davis and Grossman (1979). Now it is widely accepted that CAIs with Group II REE patterns are condensates from a fractionated nebular reservoir from which a high temperature phase containing the most refractory REEs had been segregated (e.g. Boynton, 1975; Davis and Grossman, 1979). The high temperature phase hosting ultra-refractory REEs was first suggested to be melilite or perovskite

(Davis and Grossman, 1979), but now it is believed to be hibonite (MacPherson and Davis, 1994).

However, it is still unclear whether such a high temperature phase (possibly hibonite) was an evaporation residue or a condensate and more importantly, whether it was formed on an equilibrium or non-equilibrium condition. Since REEs tend to partition into the Ca-bearing minerals and volatility fractionation of REEs and Ca isotopic fractionation occur in the same temperature range (e.g. MacPherson and Davis, 1994), the systematic study on REE abundances and Ca isotopes for the same CAIs promises to enhance our understanding of the formation of CAIs and the high temperature phase cosmochemistry. Here we measured the elemental abundances of three CAIs from the Allende meteorite. Dr. Huang and Dr. Farkaİ in the Jacobsen Group measured the Ca isotopic composition of the same aliquots of the CAIs. Our results reveal a correlation between $\delta^{44/40}$Ca and REE patterns of CAIs, implying the segregation of up to 3% of an ultra-refractory evaporation residue from a chondritic reservoir prior to the formation of refractory inclusions.

It has been recently suggested that knowledge about partitioning of some slightly siderophile elements (V, Cr, Mn and Si) between the Earth's mantle and core can provide some unique information (i.e. temperature and oxidation state) about core formation conditions (Wood et al., 2008; Rubie et al., 2011). For example, the known core-mantle partitioning of V

for the Earth has been suggested to be produced by either a high temperature (Chabot and Agee, 2003) or a very reduced core formation process (Wood et al., 2008). However, previous estimates of core-mantle partitioning of those elements are not very precise due to the poor constraints on their bulk Earth concentrations (Allègre et al., 1995; McDonough, 2003).

Allègre et al. (1995) developed a method to estimate the elemental concentrations in the bulk Earth via a volatility trend defined by chondritic meteorites. However, this method has not been applied to those slightly siderophile elements (e.g. V) due to the limited precise data of carbonaceous chondrites, especially the CV chondrites – the closest one to the bulk Earth when speaking of volatile depletion. Here we measured trace element concentrations of the bulk Allende CV chondrite, with which we can re-construct the volatile trends and make more precise estimates on bulk Earth abundances of slightly siderophile elements (V, Cr, Si and Mn) and their core-mantle partition coefficients.

2.2 Sample Description

The Allende meteorite is a CV3 carbonaceous chondrite. As a chondrite, it consists of four major components: chondrules, Fe-Ni metal, refractory inclusions (Ca-Al-rich inclusions, CAIs; and amoeboid olivine aggregates, AOAs), and fine-grained matrix material. It belongs to the

group of the Vigarano-like carbonaceous chondrite (CV), which is characterized by high matrix/chondrule ratios (0.5-1.2), high abundances of millimeter-to-centimeter-sized CAIs and AOAs, and common occurrence of igneous melilite-spinel-pyroxene-anothite (type-B) CAIs (Krot et al., 2003). Its petrologic type is 3, indicating that it is the least modified CV by secondary processes.

An aliquot of the bulk sample of the Allende CV3 chondrite and aliquots of three CAIs from the chondrite were selected for this study. The bulk Allende sample was made from crushing, powdering and mixing of an about 200 g piece of the Allende meteorite, from which no CAIs had been extracted. Then, the bulk sample was ashed under 500 ℃ for 8 hours in order to remove organic matter.

Three CAI samples (SJ101, SJ102 and SJ103) were extracted from the Allende meteorite in Jacobsen Lab at Harvard University. Complete petrology studies have been done (Jacobsen et al., 2008; Petaev and Jacobsen, 2009) and found that SJ101 is a large (~25×15 mm), forsterite-bearing Type B CAI; SJ102 is a small (~5 mm) spherical Type B1 CAI; SJ103 is a small (~10 mm) irregular Type B2 CAI (Figure 2.2).

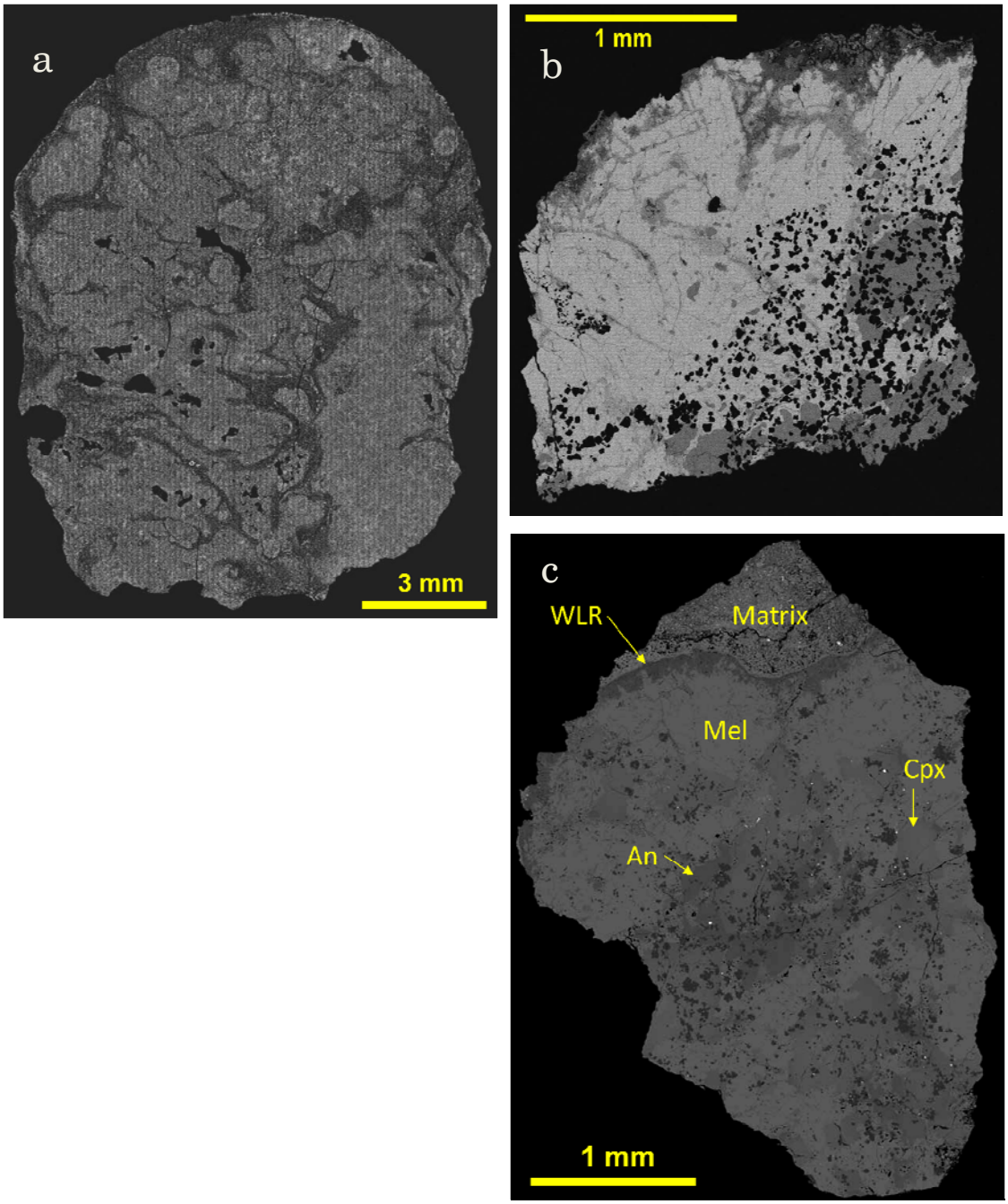

Figure 2.2 (a) Al X-ray map of SJ101, (b) Ca X-ray map of SJ102, (c) Back-scattered Electron (BSE) map of SJ103 (from the presentation of Jacobsen et al., 2007).

2.3 Elemental Abundance Analysis

2.3.1 Sample Dissolution

The bulk Allende sample weighs 24.7 mg from the ashed Allende powder. CAIs samples are small chips, weighing from several to tens of milligrams. All samples were first dissolved in a 1:1 mixture of concentrated HF and HNO_3 at 120 °C for 2 weeks. Then, the sample solutions were dried down and re-dissolved in 1 mL concentrated HNO_3. Altogether, the sample solutions were dried down and re-dissolved three times with the concentrated HNO_3 and one time with 6N HCl in order to break down insoluble CaF_2. Some aliquots of the solutions were used for Ca isotope measurements (measurement details in Huang et al. (2012)). Some aliquots were dried down again and re-dissolved in a 10 ppb Indium (In) + 1% HNO_3 solution. They were further diluted with the 10 ppb In + 1% HNO_3 solution to make 1:5000 solutions for elemental abundance measurement by inductively coupled plasma mass spectrometry (ICP-MS). No residue was observed in any of our sample solutions.

2.3.2 Elemental Abundance Measurement

Aliquots of 1:5000 sample solutions were analyzed to determine the elemental abundances by solution-ICP-MS technique using a GV Platform XS Quadrupole ICP mass spectrometer at Harvard University. Four USGS rock standards -- AGV-1, BCR-1, BHVO-1 and SGR-1 -- were used

to construct the standard calibration curves. Elemental abundances of those rock standards are decided based on the USGS published values and the standard values obtained in Jacobsen Lab. Each analytical sequence contained two procedure blanks, four rock standard solutions (BHVO-1, BCR-1, AGV-1 and SGR-1) and three unknown sample solutions. An additional BHVO-1 standard was analyzed every fourth sample and was used to correct the sensitivity drift. Moreover, 10 ppb In was added in solutions of blanks, rock standards and unknowns as the internal drift monitor for matrix effects. The monitored isotopes of the major and trace elements of interest are: ^{24}Mg, ^{27}Al, ^{44}Ca, ^{47}Ti, ^{51}V, ^{52}Cr, ^{55}Mn, ^{57}Fe, ^{59}Co, ^{60}Ni, ^{63}Cu, ^{66}Zn, ^{72}Ge, ^{88}Sr, ^{89}Y, ^{90}Zr, ^{91}Zr, ^{93}Nb, ^{118}Sn, ^{137}Ba, ^{139}La, ^{140}Ce, ^{141}Pr, ^{146}Nd, ^{147}Sm, ^{153}Eu, ^{157}Gd, ^{159}Tb, ^{163}Dy, ^{165}Ho, ^{166}Er, ^{169}Tm, ^{172}Yb, ^{175}Lu, ^{178}Hf, ^{181}Ta, ^{232}Th and ^{238}U. Analytical uncertainties for all elements are better than 5%, which were derived from the multiple measurements of BHVO-2 and BHVO-1 solutions treated as unknowns.

2.4 Results

Elemental abundances of the bulk Allende and the three CAIs are listed in Table 2.1 and shown in Figures 2.3 and 2.4. The relative abundances of rare earth elements (REE) of CAIs are used to distinguish different types of CAIs (See Figure 2.1 and related text). The relative

abundances of REE are calculated by dividing the concentration of each rare earth element by its concentration in the CI chondrite, which is widely believed to represent the average composition of the Solar System for most elements. The relative REE abundances of SJ103 show mostly a flat pattern at the ~20 folds chondritic level as the typical Group I REE pattern, while SJ101 and SJ102 exhibit the generic Group II REE patterns with some variations (Figure 2.3). SJ101 has the typical Group II REE pattern with the refractory light rare earth elements (LREEs: La, Ce, Pr, Nd and Sm) and Tm at the ~20 folds chondritic level and variable depletions in ultra-refractory (Gd, Tb, Dy, Ho, Er and Lu) and more volatile (Eu and Yb) REEs. In contrast, SJ102 has LREE and Tm abundances at only 4-5 folds chondritic levels, strong depletions in ultra-refractory REE (Gd, Tb, Dy, Ho, Er and Lu), a slight depletion in Yb and a positive Eu anomaly. An apparent conclusion we can draw from the REE patterns of the three CAIs is, as already suggested in literature, that formation of the CAIs is mainly controlled by evaporation and condensation processes rather than melting processes. Otherwise we would see a much smoother REE pattern than the group II pattern due to the fact that all REE elements have similar ionic radius and thus should show similar geochemical behavior during melting.

Table 2.1 Elemental abundances in Bulk Allende and three CAIs extracted from the meteorite (in ppm)

Elements	Bulk Allende	SJ101	SJ102	SJ103	CI
Mg	151582	109588	25863	90225	98900
Al	17718	123598	84205	138056	8680
Ca	19051	131256	111426	156686	9280
Sc	9.1	21	5.1	111	5.82
Ti	855	5962	1578	11136	436
V	93	461	254	2045	56.5
Cr	3586	768	193	873	2660
Mn	1424	27	36	65	1990
Ge	7.2	0.32	0.23	0.59	32.7
Sr	15	74	84	134	7.8
Y	2.8	3.0	1.0	33	1.56
Zr	6.7	6.4	1.5	78	3.94
Nb	0.50	2.4	1.3	4.2	0.246
Ba	4.8	19	23	55	2.34
La	0.54	4.3	1.0	4.6	0.2347
Ce	1.3	12	3.1	13	0.6032
Pr	0.20	1.8	0.4	1.9	0.0891
Nd	1.0	9.2	2.0	9.0	0.4524
Sm	0.34	2.9	0.74	3.1	0.1471
Eu	0.11	0.59	0.56	1.0	0.056
Gd	0.39	1.9	0.19	3.6	0.1966
Tb	0.07	0.31	0.023	0.72	0.0363
Dy	0.48	1.7	0.15	5.0	0.2427
Ho	0.10	0.14	0.04	1.1	0.0556
Er	0.29	0.34	0.11	3.3	0.1589
Tm	0.057	0.53	0.10	0.57	0.0242
Yb	0.33	1.6	0.64	3.3	0.1625
Lu	0.045	0.04	b.d.	0.52	0.0243
Hf	0.18	0.18	0.045	1.9	0.104
Ta	0.041	0.29	0.076	0.31	0.0142
Th	0.069	0.30	0.043	0.54	0.0294
U	0.017	0.063	0.033	0.067	0.0081

b.d.: below detection limit.

CI: The average composition of CI chondrite from (Anders and Grevesse, 1989). Analytical uncertainties for all elements are better than 5%, which were derived from the multiple measurements of BHVO-2 and BHVO-1 solutions treated as unknowns.

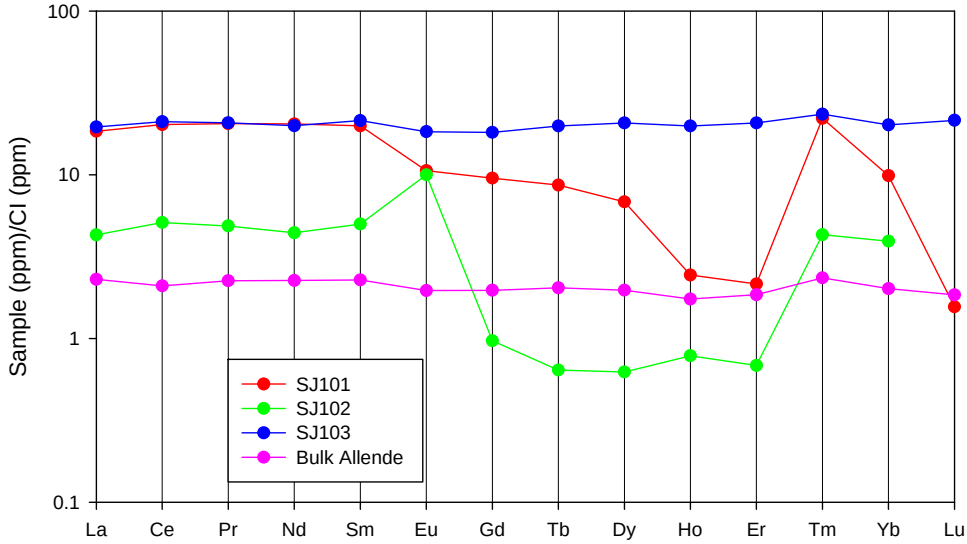

Figure 2.3 Relative REE abundances of the bulk Allende and its three CAIs shown in reverse order of ionic radius. REE abundances of CI chondrite come from Anders and Grevesse (1989).

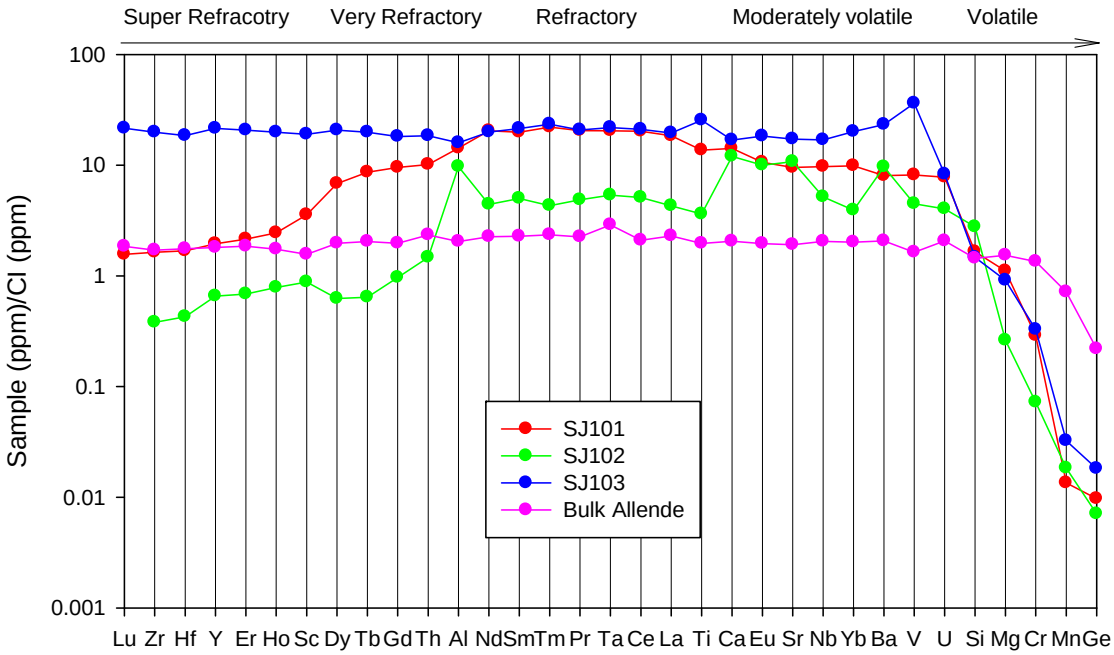

Figure 2.4 Relative elemental abundances of Allende and its three CAIs shown in order of increasing volatility (left to right). Elemental abundances of CI chondrite come from Anders and Grevesse (1989).

In order to understand the evaporation and condensation processes related to formation of the CAIs, we put all the measured elements in an order to generate a smooth relative abundance variation for the normal Group II CAI (SJ101). As shown in Figure 2.4, the order of elements indicates their relative volatility during the evaporation and condensation processes related to formation of CAIs. It provides a criterion to test any proposed hypothesis for formation of CAIs, because any plausible hypothesis should be able to explain the volatility trend of those elements.

The bulk Allende shows a generally flat pattern for relative abundances of most elements except those volatile ones (Figure 2.4). Figure 2.5 shows a closer look at the relative REE pattern of the bulk Allende. We can see that, in fact, the bulk Allende shows a Group II-like REE pattern, attributed to its CAIs with Group II REE pattern. The result is consistent with the literature data (Figure 2.5; Shinotsuka et al., 1995; Makishima and Nakamura, 2006; Lu et al., 2007; Barrat et al., 2012; Pourmand et al., 2012).

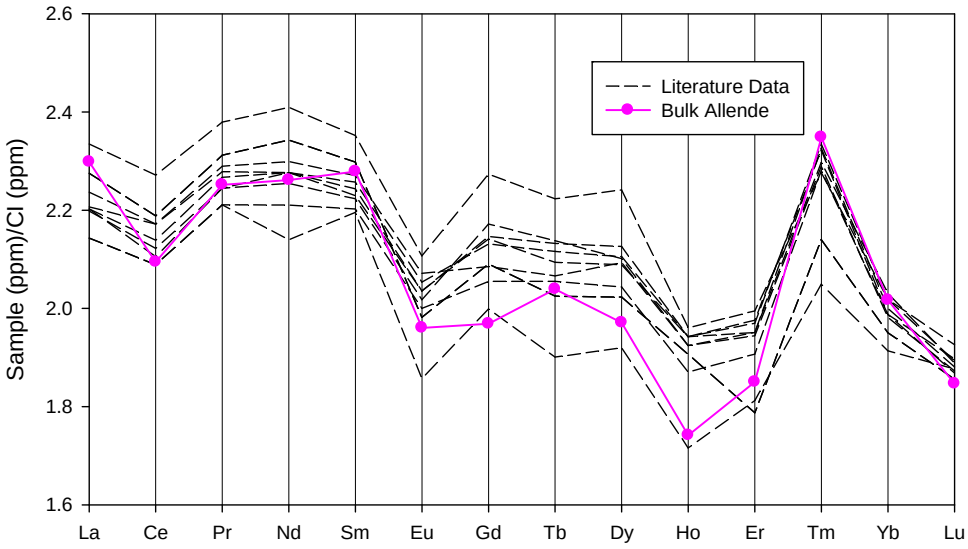

Figure 2.5 Relative REE abundances of the bulk Allende. The dashed lines represent the literature data from (Shinotsuka et al., 1995; Makishima and Nakamura, 2006; Lu et al., 2007; Barrat et al., 2012; Pourmand et al., 2012). REE abundances of CI chondrite come from Anders and Grevesse (1989).

2.5 Discussion

2.5.1 Correlation between REE Pattern and $\delta^{44/40}$Ca: Implication to the Origin of CAIs

Our REE abundances and Ca isotope data of the three CAIs as well as those of other three refractory inclusions from Allende (CGI, WFG and GFG from Huang et al., 2012) are shown in Figure 2.6. There are negative correlations in $\delta^{44/40}$Ca vs. $(Tm/Er)_{CI}$ and $\delta^{44/40}$Ca vs. $(Nd/Er)_{CI}$ (the subscript CI denotes CI chondrite normalization), with R^2 of 0.60 and

0.84, respectively. It is well accepted that inter-mineral elemental fractionation cannot generate the Group II REE pattern (e.g., Table 1 in Beckett et al., (2006)). The inter-mineral Ca isotopic fractionation have been observed among different rock-forming minerals, such as orthopyroxene and clinopyroxene (Huang et al., 2010). However, it is much smaller (<1‰ in $\delta\ ^{44}Ca/^{40}Ca$) compared to the observed $\delta^{44/40}Ca$ variation in our analyzed refractory inclusions (from -5.60 to +0.35; Figure 2.6). Then, the large correlated isotopic-elemental fractionation effects ($\delta^{44/40}Ca$ vs. Tm/Er and Nd/Er) must reflect the primary formation process of the CAIs.

Since the equilibrium isotope partition coefficients approach 1 at high temperature (Urey, 1947; Richter et al., 2002), the equilibrium isotopic fractionation between gas and condensed phases at the temperatures of interest here should be very small (less than 1-2‰ per amu). Alternatively, some kinetic (non-equilibrium) fractionation processes are independent of temperature and thus capable of producing significant isotopic fractionation even at high temperature. In the kinetic cases, an evaporation residue tends to be enriched in heavy isotopes (Ireland et al., 1992; Simon and DePaolo, 2010), while a condensate would be enriched in light isotopes until an element is fully condensed (Richter, 2004; Simon and DePaolo, 2010).

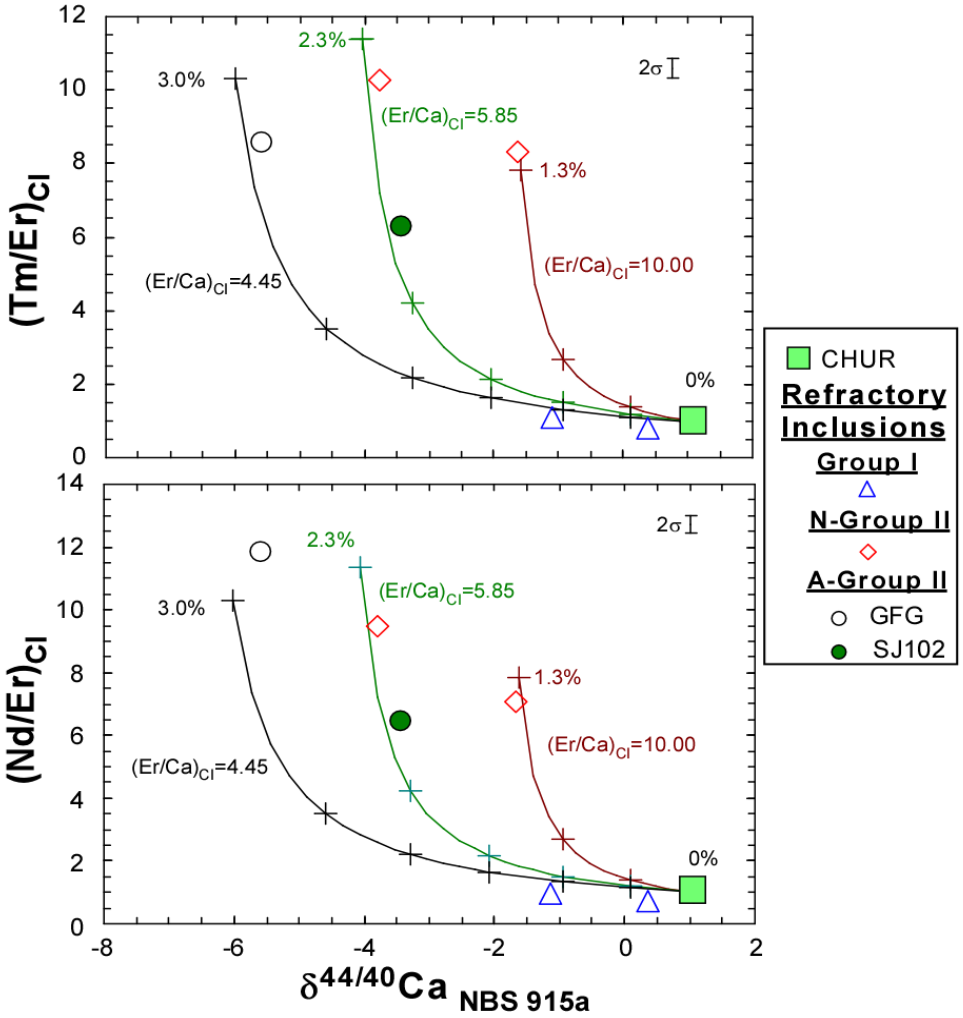

Figure 2.6 The relationship between the $\delta^{44/40}$Ca, $(Tm/Er)_{CI}$ and $(Nd/Er)_{CI}$ ratios in the three CAIs we studied as well as the other three refractory inclusions from (Huang et al., 2012). The analytical error on $\delta^{44/40}$Ca is smaller than the symbols, and the typical analytical errors on Tm/Er and Nd/Er are shown in the upper right corner. The subscript CI denotes CI chondrite normalized values. The curves show the evolution of $\delta^{44/40}$Ca, $(Tm/Er)_{CI}$ and $(Nd/Er)_{CI}$ ratios of a chondritic system after segregation of different amounts of a ultra-refractory evaporation residue from it. The ultra-refractory evaporation residue is assumed to have both $(Tm/Er)_{CI}$ and $(Nd/Er)_{CI}$ ratio of 0.25 (El Goresy et al., 2002; Hiyagon et al., 2003) and a hibonite-like CaO of 9% and $\delta^{44/40}$Ca of +28 (Lee et al., 1979; Ireland et al., 1992). Three curves show the cases that the ultra-refractory evaporation residues have different $(Er/Ca)_{CI}$ ratios. The tick marks on the curves show the amounts of the ultra-refractory residues (wt%), with 0.5% increments, segregated from a CHUR reservoir.

Our data shows that the Allende CAIs with Group II REE patterns have lighter Ca isotopes than those with Group I REE patterns. Therefore, it is very likely that the observed $\delta^{44/40}$Ca vs. Tm/Er and Nd/Er correlations are resulted from incomplete evaporation of some early material in the early Solar System. The process is also capable of producing very high $\delta^{44/40}$Ca in the evaporation-leftover refractory grains (Mason and Taylor, 1982; Niederer and Papanastassiou, 1984), which is consistent with the very heavy Ca isotopes found in HAL-type hibonites from the CV3 Allende, H3 Dhajala and CM2 Murchison chondrites (Lee et al., 1979; Hinton et al., 1988; Ireland et al., 1992).

Therefore, we propose the following CAI formation model to explain the observed negative $\delta^{44/40}$Ca-$(Tm/Er)_{CI}$ and $\delta^{44/40}$Ca-$(Nd/Er)_{CI}$ trends (Figure 2.6). The process started with a high-temperature heating event that partially vaporized dusts suspending in the solar nebula, leaving behind a small amount of an ultra-refractory residue (maybe hibonite), characterized by high $\delta^{44/40}$Ca and low $(Tm/Er)_{CI}$ and $(Nd/Er)_{CI}$. Correspondingly, the vapor phase is characterized by low $\delta^{44/40}$Ca and a Group II REE pattern, i.e., high $(Tm/Er)_{CI}$ and $(Nd/Er)_{CI}$. Then the temperature dropped as the system cooled down. The subsequent condensation of the vapor produced refractory inclusions or their precursors. Therefore, the new condensate formed the refractory inclusions with a Group II REE pattern coupled with light Ca isotopes. The

refractory inclusions that formed from the mixture of the newly condensate and the ultra-refractory evaporation residue ended up with a REE pattern varied from the Group II to the Group I (flat), and a Ca isotopic composition varied from the light one towards the chondritic value.

It is assumed that the starting dusts in the Solar System have chondritic REE pattern and Ca isotopic composition ($\delta^{44/40}$Ca = +1.05) and the ultra-refractory evaporation residue have a hibonite-like CaO content of 9%, $\delta^{44/40}$Ca of +28, and both $(Tm/Er)_{CI}$ and $(Nd/Er)_{CI}$ ratios of 0.25 as was found in the ultra-refractory nodules (Lee et al., 1979; Boynton et al., 1980; Ireland et al., 1988; Ireland et al., 1992; Simon et al., 1996; El Goresy et al., 2002; Simon et al., 2002; Hiyagon et al., 2003). Curves in Figure 2.6 illustrate the evolution of Tm/Er and Nd/Er ratios, and Ca isotopic compositions in a chondritic system that has lost different amounts of an ultra-refractory evaporation residue. The results are also a function of $(Er/Ca)_{CI}$ ratios in the ultra-refractory evaporation residue.

The model calculations imply that the observed $\delta^{44/40}$Ca-$(Tm/Er)_{CI}$ and $\delta^{44/40}$Ca-$(Nd/Er)_{CI}$ trends could be produced by segregation of a small amount of the ultra-refractory residue, which accounts for only 0.5-3 wt% of the initial chondritic reservoir. Nevertheless, these small amounts (0.5-3%) of segregated ultra-refractory residue contain 3% to 20% of the Ca budget in the initial chondritic reservoir.

2.5.2 Concentrations of Slightly Volatile and Siderophile Elements in Bulk Earth

Here, following (Allègre et al., 1995), we construct the volatile trends with our Allende data and average compositions of other carbonaceous chondrites from our complied dataset in the plots of $(Mg/Ca)_{CI}$ ratio vs. $(V/Ca)_{CI}$, $(Cr/Ca)_{CI}$, $(Mn/Ca)_{CI}$ or $(Si/Ca)_{CI}$ ratio (Figure 2.7) in order to estimate the bulk Earth concentrations of V, Cr, Mn and Si. It can be seen that carbonaceous chondrites do show clear linear correlations in the plots.

Since Mg and Ca generally do not enter the Fe-Ni metal phase, the bulk Earth should have a same Mg/Ca ratio to that of bulk silicate Earth ($(Mg/Ca)_{CI}$ = 0.80±0.06 from (Palme and O'Neill, 2003)). Moreover, by mass balance, the Ca concentration in bulk Earth is

$$C_{Ca,BE} = C_{Ca,BSE}(1 - r_c) \tag{2.1}$$

where the $C_{Ca,BSE}$ is the Ca concentration in bulk silicate Earth from (McDonough and Sun, 1995; Palme and O'Neill, 2003). r_c is the mass fraction of the Earth's core (~0.325).

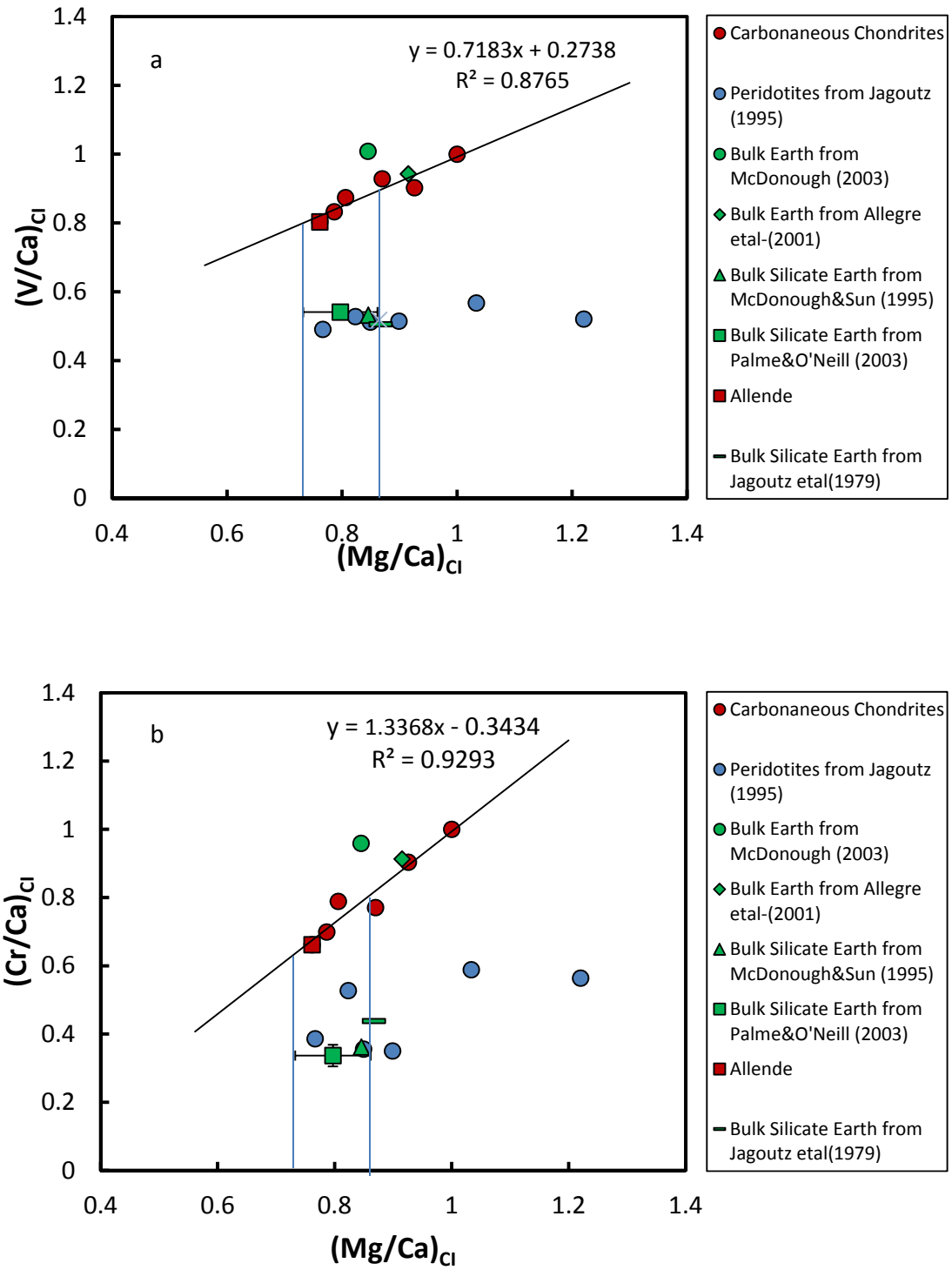

Figure 2.7 Estimation of V, Cr, Mn and Si abundances in bulk Earth by the volatility trends defined by carbonaceous chondrites. The subscript CI indicates that the ratio has been normalized to that of CI.

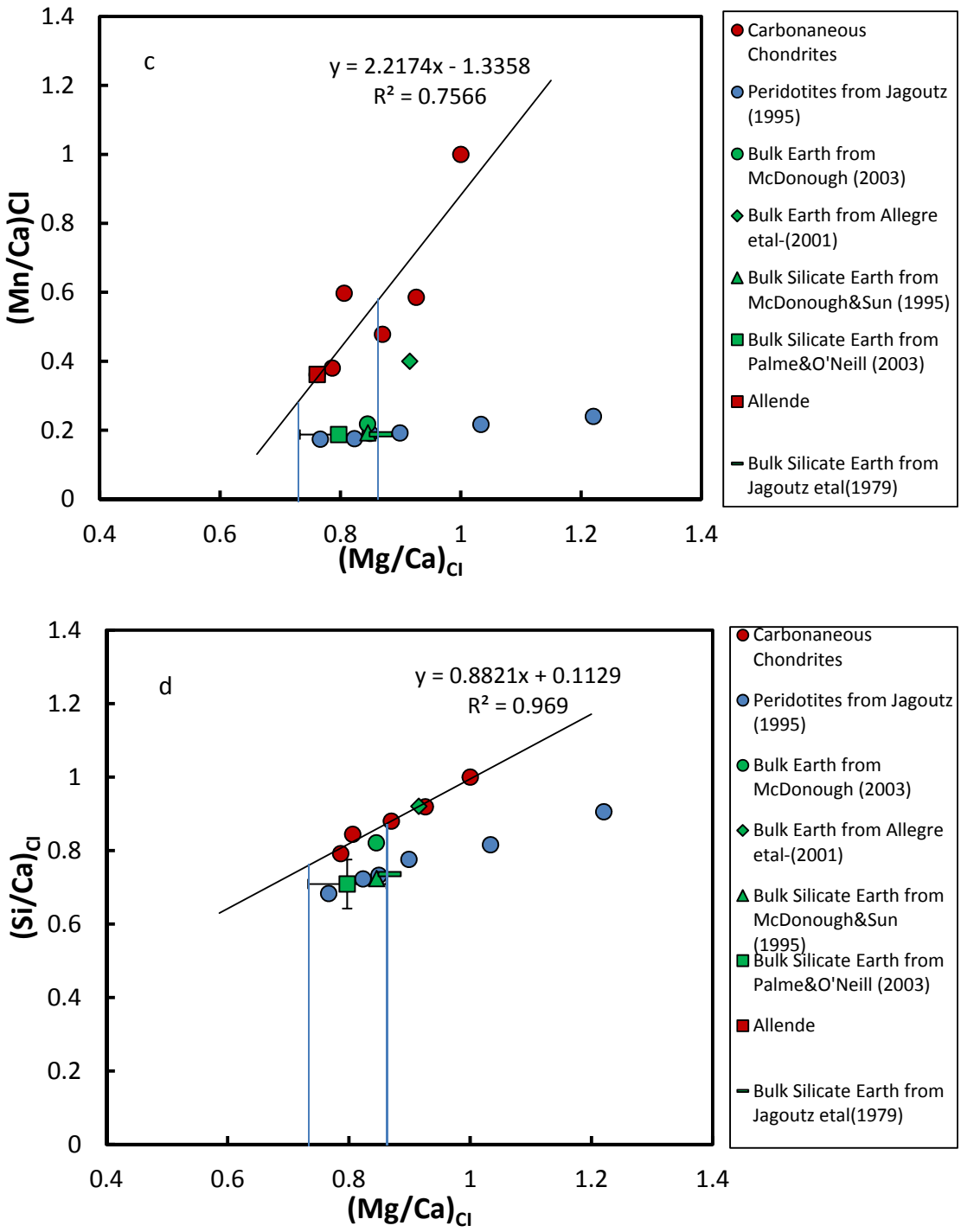

Figure 2.7 (Continued) Estimation of V, Cr, Mn and Si abundances in bulk Earth by the volatility trends defined by carbonaceous chondrites. The subscript CI indicates that the ratio has been normalized to that of CI.

In terms of those linear correlations in Figure 2.7 and Ca concentrations in bulk Earth, we can obtain the $(V/Ca)_{CI}$, $(Cr/Ca)_{CI}$, $(Mn/Ca)_{CI}$ and $(Si/Ca)_{CI}$ ratios in bulk Earth and then V, Cr, Mn and Si concentrations in bulk Earth. By mass balance, we can easily calculate the concentrations of those elements in Earth's core. Consequently, it allows us to calculate core-mantle partitioning of those slightly siderophile elements for Earth as follows:

$$D_M = \frac{C_{M,core}}{C_{M,mantle}}, \qquad M = V, Si, Cr, Mn \tag{2.2}$$

where $C_{M,\mathrm{mantle}}$ is the concentration of element M in Earth's mantle from (McDonough and Sun, 1995; Palme and O'Neill, 2003). The new partition coefficients of V, Cr, Mn and Si between Earth's core and mantle are D_{V} = 1.3 ±0.3; D_{Cr} = 2.4±0.7; D_{Mn} = 23.7±1.9 and D_{Si} = 0.39 ±0.07 as listed in Table 2.2, which are consistent with the previous estimates on Cr, Mn and Si (D_{Cr} = 2.9; D_{Mn} = 5; D_{Si} = 0.34 from Allègre et al (1995)), but with much narrower variance.

Table 2.2 Comparison of the calculated core-mantle partition coefficients of V, Cr, Mn and Si.

Core-Mantle Partition Coefficients	McDonough (2003)	Allègre (1995)	This work[a]	This work[b]
D_V	~1.80		1.17±0.13	1.3±0.3
D_{Cr}	~3.40	~2.9	2.4±0.4	2.4±0.7
D_{Mn}	~0.29	~5	2.7±1.0	3.7±1.9
D_{Si}	~0.29	~0.34	0.31±0.03	0.39±0.07

a, using bulk silicate Earth concentrations from (Palme and O'Neill, 2003). b, using bulk silicate Earth concentrations from (McDonough and Sun, 1995)

2.6 Conclusions

Our elemental abundance data combined with Ca isotope data on the same aliquot of three CAIs and other three refractory inclusions from Allende CV3 chondrite reveal the following important findings:

1. All studied refractory inclusions have a Ca isotopes composition lighter than the bulk silicate Earth.

2. Variation of REE patterns of CAIs represented by fractionations of Tm or Nd from Er are correlated with the fractionation of Ca isotopes.

3. The above observations can be explained by the segregation of 0.5-3 wt% of an ultra-refractory evaporation residue, characterized by relatively high $\delta^{44}Ca/^{40}Ca$ and low Tm/Er and Nd/Er, from the chondritic reservoir before condensation of CAI and other refractory inclusions or their precursors from the reservoir.

In addition, based on our new elemental abundances results for the Allende, we obtained new core-mantle partition coefficients of V, Cr, Mn and Si for Earth (D_V = 1.3 ±0.3; D_{Cr} = 2.4±0.7; D_{Mn} = 23.7±1.9 and D_{Si} = 0.39 ±0.07) with improved precision. The results of Cr, Mn and Si are consistent with the previous studies within errors (Allègre et al., 1995).

Chapter 3

Fast Accretion of Earth with a Low Probability Late Moon-forming Giant Impact: Evidence from ^{182}Hf-^{182}W Chronometry

Part of this chapter has been published in Yu and Jacobsen (2011), PNAS, vol. 108, no. 43, 17604-17609 and presented at the Gordon Research Conferences 2011- Origins of Solar Systems

3.1 Introduction

Solid planets are believed to form through sticking and collisions of sun-orbiting tiny objects. Accretion of solid planets begins with a young sun with a disk of gas and dust. Then dusts stick with each other to form km-sized planetesimals. In the post-planetesimal accretion stages, gravitational interaction plays a more important role and larger bodies grow faster than smaller bodies. Then, most planetesimals get swept and end up with a number of Moon- or Mars-sized planetary embryos. Finally, the solid planets form from collisions of the planetary embryos. During the accretion history of solid planets, similar growth stages have been

predicated from a variety of methods and simulations: planetesimals growth → runaway growth → oligarchic growth → chaotic growth (e.g. Agnor et al., 1999; Chambers, 2004; O'Brien et al., 2006; Canup, 2008). It was first demonstrated by (Wetherill, 1985) that the last stage of planet formation was dominated by giant impacts and it has now become well accepted (Canup, 2008). Those giant impacts in the late accretion stage of planet formation have been described as highly stochastic processes based on simulations results (Chambers, 2004), but the stochasticity has not been thoroughly studied. More specifically, the last giant impact in the Earth's accretion history between the proto-Earth and a Mars-sized impactor possibly leads to formation of the Moon (Canup and Asphaug, 2001). The hypothesis has been well studied and become the leading theory on formation of the Moon (Canup and Asphaug, 2001; Canup, 2008).

Current theories and numerical simulations argue that the Earth grew by numerous collisions between small objects to form larger ones and the last collision with a Mars-sized impactor probably gave rise to the Moon (Agnor et al., 1999; Cameron, 2000; Canup and Asphaug, 2001; Chambers, 2004; O'Brien et al., 2006). Because the core formation processes are thought to occur continuously during the accretion, the timescale of core formation in the growing Earth provides a basis for determining the timescale of formation of the Earth-Moon system (Harper

and Jacobsen, 1996; Jacobsen and Harper, 1996; Jacobsen, 2005; Rudge et al., 2010). So far, the best constraint on the timescale of formation of the Earth-Moon system is derived from a combination of ^{182}Hf-^{182}W chronology and core formation models (e.g. Harper and Jacobsen, 1996; Jacobsen, 2005; Kleine et al., 2009). A two-stage model with a single core formation event gives the time of Earth's formation of 28-35 Myr after the onset of the Solar System (Kleine et al., 2002; Schoenberg et al., 2002; Yin et al., 2002). A model with a continuous accretion and core formation process and an exponentially decreasing accretion rate leads to a mean time of the Earth's formation of 11 ±1 Myr (Yin et al., 2002). This is the time needed to accumulate ~63% of the present Earth's mass (Harper and Jacobsen, 1996). A model with an early continuous accretion and core formation immediately followed by a Moon-forming giant impact (Jacobsen, 2005) yielded a mean time of Earth's formation of ~11.5 Myr and a time of the Moon-forming giant impact of ~32 Myr (Jacobsen, 2005). Overall, all such models consistently show that the major mass of the Earth has a mean time of formation of ~11 Myr with the complete formation time of Earth, including the Moon-forming giant impact, being 30-35 Myr (cf. Kleine et al., 2009). In contrast, both recent ^{182}Hf-^{182}W isotope results and re-evaluation of ^{87}Rb-^{87}Sr isotope results for lunar rocks have been used to argue for a later formation of the Moon at 50-152 Myr or 70-110 Myr respectively (Touboul et al., 2007; Halliday, 2008). This conclusion is also

consistent with some old N-body simulations of accretion of the terrestrial planets predicting a late time (100-200 Myr) for the last giant impact on Earth (Agnor et al., 1999). One explanation for the apparent discrepancy between the ^{182}Hf-^{182}W timescale of the Earth's formation and the late time of Moon formation is an Earth core formation model assuming only partial metal-silicate equilibration (cf. Touboul et al., 2007; Halliday, 2008; Rudge et al., 2010). Unfortunately, such a disequilibrium model introduces an additional and completely unconstrained parameter -- the degree of equilibration. While this may be possible, we think an addition of a new unconstrained parameter would be justified only if the equilibrium models fail completely.

Here we developed and explored an equilibrium model of metal-silicate differentiation in the growing proto-Earth parameterized specifically to allow a simple evaluation of the conditions and timing of the Moon-forming giant impact relative to the main growth-stage of the Earth. We show that this model can explain the discrepancy between the timescale of Earth's formation deduced from the ^{182}Hf-^{182}W isotopic composition of the Earth and the recent estimates of late formation of the Moon without invoking metal-silicate disequilibrium.

By fitting the best and most reliable W isotopic data and concentrations of the five refractory siderophile elements (W, Ni, Co, V and Nb) in the Earth's mantle, we found that:

(i) the siderophile element pattern is consistent with the metal-silicate equilibration in a terrestrial magma ocean and cannot be a remnant of equilibration in Mars-sized or smaller impactors;

(ii) a late Moon formation at ~50-110 Myr, if real, requires the main stage of Earth's accretion to be completed in 8 to 12 Myr, much faster than previously recognized.

So far, no one has evaluated the giant impact from the probability perspective. Based on the model above, we developed a simple analytical formulation to parameterize the probability of the Moon-forming giant impact in terms of the timing of the impact (the age of the Moon). Combined with the modeling result above, we can calculate the probability of the Moon-forming giant impact that is believed to have terminated the Earth's accretion, which could provide some complementary information about this event.

3.2 Our Approch for Accretion and Differentiation of Terrestrial Planets

The accretion of the terrestrial planets (illustrated in Figure 3.1) is now thought to include three main stages with different accretion regimes (cf. O'Brien et al., 2006). At the first stage, the dust that settled to the mid-plane of the solar nebula coagulates to form a large population of small bodies (planetesimals). Then, within ~10^5 years, mutual collisions

and runaway accretion of planetesimals produced larger objects with the size distribution being skewed towards Moon- to Mars-sized planetary embryos, some of which eventually became terrestrial planets. At the third and final stage, some of the embryos sweep-up the smaller ones by giant impact collisions to form the terrestrial planets. At some time, one of the embryos that became dominant at 1 AU, could be identified as proto-Earth. The last major Earth-forming collision, the Moon-forming giant impact (MGI), is commonly thought to involve the proto-Earth and a Mars-sized impactor. At the end of accretion, only the Earth remained at approximately 1 AU, and the accretion process is effectively completed. It is important to realize that many larger bodies will be differentiated because of the extensive melting that is caused by giant collisions (Rubie et al., 2007). It is also widely believed that during the third stage the nebular gas has dissipated as indicated in Figure 3.1 (based on evidence from proto-stars (Haisch et al., 2001)). This astrophysical scenario for the Earth's accretion is now considered as the standard (cf. Canup and Agnor, 2000; Kortenkamp et al., 2000; Chambers, 2004; Jacobsen, 2005; O'Brien et al., 2006). An approximate schematic timescale of the Earth's accretion is shown in Figure 3.1, with the lower part of the figure illustrating the ideas about mass accretion of the Earth discussed here.

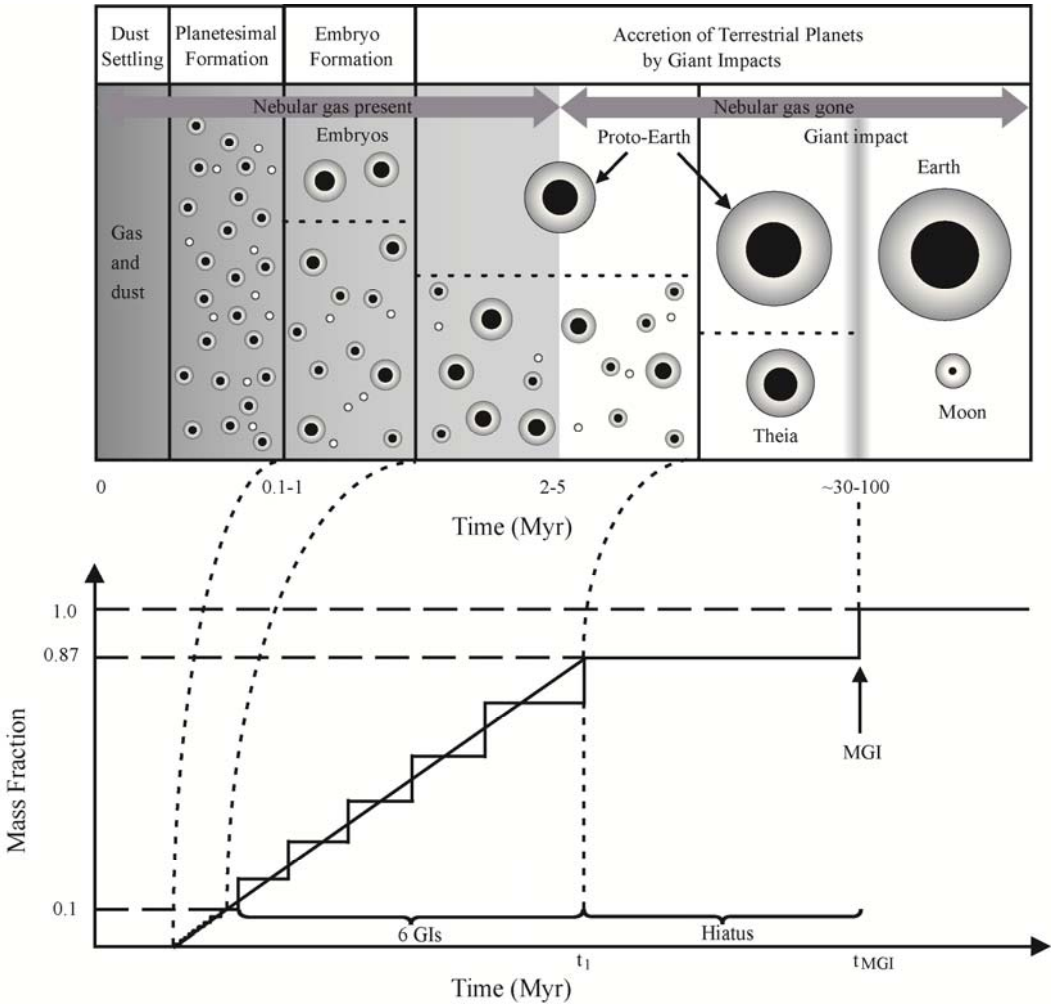

Figure 3.1 (a) The upper part is a schematic illustration of the formation of the Earth with a possible late giant moon-forming impact. There are four accretion stages: I (Dust Settling), II (Planetesimal Formation), III (Embryo Formation) and IV (Accretion of Terrestrial Planets by Giant Impact). The bodies below the dotted lines represent the left-over material in Earth's feeding zone. The shaded zone represents the presence of solar nebula which was dissipated at 2-5 million years. An approximate timescale is shown. (b) The lower part of this figure shows schematically the mass accretion history of the Earth. Initially (up to about 10%) the accretion is of planetesimals forming embryos. The main phase of accretion is by giant impacts and (~ 6 Mars-sized giant impacts or more if some are smaller) and is shown as ending at time t_{PE}. Then, there may have been a significant hiatus, before a possibly late Moon-forming giant impact (MGI) adds the last ~ 13% of the mass of the Earth at time t_{MGI}. The figure is not in scale.

The initial stage of planetesimal accretion yields numerous embryos weighing up to ~10% of the Earth's mass, with one of them eventually becoming the Earth. The Moon-forming giant impact adds the last ~ 13% of Earth's present mass. In between, the mass accreted to the Earth's embryo and then the proto-Earth was probably delivered in a series of giant impacts (GIs) involving ~ 6 Mars-sized objects or more, if the impactors were small. Previous work on the ^{182}W evolution of the Earth (Jacobsen, 2005) shows that giant impacts always erase most of the ^{182}W excess (compared to the chondritic W) in the silicate Earth. In the first ~30 Myr, the ongoing decay of the remaining ^{182}Hf (half-life = 9 Myr) can build up the ^{182}W excess again, so the observed ^{182}W excess in the Earth's mantle allows many giant impacts to occur during this period. After ~50 Myr, the recovery of the ^{182}W excess in the silicate Earth after a giant impact is insignificant, so only one such late giant impact can be allowed as described quantitatively later in the paper. Moreover, two or more late (>50 Myr) giant impacts if any would yield the Earth's mantle with essentially chondritic W, which is clearly inconsistent with the observed ^{182}W excess in the mantle (Yin et al., 2002).

Now let's quantitatively demonstrate why only one late (i.e. >50 Myr) giant impact is allowed by the W isotope constraint on the model. For simplification, we assume that the amount of ^{182}W, decaying from ^{182}Hf in the Earth's mantle, can be neglected after a "so-called" late

(i.e. >50 Myr) Mars-sized giant impact because ^{182}Hf with a short half-life of 8.9 Myr would almost completely die out by that time. Then the $\varepsilon_{W(CHUR)}$ of the Earth's mantle right after the MGI ($\varepsilon_{W(CHUR)}$ (t_f)) should be close to the observed $\varepsilon_{W(CHUR)}$ in the Earth's mantle today (~1.9). Since the bulk impactor has a $\varepsilon_{W(CHUR)}$ of 0 by definition and the impact timescale is very short compared to the timescale of ^{182}Hf decay, the $\varepsilon_{W(CHUR)}$ of the mantle before the MGI ($\varepsilon_{W(CHUR)}$ (t_i)) can be calculated using equation 76 of Jacobsen (2005):

$$\varepsilon_{W(CHUR)}(t_f) = \varepsilon_{W(CHUR)}(t_i)\left[\frac{M_{mantle}(t_i)}{M_{mantle}(t_f)}\right]^{a_{Hf/W}} \tag{3.1}$$

Given the mass ratio of the impactor to the total system is $M_E(t_{PE})/M_E(\tau_0)$ = 0.87 and $a_{Hf/W} = f^{Hf/W} + 1 = 16$ (Jacobsen, 2005), the $\varepsilon_{W(CHUR)}$ (t_i) of the mantle is 17.6. The reason for the large difference between the ε_W values before (t_i) and after (t_f) the impact is the very strong partitioning of W into the metal phase that enters the core.

From $\varepsilon_{W(CHUR)}$ (t_i) of the mantle before the MGI, a first order estimate of the time t_{PE} can be obtained for a two-stage model of core-mantle differentiation (equation 14 of (Jacobsen, 2005)):

$$t_{2stage} = \tau_{^{182}Hf} \ln\left[\frac{q_W\left(\frac{^{182}Hf}{^{180}Hf}\right)_{T_0} f^{Hf/W}}{\varepsilon_{W(CHUR)}(t_i)}\right] \tag{3.2}$$

Thus, using τ_{182Hf}= 13 Myr (the mean life of ^{182}Hf), the initial ^{182}Hf /^{180}Hf ratio of the Solar System of (^{182}Hf /^{180}Hf)$_{T0}$ =10^{-4}, q_W = 1.55×10^4 and $f^{Hf/W}$ = 15, we obtain t_{PE} = 3.6 Myr. This simple calculation strongly suggests that a late giant Moon-forming impact will require very rapid accretion of the initial 87% of the modern Earth. Repeating this calculation for two late giant impacts ($M_E(t_{PE})/M_E(\tau_0)$= 0.74), an $\varepsilon_{W(CHUR)}$ (t_i) of 164 in Earth's mantle prior to the first of these two giant impacts would be required to yield the currently observed $\varepsilon_{W(CHUR)}$ value. This high $\varepsilon_{W(CHUR)}$ (t_i) of 164 is in fact much higher than the $\varepsilon_{W(CHUR)}$ of 23.3, the maximum value that could possibly be generated (with $f^{Hf/W}$ = 15) if the first ~74% all accreted at time 0. In general, only one late Mars-sized giant impact is allowed in our model in order to yield the observed $\varepsilon_{W(CHUR)}$ of 1.9 in the Earth's mantle today. Two late Mars-sized giant impacts would essentially erase any radiogenic W isotopic effect in the Earth's mantle relative to the chondritic value that is inconsistent with observation.

In this paper we focus on evaluating how the duration of a “hiatus” between the end of the main-stage of Earth accretion and a late MGI affects the timing of these events. For the sake of analytical simplicity, the step function of the Earth’s main growth stage during accretion was approximated by a smooth function of exponential growth (illustrated by straight line in Figure 3.1). This allows a simple parameterization of the

timing of the MGI relative to the timescale of the main growth stage of the Earth (up to 87%), as discussed in the next section.

Mars-sized giant impactors supply sufficient energy to melt the entire Earth and support a deep magma ocean over the accretion history of the Earth. Also, during the main stage of the Earth's accretion and during the Moon-forming giant impact, the impactors are likely to be completely differentiated (Rubie et al., 2007). Therefore, it is crucial to develop a model that can address both the metal-silicate equilibration at different temperatures and pressures in a magma ocean and the accretion timescale based on the ^{182}Hf-^{182}W system.

Our approach to model core-mantle differentiation during the Earth's accretion is sketched in Figure 3.2. The reservoir model includes three reservoirs. The Earth is considered to grow by accreting objects from the solar nebula (reservoir 1). As the Earth grows, the accreted material is added to the silicate mantle (reservoir 2). The metallic core (reservoir 3) is segregated (no back reaction) from the mantle, therefore during accretion small metal parcels (equilibrated at some P and T in the magma ocean) are considered isolated once they enter the core.

Following (Jacobsen, 2005), we use a system of transport equations for the Hf-W system and other siderophile elements to describe evolving chemical and isotopic compositions of the Earth's mantle and core. The partitioning of elements between the silicate and metallic liquids is

calculated based on the experimental partition coefficients that vary with pressure (P) and temperature (T) during core formation. Numerical solution of these equations allows determination of P, T conditions during core formation and the timescale of the process. This model essentially combines the approaches of (Jacobsen, 2005) and (Wade and Wood, 2005).

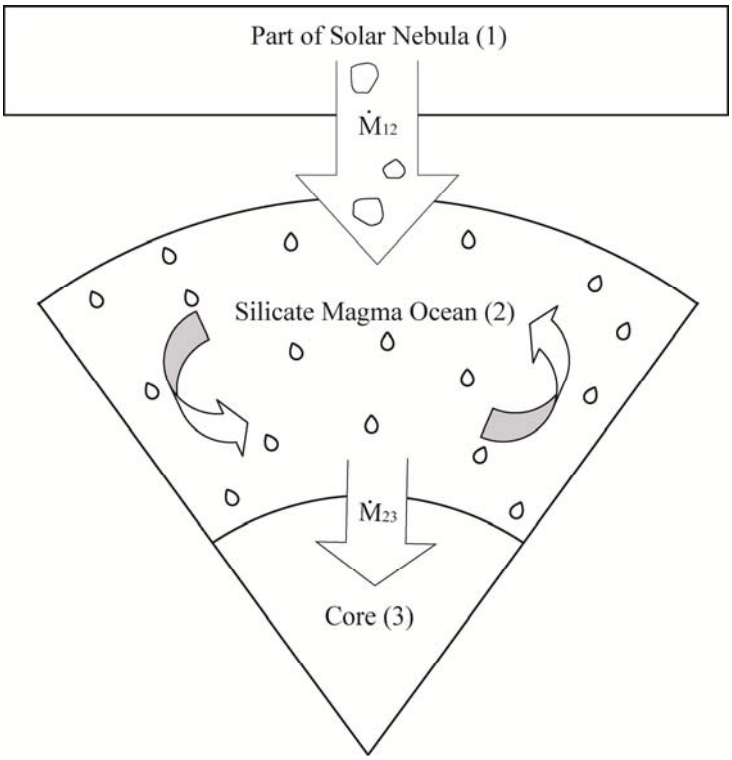

Figure 3.2 Sketch of the accretion and core formation model used in this work. The Earth is considered to grow by accreting objects from the solar nebula (reservoir 1) with a mass flux $\dot{M}_{12}(t)$. As the Earth grows, the accreted material is added to the silicate mantle (reservoir 2). The metallic core reservoir (3) is segregated as small metal parcels (chemically equilibrated with the whole magma ocean) from the mantle during accretion (with a mass flux $\dot{M}_{23}(t)$) and once in the core the metal is considered isolated (no back reaction) from the mantle. There is no direct mass transport flux from the solar nebula to the metallic core ($\dot{M}_{13}(t) = 0$). The whole mantle maintains homogeneity by rapid convection.

The previous studies show that the metal-silicate equilibrium in the terrestrial magma-ocean was attained at pressures in excess of 30-50 GPa (Li and Agee, 1996; Wade and Wood, 2005; Kegler et al., 2008) implying that at each giant impact event both the target and impactor materials must have been re-equilibrated in the Earth's mantle but not in the impactors which have core-mantle boundary pressures of less than ~20 GPa. The mechanisms of metal-silicate equilibration in the terrestrial magma ocean have been discussed by (Rubie et al., 2003). Their results show that large metal blobs (hundreds of km in size) will be reduced to cm-sized droplets while sinking through the magma ocean. Such metal droplets reach equilibrium with the surrounding silicate melt very quickly (Rubie et al., 2003).

3.3 Parameterization of the Mass Accretion History of the Earth and Probability Analysis of the Moon-forming Giant Impact

The mass of the Earth (M_E) is considered to grow from a primitive solar nebular reservoir with a growth rate proportional to the available mass [$M_E(\infty)$ - $M_E(t)$] at any time t, where $M_E(\infty)$ is the mass of the Earth at infinite time when the accretion of the Earth ends and α is the growth constant:

$$\frac{dM_E}{dt} = \alpha\left[M_E(\infty) - M_E(t)\right] \tag{3.3}$$

Integrating from t = 0 to t results in an exponentially decreasing accretion rate expressed as: $M_E(t)/M_E(\infty) = 1 - e^{-\alpha t}$. Because the present mass of Earth $M_E(\tau_0) \approx M_E(\infty)$, and τ_0 is the age of the Solar System (~4567 Myr (Amelin et al., 2010)), the growth rate equation can be simplified to yield: $dM_E/dt = M_E(\tau_0)\, e^{-\alpha t}$. Then the mean time of formation needed to accumulate ~63% of the Earth's present mass is $t_m(\tau_0) \approx 1/\alpha$. This equation closely reproduces the Earth's growth histories predicted by stochastic accretion simulations (e.g. Wetherill, 1986; Agnor et al., 1999; Canup and Agnor, 2000; O'Brien et al., 2006) and is a good approximation of the Earth's growth history, perhaps with the exception that there may be one very late giant impact that deviates to a substantially later time compared to the exponential growth approximation.

Now let's develop an analytical formulation that helps evaluate the relationship between the timescale of the main stage of Earth's accretion and the timing of the Moon-forming giant impact. The main stage of accretion (it probably involves numerous giant impacts), assumed to follow exponential growth, ends at time t_{PE} when the proto-Earth's mass (PE) reaches $M_E(t_{PE})$. Then, the mass of the proto-Earth before the Moon-forming giant impact is given by:

$$\frac{M_E(t_{PE})}{M_E(\tau_0)} = 1 - e^{-\alpha t_{PE}} \tag{3.4}$$

The mean time of the main accretion stage of the Earth $t_m(t_{PE})$ is given by:

$$\begin{aligned} t_m(t_{PE}) &= \frac{1}{M_E(t_{PE})}\int_0^{t_{PE}} t\frac{dM_E(t)}{dt}dt \\ &= \frac{M_E(\tau_0)}{M_E(t_{PE})}\int_0^{t_{PE}} \alpha t e^{-\alpha t}dt \\ &= \frac{M_E(\tau_0)}{M_E(t_{PE})}\frac{1}{\alpha}\left[1-(1+t_1\alpha)e^{-\alpha t_1}\right] \end{aligned} \tag{3.5}$$

and since

$$\begin{aligned} e^{-\alpha t_{PE}} &= 1 - \frac{M_E(t_{PE})}{M_E(\tau_0)} \\ \Rightarrow -\alpha t_{PE} &= \ln\left[1 - \frac{M_E(t_{PE})}{M_E(\tau_0)}\right] \end{aligned} \tag{3.6}$$

We have that $t_m(t_{PE})$ is

$$\begin{aligned} t_m(t_{PE}) &= \frac{M_E(\tau_0)}{M_E(t_{PE})}\frac{1}{\alpha}\left[1-(1+t_{PE}\alpha)\left(1-\frac{M_E(t_{PE})}{M_E(\tau_0)}\right)\right] \\ &= \frac{-t_{PE}\left[1+\frac{M_E(\tau_0)}{M_E(t_{PE})}\left(1-\frac{M_E(t_{PE})}{M_E(\tau_0)}\right)\ln\left(1-\frac{M_E(t_{PE})}{M_E(\tau_0)}\right)\right]}{\ln\left(1-\frac{M_E(t_{PE})}{M_E(\tau_0)}\right)} \end{aligned} \tag{3.7}$$

The Moon-forming giant impact always occurs later than t_{PE} at time t_{MGI}, so $t_{MGI} \geq t_{PE}$. Simulations of the Moon-forming impact require the mass fraction of the impactor to be ~0.13 of the final Earth-Moon system in order to match its astronomical characteristics (Canup, 2004). Neglecting the small mass of the Moon, the mass ratio of the pre-impact

Earth to the Earth is $M_E(t_{PE})/M_E(\tau_0)$ = 0.87. This results in t_{PE} = 2.93t_m. Figure 3.3a shows an example of an accretion history of the Earth assuming $M_E(t_{PE})/M_E(\tau_0)$ = 0.87 and a Moon-forming giant impact at t_{MGI} = 45 Myr. In this case, in order to match the Hf/W ratio and the W isotopic composition of the present Earth's mantle, 87 % of Earth's mass has to be accreted in t_{PE} = 10.2 Myr, corresponding to a mean time for the main accretion stage of t_m = 3.5 Myr.

We treat the Moon-forming giant impact as a stochastic event and t_{MGI} as a random variable. Thus, the time gap between the first continuous accretion stage and the Moon-forming giant impact (t_h) is also a random variable (t_h = t_{MGI} – t_{PE}). Since t_h is the waiting time for occurrence of the Moon-forming giant impact, it should naturally follow an exponential distribution and has the following probability density function:

$$f(t)=\begin{cases}\theta e^{-\theta t} & t \geq 0 \\ 0 & t<0\end{cases} \tag{3.8}$$

where $\theta = 1/E(t_h)$ by definition and $E(t_h)$ is the expected waiting time of occurrence of the Moon-forming giant impact ($E(t_h) = E(t_{MGI})$ – t_{PE}). Assuming the expected timing of the Moon-forming giant impact ($E(t_{MGI})$) will be on the accretion path extended from the stage I and actually $E(t_{MGI})$ is the mean time of the continuous process that the Earth's mass accreted from $M_E(t_{PE})$ to $M_E(\tau_0)$ following the same exponential accretion

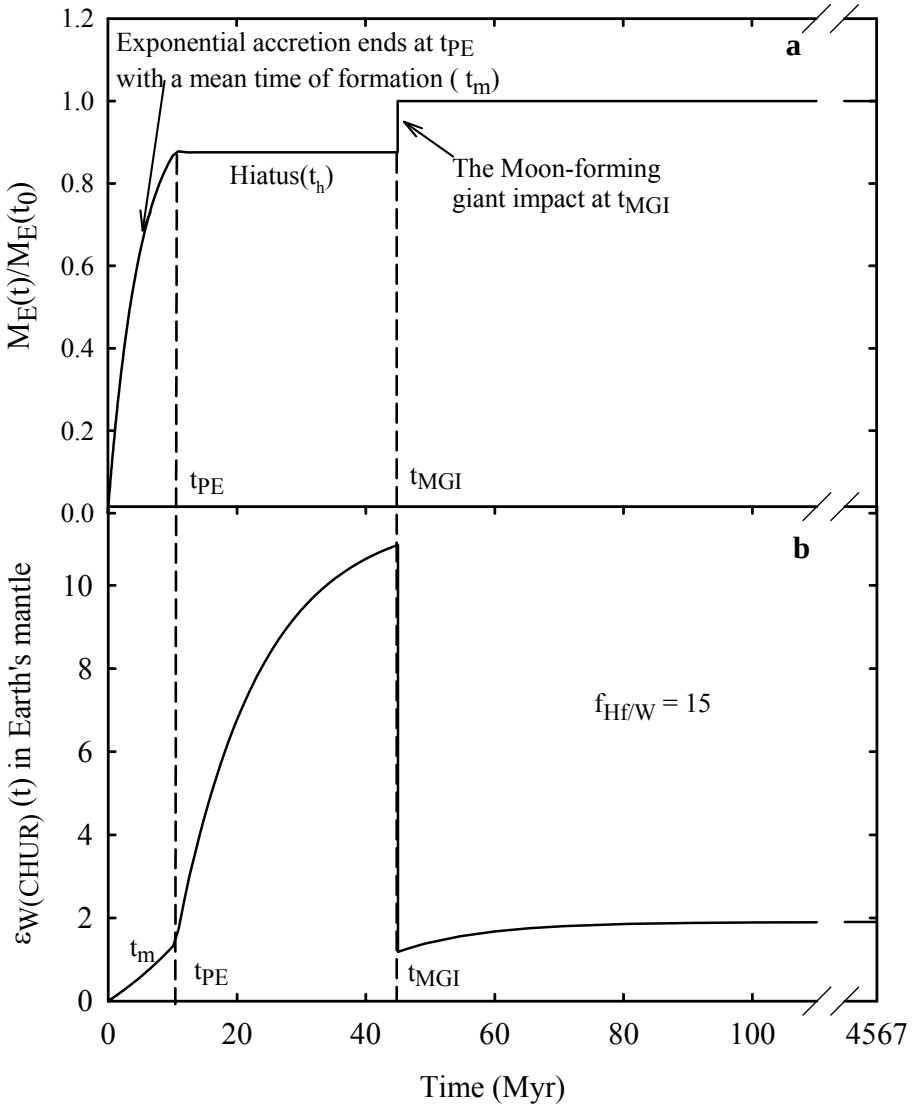

Figure 3.3 (a) The fractional mass of Earth as a function of time in our model which is composed of an early continuous accretion and core formation stage and a later Moon-forming giant impact. The growth curve shows an early continuous accretion and core formation process with a mean time of 3.5 Myr (t_m = 3.5 Myr) and the Moon-forming giant impact occurs at t_{MGI} = 45 Myr. The mean time of formation of the proto-Earth in this model is defined as the time taken to build ~63% of Earth's present mass. (b) The calculated W isotopes evolution in the silicate Earth corresponding to the accretion scenario in (a) with a Hf/W ratio ($f^{Hf/W}$ = 15) and matching the present W isotopic composition of the Earth's mantle ($\varepsilon_{W(CHUR)}$ = 1.9 ± 0.2).

rate:

$$E(t_{MGI}) = \frac{1}{1 - M_E(t_{PE})} \int_{t_{PE}}^{\tau_0} t \frac{dM_E(t)}{dt} dt = t_{PE} + \frac{t_{PE}}{\ln\left[\frac{1}{1 - M_E(t_{PE})}\right]} \tag{3.9}$$

τ_0 is the age of the Solar System (~4567 Myr (Amelin et al., 2010)).

Then,

$$\theta = \frac{1}{E(t_h)} = \frac{1}{E(t_{GI}) - t_{PE}} = \frac{1}{t_{PE}} \ln\left[\frac{1}{1 - M_E(t_{PE})}\right] \tag{3.10}$$

Therefore, the probability (Pr) that the Moon-forming giant impact happens later than a specific time T is:

$$\begin{aligned} \Pr(t_{MGI} > T) &= \Pr(t_h > T - t_{PE}) \\ &= \int_{T - t_{PE}}^{\infty} f(t) dt \\ &= \int_{T - t_{PE}}^{\infty} \theta e^{-\theta t} dt \\ &= e^{-\theta(T - t_{PE})} \\ &= e^{\ln[1 - M_E(t_{PE})]\left(\frac{T}{t_{PE}} - 1\right)} \end{aligned} \tag{3.11}$$

3.4 Modeling Siderophile Element and W Isotopic Evolution of the Growing Earth

During accretion and core formation of the Earth, the conditions of the metal-silicate equilibration, such as temperature, pressure, redox conditions are changing with time as the Earth grows. To model this effect explicitly, we adopted the 'deep magma ocean' core formation model of (Jacobsen, 2005) developed for the ^{182}Hf-^{182}W system. We added to this

model transport equations describing partitioning (maintaining system mass balance) of the siderophile elements Ni, Co, V and Nb (in addition to W) between metal and silicate liquids using metal/silicate partition coefficients that are allowed to vary as Earth grows in response to the changing pressure, temperature and redox condition. To reflect the physical conditions in the mantle up to the values at the core-mantle boundary as Earth grows, we used available thermodynamic fits (to *P*, *T* and f_{O2}) of experimentally determined metal-silicate partition coefficients (Righter, 2003; Wade and Wood, 2005; Corgne et al., 2008; Cottrell et al., 2009, 2010).

Because the partition coefficients depend upon redox conditions, we use the Fe content in the mantle as a proxy for redox condition at each step, thus cancelling out the f_{O2} dependence. During the early continuous accretion (mass fraction of the Earth is <0.2) the Fe content in the mantle is assumed equal to 14%, close to the average Fe contents in mantles of Mars and Vesta (Righter et al., 2006). After the Moon-forming giant impact (mass fraction of the Earth is >0.87), the Fe content is assumed to be 6.26%, which is the average Fe content in Earth's mantle today (McDonough and Sun, 1995). In the intermediate stage, the Fe content is 1.01% corresponding to a reduced accretion stage that is required to make the observed core-mantle concentration ratio of V consistent with the calculated one using experimental partition coefficient

of V (Wood et al., 2008).

At each step before the Moon-forming giant impact, after adding a parcel of new material (with chondritic average composition) to the growing Earth, we calculate new concentrations of trace elements and the W isotope composition of the mantle. The pressure at the core-mantle boundary in the accreting Earth is assumed to evolve as

$$P_{CMB}(t) = P_{CMB}(\tau_0)\left[\frac{M_E(t)}{M_E(\tau_0)}\right]^{2/3} \tag{3.12}$$

where $P_{\mathrm{CMB}}(\tau_0)$ is the pressure at the core-mantle boundary of Earth today (~136 GPa). The pressure of metal-silicate equilibration is set to be the pressure at the core-mantle boundary in the accreting Earth except during the Moon-forming giant impact when it is inferred by best fitting the modeled current mantle concentrations of five siderophile elements with the observed values. The temperature of metal-silicate equilibrium is always fixed on the peridotite liquidus as a function of pressure by

$$T(t)=1973+28.57P(t) \tag{3.13}$$

following Wood (2008).

Then we calculate the partition coefficients at these conditions, the amount of newly-formed metallic liquid assuming constant core mass fraction in the Earth of 0.325, and the concentrations of trace elements in the metallic liquid. Finally, after segregating the newly-formed metal into the core, the concentrations of trace elements in the mantle and the core,

the concentration ratios in the core relative to the mantle (C_{core}/C_{mantle}), and W isotopic composition of the mantle are calculated.

3.4.1 Element and Isotope Transport Model

The model used throughout this work is a geochemical reservoir model, which was first introduced by Harper and Jacobsen (1996) and evaluated in greater details with new data by Jacobsen (2005). In this model, $M_j(t)$ is defined to be the total mass of reservoir j at time t . Three reservoirs are considered (j = 1, 2, 3): reservoir 1 is part of solar nebular reservoir, reservoir 2 is the Earth's silicate mantle reservoir and reservoir 3 is the Earth's metal core reservoir. As above, $M_E(t)$ is the total mass of the growing Earth at time t, and thus, by mass balance,

$$M_E(t)=M_2(t)+M_3(t) \tag{3.14}$$

We use dM_{jk} to denote the mass flux from reservoir j to k. The rate of growth of Earth (the mass accretion rate) is then $dM_E(t)/dt=dM_{12}$ and at any time point, the mass fraction of newly formed core is defined as $\gamma = dM_{23}/dM_{12}$. In the case, γ is constant and we can obtain very simple relationship between our parameterized accretion of the Earth given above and the core formation process.

$$M_2(t) = (1-\gamma)M_E(t) \tag{3.15}$$

$$M_3(t) = \gamma M_E(t) \tag{3.16}$$

In this work we used the transport equations for the Hf-W system

of Jacobsen (2005) but integrated with a W partition coefficient that is allowed to vary as a function of time during core formation ($D_W^{metal/silicate}(t)$). The value of this parameter is obtained from the experimental data in section 3.4.3.

We have divided the calculations up in four stages consistent with the accretion scenario in Figure 3.3. The core formation model of Jacobsen (2005) for the ^{182}Hf-^{182}W system is generalized to include variable partition coefficients, using experimental constraints on W partitioning as a function of pressure (P), temperature (T) and mantle iron content (instead of f_{O_2}) during segregation of metallic core material from the silicate mantle. Other trace elements that are used to constrain the P, T conditions core formation follow the same treatment as for W concentrations.

(I) Stage 1 ($0 \le t \le t_1$): Continuous accretion and core formation

For this stage we integrated numerically the following differential equations for the ^{182}Hf-^{182}W system ($D_{Hf} = 0$) for the chemical and isotopic evolution of the Earth's mantle:

$$\begin{cases} \dfrac{dC_{W2}(t)}{dt} = \dfrac{C_{W1} - [\gamma D_W(t) + 1 - \gamma] C_{W2}(t)}{(1-\gamma) M_E(t)} \dfrac{dM_E(t)}{dt} \\ \dfrac{df_2^{Hf/W}(t)}{dt} = \dfrac{\left[\gamma D_W(t) - \dfrac{C_{W1}}{C_{W2}(t)}\right] f_2^{Hf/W}(t) + \gamma D_W(t)}{(1-\gamma) M_E(t)} \dfrac{dM_E(t)}{dt} \\ \dfrac{d\varepsilon_{W2}^*(t)}{dt} = Q_d^*(t) f_2^{Hf/W}(t) - \dfrac{C_{W1}}{C_{W2}(t)(1-\gamma)} \dfrac{dM_E(t)}{M_E(t)} \varepsilon_{W2}^*(t) \end{cases} \tag{3.17}$$

The differential equation for $\varepsilon_{W2}^*(t)$ in the mantle is the same as equation (72) in Jacobsen (2005). The initial conditions are:

$$\begin{cases} C_{W2}(0) = \dfrac{C_{W1}}{\gamma D_W(0) + 1 - \gamma} \\ f_2^{Hf/W}(0) = \dfrac{\gamma D_W(0)}{1-\gamma} \\ \varepsilon_{W2}^*(0) = 0 \end{cases} \tag{3.18}$$

(II) Stage 2 ($t > t_{PE}$): The hiatus prior to the Moon-forming giant impact

In this stage, there is a hiatus before the Moon-forming giant impact happening at t_{MGI}. During the hiatus, there is no accretion or core formation. So the ^{182}Hf-^{182}W system in the Earth's mantle follows the equations of the standard closed system with free decay only.

(III) Stage 3: Evolution of Earth's mantle during and shortly after the giant impact

At t_{MGI}, the Moon-forming giant impact by a Mars-sized impactor terminates the Earth's accretion and forms the Earth-Moon system. We employ a mass ratio of impactor and proto-Earth of 0.13/0.87 (an average ratio from Canup (2004)) and mass of Moon is ignored in calculation. The mixing and core formation processes right after the Moon-forming giant impact will end very quickly (<10^3 years; Cameron (2000); Canup (2004); Canup (2008); Canup and Asphaug (2001)). Let t_{MGI}^{+} be the time when core formation process caused by the giant impact ends. Therefore, during Δt (t_{MGI}^{+} -t_{MGI}), the radioactive decay can be assumed to be negligible. The masses of the Earth before and after the Moon-forming giant impact are, respectively

$$\begin{cases} M_E\left(t_{MGI}\right) = M_E\left(t_{PE}\right) \\ M_E\left(t_{MGI}^{+}\right) = 1 \end{cases} \tag{3.19}$$

The same differential equation are still valid but can now be integrated by neglecting radioactive decay to yield:

$$\begin{cases} C_{W2}\left(t_{MGI}^{+}\right) = C_{W2}\left(t_{MGI}\right)\left[\dfrac{M_E\left(t_{MGI}\right)}{M_E\left(t_{MGI}^{+}\right)}\right]^{a_{Hf/W}} + \dfrac{C_{W1}}{\gamma d_{W23} + 1 - \gamma}\left[1 - \left(\dfrac{M_E\left(t_{MGI}\right)}{M_E\left(t_{MGI}^{+}\right)}\right)^{a_{Hf/W}}\right] \\ f_2^{Hf/W}\left(t_{MGI}^{+}\right) = f_2^{Hf/W}\left(t_{MGI}\right)\dfrac{C_{W2}\left(t_{MGI}\right)}{C_{W2}\left(t_{MGI}^{+}\right)}\left(\dfrac{M_E\left(t_{MGI}\right)}{M_E\left(t_{MGI}^{+}\right)}\right)^{a_{Hf/W}} \\ \varepsilon_{W2}^{*}\left(t_{MGI}^{+}\right) = \varepsilon_{W2}^{*}\left(t_{MGI}\right)\dfrac{C_{W2}\left(t_{MGI}\right)}{C_{W2}\left(t_{MGI}^{+}\right)}\left(\dfrac{M_E\left(t_{MGI}\right)}{M_E\left(t_{MGI}^{+}\right)}\right)^{a_{Hf/W}} \end{cases} \tag{3.20}$$

where $a_{Hf/W}=(\gamma D_W+(1-\gamma))/(1-\gamma)$ and for this stage D_W is considered a constant as we are solving for a single equilibration condition for the giant impact stage.

(IV) Stage 4: Evolution after the giant impact and till the present

Similar to the hiatus, after t_{MGI}, there is another free decay period (up to the present) without accretion and transport of elements and isotopes following the closed system equations.

3.4.2 Equilibrium Partitioning between Metal and Silicate during Core Formation

For metal-silicate partitioning of an element (M) we use the standard definition of the partition coefficient (D):

$$D_M^{met-sil}=\frac{C_M^{metal}}{C_M^{silicate}} \tag{3.21}$$

where C_M^{metal} and $C_M^{silicate}$ represent the concentrations in weight fractions of M in the metal and silicate phase, respectively.

Core formation process in Earth could be mainly described as an iron and wüstite reaction and similar reactions for other siderophile elements (M):

$$\begin{cases} FeO_{silicate} \leftrightarrow Fe_{metal} + \dfrac{1}{2}O_2 \\ MO_{\frac{\upsilon}{2}silicate} \leftrightarrow M_{metal} + \dfrac{\upsilon}{4}O_2 \end{cases} \tag{3.22}$$

where v is the effective valence of metal M. These equilibria depend directly on the oxygen fugacity (f_{O_2}). The direct f_{O_2} dependence can be cancelled out by instead considering exchange equilibria. The metal-silicate exchange reaction between Fe and metal M is:

$$\frac{\upsilon}{2}Fe_{metal} + MO_{\frac{\upsilon}{2}silicate} \leftrightarrow M_{metal} + \frac{\upsilon}{2}FeO_{silicate} \tag{3.23}$$

In this way, the partitioning of M becomes a direct function of the Fe content in Earth's core and mantle through the D_{Fe} partition coefficients. The thermodynamic equilibrium constant for this reaction is

$$\begin{aligned} K &= \frac{a_M^{Metal}\left(a_{FeO}^{silicate}\right)^{\frac{\upsilon}{2}}}{\left(a_{Fe}^{metal}\right)^{\frac{\upsilon}{2}} a_{MO_{\frac{\upsilon}{2}}}^{silicate}} \\ &= \frac{X_M^{metal}\gamma_M^{metal}\left(X_{FeO}^{silicate}\right)^{\frac{\upsilon}{2}}\left(\gamma_{FeO}^{silicate}\right)^{\frac{\upsilon}{2}}}{\left(X_{Fe}^{metal}\right)^{\frac{\upsilon}{2}}\left(\gamma_{Fe}^{metal}\right)^{\frac{\upsilon}{2}} X_{MO}^{silicate}\gamma_{MO}^{silicate}} \end{aligned} \tag{3.24}$$

where a is activity, X is mole fraction and γ is the activity coefficient. Thus,

$$\log_{10} K = \log_{10}\frac{X_M^{metal}}{X_{MO_{\frac{\upsilon}{2}}}^{slicate}} + \frac{\upsilon}{2}\log_{10}\frac{X_{FeO}^{silicate}}{X_{Fe}^{metal}} + \log_{10}\frac{\gamma_M^{metal}}{\gamma_{MO_{\frac{\upsilon}{2}}}^{silicate}} + \frac{\upsilon}{2}\log_{10}\frac{\gamma_{FeO}^{silicate}}{\gamma_{Fe}^{metal}} \tag{3.25}$$

and we replace the mole fraction terms with weight fractions or D values through the following relationship

$$\frac{X_M^{metal}}{X_{MO_{\frac{\upsilon}{2}}}^{silicate}} = k\frac{C_M^{metal}}{C_M^{silicate}} = kD_M^{met-sil} \tag{3.26}$$

and we obtain:

$$\begin{aligned}\log_{10} D_M^{met-sil} = \frac{\upsilon}{2}\log_{10} D_{Fe}^{met-sil} + \log_{10} K + \log_{10} k\left(\frac{\upsilon}{2}-1\right) \\ -\log_{10}\frac{\gamma_M^{metal}}{\gamma_{MO_{\frac{\upsilon}{2}}}^{silicate}} - \frac{\upsilon}{2}\log_{10}\frac{\gamma_{FeO}^{silicate}}{\gamma_{Fe}^{metal}}\end{aligned} \tag{3.27}$$

Here k is a constant due to the conversion from mole fractions to weight fractions. For partitioning between a typical terrestrial peridotite mantle and the core, we obtained $k \approx 0.9714$.

3.4.3 Experimentally Determined Partition Coefficients

The equilibrium partitioning data in the literature has been fitted to the following equation:

$$\log_{10} K = \frac{\Delta S_r^0(T_0)}{R^*} - \frac{\Delta H_r^0(T_0)}{R^*}\frac{1}{T} - \frac{\Delta V_r^0}{R^*}\frac{P}{T} \tag{3.28}$$

where $R^* = R\log_{10}(e)$ where R is the gas constant, S is entropy, H is enthalpy, V is volume and T_0 is some reference temperature. This form assumes that $\Delta C_p = 0$ (C_p is heat capacity at constant pressure) and ΔV^0 remains constant as a function of temperature and pressure.

The effect of chemical composition of silicate ($\gamma_{MO_{\frac{\upsilon}{2}}}^{silicate}$) is typically expressed as a function of N (the molar ratio of non-bridge oxygen tetrahedral cations in the silicate melt), where N =2.7 for peridotite. Thus

$D_M^{met-sil}$ can be expressed as a function of temperature, pressure and composition through the following relationship:

$$\log_{10} D_M^{met-sil} = \frac{\upsilon}{2}\log_{10} D_{Fe}^{met-sil} + a + b\frac{1}{T} + c\frac{P}{T} + dN - \log_{10} \gamma_M^{metal} + \frac{\upsilon}{2}\left(\log_{10} \gamma_{Fe}^{metal} - \log_{10} \gamma_{FeO}^{silicate}\right) \tag{3.29}$$

where the constants a, b, c and d can be identified by the following thermodynamic parameters:

$$\begin{cases} a = \dfrac{\Delta S_r^0(T_0)}{R^*} + \log_{10} k\left(\dfrac{\upsilon}{2} - 1\right) \\ b = -\dfrac{\Delta H_r^0(T_0)}{R^*} \\ c = -\dfrac{\Delta V_r^0(T_0)}{R^*} \end{cases} \tag{3.30}$$

The activity coefficients of elements in the metal phase are assumed to depend on temperature as

$$\gamma_M^{metal}(T) = \left[\gamma_M^{metal}(T^*)\right]^{T^*/T} \tag{3.31}$$

where T^* is a reference temperature of 1,873 K.

The parameters for the partition coefficients of Ni, Co, V, Nb, W and Fe we use in our models are given in the Table 3.1. The values for W are from Cottrell et al. (2009, 2010). The values for Ni, Co and V are from Wade and Wood (2005) and Wood (2008) (including corrections communicated to us by B. Wood). The values for Nb and Fe are from Corgne et al. (2008). The γ_M^{metal} values in Table 3.1 and $\gamma_{FeO}^{silicate} = 3$ are also from Corgne et al. (2008).

Table 3.1 Parameters for the metal-silicate partition coefficients of Ni, Co, V, Nb, W and Fe

$$(\log_{10} D_M^{met-sil} = \frac{\upsilon}{2}\log_{10} D_{Fe}^{met-sil} + a + b\frac{1}{T} + c\frac{P}{T})$$

	a	*b*	*c*	*d*	υ/2	$\gamma_M^{metal}(T^*)$
Ni	0.5	3100	-78±5	-0.073±0.015	1	0.6819
Co	0.01	2511	-45±11	0	1	0.479
Nb	4.09	-15500	-166±31	-0.75±0.16	2.5	0.1107
V	0.855	-8548	-62±19	-0.101±0.029	1.5	0.1076
W	3.2	-1605	553±93	-0.85±0.03	2.26	0.9411
Fe						0.8762

* refer to main text for data sources.

To evaluate the $D_{Fe}^{met-sil}$ term, the Fe content in Earth's core is fixed to 85.5%. Fe content in Earth's mantle is set to be 14 % in the early accretion stage (mass fraction of the Earth is <0.2), which is close to the average Fe contents in mantles of Mars and Vesta during core formation, and 6.26% in the last accretion stage (mass fraction of the Earth is >0.87), which is the average Fe content in Earth's mantle today. In the intermediate stage (mass fraction of the Earth is 0.2-0.87), the Fe content is determined to fit the observed elemental abundances and experimental partitioning data above. This yields a value of 1.01% for this stage.

3.4.4 Basic Constraints for the Model

The "observed" concentration ratios of the refractory siderophile elements Ni, Co, W, V and Nb in the core relative to the mantle (C_{core}/C_{mantle}) can be estimated with some certainty from bulk silicate Earth and chondritic abundances (McDonough and Sun, 1995) (Table 3.2),

because no correction for the volatile loss during Earth's formation is needed.

Table 3.2 The observed and inferred concentrations of siderophile elements (in ppm) and W isotopic composition in Earth's mantle (the bulk silicate Earth), the bulk Earth and the core

	Mantle	Bulk Earth	Core	Core/Mantle
C_{Ni}	1,995±135	18200	51,857	26±2
C_{Co}	102±6	880	2,496	24.5±1.5
C_{W}	0.01575±0.00250	0.17	0.4906	31.15±6.2
C_{V}	86±7	94	111	1.3±0.3
C_{Nb}	0.546±0.076	0.44	0.22	0.4±0.4
C_{Fe}	62,600	320,130	855,000	13.66
C_{Hf}	0.283	0.191	0	0
$f^{Hf/W}$	15 ±3	≡0	-1	
$\varepsilon_{W(CHUR)}$	1.9 ±0.2	≡0	-1	

* refer to main text for data sources.

Table 3.2 gives the observed and inferred concentrations (in ppm) in Earth's mantle (the bulk silicate Earth), the bulk Earth and the core, as well as current estimates of

$$f^{Hf/W} = \frac{(Hf/W)_{mantle}}{(Hf/W)_{CHUR}} - 1 \tag{3.32}$$

and

$$\varepsilon_{W(CHUR)} = \left[\frac{\left(^{182}W/^{183}W\right)_{mantle}}{\left(^{182}W/^{183}W\right)_{CHUR}} - 1 \right] \times 10^4 \tag{3.33}$$

in the mantle. Here CHUR indicates the values in average chondritic meteorites and assumed to be equal to the bulk Earth ratios. These

estimates are used as constraints for the modeling in this chapter.

The bulk Earth (BE), mantle and core concentrations of Ni, Co, Nb and Fe are from McDonough (2003) and the values and uncertainties for C_{core}/C_{mantle} are from Wood (2008) and Chapter 2. The parameters in Table 3.2 are related through the simple mass balance relationship:

$$C_{BE} = (1-\gamma)C_{BSE} + \gamma C_{core} \tag{3.34}$$

where γ = 0.325 is the core mass fraction in the Earth. The mantle and core concentrations have been adjusted to be consistent with the equation above and the C_{core}/C_{mantle} values and uncertainties of Wood (2008) and Chapter 2. The Hf concentration in the core is assumed to be 0 and the mantle and bulk Earth values are from McDonough and Sun (1995). The $f^{Hf/W}$ value includes the range given in several recent publications (Jacobsen, 2005; Arevalo and McDonough, 2008; König et al., 2011). The W concentrations in the Table 3.2 are inferred from the Hf concentrations and $f^{Hf/W}$ values. The V concentrations are from a combination of our own unpublished data and those cited by McDonough and Sun (1995) and Wood (2008).

A successful model of Earth's accretion must satisfy the present isotopic composition of the Earth's mantle ($\varepsilon_{W(CHUR)}$ = 1.9 ±0.2; (Yin et al., 2002)) and a Hf/W weight ratio of 18 ±3 (Jacobsen, 2005; Arevalo and McDonough, 2008; König et al., 2011). This corresponds to a Hf/W fractionation factor relative to chondrites of $f^{Hf/W}$ =

$(^{180}Hf/^{183}W)_{mantle}/(^{180}Hf/^{183}W)_{CHUR} - 1 = 15 \pm 3$.

^{182}Hf decays to ^{182}W with a half-life of 8.90 ±0.09 Myr and a decay constant $\lambda_{^{182}Hf}$ = 0.078 ±0.001 Myr^{-1} (Vockenhuber et al., 2004). The initial $^{182}Hf/^{180}Hf$ and $^{182}W/^{183}W$ of the solar system are (1.0 ±0.1)×10^{-4} and 1.850664 ±37 respectively. The best estimates on $^{180}Hf/^{183}W$ and $^{182}W/^{183}W$ of the chondritic reference value (CHUR=chondritic uniform reservoir) are 2.836 and 1.850948 ±37 respectively (Jacobsen, 2005). Thus, the $Q_W^*(t)$ parameter used in evaluating the W isotopic evolution in the earth can be calculated as follows:

$$Q_W^*(t) = \lambda_{^{182}Hf} e^{-\lambda_{^{182}Hf} t} \left[\frac{^{182}Hf(0)}{^{180}Hf(0)}\right]_{CHUR} q_W = 0.078\times10^{-4}\times e^{-0.078t}\times q_W \qquad (3.35)$$

Where $q_W = \left[\frac{^{180}Hf(0)}{^{180}W(t)}\right]_{CHUR}\times10^4 \approx \left[\frac{^{180}Hf(0)}{^{180}W(0)}\right]_{CHUR}\times10^4 = 1.55\times10^4$

Thus, q_W can to a very good approximation be treated as a constant.

3.5 Results and Discussion

3.5.1 Metal-silicate Equilibration Pressure during Earth's Growth

At the last step, after the addition of the final 13% of the Earth mass by the Moon-forming giant impact, we calculate the pressure and temperature of the metal-silicate equilibration in an iterative procedure

that involves (i) initial assumption on the value of equilibration pressure, (ii) calculation of the corresponding temperature from the peridotite liquidus curve, (iii) calculation of partition coefficients and values of C_{core}/C_{mantle}, (iv) comparison of the calculated (C_{core}/C_{mantle}) values with the "observed" ones in the present Earth using a least square fitting technique, and (v) changing the pressure and repeating steps ii through iv until the best fit between the modeled and "observed" ratios is obtained for all five elements (see Figure 3.4). Finally, the Hf/W ratio and the W isotopic composition in the mantle are calculated.

We explored a range of *P*, *T* conditions of the metal-silicate equilibration in the growing Earth by assuming the pressure of metal-silicate equilibration to be a fraction of that of the core-mantle boundary at any given Earth mass. Overall, regardless of the assumed equilibration pressure before the MGI, the equilibration pressure after the MGI is always in the range of 40-50 GPa. We also found that a decrease in the pressure of metal-silicate equilibration, relative to the core mantle boundary pressure, during the Earth's main accretion stage invariably results in an increase, by up to ~25 %, in the pressure of the final metal-silicate equilibration after the MGI. Therefore, in order to place lower limits on the pressure of the final metal-silicate equilibration below we discuss only the scenarios assuming equilibration at the core-mantle boundary during the main stage of Earth accretion.

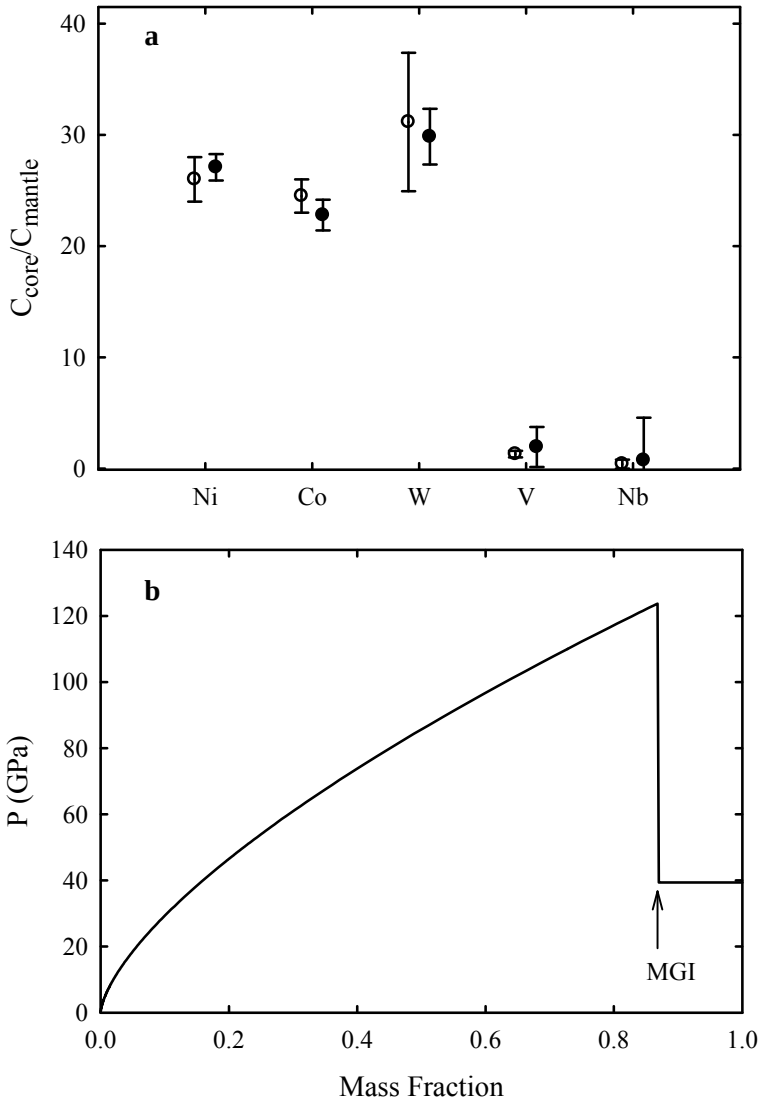

Figure 3.4 a) Observed (open symbols) concentration ratios of five siderophile and refractory elements (Ni, Co, W, V and Nb) between Earth's mantle and core are compared with the corresponding values calculated from our model and experimentally determined partition coefficients (solid symbols). b) The metal-silicate equilibration pressure during the Earth's accretion and core formation history is shown as a function of the fractional mass of the accreting Earth. The equilibration pressure in the magma ocean is fixed to to be at the core/mantle boundary except during the Moon-forming giant impact when it is calculated to be ~40 GPa to be consistent with observational and experimental constraints.

Figure 3.4a shows an example of the final concentration ratios calculated for the accretion scenarios as the example shown in Figure 3.4b. There is excellent agreement between the modeled and "observed" concentration ratios. The final concentration ratios of W, Ni and Co are primarily controlled by the MGI stage, because their strongly siderophile behavior has depleted themselves from the pre-MGI Earth's mantle. In contrast, the concentration ratios of the less siderophile V and Nb could potentially provide more information on the physical conditions of metal-silicate equilibration in the pre-MGI Earth's mantle, but their concentration ratios are less well established. The final equilibration pressure (~40 GPa) obtained for this accretion scenario (Figure 3.4b) is consistent with previous estimates for both static and continuous magma ocean models that are typically in the range of ~30-50 GPa (Li and Agee, 1996; Righter, 2003; Wade and Wood, 2005; Wood et al., 2008; Cottrell et al., 2009, 2010).

Thus, both previous and our results show that the siderophile element pattern of the Earth's mantle is consistent with high-pressure metal-silicate equilibration in a terrestrial magma ocean and cannot be inherited from the Mars-sized or smaller impactors. Therefore, there is no need to introduce the degree of equilibration as an additional parameter. The lower than the current core-mantle boundary pressure (~136 GPa) of metal-silicate equilibration estimated by us may indicates either (i) a

problem with extrapolating the experimental partition coefficients to core-mantle boundary conditions, beyond their experimentally determined range (typically < 25 GPa) or (ii) some important contributions from additional factors are not included in our model, such as ponding of metal above a crystal cumulate pile filling up the magma ocean with time (c.f Li and Agee, 1996).

3.5.2 The Timing of the Moon-formation and the Rate of Main-stage Accretion for the Earth

To facilitate comparison with earlier work and evaluate the effect of including variations in the Hf/W ratio during accretion on the resulted timescale of the main accretion stage of the Earth (t_{PE}) and the timing of the Moon-forming giant impact (t_{MGI}), we explored accretion models with both a constant and variable partition coefficient for W (D_W). The more realistic variable D_W case results in a Hf/W ratio that varies by more than an order of magnitude during accretion.

First, for simplicity, let's discuss a case of constant D_W (and therefore $f^{Hf/W}$). Figure 3.3b shows the evolution of the W isotopic composition of the silicate Earth calculated for the accretion scenario of Figure 3.3a with the MGI at 45 Myr and a constant $f^{Hf/W}$ = 15. The W isotopic composition during the Earth's main growth stage increases slowly because of the continuing addition of material with the average

chondritic W and ongoing segregation of radiogenic W into the core. After the completion of the main stage of Earth accretion (t_{PE} in Figure 3.3b), the mantle remains as a closed system and retains radiogenic W causing rapid growth of $\varepsilon_{W(CHUR)}$ because of its high Hf/W ratio and that ^{182}Hf is still live. The Moon-forming giant impact (t_{MGI} in Figure 3.3b) induces the last major episode of metal segregation that removes much of the accumulated radiogenic W isotope signature and results in a sharp drop in the $\varepsilon_{W(CHUR)}$ value. This sharp drop is due to addition of large amounts of W with average chondritic isotopic composition ($\varepsilon_{W(CHUR)}$ = 0). It will be discussed quantitatively later. The final W isotopic composition matches that of the present Earth's mantle.

Figure 3.5 shows the relationships between the timing of the Moon-forming giant impact (t_{MGI}), the timescale of the main accretion stage of the Earth (t_{PE}), and the mean time of accretion (t_m) for models with constant D_W and $f^{Hf/W}$ = 15 (curves with open symbols) and variable D_W (curves with solid symbols). All curves show a clear inverse relationship between the timing of the Moon-forming giant impact (t_{MGI}) and the timescale of the main accretion stage (t_{PE}). We note that the inverse relationship between t_{PE} and t_{MGI} is robust and not strongly dependent on the exact evolution of D_W metal-silicate partition coefficient during accretion. For t_{MGI} less than 40 Myr, there is a little difference between the models with constant and variable D_W. However, for t_{MGI} > 60 Myr,

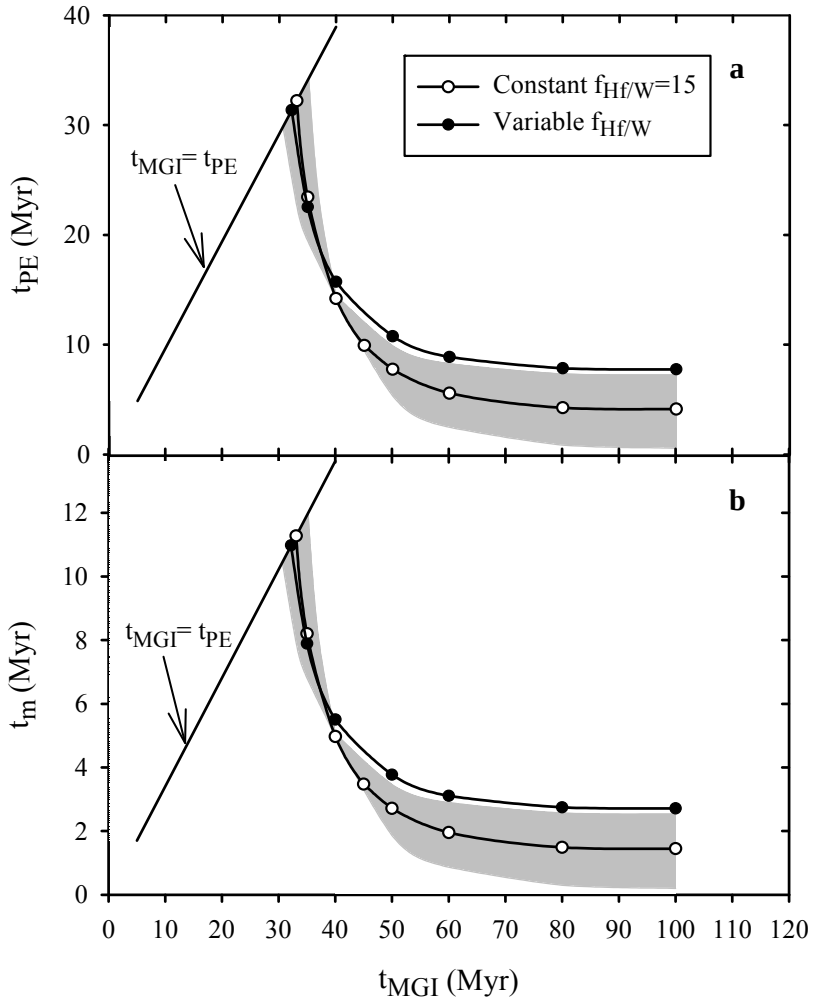

Figure 3.5. a) The time scale (t_{PE}) of the main accretion stage of the proto-Earth as a function of the timing of the Moon-forming giant impact (t_{MGI}) inferred from the W isotopic composition in Earth's mantle today. The curve with the solid symbols shows the result that includes using experimentally determined partition coefficients for Ni, Co, W, V and Nb to determine their partitioning into the core during accretion. This results in $f^{Hf/W}$ of the mantle varying by over an order of magnitude during accretion but being constrained to end with a value of 15. The curve with the open symbols is for the case that $f^{Hf/W}$ of the mantle has the current value of 15 throughout accretion history of Earth. An error band for this curve is shown as the shaded area. The upper limit for t_{MGI} > 40 Myr corresponds to $f^{Hf/W}$ = 12 and the lower to $f^{Hf/W}$ = 18. A similar error band (not shown for clarity) applies to the curve with the solid symbols. The solid straight line shows the case that the Moon-forming giant impact happens right after the early continuous accretion (t_{MGI} = t_{PE}). b) The mean time of formation of the proto-Earth (t_m) as a function of the timing of the Moon-forming giant impact (t_{MGI}) for the same case shown in a).

the model with constant D_W predicts accretion rates (in terms of t_m and t_{PE}) that are two times faster than in the case of variable D_W. For example, the model with constant D_W yields t_{PE} ~ 5 Myr, while the more realistic model with variable D_W yields t_{PE} ~ 10 Myr (Figure 3.5a).

The earliest possible time of a Moon-forming giant impact is ~30 Myr, immediately after the completion of the main accretion (straight line labeled $t_{MGI} = t_{PE}$ in Figure 3.5). Such an accretion scenario is broadly consistent with the results from some recent high resolution N-body simulations (O'Brien et al., 2006) which give an average timescale of 14^{+11}_{-9} Myr for Earth-sized objects to reach 50% of their final mass and 34^{+42}_{-10} Myr to reach 90% of their final mass.

For late formation of the Moon (>52 Myr), our modeling results (Figure 3.5) imply that the main stage of the Earth's accretion has to complete rapidly in 10.7±2.5 Myr for a giant impact at 52 Myr and more rapidly in 7.9±3.3 Myr for a giant impact at 100 Myr. In this case, there is a long (>40 Myr) hiatus between the early continuous accretion stage and the Moon-forming giant impact. A late formation of Moon is supported by the W isotopes results on lunar rocks (Touboul et al., 2007). In particular, an upper limit to Moon formation is placed by estimates of the time of its magma ocean crystallization. Equilibration of W isotopes within the lunar magma ocean has been constrained to 62^{+90}_{-10} Myr after Solar System formation (Touboul et al., 2007), and is consistent with the

^{146}Sm-^{142}Nd results on lunar rocks (Brandon et al., 2009) suggesting the late (150^{+16}_{-13} Myr with the new ^{146}Sm half-life of 68 Myr (Kinoshita et al., 2011)) crystallization of the lunar magma ocean. Such fast accretion is broadly consistent with the ^{182}Hf-^{182}W evidence that Mars also accreted very fast in 0-5 Myr (Jacobsen, 2005), 0.9-4.8 Myr (Yu and Jacobsen, 2008) or 2-4 Myr (Dauphas and Pourmand, 2011). Fast accretion of Mars combined with our result for late formation of Moon suggests that the main stage of planetary accretion may have occurred very early, within the first ~10 Myr of the Solar System.

3.5.3 Probability Analysis of Different Accretion Scenarios

Here we employ a mass ratio of the impactor and proto-Earth as 0.13:0.87 for the Moon-forming giant impact, which is an average value from (Canup, 2004) (the mass of the Moon is ignored in calculation). It leads to the mass fraction of the proto-Earth prior to the Moon-forming giant impact ($M_E(t_{PE})$) to be 0.87. Then we plug the value into equations (3.9-3.11) and we have $t_m = 0.34t_{PE}$ and other variables as a function of t_{PE} *or* t_m: $E(t_{\rm MGI}) = 1.49t_{\rm PE}$ (or $E(t_{\rm MGI}) = 0.37t_m$), $E(t_{\rm h}) = 0.49t_{\rm PE}$ (or $E(t_{\rm h}) = 1.44t_m$), $\theta = 2.04/t_{\rm PE}$ (or $\theta = 0.70/t_m$) and the probability (Pr) that the Moon-forming giant impact happens later than a specific time T is

$$\Pr\left(t_{MGI} \geq T\right) = e^{-2.04\left(\frac{T}{t_{PE}}-1\right)} \text{ or } \Pr\left(t_{MGI} \geq T\right) = e^{-0.70\left(\frac{T}{t_m}-2.94\right)} \quad (3.36)$$

In Figure 3.6, the end point of the first continuous accretion stage is shown by the solid straight line (t_{MGI} = t_{PE} or t_{MGI} = 2.94t_m), which indicates the upper limits when the Moon-forming giant impact could occur. In general, a later Moon-forming giant impact is less likely. There is a 90% probability that the Moon-forming giant impact will occur within a narrow area between the solid straight line and the dotted line marked by 0.1 in Figure 3.6 (t_{MGI} = 2.13t_{PE} or t_{MGI} = 6.25t_m).

A inverse correlation between the timing of the Moon-forming giant impact and formation timescale of proto-Earth prior to the impact has been constrained by the ^{182}Hf-^{182}W chronometry (Yu and Jacobsen, 2011). It has been also pointed out that the inverse relationship is robust and not strongly dependent on the exact evolution of D_W metal-silicate partition coefficient during accretion. Results from models with constant D_W and $f^{Hf/W}$ = 15 (curves with open symbols) and variable D_W (curves with solid symbols) are shown in **Figure 3.6**. Combined with the constraints from the ^{182}Hf-^{182}W chronometry, we can conclude that 90% of chance the Moon-forming giant impact will occur at a narrow time interval of 30-40 Myr after the beginning of the Solar System. Correspondingly, accretion of the proto-Earth has a mean time of 6-12 Myr and ends at 18-35 Myr with a probability of 90%.

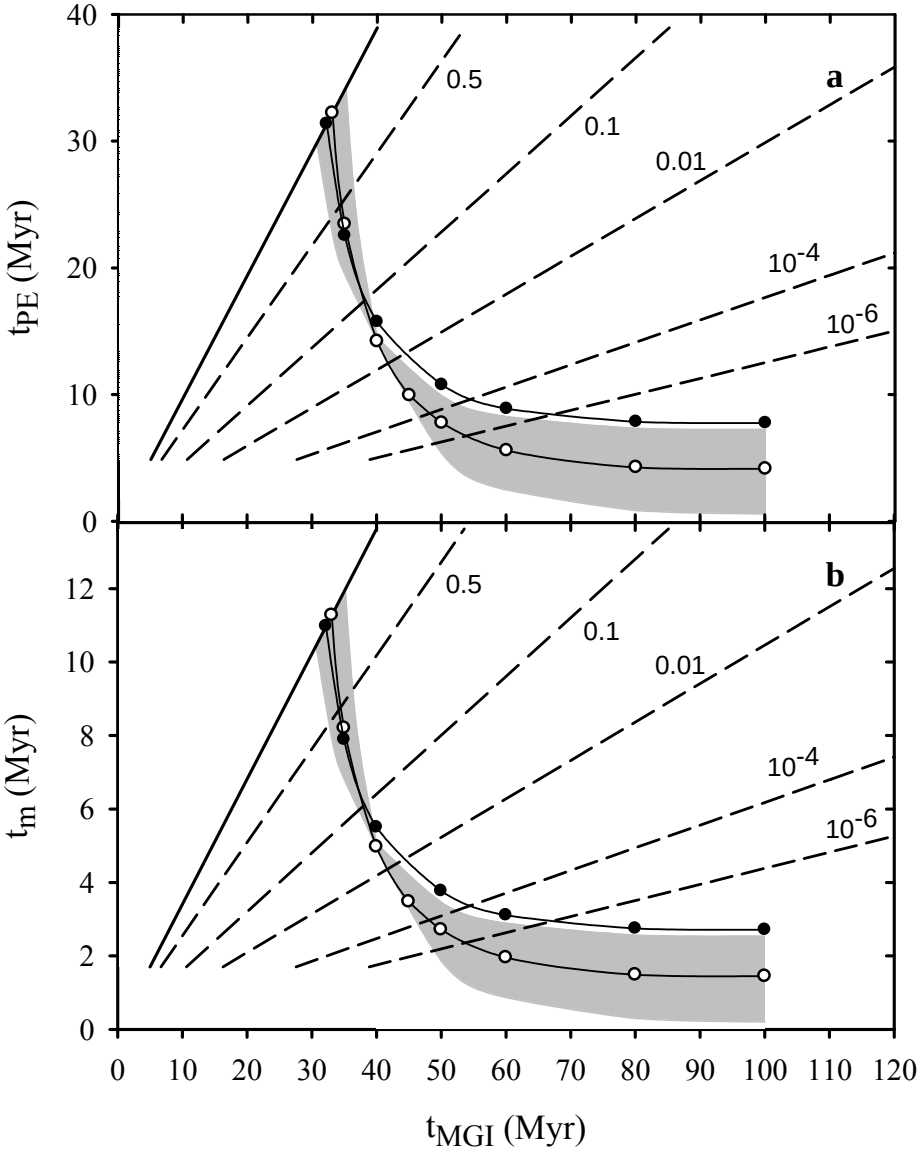

Figure 3.6 Probability of the Moon-forming giant impact occurs later than a specific time as a function of the end time (a) and mean time (b) of the proto-Earth formation. The solid straight lines (t_{MGI} = t_{PE} in (a) or t_{MGI} = 2.94t_m in (b)) show the end point of the first continuous accretion stage, which indicates the upper limit when the Moon-forming giant impact could occur. The probability that the Moon-forming giant impact happens later than a specific time is shown by the dashed straight lines. Correlations between the timescale of the proto-Earth formation and the timing of the Moon-forming giant impact (t_{MGI}) are illustrated by curves (Refer to Figure 3.5).

The late formation of the Moon (>52 or >100 Myr) suggested by isotope results of lunar rocks (Touboul et al., 2007; Halliday, 2008) implies that the proto-Earth must have formed by very rapid growth and to be completed in 10.7 ± 2.5 Myr for a giant impact at 52 Myr and 7.9 ± 3.3 Myr for a giant impact at 100 Myr based on the ^{182}Hf-^{182}W chronometry. In those cases, our probability analysis indicates that the probabilities that the Moon-forming giant impact occurred later than 52 or 100 Myr are ~3×10^{-4} and ~1×10^{-10} respectively. Therefore, the late Moon-forming giant impact (later than 52 Myr) is a very low probability event.

3.6 Conclusions

We have developed a model for accretion and core formation in the Earth that combines previous models of both ^{182}Hf-^{182}W chronometry (Jacobsen, 2005) and experimental results for refractory siderophile elements (Ni, Co, W, V and Nb) partitioning (Wade and Wood, 2005; Corgne et al., 2008; Wood et al., 2008; Cottrell et al., 2009, 2010). Our model also includes a parameterization that allow for a Moon-forming giant impact that could be substantially later than the main stage of Earth's accretion. Our conclusions are as follows:

(1) The concentrations of the refractory siderophile elements of the Earth's mantle are consistent with high-pressure metal-silicate

equilibration in a terrestrial magma ocean during the Earth's accretion. This feature cannot be inherited from Mars-sized or smaller impactors and the fact that the data are consistent with equilibrium conditions that existed only in the deep Earth and not the impactors, shows that introducing disequilibrium into the problem is not necessary.

(2) The timing of the Moon-forming giant impact is inversely correlated with the timescale of the main accretion stage of the Earth. Specifically, the earliest possible time for the Moon-forming giant impact could be at ~30 Myr, in this case also corresponding to the end of main stage accretion at ~30 Myr. A late Moon-forming giant impact (>52 Myr) requires the main stage of the Earth's accretion to be completed rapidly in 10.7±2.5 Myr for a giant impact at 52 Myr and 7.9±3.3 Myr for a giant impact at 100 Myr.

(3) Results in (2) are the two end member solutions and a continuum of solutions exists between these extremes.

(4) Only one late (>~50 Myr) Mars-sized giant impact is allowed over the accretion history of the Earth, because two would completely erase the ε_W-anomaly in the Earth's mantle, which is inconsistent with the observed ε_W anomaly (~1.9 (Kleine et al., 2002; Yin et al., 2002)).

(5) The apparent conflict between ^{182}Hf-^{182}W chronometry of terrestrial rocks when compared to recent estimates for a late formation of the Moon (>52 to 100 Myr) can be clearly understood from our results.

A late formation of the Moon is possible, but requires very fast formation of the Earth prior to the late Moon forming impact.

(6) The late Moon-forming giant impact is a very low probability event. Specifically, the probabilities that the Moon-forming giant impact occurred later than 52 or 100 Myr are ~3×10^{-4} and ~1×10^{-10} respectively, suggesting the late stage of terrestrial planet formation is highly stochastic.

Chapter 4

The Accretion Timescale of Mars Constrained by the ^{182}Hf-^{182}W Isotope System in the "Deep Magma Ocean" Core Formation Processes

4.1 Introduction

Terrestrial planets have been thought to be formed from collisions between Moon- and/or Mars-size planetary embryos (e.g. Chambers, 2004). Especially for Earth, the last one of these collisions was with a Mars-size embryos, that led to the formation of the Moon (e.g. Canup and Asphaug, 2001). Model simulation of growth of terrestrial planets (e.g. N-body simulations) has been successful to reproduce the mass and dynamic parameters of Earth and Venus, but fail to explain the small size of Mars (Wetherill, 1991; Raymond et al., 2009). Whether Mars is a leftover planetary embryo is still unclear. Timescale of formation of Mars is likely to answer the question.

The ^{182}Hf-^{182}W decay system with a half-life of 8.9 Myr (Vockenhuber et al., 2004) has been considered as the most suitable tool for dating accretion and core formation of terrestrial planets (Harper and Jacobsen, 1996; Yin et al., 2002; Jacobsen, 2005) because of its three characteristics: (1) Its half-life is comparable to the timescale of formation of planetary cores (Rubie et al., 2007). (2) Both Hf and W are refractory elements and their concentrations in planetary mantles can be estimated with some certainty compared to other isotopic systems (e.g. U-Pb and Pd-Ag). Those isotopic systems suffer from the fact that one or both parent and daughter elements is more or less volatile during accretion and their volatile loss is still difficult to be precisely determined (McDonough and Sun, 1995). (3) W is moderately siderophile (metal-loving) and Hf is lithophile (silicate-loving). Thus metal segregation during core formation would significantly fractionate Hf/W ratio in planetary mantles and then result in a significant ^{182}W anomaly after millions of years . So far most of young terrestrial rocks show a homogeneous ^{182}W anomaly ($\varepsilon_{W(CHUR)}$ = 1.9 ± 0.2 (Schoenberg et al., 2002; Yin et al., 2002; Schersten et al., 2004)). A simple two-stage model with a single core formation event suggests the Earth formed at 28-35 Myr after the onset of the Solar System (Kleine et al., 2002; Schoenberg et al., 2002; Yin et al., 2002). A model with a continuous accretion and core formation process and an exponentially decreasing accretion rate leads to a mean time of

the Earth's formation of 11 ±1 Myr after the beginning of the Solar System, corresponding to 33 ± 3 Myr when the Earth reaches 95% of its present mass (Yin et al., 2002; Jacobsen, 2005). Those previous models simply assumed a global homogeneous planetary mantle (or a "global whole-mantle magma ocean") during formation of a planetary core. However, the assumption is not supported by observations on siderophile elements in the mantles of Earth and Mars. Current results on siderophile elements (Ni, Co, V, Mo, Ga, Cu and Sn etc.) in the Earth's mantle are consistent with a core-formation model with an intermediate deep magma ocean with a thickness corresponding to 31-35% of the depth of the Earth's mantle (Wade and Wood, 2005; Wood et al., 2008b; Rudge et al., 2010; Rubie et al., 2011). Similarly, recent estimate on siderophile elements' abundances in the martian mantle suggests a metal-silicate equilibrium at 11-17 GPa during the last core formation event on Mars (Righter and Chabot, 2010), which corresponds to an intermediate deep magma ocean with a thickness of ~46-71% of the martian mantle depth. So far, the ^{182}Hf-^{182}W system in the "deep magma ocean" core formation model has not been studied yet.

Another difficulty for the "global magma ocean" core formation model is to interpret W isotopic composition of Mars. It has been reported that martian meteorites show a range of W isotope compositions. Shergottites have a $\varepsilon_{W(CHUR)}$ of 2.23 ± 0.21 and nakhlites + chassignites

have a $\varepsilon_{W(CHUR)}$ of 5.15 ± 0.50 (Foley et al., 2005). Applying the "global magma ocean" core formation model to Mars has to assume that bulk martian mantle has a shergottites-like W isotopic composition and ignoring nakhlites + chassignites with more radiogenic ^{182}W. With the assumptions, the Hf-W age of Mars varied from 0 to 15 Myr (Kleine et al., 2004; Foley et al., 2005; Nimmo and Kleine, 2007; Kleine et al., 2009; Dauphas and Pourmand, 2011). Since they ignored nakhlites and chassignites with more radiogenic ^{182}W, the relationship of the reported ages to Mars' age is not clear. In contrast, in the "deep magma ocean" core formation model, by definition, segregated core material only reaches chemical equilibrium with the upper magma ocean (part of planet's mantle) (Wade and Wood, 2005; Wood et al., 2008b; Righter and Chabot, 2011). This scenario makes it possible to produce different W isotopic compositions in the upper and lower mantle reservoirs of a planet, which may match the bimodal W isotopic composition of martian meteorites, but it hasn't been confirmed yet.

The wide range of the previous Hf-W ages comes from the poor constrained Hf/W ratio in martian mantle due to the limited ICP-MS data of martian meteorites. Two important martian meteorites – Zagami and Nakhla representing shergottite and nakhlite respectively, have no published ICP-MS data yet. Here we measure trace element concentrations of two martian meteorites – zagami and nakhla from

shergottite and nakhlite groups respectively. The results help to recognize and estimate the distinct Hf/W ratios in the mantle sources of shergottites and nakhlites + chassignites during core formation.

We also formulate a core formation model with a deep magma ocean and a solid lower mantle for the ^{182}Hf-^{182}W system and apply it to Mars. The model can lead to different Hf/W ratios and W isotopic compositions in the upper and lower mantle reservoirs of the growing Mars, which can explain the estimated Hf/W ratios and the observed W isotopic compositions of shergottites and nakhlites + chassignites. Correspondingly, a new accretion timescale of Mars is calculated based on the model.

4.2 Elemental Abundance Analysis

Two martian meteorites -- Zagami and Nakhla from shergottites and nakhlites groups respectively, were chosen for elemental concentration analyses. Zagami is basaltic shergottite and Nakhla is clinopyroxenite. About 200 mg of Zagami and Nakhla powders were dissolved for analysis. Elemental concentration analyses were performed on aliquots of the solutions at Harvard University. The sample preparation procedures and analytical methods are same as those used for Allende and CAIs analysis and have been described in Chapter 2.

Trace elements results of Zagami and Nakhla acquired in this study as well as the published ICP-MS data for other martian meteorites are listed in Table 4.1. It is known that U concentrations in martian meteorites are much lower than in the continental crust and U is easily mobilized in water-involved events. So, U/Th ratio of meteorites can be used as an indicator of contamination with terrestrial material during residence on the Earth's surface (Barrat et al., 2001). Hence six samples from two shergottites (Dar al Gani 476 and Dhofar 019) that have significantly higher U/Th ratios than the mean of chondrites (U/Th_{CI} ~ 0.276, (Anders and Grevesse, 1989)) were excluded from the following Hf/W ratio calculations.

The Hf/W ratios in mantle sources of Zagami and Nakhla cannot be directly obtained from their apparent Hf/W ratios because Hf and W behaved differently during mantle melting and crystallization. Instead, their mantle Hf/W ratio can be calculated as

$$\left(\frac{Hf}{W}\right)_{mantle} = \left(\frac{M}{W}\right)_{measured}\left(\frac{Hf}{M}\right)_{mantle} \qquad (4.1)$$

where M is a lithophile element showing similar geochemical behavior with W during mantle melting and crystallization and $(Hf/M)_{mantle}$ is assumed to be the chondritic value. Now the suitable candidates for M are Ba, Th or U (Nimmo and Kleine, 2007; Arevalo and McDonough, 2008). Ba is also a mobile element during surface weathering processes

and all samples of Dar al Gani 476 and Dhofar 019 and one sample of NWA 1068 show abnormally high Ba/W ratios. Therefore, we chose Th as the best proxy to calculate the mantle Hf/W ratio. In Figure 4.1b, Th/W ratios of martian meteorites show no significant correlation with their W concentrations although W concentration varies from 100 to 660 ppb, which supports that Th has a similar geochemical behavior with W and Th/W remain mostly unchanged during mantle melting and crystallization. It is apparent that two groups of martian meteorites -- shergottites and nakhlites + chassignites have distinct Th/W ratios. The average Th/W ratios of the two groups of martian meteorites are 0.770 ± 0.095 and 1.19 ± 0.11 respectively. Then, the corresponding Hf/W ratios in the mantles of two groups of martian meteorites can be calculated by the equation (4.1) and are expressed as $f^{Hf/W}$ = 2.56 ± 0.46 and $f^{Hf/W}$ = 4.50 ± 0.53 respectively. Here, $f^{Hf/W}$ is defined as

$$f^{Hf/W} = \frac{\frac{Hf}{W}}{\left(\frac{Hf}{W}\right)_{CHUR}} - 1 \qquad (4.2)$$

where Hf/W_{CHUR} is the average Hf/W ratio of chondrites.

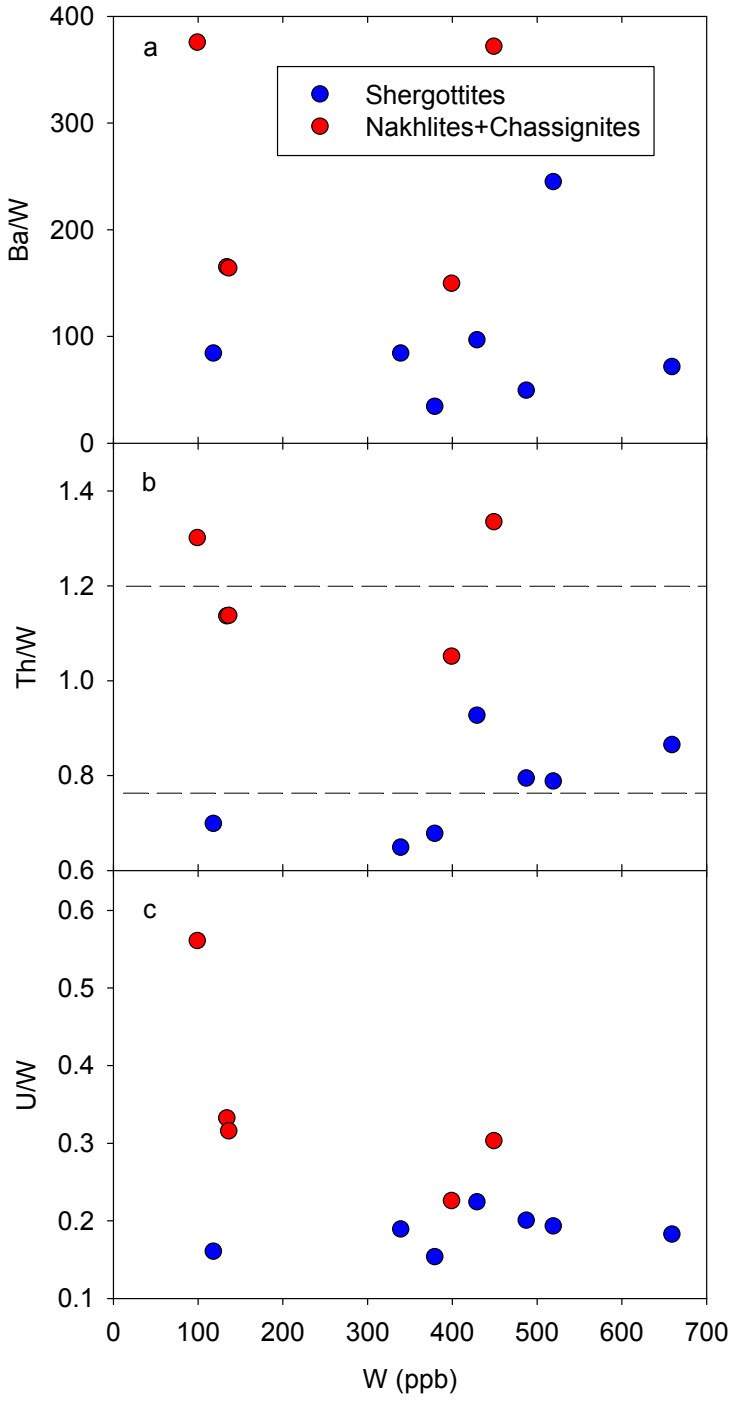

Figure 4.1 W concentration versus Ba/W (a), Th/W (b) and U/W (c) ratios in martian meteorites. Dash lines indicate the average Th/W ratios for the two groups of martian meteorites -- shergottites and nakhlites + chassignites. Data sources are listed in Table 4.1.

Table 4.1 Trace Element Concentrations of Martian Meteorites

Groups	Shergottites					
Meteorites	Dar al Gani 476			Dhofar 019		
References	a	a	a	b	b	c
Weight(mg)	93.7	62.2	138.2			115
(wt%)						
SiO_2						
TiO_2	0.33	0.41	0.38	0.49		0.49
Al_2O_3	4.53	4.96	4.17	6.65		6.65
Fe_2O_3						
FeO*	16.12	15.39	16.43	19.9		19.9
MnO	0.47	0.47	0.48	0.48		0.48
CaO	7.28	7.48	7.57	9.42		9.42
MgO	19.18	18.12	19.24	14.6		14.6
Na_2O	0.71	0.7	0.66	0.89		0.89
K_2O						
P_2O_5				0.4		0.4
(ppm)						
Li				2.88	2.84	2.86
Be				0.04	0.02	0.03
Sc	32	34	29	30.2	32.2	31.2
V				168.5	181.6	175.1
Cr				3164	3670	3417
Co	49	46.5	51.3	42.9	46.1	44.5
Ni	225	211	230	63.8	66.8	65.3
Cu	8.5	8.4	8.3	9.4	9.68	9.54
Zn	44	61	49	61.9	62.1	62
Ga	8.56	9.08	7.97	9.81	10.6	10.21
Rb	1.19	0.66	0.51	0.52	0.46	0.49
Sr	70	47	47	361	364	363
Y	7.99	9.2	8.37	6.81	6.75	6.78
Zr	9.19	10.1	9.02	15.2	19.6	17.4
Nb	0.18	0.16	0.13	0.29	0.31	0.3
Mo				0.42	0.63	0.52
Pd (ppb)				1.718		1.718
Cd (ppb)						
Sn						
Sb(ppb)				20	10	

a, (Barrat et al., 2001); b, (Neal et al., 2001) ;c, (Taylor et al., 2002)

Table 4.1(continued) Trace Element Concentrations of Martian Meteorites

Groups	Shergottites					
Meteorites	Dar al Gani 476			Dhofar 019		
References	a	a	a	b	b	c
Cs	0.02	0.013	0.012	0.02	0.03	0.03
Ba	36.4	74.3	55.7	20	18.8	19.4
La	0.157	0.121	0.111	0.24	0.24	0.24
Ce	0.372	0.327	0.286	1.48	1.42	1.45
Pr	0.06	0.062	0.049	0.1	0.11	0.11
Nd	0.42	0.494	0.422	0.65	0.73	0.69
Sm	0.304	0.391	0.352	0.51	0.45	0.48
Eu	0.186	0.201	0.179	0.17	0.23	0.2
Gd	0.751	0.967	0.922	0.96	1.01	0.99
Tb	0.163	0.227	0.204	0.2	0.2	0.2
Dy	1.23	1.59	1.46	1.32	1.28	1.3
Ho	0.282	0.352	0.328	0.27	0.27	0.27
Er	0.798	1	0.932	0.86	0.75	0.81
Tm				0.11	0.12	0.12
Yb	0.746	0.942	0.83	0.85	0.76	0.81
Lu	0.115	0.142	0.122	0.13	0.11	0.12
Hf	0.34	0.42	0.4	0.46	0.5	0.48
Ta	0.011	0.012	0.009	0.02	0.02	0.02
W(ppb)	40	20	20	10	40	30
Re ppb	0.633					
Os ppb	2.008					
Ir ppb				0.127		0.127
Pt				3.969		3.969
Ru ppb				0.354		0.354
Rh ppb				0.295		0.295
Pb						
Th	0.025	0.016	0.011	0.04	0.03	0.04
U	0.107	0.063	0.081	0.1	0.12	0.11
Ratios						
U/Th	4.28	3.94	7.36	2.50	4.00	2.75
Ba/W	910	3715	2785	2000	470	647
U/W	2.68	3.15	4.05	10.00	3.00	3.67
Th/W	0.625	0.800	0.550	4.00	0.750	1.33
Group Average Th/W						
Group Average $f^{Hf/W}$						

a, (Barrat et al., 2001); b, (Neal et al., 2001) ;c, (Taylor et al., 2002)

Table 4.1 (continued) Trace Element Concentrations of Martian Meteorites

Groups	Shergottites						
Meteorites	LosAngeles	NWA 480	NWA 856	NWA 1068	NWA 1950	RBT 04262	Zagami
References	d	e	d	e	f	g	h
Weight(mg)		182	500			~300	190.3
(wt%)							
SiO_2						47.6	
TiO_2	1.12	1.16	0.81	0.77	0.55	0.43	0.79
Al_2O_3	10.86	6.46	6.83	5.75	4.02	3.32	
Fe_2O_3							
FeO*	21.07	19.44	17.81	20.48	21.65	20.6	19.33
MnO	0.46	0.51	0.49	0.46	0.46	0.53	0.51
CaO	9.92	9.32	10.24	7.91	4.09	5.66	10.24
MgO	3.91	10.06	9.51	16.5	25.06	21.6	
Na_2O	2.24	1.26	1.28	1.14	0.81	0.59	1.14
K_2O	0.36	0.1	0.13	0.16		0.08	0.12
P_2O_5					0.65	0.39	0.74
(ppm)							
Li	5.03	2.93	4.06	4.34			
Be	0.54	0.21	0.355	0.35			0.34
Sc	41.3	28	55.7	37		31	99.2
V		202	295	280		218	308.6
Cr	219	2121	3361	4317	6400	7152	2882
Co	29.2	37.6	36.3	56.2	71	63	40.02
Ni	32	63	77	232	306	291	88.94
Cu	22.6	17.6	14	14	7.6	6.6	17.05
Zn	62.3	64	59.1	49	48.8	74	67.09
Ga	22.09	16.27	14.66	13.4	9.3	8.2	13.47
Rb	12	2.67	6.24	5.75	0.78	4	4.86
Sr	81	49.3	48.7	67	21.5	22.2	43.67
Y	29.39	16.46	18.81	17.19	9.61	9.3	17.78
Zr	79.6	58.74	62.8	62.14	26	23	59.74
Nb	4.99	1.99	3.37	4.37	1.12		4.12
Mo						0.4	
Pd (ppb)							
Cd (ppb)						42	40.20
Sn						0.11	0.30
Sb(ppb)						83	18.02

d, (Jambon et al., 2002); e, (Barrat et al., 2002); f, (Gillet et al., 2005); g, (Anand et al., 2008); h, This study;

Table 4.1 (continued) Trace Element Concentrations of Martian Meteorites

Groups	Shergottites						
Meteorites	LosAngeles	NWA 480	NWA 856	NWA 1068	NWA 1950	RBT 04262	Zagami
References	d	e	d	e	f	g	h
Cs	0.88	0.19	0.43	0.45	0.041	0.29	0.348
Ba	46.8	28.4	41.3	127	9.94	12.8	23.82
La	3.97	1.48	2.16	2.25	0.586	1.15	1.97
Ce	9.84	3.77	5.49	5.38	1.51	2.81	4.76
Pr	1.43	0.619	0.786	0.783	0.24	0.414	0.657
Nd	7.07	3.7	3.88	3.82	1.34	2.07	3.40
Sm	2.64	1.73	1.5	1.49	0.739	0.81	1.42
Eu	1.02	0.76	0.582	0.552	0.343	0.314	0.538
Gd	4.28	2.67	2.51	2.14	1.37	1.36	1.97
Tb	0.792	0.477	0.474	0.414	0.261	0.26	0.423
Dy	5.04	3.05	3.12	2.8	1.77	1.75	2.84
Ho	1.03	0.62	0.677	0.59	0.367	0.4	0.590
Er	2.76	1.57	1.87	1.63	0.984	1.07	1.70
Tm					0.141	0.155	0.265
Yb	2.35	1.33	1.64	1.37	0.81	0.96	1.58
Lu	0.331	0.19	0.251	0.198	0.12	0.145	0.230
Hf	2.19	1.64	1.55	1.58	0.82	0.97	1.72
Ta	0.28	0.1	0.16	0.2	0.064		0.202
W(ppb)	660	340	430	520	119	380	488.2
Re ppb							
Os ppb							
Ir ppb							
Pt							
Ru ppb							
Rh ppb							
Pb	1.12						0.454
Th	0.57	0.22	0.398	0.409	0.083	0.257	0.39
U	0.12	0.064	0.096	0.1	0.019	0.058	0.097
Ratios							
U/Th	0.211	0.291	0.241	0.244	0.229	0.226	0.252
Ba/W	70.91	83.53	96.05	244.2	83.53	33.68	48.79
U/W	0.182	0.188	0.223	0.192	0.160	0.153	0.200
Th/W	0.864	0.647	0.926	0.787	0.697	0.676	0.793
Group Average Th/W			0.770±0.095				
Group Average $f^{Hf/W}$			2.56±0.46				

d, (Jambon et al., 2002); e, (Barrat et al., 2002); f, (Gillet et al., 2005); g, (Anand et al., 2008); h, This study;

Table 4.1 (continued) Trace Element Concentrations of Martian Meteorites

Groups	Nakhlites				Chassignites
Meteorites	MIL 03346	Nakhla	Nakhla	NWA 817	NWA 2737
References	i	h	h	j	k
Weight(mg)		174.5	174.5	106.9	611
(wt%)					
SiO_2					37
TiO_2	0.69	0.32	0.31	0.61	0.13
Al_2O_3	3.66	1.10	1.07	3.28	0.86
Fe_2O_3					21.79
FeO*	19.12	21.38	20.37	19.84	
MnO	0.46	0.53	0.50	0.53	0.4
CaO	15.75	15.72	15.12	13.07	0.84
MgO	9.99	11.78	11.32	10.31	37.1
Na_2O	1	0.45	0.41	0.94	0.17
K_2O	0.27	0.10	0.09	0.32	0.05
P_2O_5	0.25	0.06	0.06		0.1
(ppm)					
Li	4.25			7.43	
Be	0.3	0.107	0.118	0.44	
Sc	54.5	47.79	44.77	47	4.6
V	208	220.1	209.1	181	70
Cr	1192	2713	2786	1519	11700
Co	35.7	52.68	50.51	49	78
Ni	49	88.78	84.92	71	875
Cu	8.2	9.63	9.27	12.7	4.3
Zn	61.3	708.7	700.2	71.52	45
Ga	6.51	3.15	3.03	6.77	1.43
Rb	4.14	3.13	2.94	6.06	1.28
Sr	131.7	54.80	52.97	145	27.2
Y	8.44	3.76	3.66	9.86	1.21
Zr	23.29		7.92	29.72	5.01
Nb	3.98	1.52	1.44	4.6	1.19
Mo				0.17	0.15
Pd (ppb)					
Cd (ppb)		554.7	586.7		
Sn		1.89	1.90		
Sb(ppb)		22.93	21.07	0.025	

h, This study; I, (Barrat et al., 2006); j, (Sautter et al., 2002); k, (Beck et al., 2006)

Table 4.1 (continued) Trace Element Concentrations of Martian Meteorites

Groups	Nakhlites				Chassignites
Meteorites	MIL 03346	Nakhla	Nakhla	NWA 817	NWA 2737
References	i	h	h	j	k
Cs	0.29	0.322	0.339	0.25	0.063
Ba	59.58	22.15	22.40	167	37.5
La	4.7	1.75	1.77	5.92	1.17
Ce	11.01	4.63	4.58	14.7	2.87
Pr	1.56	0.659	0.649	2.11	0.363
Nd	7.07	3.08	3.05	9.02	1.43
Sm	1.64	0.753	0.747	1.97	0.266
Eu	0.522	0.219	0.209	0.576	0.0721
Gd	1.73	0.671	0.704	1.96	0.237
Tb	0.266	0.114	0.116	0.305	0.0367
Dy	1.57	0.631	0.673	1.81	0.213
Ho	0.317	0.132	0.133	0.36	0.0427
Er	0.851	0.374	0.382	0.953	0.117
Tm		0.057	0.057		
Yb	0.766	0.360	0.346	0.817	0.105
Lu	0.114		0.053	0.121	0.017
Hf	0.69	0.249	0.245	0.78	0.14
Ta	0.23	0.082	0.078	0.248	0.07
W(ppb)	400	134.7	137.1	450	100
Re ppb					
Os ppb					
Ir ppb					
Pt					
Ru ppb					
Rh ppb					
Pb	0.91	0.723	0.750	1.9	
Th	0.42	0.153	0.156	0.6	0.13
U	0.09	0.045	0.043	0.136	0.056
Ratios					
U/Th	0.214	0.292	0.277	0.227	0.431
Ba/W	149.0	164.4	163.4	371.1	375.0
U/W	0.225	0.331	0.315	0.302	0.560
Th/W	1.05	1.13	1.14	1.33	1.30
Group Average Th/W			1.19±0.11		
Group Average $f^{Hf/W}$			4.50±0.53		

h, This study; I, (Barrat et al., 2006); j, (Sautter et al., 2002); k, (Beck et al., 2006)

4.3 Governing Equations for the "Deep Magma Ocean" Core Formation Model

The continuous accretion and core formation model employed in our model for a terrestrial planet incorporated the model frame from (Jacobsen, 2005; Wade and Wood, 2005), but a two-layer mantle with an upper magma ocean and a solid lower mantle is taken into account instead of one with a global magma ocean. The model (Figure 4.2) includes four reservoirs: (1) a primitive solar nebula reservoir, (2) an upper silicate magma ocean reservoir, (3) a solid silicate lower mantle reservoir and (4) a metallic core reservoir.

We define $M_{\oplus}(t)$ to be the total mass of a growing planet at time t and $M_j(t)$ to be the total mass of reservoir j at time t (j=1, 2, 3 or 4). Thus, by mass balance,

$$M_1(0) = M_1(t) + M_{\oplus}(t) \quad (4.3)$$

$$M_{\oplus}(t) = M_2(t) + M_3(t) + M_4(t) \quad (4.4)$$

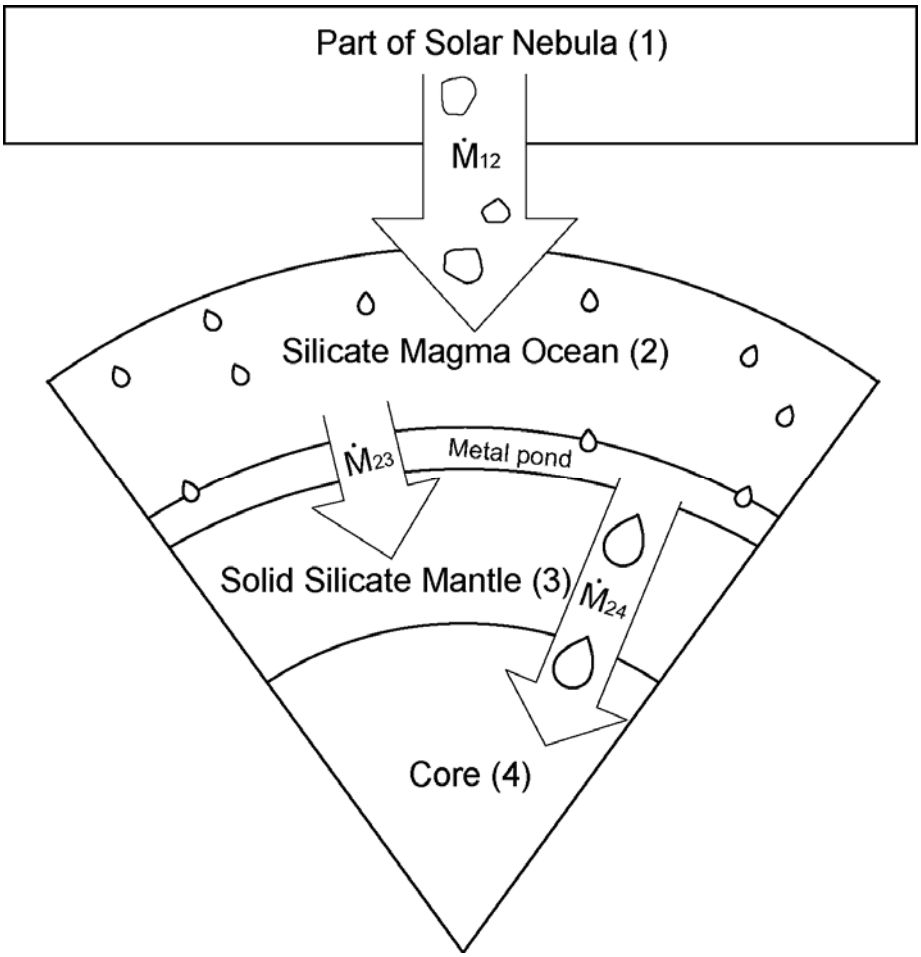

Figure 4.2 A sketch of the "deep magma ocean" core formation model. Mars is considered to grow from a primitive solar nebula (reservoir 1) with a mass flux $\dot{M}_{12}(t)$. The newly segregated metals pond at the bottom of the magma ocean and later quickly sink through the solid lower mantle into the core as diapirs with a mass flux of $\dot{M}_{24}(t)$. In the mean time, the silicate magma ocean solidify gradually and the mass flux from the magma ocean to the solid lower mantle reservoir is $\dot{M}_{23}(t)$, which is set to maintain the pressure at the base of the upper magma ocean as a fixed proportion of the pressure at core-mantle boundary. It is assumed that only newly segregated metals and newly crystallized solid silicate reach chemical equilibrium with the upper magma ocean. There are no back reactions between upper and lower mantles or between core and mantles. And there is no direct mass transport flux from the solar nebula to the solid lower mantle or to the metallic core ($\dot{M}_{13}(t) = \dot{M}_{14}(t) = 0$).

Let $\dot{M}_{jk}(t)$ be the mass flux from reservoir j to k. A terrestrial planet is considered to grow from a primitive solar nebula (reservoir 1) with a mass flux $\dot{M}_{12}(t)$. As the planet grows, the accreted material is well mixed with the upper magma ocean before segregating core material. The newly segregated metal was emulsified to form small (cm-sized) droplets while sinking through the upper magma ocean and those metal droplets finally pond at the bottom of the magma ocean (Wood et al., 2008a). It is assumed that metal droplets reach equilibrium with the surrounding silicate melt very quickly (Rubie et al., 2003) and the upper magma ocean maintains homogeneity by quick convection. Then metal droplets only reflect the metal-silicate equilibrium with the overlying magma ocean at the base of the upper magma ocean. When metal ponding at the base of upper magma ocean become gravitationally unstable, it will later quickly sink through the solid lower mantle into the core as large diapirs with a mass flux of $\dot{M}_{24}(t)$. The chemical equilibrations between the metals and the solid lower silicate mantles are ignored. In the mean time, the silicate magma ocean solidifies gradually from the bottom up and the mass flux from the magma ocean to the solid lower mantle reservoir is $\dot{M}_{23}(t)$. For simplification, $\dot{M}_{23}(t)$ is set to maintain the pressure at the base of the upper magma ocean as a fixed proportion of the pressure at core-mantle boundary (Wade and Wood, 2005). It is assumed that only newly crystallized solid silicate reaches

chemical equilibrium with the upper magma ocean. In addition, we assume there is no direct mass transport flux from the solar nebula to the solid lower mantle or to the metallic core ($\dot{M}_{13}(t) = \dot{M}_{14}(t) = 0$). It is likely that energies from impacts, metal segregation and crystallizations would support the deep magma ocean to exist over the accretion history of Mars.

The mass accretion rate of a growing terrestrial plant is equivalent to the mass transport flux from the solar nebula to the silicate magma ocean reservoir:

$$\frac{dM_{\oplus}(t)}{dt} = \dot{M}_{\oplus}(t) = \dot{M}_{12}(t). \tag{4.5}$$

Assuming mass transport fluxes from the upper magma ocean to the solid lower mantle and to the metallic core are proportional to the accretion rate of the planet, then the mass changing rates of all reservoirs within the planet are given as:

$$\begin{cases} \dot{M}_2(t) = \dot{M}_{12} - \dot{M}_{23} - \dot{M}_{24} = (1 - \gamma_3 - \gamma_4)\dot{M}_{12} & (4.6) \\ \dot{M}_3(t) = \dot{M}_{23} = \gamma_3 \dot{M}_{12} & (4.7) \\ \dot{M}_4(t) = \dot{M}_{24} = \gamma_4 \dot{M}_{12} & (4.8) \end{cases}$$

where γ_3 and γ_4 are proportional factors. Assuming that γ_3 and γ_4 are constant over the course of accretion and core formation, we can obtain

$$\begin{cases} M_2(t) = (1 - \gamma_3 - \gamma_4)M_{\oplus}(t) & (4.9) \\ M_3(t) = \gamma_3 M_{\oplus}(t) & (4.10) \\ M_4(t) = \gamma_4 M_{\oplus}(t) & (4.11) \end{cases}$$

where γ_3 and γ_4 actually are the mass fractions of the solid lower mantle and the metallic core respectively.

We define $N_{ij}(t)$ to be the number of atoms of species i in reservoir j at time t and $C_{ij}(t)\left(=\frac{N_{ij}(t)}{M_j(t)}\right)$ to be the concentration of species i in reservoir j, respectively. Four different types of species will be considered in the model: (1) radioactive species r (such as ^{182}Hf), (2) radiogenic species d (such as ^{182}W), (3) one stable species (ρ) of the same element as r (normally ^{180}Hf if r is ^{182}Hf) and (4) one stable species (s) of the same element as d (^{183}W if d = ^{182}W). Assuming reservoir 1 (part of the solar nebula) has a fixed composition except for variations owing to radioactive decay or production, we obtain:

$$\begin{cases} C_{s1}(t) = C_{s1}(0) \\ C_{\rho 1}(t) = C_{\rho 1}(0) \\ C_{r1}(t) = C_{r1}(0)\, e^{-\lambda t} \\ C_{d1}(t) = C_{d1}(0) + C_{r1}(0)\left(1 - e^{-\lambda t}\right) \end{cases} \tag{4.12}$$

The concentrations of species i in the mantles ($C_{i2}(t)$ and $C_{i3}(t)$) and the core ($C_{i4}(t)$) are affected by the simultaneous solid silicate-liquid silicate and metal-liquid silicate partition coefficients ($d_{i23}(t)$ and $d_{i24}(t)$, respectively):

$$d_{i23}(t) = \frac{c_{i3}(t)}{C_{i2}(t)} \tag{4.13}$$

$$d_{i24}(t) = \frac{c_{i4}(t)}{C_{i2}(t)} \tag{4.14}$$

where $c_{i3}(t)$ and $c_{i4}(t)$ are the concentrations of species i in the new additions to the solid lower mantle and the core respectively.

Correspondingly, the effective partition coefficients are defined as ratios of concentrations in reservoirs:

$$\begin{cases} D_{i23}(t) = \dfrac{C_{i3}(t)}{C_{i2}(t)} & (4.15) \\ D_{i24}(t) = \dfrac{C_{i4}(t)}{C_{i2}(t)} & (4.16) \end{cases}$$

The governing equations for transports of mass and species in our model are shown below.

4.3.1 Transport of Stable Trace Species (s and ρ)

If the flux of species i from reservoir j to k is J_{ijk}, then the changing rate of the number of atoms of stable species s in the upper mantle is given as:

$$\begin{aligned} \dot{N}_{s2}(t) &= J_{s12} - J_{s23} - J_{s24} \\ &= [C_{s1} - \gamma_3 d_{s23}(t) C_{s2}(t) - \gamma_4 d_{s24}(t) C_{s2}(t)] \dot{M}_{\oplus}(t) \end{aligned} \tag{4.17}$$

Thus, the changing rate of the concentration of the stable species s in the upper mantle and its initial value can be obtained:

$$\begin{cases} \dot{C}_{s2}(t) = \dfrac{C_{s1} - C_{s2}(t) a(s,t)}{(1-\gamma_3-\gamma_4) M_{\oplus}(t)} \dot{M}_{\oplus}(t) \\ C_{s2}(0) = \dfrac{C_{s1}}{a(s,0)} \end{cases} \tag{4.18}$$

where $a(s,t) = 1 + \gamma_3[d_{s23}(t) - 1] + \gamma_4[d_{s24}(t) - 1]$. The changing rate of concentration of stable species s in the solid lower mantle and its initial value can be obtained in a similar way and given by:

$$\begin{cases} \dot{C}_{s3}(t) = \dfrac{d_{s23}(t)C_{s2}(t) - C_{s3}(t)}{M_{\oplus}(t)}\dot{M}_{\oplus}(t) \\ C_{s3}(0) = d_{s23}(0)C_{s2}(0) \end{cases} \tag{4.19}$$

Note that the equations for the stable species ρ are exactly the same to those for s.

4.3.2 Transport and Evolution of Radioactive Isotopes (r)

The changing rate of the concentration of radioactive isotope r in the upper mantle is given as:

$$\begin{aligned} \dot{C}_{r2}(t) &= \frac{C_{r1}(t) - C_{r2}(t)a(r,t)}{(1-\gamma_3-\gamma_4)M_{\oplus}(t)}\dot{M}_{\oplus}(t) - \lambda_r C_{r2}(t) \\ C_{r2}(0) &= \frac{C_{r1}(0)}{a(r,0)} \end{aligned} \tag{4.20}$$

We use the chemical fractionation factors ($f^{r/s}$ values) to describe the enrichment of r/s ratio in a reservoir relative to reservoir 1. $f^{r/s}$ in the upper mantle is defined as:

$$f_2^{r/s}(t) = \frac{\dfrac{C_{r2}(t)}{C_{s2}(t)}}{\dfrac{C_{r1}(t)}{C_{s1}(t)}} - 1 \tag{4.21}$$

Thus,

$$\begin{aligned} \dot{f}_2^{r/s}(t) = {} & \frac{a(s,t) - a(r,t)}{(1-\gamma_3-\gamma_4)M_{\oplus}(t)}\dot{M}_{\oplus}(t) \\ & - \frac{f_2^{r/s}(t)\left[\dfrac{C_{s1}}{C_{s2}(t)} - a(s,t) + a(r,t)\right]}{(1-\gamma_3-\gamma_4)M_{\oplus}(t)}\dot{M}_{\oplus}(t) \end{aligned} \tag{4.22}$$

There is a singularity for $f_2^{r/s}(t)$ at $t = 0$, the initial value of $f_2^{r/s}(t)$ can be calculated from the initial values of $C_{s2}(0)$ and $C_{r2}(0)$:

$$f_2^{r/s}(0) = \frac{\frac{C_{r2}(0)}{C_{s2}(0)}}{\frac{C_{r1}(0)}{C_{s1}(0)}} - 1 = \frac{a(s,0) - a(r,0)}{a(r,0)} \tag{4.23}$$

Similarly, the changing rate of $f^{r/s}$ in the solid lower mantle is given as

$$\begin{aligned} \dot{f}_3^{r/s}(t) = & \frac{\left[d_{r23} f_2^{r/s}(t) - d_{s23} f_3^{r/s}(t) + d_{r23} - d_{s23}\right]}{M_\oplus(t)} \frac{C_{s1}}{C_{s2}(t)} \dot{M}_\oplus(t) \\ & = d_{r23} f_2^{r/s}(t) \frac{C_{s1}}{C_{s2}(t)} \frac{\dot{M}_\oplus(t)}{M_\oplus(t)} - d_{s23} f_3^{r/s}(t) \frac{C_{s1}}{C_{s2}(t)} \frac{\dot{M}_\oplus(t)}{M_\oplus(t)} \\ & + [d_{r23} - d_{s23}] \frac{C_{s1}}{C_{s2}(t)} \dot{M}_\oplus(t) M_\oplus(t) \end{aligned} \tag{4.24}$$

And its initial value is

$$f_3^{r/s}(0) = \frac{d_{r23}(0)}{d_{s23}(0)} \left[f_2^{r/s}(0) + 1\right] - 1 \tag{4.25}$$

4.3.3 Transport and Evolution of Radiogenic Isotopes (d)

The differential equation for concentration of the radiogenic isotope d in the upper mantle:

$$\begin{cases} \dot{C}_{d2}(t) = \dfrac{C_{d1}(t) - C_{d2}(t) a(d,t)}{(1 - \gamma_3 - \gamma_4) M_\oplus(t)} \dot{M}_\oplus(t) + \lambda_r C_{r2}(t) \\ C_{d2}(0) = \dfrac{C_{d1}(0)}{a(d,0)} \end{cases} \tag{4.26}$$

The deviations of the radiogenic isotope ratios in parts per 10^4 from the ratios in reservoir 1 are defined by:

$$\varepsilon_{d2}(t) = \left(\frac{\frac{C_{d2}(t)}{C_{s2}(t)}}{\frac{C_{d1(t)}}{C_{s1(t)}}} - 1 \right) 10^4 \tag{4.27}$$

The differential equation for $\varepsilon_{d2}(t)$ in the upper mantle is:

$$\dot{\varepsilon}_{d2}(t) \approx q_d e^{-\lambda_r t} f_2^{r/s}(t) - \varepsilon_{d2}(t) \frac{C_{s1}\dot{M}_{\oplus}(t)}{C_{s2}(t)(1-\gamma_3-\gamma_4)M_{\oplus}(t)} \tag{4.28}$$

where $q_d = \frac{C_1^r(0)}{C_1^d(t)}\lambda_r 10^4 \approx \frac{C_1^r(0)}{C_1^d(0)}\lambda_r 10^4$. Similarly, the differential equation for $\varepsilon_d(t)$ in the lower mantle is:

$$\dot{\varepsilon}_{d3}(t) \approx q_d e^{-\lambda_r t} f_3^{r/s}(t) - \left[\varepsilon_{d3}(t) - \varepsilon_{d2}(t)\right] \frac{C_{s2}(t) d_{s23}(t) \dot{M}_{\oplus}(t)}{C_{s3}(t) M_{\oplus}(t)} \tag{4.29}$$

4.3.4 Summary of Model Governing Equations for the ^{182}Hf-^{182}W System

Assuming the metal-silicate partition coefficient of Hf is equal to 0 ($d_{\mathrm{Hf24}} = 0$), the changing rates of ^{183}W in the magma ocean and the solid deep mantle are:

$$\begin{cases} \dot{C}_{^{183}\mathrm{W}_2}(t) = \dfrac{C_{^{183}\mathrm{W}_1} - C_{^{183}\mathrm{W}_2}(t)a(\mathrm{W},t)}{(1-\gamma_3-\gamma_4)M_{\oplus}(t)}\dot{M}_{\oplus}(t) \\ C_{^{183}\mathrm{W}_2}(0) = \dfrac{C_{^{183}\mathrm{W}_1}}{a(\mathrm{W},0)} \end{cases} \tag{4.30}$$

And,

$$\begin{cases} \dot{C}_{^{183}\mathrm{W}_3}(t) = \dfrac{d_{\mathrm{W23}}(t)C_{^{183}\mathrm{W}_2}(t) - C_{^{183}\mathrm{W}_3}(t)}{M_{\oplus}(t)}\dot{M}_{\oplus}(t) \\ C_{^{183}\mathrm{W}_3}(0) = d_{\mathrm{W23}}(0)C_{^{183}\mathrm{W}_2}(0) \end{cases} \tag{4.31}$$

respectively, where $a(\mathrm{W},t) = 1 + \gamma_3(d_{\mathrm{W23}}(t) - 1) + \gamma_4(d_{\mathrm{W24}}(t) - 1)$.

Let $f^{\mathrm{Hf/W}}$ stand for $f^{\ ^{182}\mathrm{Hf}/^{183}\mathrm{W}}$, then the changing rate of $f^{\mathrm{Hf/W}}$ values in the magma ocean and the solid deep mantle are:

$$\dot{f}_2^{\mathrm{Hf/W}}(t) = \frac{[(d_{\mathrm{W23}}(t) - d_{\mathrm{Hf23}}(t))\gamma_3 + \gamma_4 d_{\mathrm{W24}}(t)]}{(1-\gamma_3-\gamma_4)M_{\oplus}(t)}\dot{M}_{\oplus}(t) - \frac{f_2^{\mathrm{Hf/W}}(t)\left[\frac{C_{^{183}\mathrm{W1}}}{C_{^{183}\mathrm{W2}}}(t) - (d_{\mathrm{W23}}(t) - d_{\mathrm{Hf23}}(t))\gamma_3 - \gamma_4 d_{\mathrm{W24}}(t)\right]}{(1-\gamma_3-\gamma_4)M_{\oplus}(t)}\dot{M}_{\oplus}(t) \quad (4.32)$$

with $f_2^{\mathrm{Hf/W}}(0) = \frac{\left(d_{\mathrm{W23}}(0) - d_{\mathrm{Hf23}}(0)\right)\gamma_3 - \gamma_4 d_{\mathrm{W24}}(0)}{1+(d_{\mathrm{Hf23}}(0)-1)\gamma_3 - \gamma_4}$.

And

$$\dot{f}_3^{\mathrm{Hf/W}}(t) = \frac{\left[d_{\mathrm{Hf23}}(t) f_2^{\mathrm{Hf/W}}(t) - d_{\mathrm{W23}}(t) f_3^{\mathrm{Hf/W}}(t) + d_{\mathrm{Hf23}}(t) - d_{\mathrm{W23}}(t)\right]}{M_{\oplus}(t)} * \frac{C_{^{183}\mathrm{W1}}}{C_{^{183}\mathrm{W2}}}(t)\dot{M}_{\oplus}(t) \quad (4.33)$$

with $f_3^{\mathrm{Hf/W}}(0) = \frac{d_{\mathrm{Hf23}}(t)}{d_{\mathrm{W23}}(t)}\left[f_2^{\mathrm{Hf/W}}(0) + 1\right] - 1$.

Let $\varepsilon_{\mathrm{W}}(t)$ stand for $\dot{\varepsilon}_{^{182}\mathrm{W2}}(t)$. Then the changing rates of $\varepsilon_{\mathrm{W}}(t)$ in the magma ocean and the solid deep mantle are

$$\dot{\varepsilon}_{\mathrm{W2}}(t) \approx q_{\mathrm{W}} e^{-\lambda_{^{182}\mathrm{Hf}} t} f_2^{\mathrm{Hf/W}}(t) - \varepsilon_{\mathrm{W2}}(t)\frac{C_{^{183}\mathrm{W1}}\dot{M}_{\oplus}(t)}{C_{^{183}\mathrm{W2}}(t)(1-\gamma_3-\gamma_4)M_{\oplus}(t)} \quad (4.34)$$

and

$$\dot{\varepsilon}_{\mathrm{W3}}(t) \approx q_{\mathrm{W}} e^{-\lambda_{^{182}\mathrm{Hf}} t} f_3^{\mathrm{Hf/W}}(t) - \left[\varepsilon_{\mathrm{W3}}(t) - \varepsilon_{\mathrm{W2}}(t)\right]\frac{C_{^{183}\mathrm{W2}}(t) d_{\mathrm{W23}}(t)\dot{M}_{\oplus}(t)}{C_{^{183}\mathrm{W3}}(t)M_{\oplus}(t)} \quad (4.35)$$

where $q_{\mathrm{W}} = \frac{C_1^{^{182}\mathrm{Hf}}(0)}{C_1^{^{182}\mathrm{W}}(0)}\lambda_{^{182}\mathrm{Hf}} 10^4$.

In order to solve the differential equations above, we need to parameterize the total mass of the planet, metal-silicate partition coefficient of W and liquid silicate-solid silicate partition coefficients of Hf and W as a function of time ($M_{\oplus}(t)$, $d_{\mathrm{W24}}(t)$, $d_{\mathrm{W23}}(t)$ and $d_{\mathrm{Hf23}}(t)$). It is demonstrated below how the parameterization is performed.

4.4 Model Parameterizations

4.4.1 Parameterization of Accretion Rates of Terrestrial Planets

The mass of the planet ($M_{\oplus}(t)$) is considered to grow from a primitive solar nebular reservoir with a growth rate approximately proportional to the available mass ($M_{\oplus}(\infty) - M_{\oplus}(t)$) at any time t, where $M_{\oplus}(\infty)$ is the final mass of planet at infinite time. This results in an exponentially decreasing accretion rate (Jacobsen, 2005; Yu and Jacobsen, 2011) which is given by:

$$\dot{M}_{\oplus} = \alpha M_{\oplus}(\tau_0) e^{-\alpha t} \tag{4.36}$$

and

$$\frac{M_{\oplus}(t)}{M_{\oplus}(\tau_0)} = 1 - e^{-\alpha t} \tag{4.37}$$

where α is the growth constant and τ_0 is the age of the Solar System (~4567 Myr), the starting point for accretion of planets. And the mean time of formation is given by (Jacobsen and Harper, 1996):

$$t_m = \frac{1}{M_{\oplus}(\tau_0)} \int_0^{\tau_0} t\dot{M}_{\oplus} dt \approx \frac{1}{\alpha} \tag{4.38}$$

4.4.2 Parameterization of Metal-Silicate Partition Coefficient of W

Metal-silicate partition coefficient of W from (Cottrell et al., 2009, 2010) shows that the partitioning of W between silicate and metal ($d_{\mathrm{W}}^{\text{met-sil}} = \frac{C_{\mathrm{W}}^{\text{metal}}}{C_{\mathrm{W}}^{\text{silicate}}}$) is dependent on pressure (P), temperature (T), oxygen fugacity (f_{O_2} which is usually represented by the relative value to iron-wüstite buffer (ΔIW)) and structure of silicate melt (Nbo/t represented by Non-bridging oxygen per tetrahedrally coordinated cations) .

The temperature of metal-silicate equilibrium is fixed on the peridotite liquidus as a function of pressure by $T = 1973 + 28.57P$ (Wood, 2008). Nbo/t is set as the value of the peridotitic melt (2.7). Oxygen fugacity of the martian mantle during core formation is ΔIW = -1.3 (Righter and Chabot, 2010). Metal-silicate equilibrium pressure at the base of the magma ocean needs to be parameterized as follows:

By Gauss' flux theorem for gravity of a uniform planet, we have

$$g(r) = G\frac{4}{3}\pi\rho r \tag{4.39}$$

where r is the distance between the place of interest within the planet and the center of a planet, $g(r)$ is the gravitational acceleration at r, G is

the gravitational constant of the universe, and ρ is the average density of a planet. The internal pressure of a planet at r can be calculated as:

$$P(r) = P_{\text{surface}} + G\frac{2}{3}\pi\rho^2(R^2 - r^2) \tag{4.40}$$

where R is the radius of a planet and P_{surface} is the surface pressure of a planet which could be treated as close to 0 comparing to $P(r)$ (because $P(r) \gg P_{\text{surface}}(r)$). Then the pressure at the core-mantle boundary is a function of radii of the growing planet and its core at time t ($R(t)$ and $r_c(t)$ respectively).

$$\begin{aligned} P_{\text{cmb}}(t) &= G\frac{2}{3}\pi\rho^2(R(t)^2 - r_c(t)^2) \\ &= G\frac{2}{3}\pi\rho^2 R(t)^2\left[1 - \left(\frac{r_c(t)}{R(t)}\right)^2\right] \end{aligned} \tag{4.41}$$

Note that

$$\begin{cases} M_{\oplus}(t) = \frac{4}{3}\pi R(t)^3\rho \\ M_4(t) = \frac{4}{3}\pi r_c(t)^3\rho \end{cases} \tag{4.42}$$

$$\Rightarrow \gamma_4 = \frac{M_4(t)}{M_{\oplus}(t)} = \left(\frac{r_c(t)}{R(t)}\right)^3$$

Given mass fraction of core is constant (γ_4=$\left(\frac{r_c(t)}{R(t)}\right)^3$ =constant), then

$$\begin{aligned} P_{\text{cmb}}(t) &\propto R(t)^2 \\ \Rightarrow P_{\text{cmb}}(t) &\propto M_{\oplus}(t)^{\frac{2}{3}} \\ \Rightarrow P_{\text{cmb}}(t) &\approx P_{\text{cmb}}(\tau_0)\left(\frac{M_{\oplus}(t)}{M_{\oplus}(\tau_0)}\right)^{\frac{2}{3}} \end{aligned} \tag{4.43}$$

where $M_{\oplus}(\tau_0)$ and $P_{\text{cmb}}(\tau_0)$ are the final total mass and final pressure at core-mantle boundary of a planet today, respectively.

Let $P_{\mathrm{eq}}(t)$ be the metal-silicate equilibrium pressure at the base of the magma ocean at any time t. Given the ratio of $\frac{P_{\mathrm{eq}}(t)}{P_{\mathrm{cmb}}(t)}$ is a constant ξ, then

$$P_{\mathrm{eq}}(t) = \xi P_{\mathrm{cmb}}(t) \approx \xi P_{\mathrm{cmb}}(\tau_0)\left(\frac{M_{\oplus}(t)}{M_{\oplus}(\tau_0)}\right)^{\frac{2}{3}} \tag{4.44}$$

From equation (4.41), $P_{\mathrm{eq}}(t) \approx G\frac{2}{3}\pi\rho^2 R(t)^2\left[1-\left(\frac{r_m(t)}{R(t)}\right)^2\right]$, where $r_m(t)$ is the depth of the magma ocean in a growing planet at time t, then,

$$\frac{r_m(t)}{R(t)} = \sqrt{1-\xi\left[1-\left(\frac{r_c(t)}{R(t)}\right)^2\right]} \tag{4.45}$$

We can find the relation between γ_3, γ_4 and ξ.

$$\gamma_3 = \left[1-\xi\left(1-\gamma_4^{\frac{2}{3}}\right)\right]^{\frac{3}{2}} - \gamma_4 \tag{4.46}$$

4.4.3 Parameterization for Solid Silicate-Liquid Silicate Partition Coefficients of Hf and W

Partition coefficients between silicate minerals and silicate melt for Hf are from (Righter and Shearer, 2003) and (Klemme et al., 2006): $d_{\mathrm{Hf}}^{\text{ol-sil}} \approx 0.07$, $d_{\mathrm{Hf}}^{\text{opx-sil}} \approx 0.08$, $d_{Hf}^{\text{cpx-sil}} \approx 0.38$, $d_{Hf}^{\text{gar-sil}} \approx 0.34$, and $d_{Hf}^{\text{sp-sil}} \approx 0.65$ (ol=olivine, cpx=clinopyroxene; opx=orthopyroxene; gar=garnet; sp=spinel). Righter and Shearer (2003) also found that crystallizations of clinopyroxene and garnet can significantly fractionate Hf/W ratio in

silicate melt $\left(\frac{d_{\mathrm{Hf}}^{\text{cpx-sil}}}{d_{\mathrm{W}}^{\text{cps-sil}}} \approx 5 \text{ and } \frac{d_{\mathrm{Hf}}^{\text{gar-sil}}}{d_{\mathrm{W}}^{\text{gar-sil}}} \approx 30\right)$, while crystallizations of olivine and orthopyroxene cannot $\left(\frac{d_{\mathrm{Hf}}^{\text{ol-sil}}}{d_{\mathrm{W}}^{\text{ol-sil}}} = \frac{d_{\mathrm{Hf}}^{\text{opx-sil}}}{d_{\mathrm{W}}^{\text{opx-sil}}} \approx 1\right)$. Then we can calculate partition coefficients of W from the ratios and partition coefficients of Hf except the partition coefficient of W between spinel and silicate melt ($d_{\mathrm{W}}^{\text{sp-sil}}$), which is 0.1 (Klemme et al., 2006).

Using the bulk mantle composition of Mars proposed by Longhi et al., (1992), the mineralogy of the martian mantle can be predicted as a function of pressure (Bertka and Fei, 1997). We simplified the mineralogy of the martian mantle from Bertka and Fei, (1997) as follows:

(1) when P < 8GPa, then $C_{\mathrm{ol}}(\mathrm{P}) = 0.6, C_{\mathrm{opx}}(\mathrm{P}) = 0.2, C_{\mathrm{cpx}}(P) = 0.1, C_{\mathrm{gar}}(P) = 0.1$;

(2) when P = 8-14 GPa, then $C_{\mathrm{ol}}(\mathrm{P}) = 0.6, C_{\mathrm{cpx}}(P) = 0.3, C_{\mathrm{gar}}(P) = 0.1$;

(3) when P = 14-24 GPa, then $C_{\mathrm{sp}}(\mathrm{P}) = 0.55, C_{\mathrm{gar}}(P) = 0.45$

where C_j is the proportion of mineral j in the martian mantle. The Mg-perovskite is ignored for simplification. Then partition coefficients between the upper magma ocean and the newly crystallized silicate for element i can be calculated as:

$$d_{i23} = C_{\mathrm{ol}}\ d_i^{\text{ol-sil}} + C_{\mathrm{cpx}} d_i^{\text{cpx-sil}} + C_{\mathrm{opx}} d_i^{\text{opx-sil}} + C_{\mathrm{gar}} d_i^{\text{gar-sil}} + C_{\mathrm{sp}} d_i^{\text{sp-sil}} \tag{4.47}$$

$d_i^{\text{j-sil}}$ is the partition coefficient of element i between mineral j and silicate melt.

4.4.4 Parameters for the ^{182}Hf-^{182}W Short-Lived System in the Bulk Mars

In our model, ^{182}Hf decays to ^{182}W with a half-life of 8.90±0.09 Myr and a decay constant of 0.078±0.001 Myr^{-1} (Vockenhuber et al., 2004). The initial ^{182}Hf/^{180}Hf and ^{182}W/^{183}W of the Solar System are (1.0±0.1)×10^{-4} and 1.850664±37, respectively (Yin et al., 2002; Jacobsen, 2005). The ^{182}Hf/^{180}Hf and ^{182}W/^{183}W of the bulk Mars are the same as the chondritic reference value (CHUR) which are 2.836 and 1.850948±37, respectively (Jacobsen, 2005). The concentrations of Hf and W in bulk Mars used in modeling are $C_{\text{Hf1}} \approx 0.23\,ppm$ and $C_{\text{W1}} \approx 0.105\,ppm$ (Taylor and McLennan, 2009). However, it is important to point out that modeling results on $f^{\text{Hf/W}}$ value, ε_{W} and accretion timescales are not related to the choice of concentrations of Hf and W in bulk Mars. The mass fraction of Mars' core (γ_4) is 0.217 (Wänke and Dreibus, 1988).

4.5 Modeling Results

4.5.1 No Hf or W Fractionation between the Upper and Lower Mantle Reservoirs. ($d_{\text{Hf23}} = d_{\text{W23}} = 1$)

We started to explore the model with a simplified case where the simultaneous partition coefficients of Hf and W between the upper magma ocean and the newly crystallized silicate are 1 ($d_{\mathrm{Hf23}} = d_{\mathrm{W23}} = 1$). Since Hf will not partition into metal phase and will not go into the core ($d_{\mathrm{Hf24}} = 0$), Hf concentrations in the upper and lower mantle reservoirs will be the same (~ 0.294 ppm) in this case. However, W concentrations in the two martian mantle reservoirs are not identical. From equations (4.28) and (4.29), the changing rates of concentration of W in the upper magma ocean reservoir and the solid lower mantle reservoir are:

$$\begin{cases} \dfrac{dC_{\mathrm{W2}}(t)}{dM_{\oplus}(t)} = \dfrac{C_{\mathrm{W1}} - C_{\mathrm{W2}}(t)a^{*}(\mathrm{W},t)}{(1-\gamma_3-\gamma_4)M_{\oplus}(t)} \\ C_{\mathrm{W2}}(0) = \dfrac{C_{\mathrm{W1}}}{a^{*}(\mathrm{W},0)} \end{cases} \tag{4.48}$$

where $a^{*}(\mathrm{W},t) = 1 + \gamma_4(d_{\mathrm{W24}}(t) - 1)$, and

$$\begin{cases} \dfrac{dC_{\mathrm{W3}}(t)}{dM_{\oplus}(t)} = \dfrac{C_{\mathrm{W2}}(t) - C_{\mathrm{W3}}(t)}{M_{\oplus}(t)} \\ C_{\mathrm{W3}}(0) = C_{\mathrm{W2}}(0) \end{cases} \tag{4.49}$$

The equation above (4.47) can be rearranged as

$$\begin{aligned} \dot{C}_{\mathrm{W3}}(t) &= \frac{C_{\mathrm{W2}}(t) - C_{\mathrm{W3}}(t)}{M_{\oplus}(t)}\dot{M}_{\oplus}(t) \\ \Rightarrow \dot{C}_{\mathrm{W3}}(t) + \frac{C_{\mathrm{W3}}(t)}{M_{\oplus}(t)}\dot{M}_{\oplus}(t) &= \frac{C_{\mathrm{W2}}(t)}{M_{\oplus}(t)}\dot{M}_{\oplus}(t) \\ \Rightarrow \dot{C}_{\mathrm{W3}}(t)M_{\oplus}(t) + C_{\mathrm{W3}}(t)\dot{M}_{\oplus}(t) &= C_{\mathrm{W2}}(t)\dot{M}_{\oplus}(t) \\ \Rightarrow d\left(M_{\oplus}(t)C_{\mathrm{W3}}(t)\right) &= C_{\mathrm{W2}}(t)\dot{M}_{\oplus}(t) \\ \Rightarrow C_{\mathrm{W3}}(t) &= \int_0^t \frac{C_{\mathrm{W2}}(\theta)\dot{M}_{\oplus}(\theta)}{M_{\oplus}(t)}d\theta \end{aligned} \tag{4.50}$$

Let $\hat{C}_{W2}(t) = \int_0^t \frac{C_{W2}(\theta)\dot{M}_{\oplus}(\theta)}{M_{\oplus}(t)} d\theta$, which is defined as the mean value of $C_{W2}(t)$ from time 0 to t. Then $C_{W3}(t) = \hat{C}_{W2}(t)$. From equation (4.46), we know variation of $C_{W2}(t)$ is negatively related to metal-silicate partition coefficient of W (d_{W24}). During the early accretion stage of Mars, the metal-silicate equilibration pressure is low ($P_{eq} < 5\,GPa$) and the metal-silicate partition coefficient of W (d_{W24}) is an increasing function of the equilibration pressure (Cottrell et al., 2009, 2010). Then $C_{W2}(t)$ is decreasing over time and $C_{W2}(t) < \hat{C}_{W2}(t) = C_{W3}(t)$ (Figure 4.3a). On the contrary, during the later accretion stage, when the metal-silicate equilibration pressure is higher than 5 GPa ($P_{eq} > 5\,GPa$), the metal-silicate partition coefficient of W (d_{W24}) is instead a decreasing function of the equilibration pressure (Cottrell et al., 2009, 2010), then $C_{W2}(t) > \hat{C}_{W2}(t) = C_{W3}(t)$. The difference in W concentrations between the upper and lower mantle reservoirs can be described by the average partition coefficient of W between the upper and lower mantle reservoirs ($D_{W23}(t) = C_{W3}(t)/C_{W2}(t)$ Figure 4.3b). The final $D_{W23}(\tau_0)$ is ~0.76, indicating that after core formation, the lower mantle reservoir has a lower W concentration than the upper mantle reservoir. That is due to the fact that only the newly segregated core material and silicate crystals reaches equilibrium with the upper mantle reservoir and then the lower mantle reservoir reflects more effect of the earlier core formation processes at lower pressure and temperature. This is the reason why the upper and lower mantle

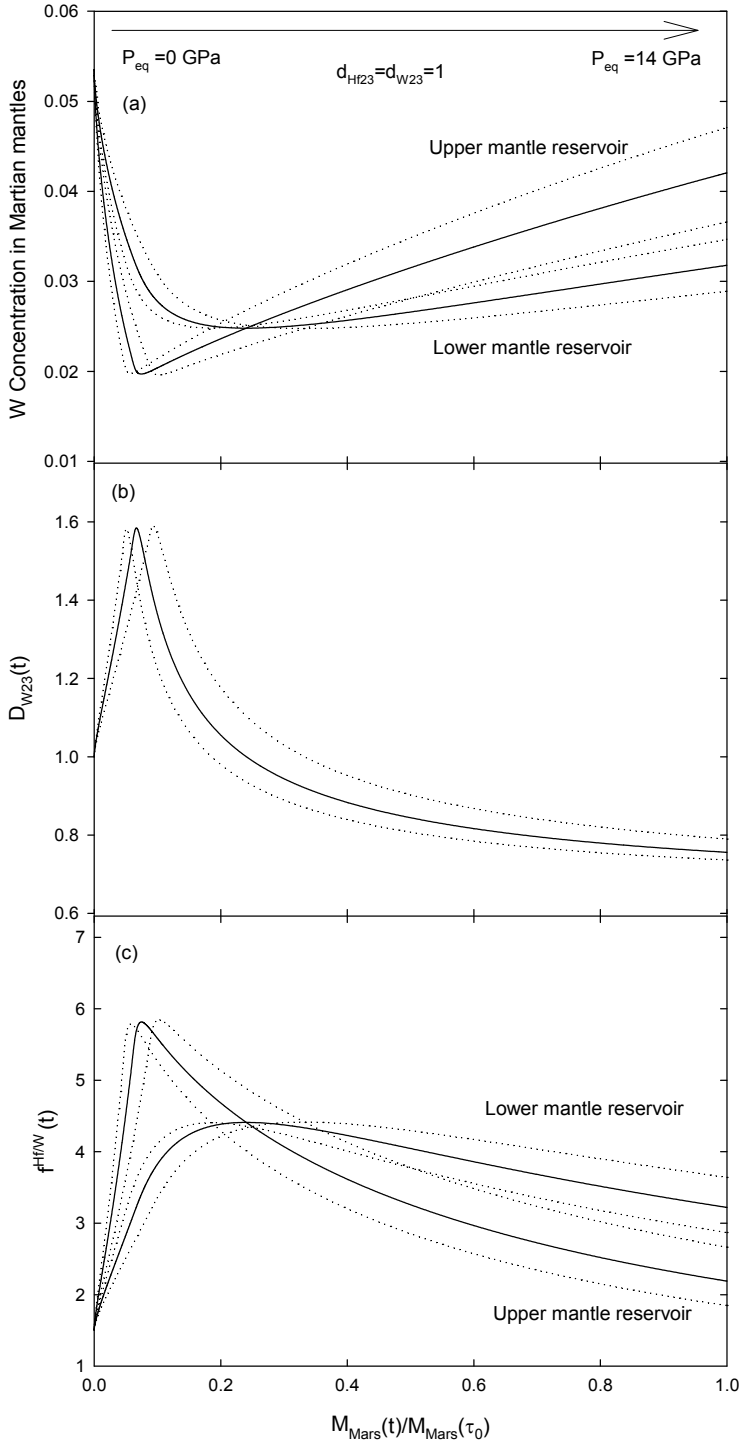

Figure 4.3 W concentrations (a) and $f^{\mathrm{Hf/W}}$ values (c) of the upper and lower martian mantle reservoirs and effective W partition coefficient between the two mantle reservoirs (b) are shown as a function of the

Figure 4.3 (Continued) mass fraction of the accreting Mars. The simultaneous partition coefficients of Hf and W between silicate minerals and silicate melt are equal to 1 (d_{Hf23}=d_{W23}=1). The final metal-silicate equilibration pressure in Mars $\left(P_{\mathrm{eq}}(\tau_0)\right)$ is 14±3 GPa which is required by the depletion of siderophile elements in the martian mantle (Righter and Chabot, 2010). The solid curves represent the results when $P_{\mathrm{eq}}(\tau_0)$=14 GPa and the dotted lines show the ranges due to the uncertainty of $P_{\mathrm{eq}}(\tau_0)$.

reservoirs have slightly different $f^{\mathrm{Hf/W}}$ as well. It is worth noting that although the W concentration results (Figure 4.3a) are dependent on the W concentration of bulk Mars we employed ($C_{\mathrm{W1}} \approx 0.105\, ppm$ (Taylor and McLennan, 2009)), the D_{W23} and $f^{\mathrm{Hf/W}}$ (Figures 4.3b and 4.3c) are not.

Given that the final metal-silicate equilibration pressure in Mars is 14±3 GPa (Righter et al 2010), $f^{\mathrm{Hf/W}}$ in both the upper and lower mantle reservoirs started at ~1.50 and sharply increased over the early accretion stage ($P_{\mathrm{eq}} \leq 5\, GPa$) and followed by slow declines in the later accretion stage ($P_{\mathrm{eq}} \geq 5\, GPa$; Figure 4.3c). During the first 25% of Mars' accretion ($M_{\mathrm{Mars}}(t)/M_{\mathrm{Mars}}(\tau_0) = 0 - 0.25$), the upper mantle reservoir has a higher $f^{\mathrm{Hf/W}}$value than the lower mantle reservoir, while during the rest of Mars' accretion ($M_{\mathrm{Mars}}(t)/M_{\mathrm{Mars}}(\tau_0) = 0.25 - 1$), it is reversed.

The final $f^{\mathrm{Hf/W}}$ values in the martian mantle reservoirs after the completion of the accretion and core formation, are in fact a function of the metal-silicate equilibration pressure, which is represented by a fixed ratio relative to the core-mantle-boundary pressure ($\xi = P_{\mathrm{eq}}/P_{\mathrm{cmb}}$) as

shown in Figure 4.4. Trends of the curves in Figure 4.4 are similar to those in Figure 4.3c. $f_2^{\mathrm{Hf/W}}(\tau_0)$ is greater than $f_3^{\mathrm{Hf/W}}(\tau_0)$ when $\xi = 0 - 0.22$ (corresponding to a shallow magma ocean with a final $P_{\mathrm{eq}}(\tau_0) = 0 - 5\ GPa$), but smaller than $f_3^{\mathrm{Hf/W}}(\tau_0)$ when $\xi = 0.22 - 1$ (corresponding to a deep magma ocean with a final $P_{\mathrm{eq}}(\tau_0) = 5 - 24\ GPa$). The depletion of siderophile elements in the martian mantle (Righter and Chabot, 2010) suggested the last metal-silicate equilibration pressure in Mars is 14±3 GPa, which is corresponding to the $\xi = 0.58 \pm 0.12$ (gray area in the Figure 4.4). Accepting $\xi = 0.58 \pm 0.12$, our model shows that after completion of core formation, Mars has an upper mantle reservoir with a $f_2^{\mathrm{Hf/W}}(\tau_0) = 2.2 \pm 0.4$ and a lower mantle reservoir with a $f_3^{\mathrm{Hf/W}}(\tau_0) = 3.2 \pm 0.4$. There is a difference between $f_2^{\mathrm{Hf/W}}(\tau_0)$ and $f_3^{\mathrm{Hf/W}}(\tau_0)$ of ~1.

Although the Hf/W ratio in the upper mantle is consistent with the observed mantle Hf/W ratio of shergottites (2.56 ± 0.46), the Hf/W ratio in the lower mantle is way lower than the observed mantle Hf/W ratio of nakhlites + Chassignites (4.50 ± 0.53). Therefore, a more realistic case incorporating a significant fractionation of Hf and W during crystallization of silicate will be discussed in the following section.

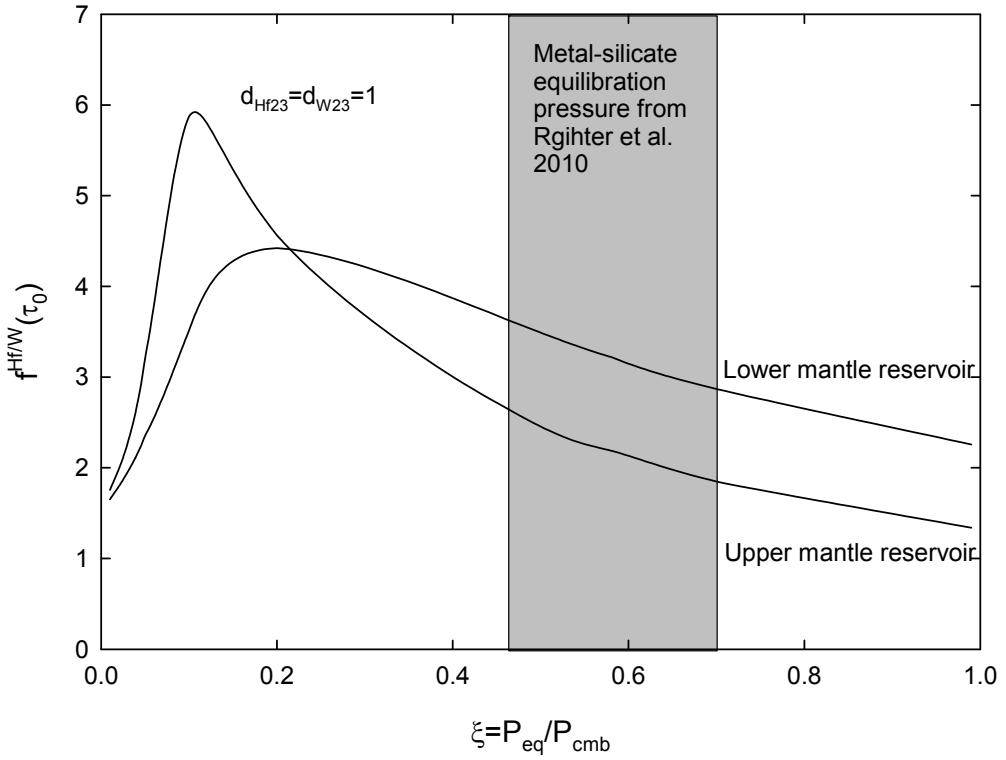

Figure 4.4 Final $f^{\mathrm{Hf/W}}$ values of the upper and lower martian mantle reservoirs at present (τ_0) as a function of the ratio of metal-silicate equilibration pressure and core-mantle boundary pressure $(\xi = P_{\mathrm{eq}}/P_{\mathrm{cmb}})$ when d_{Hf23}=d_{W23}=1. The gray area represents $\xi = 0.58 \pm 0.12$, equivalent to the final metal-silicate equilibrium pressure $P_{eq}(\tau_0) = 14 \pm 3$, which is required by the depletion of siderophile elements in the martian mantle (Righter and Chabot, 2010). Corresponding to the gray area, after core formation, Mars has an upper mantle reservoir with an $f_2^{\mathrm{Hf/W}}(\tau_0) = 2.2 \pm 0.4$ and a lower mantle reservoir with an $f_3^{\mathrm{Hf/W}}(\tau_0) = 3.2 \pm 0.4$.

4.5.2 Existence of Hf and W Fractionation between the Upper Magma Ocean and Solid Lower Mantle.

We have discussed the case where there is no Hf and W fractionation between the two mantle reservoirs. But it is more realistic to include the effect of Hf and W fractionation between the upper and lower mantle reservoirs in the model. The parameterization of the simultaneous partition coefficients of Hf and W between the newly crystallized silicate and the upper magma ocean (d_{Hf23} and d_{W23}) is described in Section 4.4.3. Since Hf and W are incompatible elements for most of mantle minerals, the upper mantle reservoir would have higher concentrations of Hf and W while the lower mantle reservoir would have lower Hf and further lower W concentrations (Figure 4.5), compared with the simplified case in Section 4.5.1. Given that the final metal-silicate equilibration pressure is 14±3 GPa (Righter and Chabot, 2010), $f_2^{\mathrm{Hf/W}}(t)$ and $f_3^{\mathrm{Hf/W}}(t)$ are shown as a function of mass fraction of the growing Mars (Figure 4.6b). In this case, $f_2^{\mathrm{Hf/W}}(t)$ is always higher than $f_3^{\mathrm{Hf/W}}(t)$ throughout the accretion history of Mars. The difference between $f_2^{\mathrm{Hf/W}}$ and $f_3^{\mathrm{Hf/W}}$ is increasing over time and the difference between final $f_2^{\mathrm{Hf/W}}(\tau_0)$ and $f_3^{\mathrm{Hf/W}}(\tau_0)$ after completion of accretion and core formation is ~10, which is much larger than the difference in the case of Section 4.5.1 (~1), due to Hf/W fractionation caused by the crystallizations of clinopyroxene, garnet and spinel. The final $f_2^{\mathrm{Hf/W}}(\tau_0)$ and $f_3^{\mathrm{Hf/W}}(\tau_0)$ as a

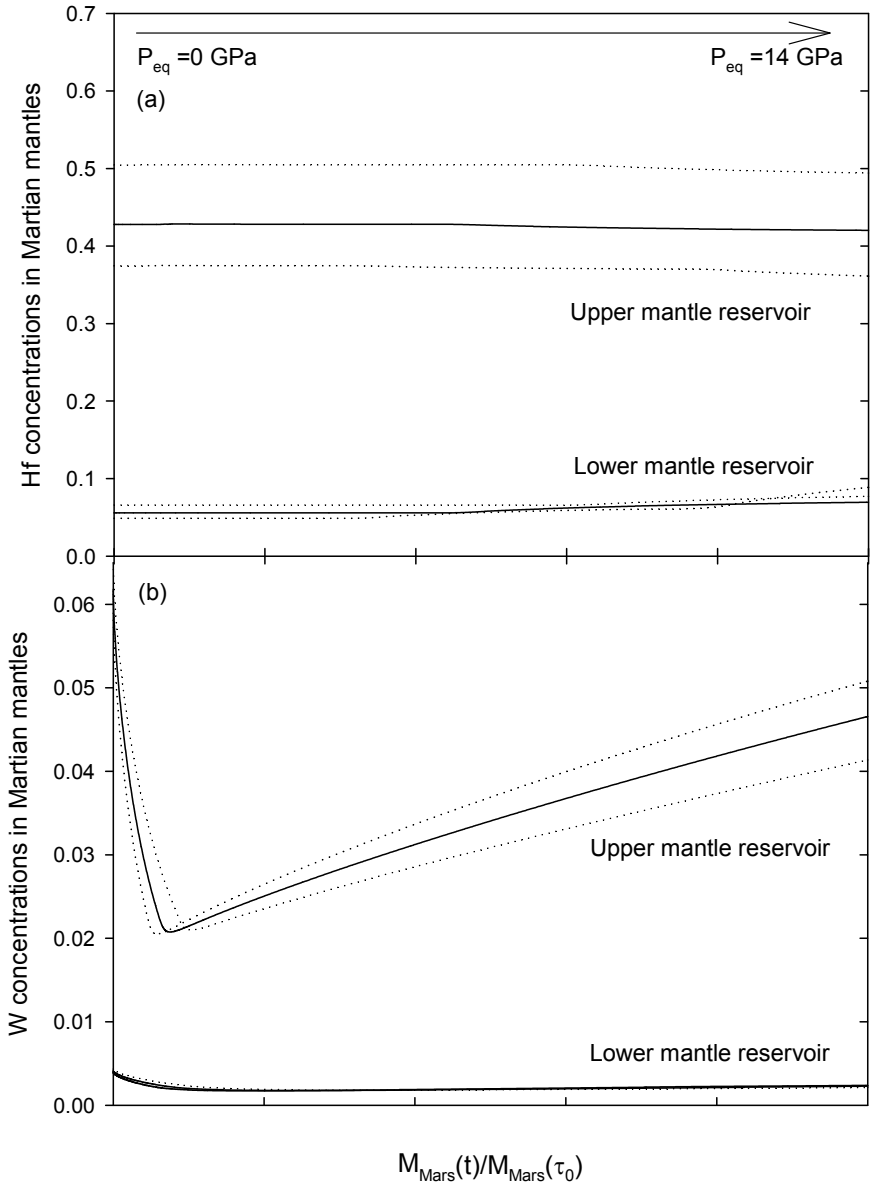

Figure 4.5 Hf and W concentrations of the upper and lower martian mantle reservoirs are shown as a function of the mass fraction of the growing Mars. Parameterization of d_{Hf23} and d_{W23} follows Section 4.4.3. The final metal-silicate equilibration pressure in Mars $\left(P_{\mathrm{eq}}(\tau_0)\right)$ is 14±3 GPa which is required by the depletion of siderophile elements in the martian mantle (Righter and Chabot, 2010). The solid curves represent the results when $P_{\mathrm{eq}}(\tau_0)$=14 GPa and the dotted lines show the ranges due to the uncertainty of $P_{\mathrm{eq}}(\tau_0)$.

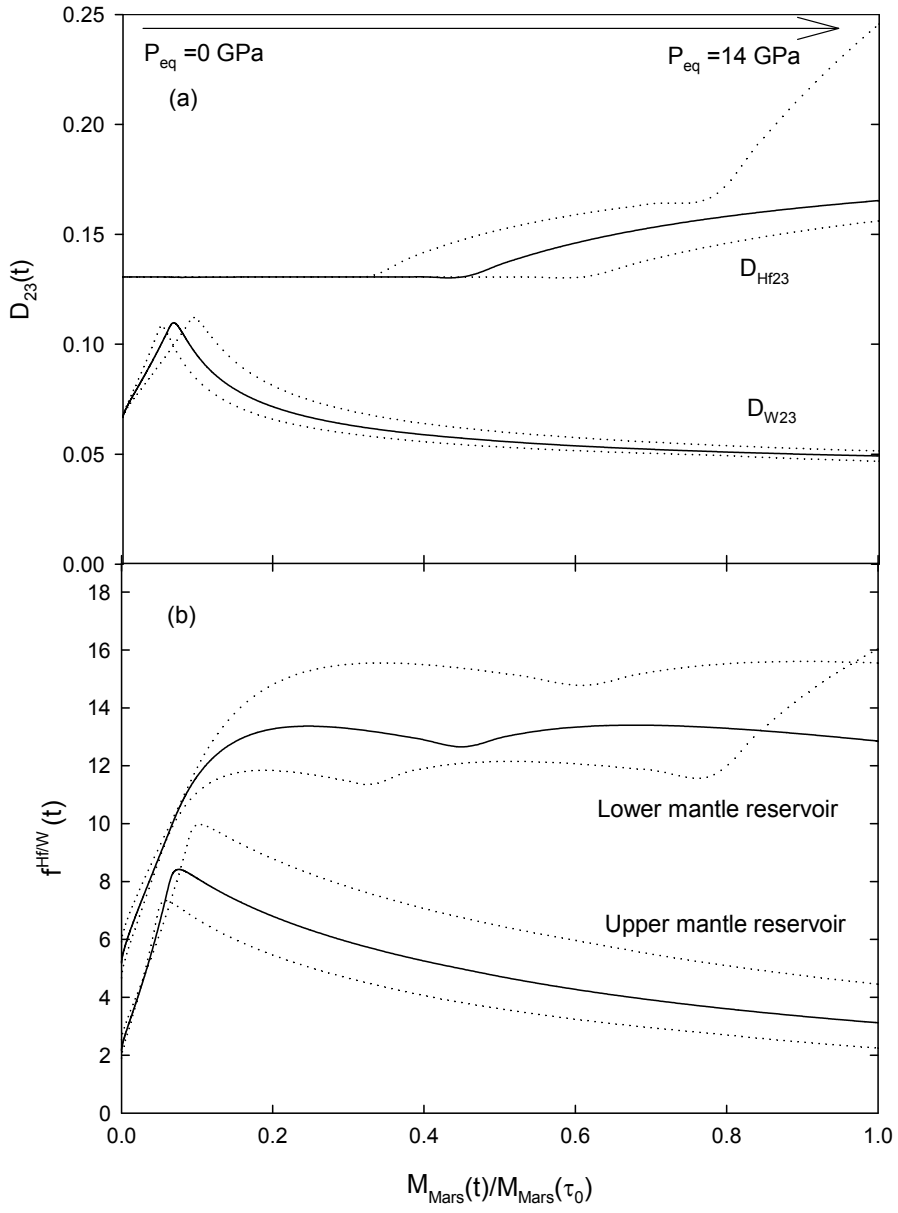

Figure 4.6 (a) Effective partition coefficients of Hf and W between the upper and lower martian mantle reservoirs as a function of the mass fraction of the accreting Mars. (b) $f^{\mathrm{Hf/W}}$ values of the mantle reservoirs as a function of the mass fraction of the accreting Mars. Parameterization of d_{Hf23} and d_{W23} follows Section 4.4.3. The final metal-silicate equilibrium pressure is set to be 14±3 GPa, which is required by the depletion of siderophile elements in the martian mantle (Righter and Chabot, 2010). The solid curves represent the results when $P_{\mathrm{eq}}(\tau_0)$ =14 GPa and the dotted lines show the ranges due to the uncertainty of $P_{\mathrm{eq}}(\tau_0)$.

function of ξ are shown in Figure 4.7. The second increase of $f_3^{\mathrm{Hf/W}}$ in the upper mantle around $\xi = 0.6$ caused by crystallization of garnet and spinel when $P_{\mathrm{eq}} \geq 14\,GPa$. The gray area in Figure 4.7 represents $\xi = 0.58 \pm 0.12$ (corresponding to the final $P_{\mathrm{eq}}(\tau_0) = 14 \pm 3$ GPa (Righter and Chabot, 2010).

Taking $\xi = 0.58 \pm 0.12$ into our model, we can obtain the final $f^{\mathrm{Hf/W}}$ in the upper and lower mantle reservoirs respectively ($f_2^{\mathrm{Hf/W}}(\tau_0) = 3.1^{+1.4}_{-0.9}$ and $f_3^{\mathrm{Hf/W}}(\tau_0) = 12.8^{+2.8}_{+3.2}$). However, the Hf/W ratio in the lower mantle reservoir is much higher than the observed Hf/W ratios in mantles of shergottites and nakhlites + Chassignites.

After obtaining the $f^{\mathrm{Hf/W}}$ values in the upper and lower mantle reservoirs, we can model the evolution of W isotopic composition in the mantle reservoirs and the final $\varepsilon_{\mathrm{W}}(\tau_0)$, and $\varepsilon_{\mathrm{W}}(\tau_0)$ as a function of the mean time of accretion of Mars (t_{m}) as shown in Figure 4.8. If the $\varepsilon_{\mathrm{W}}(\tau_0)$ of the shergottites (2.23 ± 0.21) represents the $\varepsilon_{\mathrm{W}}(\tau_0)$ of the upper mantle reservoir of Mars in our model, it would require Mars to have a mean time of formation of 5.3 ± 2.4 Myr. Corresponding to this timescale, the lower mantle reservoir should have a $\varepsilon_{\mathrm{CW}}(\tau_0)$ of ~14-19, which is much higher than $\varepsilon_{\mathrm{W}}(\tau_0)$ of nakhlites + chassignites and has not been observed in any martian meteorites yet.

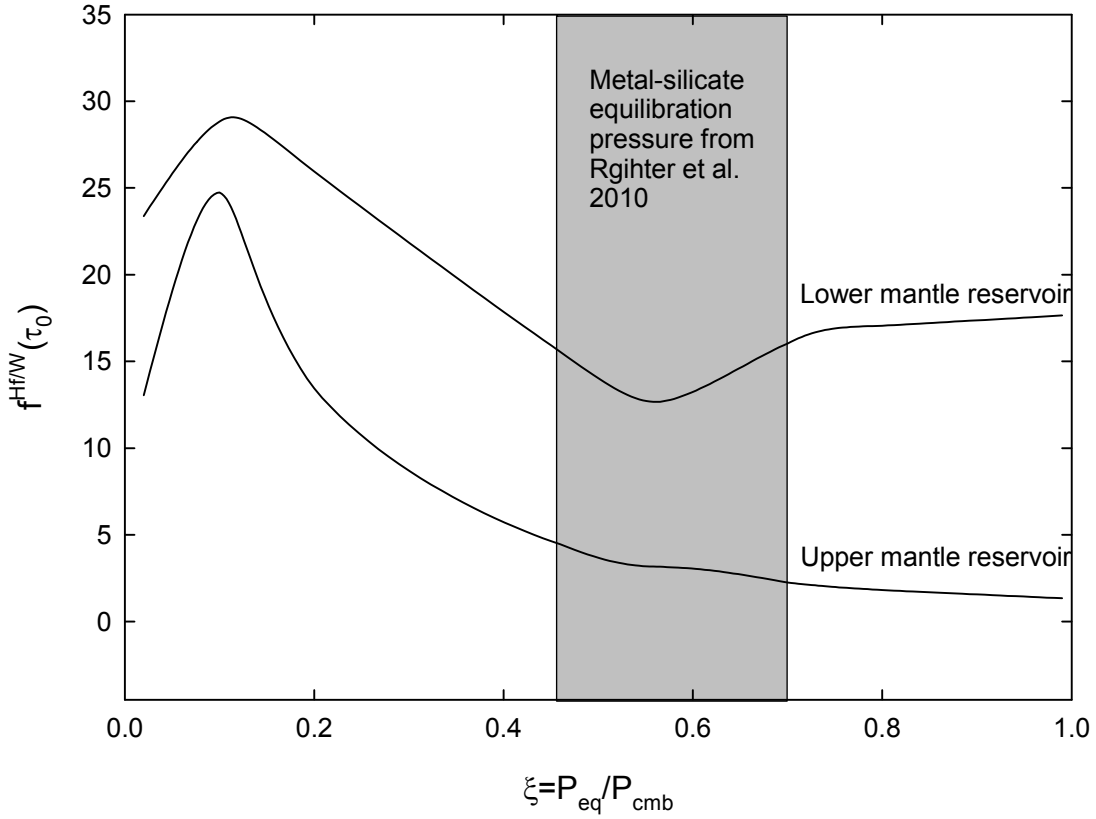

Figure 4.7 Final $f^{\mathrm{Hf/W}}$ of the upper and lower martian mantle reservoirs at present (τ_0) as a function of the ratio of metal-silicate equilibration pressure and core-mantle boundary pressure $(\xi = P_{\mathrm{eq}}/P_{\mathrm{cmb}})$. Parameterization of d_{Hf23} and d_{W23} follows Section 4.4.3. Gray area represents $\xi = 0.58 \pm 0.12$, equivalent to the final metal-silicate equilibrium pressure $P_{\mathrm{eq}}(\tau_0) = 14 \pm 3$ GPa (Righter and Chabot, 2010). Corresponding to the gray area, Mars has an upper mantle reservoir with an $f_2^{\mathrm{Hf/W}}(\tau_0) = 3.1^{+1.3}_{-0.9}$ and a lower mantle reservoir with an $f_3^{\mathrm{Hf/W}}(\tau_0) = 12.8^{+3.5}_{+4}$.

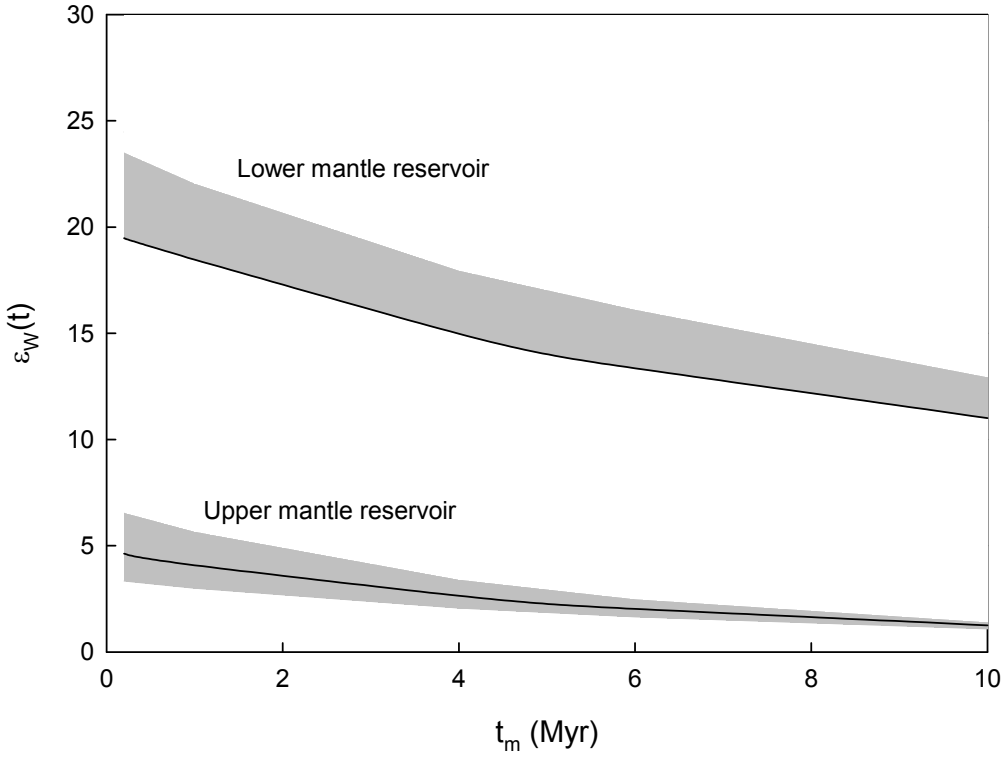

Figure 4.8 Final ε_W of the upper and lower martian mantle reservoirs at present (τ_0) as a function of the mean time of accretion of Mars (t_{m}). Parameterization of d_{Hf23} and d_{W23} follow Section 4.4.3. Gray areas represent the possible range of $\varepsilon_{\mathrm{W}}(\tau_0)$ corresponding to the uncertainty of the final metal-silicate equilibrium pressure (P_{eq}=14±3 GPa (Righter and Chabot, 2010)). If the $\varepsilon_{\mathrm{W}}(\tau_0)$ of the shergottites (2.23 ± 0.21) represents the $\varepsilon_{\mathrm{W}}(\tau_0)$ of the upper mantle, it requires Mars to have a mean time of formation of 5.3±2.4 Myr. Consequently, the lower mantle would have a $\varepsilon_{\mathrm{W}}(\tau_0)$ of ~14-19, which so far has not been observed in any martian meteorites.

4.5.3 Incomplete Separation of Silicate Crystal and Silicate Melt

Besides the two scenarios discussed above, another possibility is that separation of silicate crystals from silicate melt is not complete during the solidification of the upper magma ocean. Therefore, what is added into the solid lower mantle reservoir from the upper magma ocean may be a crystal-melt mush. In this case, all model governing equations remain the same but simply replace the simultaneous partition coefficients between silicate and silicate melt (d_{23}) with an effective enrichment factor ($d_{23}^{*} = d_{23}(1-F)+F$, where F is the mass fraction of silicate melt in the segregated crystal-melt mush and $0 \leq F \leq 0.5$). The upper limit of 0.5 comes from the fact that the presence of silicate melt would decrease the viscosity of the crystal-melt mush and when the fraction of melt (F) is greater than a critical value (~0.4-0.5; (Lejeune and Richet, 1995)), the viscosity will become close to that of melt and hence might not be able to impede the sinking of liquid metal. When $F = 0$, $d_{23}^{*} = d_{23}$, which is the previous case of a complete separation of silicate crystals from the upper magma ocean (Section 4.5.2). Now we explore the cases where the F values are equal to 0.1, 0.3 and 0.5 respectively.

The final $f^{\mathrm{Hf/W}}(\tau_0)$ in the upper and lower mantle reservoirs as a function of ξ and F are shown in Figure 4.9. Given the final metal-silicate equilibration pressure of 14 ± 3 GPa (Righter and Chabot, 2010),

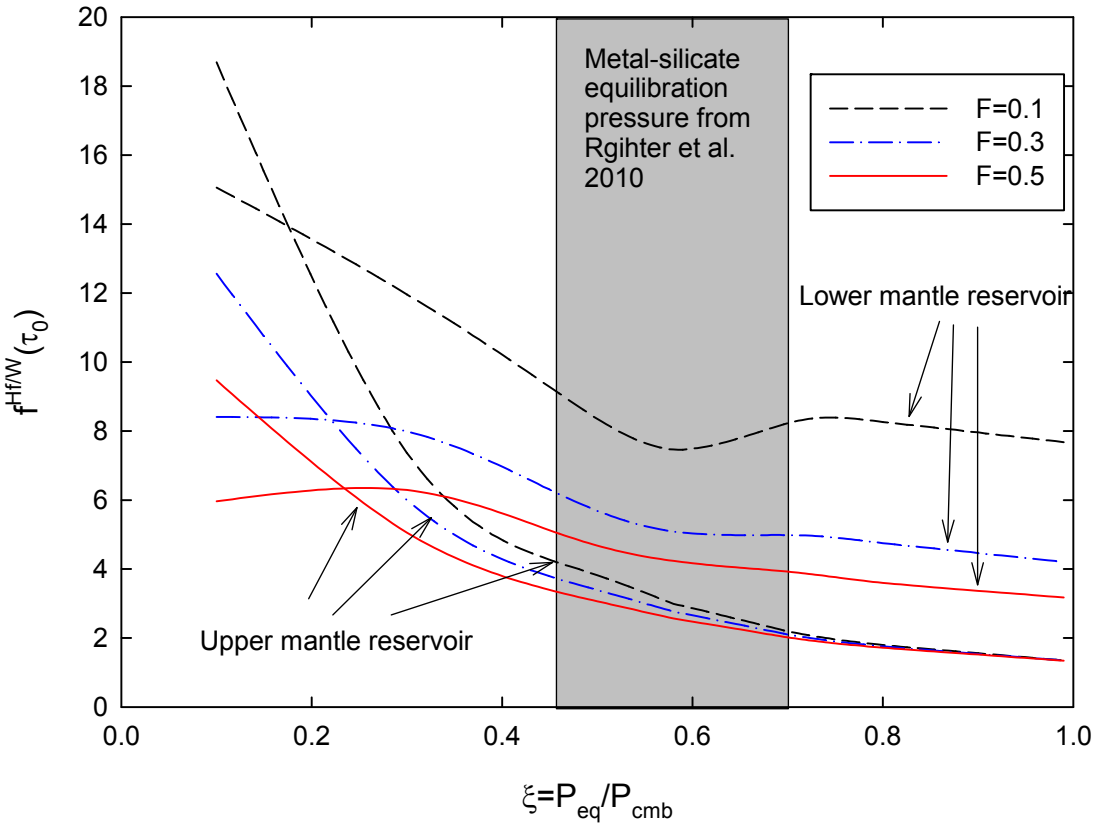

Figure 4.9 Final $f^{\mathrm{Hf/W}}$ of the upper and lower martian mantle reservoirs at present (τ_0) as a function of the ratio of metal-silicate equilibration pressure and core-mantle boundary pressure ($\xi = P_{\mathrm{eq}}/P_{\mathrm{cmb}}$) for different mass fractions of silicate melt in the segregated crystal-melt mush (F = 0.1, 0.3 or 0.5). Parameterization of d_{Hf23} and d_{W23} follows Section 4.4.3. Gray area represents $\xi = 0.58 \pm 0.12$, equivalent to the final metal-silicate equilibrium pressure $P_{\mathrm{eq}}(\tau_0) = 14 \pm 3$ GPa (Righter and Chabot, 2010). For the case of F = 0.5, the gray area constrains that Mars has an upper mantle reservoir with an $f_2^{\mathrm{Hf/W}}(\tau_0) = 2.6 \pm 0.6$ and a lower mantle reservoir with an $f_3^{\mathrm{Hf/W}}(\tau_0) = 4.2^{+0.8}_{-0.3}$.

the $f^{\mathrm{Hf/W}}(\tau_0)$ in the upper mantle reservoir only slightly decreases from $f_2^{\mathrm{Hf/W}}(\tau_0) = 3.0\pm^{1.2}_{0.8}$ when $F = 0.1$ to $f_2^{\mathrm{Hf/W}}(\tau_0) = 2.6 \pm 0.6$ when $F = 0.5$. On the other hand, the $f^{\mathrm{Hf/W}}(\tau_0)$ in the lower mantle reservoir dramatically decreases from $f_3^{\mathrm{Hf/W}}(\tau_0) = 7.5\pm^{1.6}_{0.7}$ when $F = 0.1$ to $f_3^{\mathrm{Hf/W}}(\tau_0) = 4.2 \pm^{0.8}_{0.3}$ when $F = 0.5$. It can be seen that only when $F = 0.5$, the calculated Hf/W ratios in the upper and lower mantle reservoirs can match the observed mantle Hf/W ratios in shergottites and nakhlites + chassignites ($f^{\mathrm{Hf/W}}$ = 2.56 ± 0.46 and $f^{\mathrm{Hf/W}}$ = 4.50 ± 0.53) respectively.

Correspondingly, $\varepsilon_{\mathrm{W}}(\tau_0)$ of the upper mantle reservoir does not change much with the varying F values, but $\varepsilon_{\mathrm{W}}(\tau_0)$ in the lower mantle reservoir dramatically decreases when the F increases (Figure 4.10). For a given accretion timescale of Mars characterized by the mean time of accretion (t_m), only the condition ($F = 0.5$) can simultaneously reproduce the observed $\varepsilon_{\mathrm{W}}(\tau_0)$ in the shergottites and the nakhlites + chassignites.

In addition, when F = 0.5 and $P_{\mathrm{eq}}(\tau_0)$ = 14±3 GPa, Hf and W concentrations in the mantle reservoirs (C_{Hf2}, C_{Hf3}, C_{W2} and C_{W3}) and the effective partition coefficients of Hf and W between the two mantle reservoirs (D_{Hf23} and D_{W23}) are shown as a function of the mass fraction of the growing Mars in Figure 4.11. The Final C_{Hf2}, C_{Hf3}, C_{W2} and C_{W3} are $0.35 \pm 0.03, 0.20 \pm 0.01, 0.044 \pm 0.005$ and 0.018 ± 0.002 ppm respectively. The final D_{Hf23} = $0.59^{+0.04}_{-0.01}$ and D_{W23} = 0.40±0.02 are equivalent to the

enrichment factors of Hf and W between the sources of the shergottites and the nakhlites + chassignites.

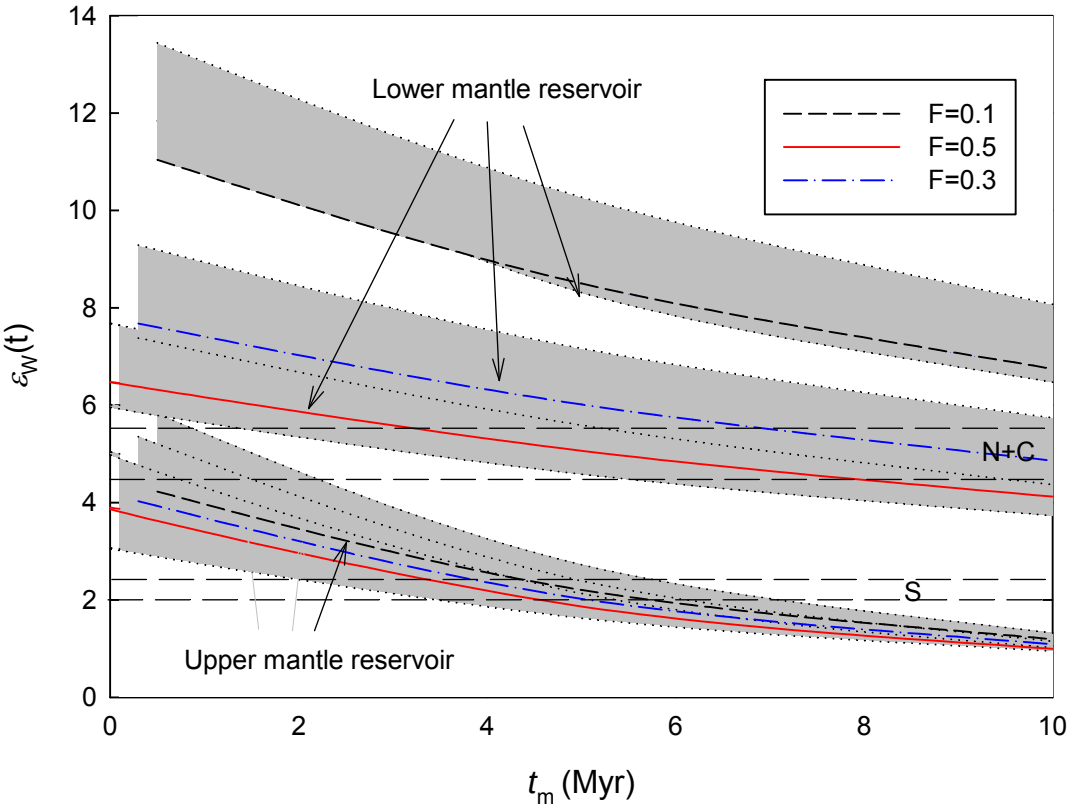

Figure 4.10 Final ε_W of the upper and lower martian mantle reservoirs at present (τ_0) as a function of the mean time of accretion of Mars (t_m) for different mass fraction of silicate melt in the segregated crystal-melt mush (F=0.1, 0.3 or 0.5). Parameterization of d_{Hf23} and d_{W23} follow Section 4.4.3. Gray areas represent the possible range of $\varepsilon_W(\tau_0)$ corresponding to the uncertainty of the final metal-silicate equilibrium pressure (P_{eq}=14 ± 3 GPa (Righter and Chabot, 2010)). Only the case when F = 0.5 can simultaneously reproduce the observed W isotopic composition of shergottites (2.23 ± 0.21) and nakhlites + chassignites (5.15 ± 0.5), which are represented by areas of S and N+C. In this case, Mars' accretion has a mean time of 3.6 ± 0.1 Myr.

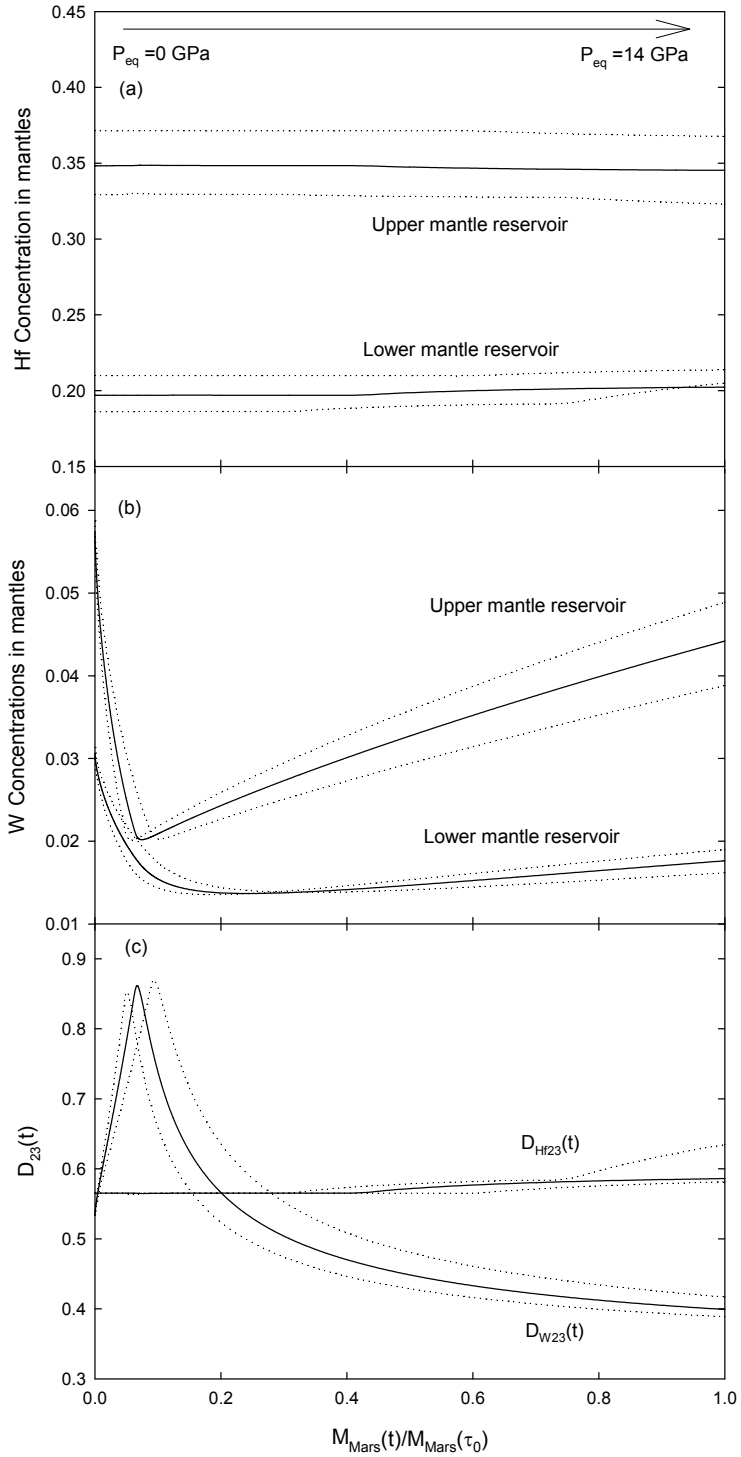

Figure 4.11 Hf and W concentrations of the upper and lower martian mantle reservoirs (a and b) and effective partition coefficients of Hf and W between the mantle reservoirs (D_{Hf23} and D_{W23}, c) are shown as a function of the mass fraction of the growing Mars when mass fraction of

Figure 4.11 (Continued) silicate melt in the segregated crystal-melt mush (F) is 0.5. Parameterization of d_{Hf23} and d_{W23} follows Section 4.4.3. The final metal-silicate equilibration pressure in Mars $\left(P_{\mathrm{eq}}(\tau_0)\right)$ is 14±3 GPa which is required by the depletion of siderophile elements in the martian mantle (Righter and Chabot, 2010). The solid curves represent the results when $P_{\mathrm{eq}}(\tau_0)$ = 14 GPa and the dotted lines show the ranges due to the uncertainty of $P_{\mathrm{eq}}(\tau_0)$.

In sum, our model shows that the scenario when ~50% of the melt was trapped during silicate crystallization can successfully explain both the observed Hf/W ratios and W isotopic composition in mantle sources of martian meteorites. Further discussion about separation of partial crystallized magma are in section 4.6.2. The accuracy of the estimate of ~50% trapped melt is dependent on the choice of the simultaneous silicate-silicate melt partition coefficients of Hf and W in our model (Section 4.4.3). Different silicate solid- silicate melt partition coefficients of Hf and W would lead to different proportion of trapped melt in crystallizing magma. In fact, the more useful information is the effective enrichment factor between the silicate and silicate melt, which can be represented by the effective partition coefficients between the upper and lower mantle reservoirs (D_{Hf23} and D_{W23}) in Figure 4.11c. Whatever choices of silicate solid- silicate melt partition coefficients and proportions of trapped melts must have to result in the effective upper and lower mantles partition coefficients in Figure 4.11c (e.g. the final D_{Hf23} = $0.59^{+0.04}_{-0.01}$ and D_{W23} = 0.40±0.02).

4.5.4 Accretion Timescale of Mars

Previous estimates on the accretion timescale of Mars (0-15 Myr) actually only provide the upper limit (longest accretion time) because they all assume that the W isotopic composition of the shergottites represents the W isotopic composition of bulk martian mantle and ignore nakhlites + chassignites with more radiogenic W isotopic composition (Foley et al., 2005; Nimmo and Kleine, 2007; Dauphas and Pourmand, 2011). The wide range of the previous Hf-W ages comes from the poor constrained Hf/W ratio in martian mantle due to the limited ICP-MS data of martian meteorites.

Our new measurements result in the distinct mantle Hf/W ratios of shergottites and nakhlites + chassginites, which can be well explained by the "deep magma ocean" core formation model when the separated crystals from the upper magma ocean keep trapping ~50% of the silicate melt. By best matching our modeling results with the observed W isotopic composition in martian meteorites, a new accretion timescale for Mars can be obtained (Figure 4.10). A Monte Carlo algorithm is introduced to run the model 1000 times to calculate the mean and uncertainty of Mars' accretion timescale. The mean time of Mars' accretion is 3.6 ± 0.1 Myr, which means that Mars reaches 63% of its present mass at 3.6 ± 0.1 Myr and reaches 95% of its preset mass at 10.8 ± 0.3 Myr after the onset of the Solar System.

4.6 Discussion

4.6.1 A Shallow Shergottite Mantle and a Deep Nakhlites + Chassignites Mantle in Mars

Besides W isotopes, Sr, Nd and Pb isotopic compositions also show that the sources of nakhlites + chassignites are distinguishable from the source of the shergottites (Jones, 2003; Bouvier et al., 2009; Debaille et al., 2009). It has been suggested that the shergottites' source was formed from progressive crystallization of a shallow magma ocean existing for ~100 million years after core formation (Debaille et al., 2007), while the sources of nakhlites + chassignites were formed earlier than the shergottites' source and located in the deeper mantle (garnet- or ilmenite-bearing, Bouvier et al., 2009; Debaille et al., 2009). A similar martian mantle structure with a deep nakhlite mantle and a shallow shergottite mantle is also required by thermal energy budget of Mars (Jones, 2003). Those results are consistent with our modeling result of F = 0.5, which can produce a martian interior where an upper and lower mantle reservoirs have the W isotopic composition of shergottites and nakhlites + chassignites, respectively.

As illustrated by Figure 4.11a, the lower mantle reservoir is more depleted in Hf concentration than the upper mantle reservoir. The result is consistent with the fact that the source of the nakhlites + chassignites is more depleted than the source of the shergottites. Moreover, the final

Hf concentration in the lower mantle reservoir ($C_{Hf3} = 0.20 \pm 0.01$ ppm, Figure 4.11a) is also similar to the estimated Hf concentration in the source of nakhlites + chassignites ($\sim 0.23 \pm 0.13$ ppm), which is calculated from (Nakamura et al., 1982).

Previous work shows that all types of martian meteorites have a similar Th/W ratio and infers that bulk martian mantle has a homogeneous $f^{Hf/W}$ (Nimmo and Kleine, 2007; Dauphas and Pourmand, 2011). However, the dataset including ICP-MS results from this study and literatures shows that the two groups of martian meteorites – shergottites and nakhlites + Chassignites have distinct Th/W ratios (Figure 4.1), corresponding to distinct mantle Hf/W ratios in the two groups of martian meteorites. Combined all pieces together, a martian mantle structure with a shallow shergottite mantle and a deep nakhlites + chassignites mantle is reasonable. The mantle structure is also consistent with the outcome of the "deep magma ocean" core formation processes, which is implied by siderophile element abundances in martian mantles.

4.6.2 Partial Crystallized Deep Mantle

In order to match the W isotopic compositions of shergottites and nakhlites + chassignites, the separation of crystals from the magma ocean into the solid lower mantle has to be incomplete (Figure 4.10). ~ 50% of silicate melt should be trapped between the sinking crystals to form a

crystal-melt mush. It is the crystal-melt mush instead of pure solid crystals to be separated from the magma ocean and added into the lower mantle reservoir. This conclusion is supported by the experimental results from (Lejeune and Richet, 1995), which shows that there is a dramatic change in viscosity of silicate melt when it includes about 50-60% crystals and its behavior becomes similar to solid silicate. So the 50/50 mixture of crystal and melt may have a high enough viscosity to impede the sinking of metal droplets. Moreover, the difficulty of complete separation of silicate crystal and melt by gravity may come from the fact that the silicate melt becomes denser under a higher pressure and even denser than some silicate minerals under a high enough pressure. For example, olivine floats in a magma ocean at 7-12 GPa (Righter and Chabot, 2011). A possible mechanism for the "deep magma ocean" core formation model has been proposed by (Righter and Chabot, 2011) that during crystallization of the magma ocean, there could be garnet- or olivine-rich layers floating in the magma ocean and impeding the mobility of metal into the core. The process is likely to trap a high percentage of melt in the lower mantle, which is consistent with our modeling results.

4.6.3 Application to the Earth

Depletion of siderophile elements in the terrestrial mantle has been suggested to be consistent with a core formation model with an

intermediate deep magma ocean with a thickness corresponding to 31-35% of the depth of the Earth's mantle (Wade and Wood, 2005; Wood et al., 2008b; Rudge et al., 2010; Rubie et al., 2011). So the "deep magma ocean" core formation model can also be applied to the Earth. As a consequence, the early Earth could also have a two-mantle-reservoir structure with different Hf/W ratios and W isotopic compositions (Figure 4.12). However, so far, all young terrestrial basalts show no detectable heterogeneity in $^{182}W/^{183}W$ ($\varepsilon_{W(CHUR)}$ = 1.9±0.2, (Schoenberg et al., 2002; Yin et al., 2002; Schersten et al., 2004; Willbold et al., 2011; Touboul et al., 2012) although small W isotope heterogeneity has been reported in the rocks of 2.8 and 3.8 Ga (Willbold et al., 2011; Touboul et al., 2012). Without knowing the specific values of the possible W isotopic compositions of terrestrial mantles produced from the "deep magma ocean" core formation processes, in practice, the "deep magma ocean" core formation model cannot be applied to the Earth.

The mechanism to erase or reduce the predicated W isotope heterogeneity in Earth's mantles from the "deep magma ocean" core formation model could be either the complete melting caused by late giant impacts (maybe Moon-forming giant impact) or the 4.5 Ga-long active mantle convection. The former is hard to test now while the latter is testable. It has been shown by (Kellogg et al., 2002, 2007) that the

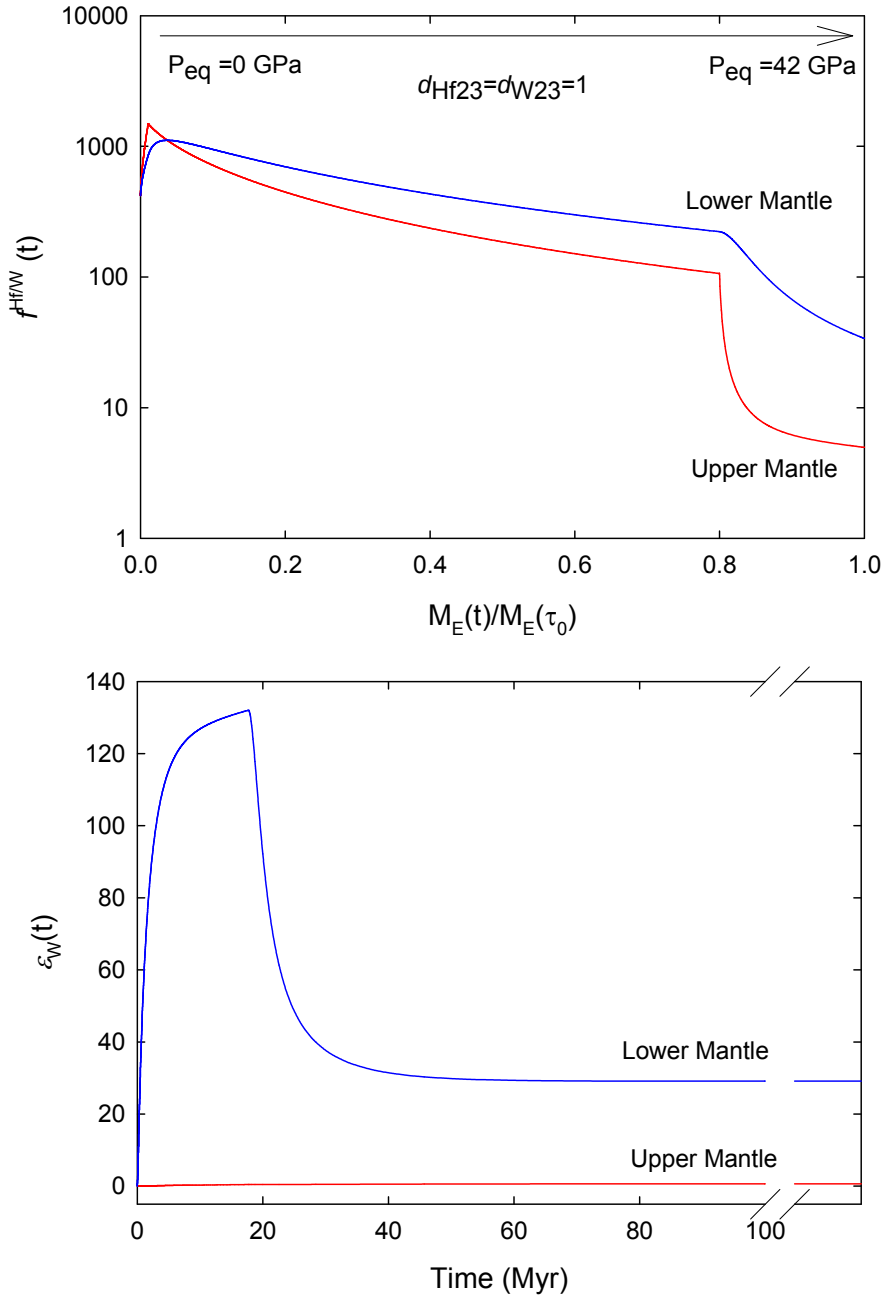

Figure 4.12 Modeling results for Earth. (a) Hf/W ratios (as $f^{Hf/W}$) in Earth's mantles as a function of the mass fraction of the growing Earth. (b) Evolution of W isotopic composition (as εW) in Earth's mantles over time (Myr).

present Earth mantle heterogeneities in the long-lived isotopic systems (^{87}Rb-^{87}Sr and ^{147}Sm-^{143}Nd) can be reproduced by a 500 Myr mantle stirring rate and 30-100 km sampling size of basalts. In next chapter (Chapter 5), we tested the latter hypothesis using the principals from (Kellogg et al., 2002, 2007). In Chapter 5, we concluded that a mantle stirring rate of 500 Myr would be able to reduce the bimodal W isotopic compositions in Earth mantles predicated by the "deep magma ocean" core formation model to a W isotopic heterogeneity scale of only ~84 m in Earth's mantle today. Given a 100 km sampling size of terrestrial basalts much larger than 84 m, a homogeneous well-mixed W isotopic composition is expected for all modern terrestrial basalts. So, in practice, the case of the Earth is more like the core formation model with one homogeneous mantle reservoir as discussed in Chapter 3 rather than the core formation model discussed in this Chapter. We can say that the results from Chapter 3 are still the best constraints on the formation timescale of the Earth-Moon system.

4.6.4 Mars is not a Planetary Embryo

The terrestrial planets are believed to form through sticking and collisions of tiny sun-orbiting objects. The widely accepted standard model for terrestrial planet formation is the planetesimal hypothesis (e.g. Agnor et al., 1999; Chambers, 2004; O'Brien et al., 2006; Canup, 2008): (1) The

young Sun is surrounded by a disk of gas and dust. Then dust grains stick together to form km-sized planetesimals. (2) Collisions of planetesimals produce a few tens of Moon-to-Mars-sized planetary embryos in a rapid "runaway" growth phase followed by a slowed-down "oligarchic" growth phase (approximately 0.1-1 million years after the onset of the Solar System at 1 AU). (3) Finally planetary embryos suffer giant impacts, leading to full size planets like Earth in 10-100 million years.

Mars was thought to be a planetary embryo because of its small size and possibly rapid formation timescale (Jacobsen, 2005; Dauphas and Pourmand, 2011). The new formation timescale of Mars presented here is significantly longer (~10 Myr), suggesting that Mars may not be a planetary embryo formed in the runaway growth stage within ~1 Myr, but instead had a similar accretion history as the Earth. The possible scenario is as follows: first Mars and proto-Earth may be formed in a similar timescale (~10 Myr) if a late (≥ 52 Myr) Moon-forming giant impact is assumed. Then later on, the Earth-Moon system was formed in the last accretion stage involving the low probability late giant impact, but Mars escaped this stage. However, it has to be pointed out that if the Moon-forming giant impact occurred early at ~30 Myr, then it took about 3 times

longer time to form the proto-Earth compared to Mars (30 Mys vs. 10 Mys).

4.7 Conclusions

We measured trace element concentrations of two martian meteorites – zagami and nakhla from shergottite and nakhlite groups respectively. The results lead to the distinct Hf/W ratios in the mantle sources of shergottites and nakhlites + chassignites during core formation as $f^{\mathrm{Hf/W}}$ = 2.56 ± 0.46 and $f^{\mathrm{Hf/W}}$ = 4.50 ± 0.53 respectively.

The short-lived ^{182}Hf-^{182}W system in a "deep magma ocean" core formation model has been studied and applied to Mars. The model results show that after completion of core formation, Mars would have two mantle reservoirs with different $f^{\mathrm{Hf/W}}$ and ε_{W} characteristics, which are mainly controlled by the metal-silicate equilibrium pressure during core formation and the fractionation of Hf and W between the upper and lower mantles.

In the case where the separation of silicate minerals from the magma ocean is complete and given that the last metal-silicate equilibrium pressure is 14 ± 3 GPa, Mars would have an upper mantle reservoir with an $f_2^{\mathrm{Hf/W}}(\tau_0) = 3.1^{+1.3}_{-0.9}$ and a lower mantle reservoir with an $f_3^{\mathrm{Hf/W}}(\tau_0) = 12.8^{+3.5}_{+4}$. The corresponding ε_{W} values in two mantle reservoirs are a function of the timescale of Mars' accretion. If the observed $\varepsilon_{\mathrm{W}}(\tau_0)$

of the shergottites (2.23 ± 0.21) represents the $\varepsilon_{\mathrm{W}}(\tau_0)$ of the upper mantle reservoir of Mars, it is required for Mars to have a mean time of formation of 5.3 ± 2.4 Myr. Corresponding to this timescale, the lower mantle reservoir would have a very high $\varepsilon_{\mathrm{W}}(\tau_0)$ of 14-19, which has not been observed in any martian meteorites yet.

When separation of silicate crystals from silicate melt is incomplete during the solidification of the upper magma ocean and ~50% melt was trapped during the solidification of the upper magma ocean, our model can reproduce the observed $\varepsilon_{\mathrm{W}}(\tau_0)$ of shergottites and nakhlites + chassignites in the upper and lower mantle reservoirs of Mars simultaneously. This is consistent with a martian interior with a shallow shergottite mantle and a deep nakhlite mantle (Jones, 2003). In that case, the $f^{\mathrm{Hf/W}}(\tau_0)$ values of the sources of shergottites and nakhlites + chassignites are 2.6 ± 0.6 and $4.2 \pm^{0.8}_{0.3}$, respectively, which are consistent with the estimated mantle Hf/W ratios of shergottites and nakhlites + chassignites. Finally, incorporation of W isotopic compositions of SNC provides a new accretion timescale for Mars. The formation of Mars has a mean time of 3.6 ± 0.1 Myr, which means that Mars finishes 63% of its accretion at 3.6 ± 0.1 Myr after the birth of the Solar System. Therefore, Mars may not be a planetary embryo, and Mars and proto-Earth may be formed on a similar timescale if the currently late Moon-forming giant impact is assumed. In contrast, if the Moon formed early at ~30 Myr

then it takes about 3 times longer to form the proto-Earth compared to Mars.

Following the "deep magma ocean" core formation model, the early Earth could also develop a two-mantle-reservoir structure with different W isotopic compositions. But the W isotope heterogeneity in Earth's mantle is very likely to be reduced to an unrecognizable small scale after the 4.5 Ga-long active mantle stirring. So in practice, the core formation model with a homogeneous mantle reservoir is more suitable for the Earth as discussed in Chapter 3.

Chapter 5

Extinct Isotope Heterogeneities in the Mantles of Earth and Mars: Implications for Mantle Stirring Rates

Part of this chapter has been presented at the 2012, 43rd Lunar and Planetary Science Conference.

5.1 Introduction

Extinct isotope heterogeneity (such as ^{182}W and ^{142}Nd) in basalts from martian meteorites demonstrates the existence of very early geochemical heterogeneity in martian mantle. It has been reported that shergottites have a ε^{182}W(CHUR) of 2.23 ± 0.21 and nakhlites + chassigny have a ε^{182}W(CHUR) of 5.15 ± 0.50 (Foley et al., 2005). ε^{142}Nd of shergottites vary over 1.5 ε units and ε^{142}Nd of nakhlites + chassigny are similar to those of the depleted shergottites (Figure 5.1). We can see that there is no apparent correlation between shergottite and nakhlites + chassigny in terms of ε^{182}W(CHUR) or ε^{142}Nd. This W and Nd isotope

heterogeneities have been suggested to be the consequence of accretion and core formation (Yu and Jacobsen (2008) and Chapter 4), solidification of magma ocean and/or other early mantle differentiation events (Foley et al., 2005; Debaille et al., 2007; Debaille et al., 2009).

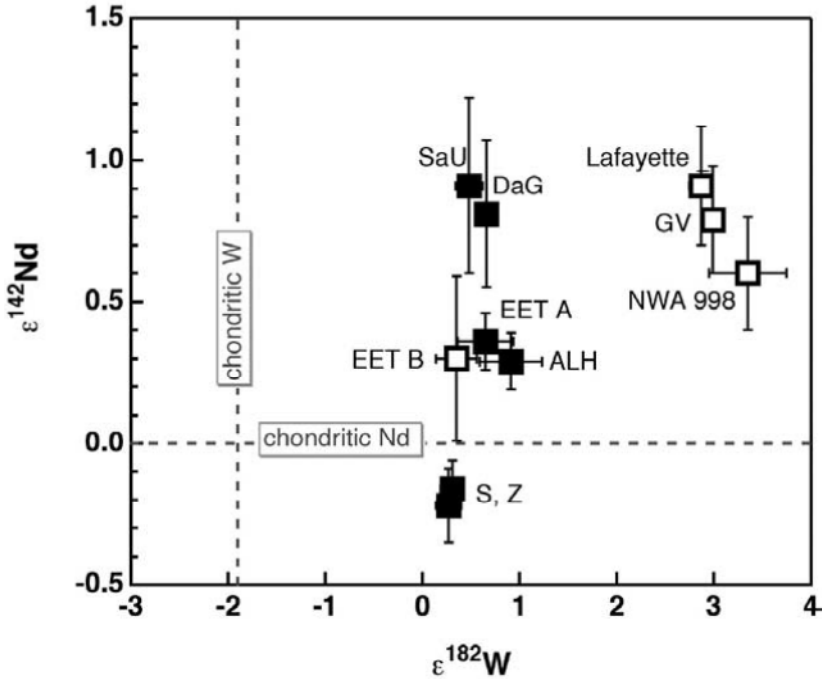

Figure 5.1 ε^{182}W vs. ε^{142}Nd in shergottites and nakhlites. The figure is from (Foley et al., 2005). S = Shergotty; Z = Zagami; EETA = EETA79001 Lithology A; EETB = EETA79001 Lithology B; DaG 476 = Dar al Gani 476; SaU 008 = Sayh al Uhaymir 008; ALH = ALHA77005; GV = Governador Valadares; Lafayette; NWA 998 = Northwest Africa 998. Solid symbols indicate that both W and Nd isotopic compositions are from (Foley et al., 2005); open symbols indicate that W isotopic compositions are from (Foley et al., 2005), and the Nd isotopic compositions are from (Harper et al., 1995; Carlson and Irving, 2004). The chondritic ε^{182}W value is from (Kleine et al., 2002; Schoenberg et al., 2002a; Yin et al., 2002); the chondritic ε^{142}Nd value here is assumed to be identical to that of the terrestrial standard.

In contrast, for the same extinct isotope systems, young terrestrial basalts show no detectable heterogeneity of ^{182}W and ^{142}Nd in spite of the data requiring these systems to be fractionated during the lifetime of their parent nuclides (^{182}Hf and ^{146}Sm) in the early Earth, which has been confirmed by the observed small isotope heterogeneity in rocks of 2.8 Ga and 3.8 Ga (Lee and Halliday, 1996; Schoenberg et al., 2002a; Schoenberg et al., 2002b; Schersten et al., 2004; Boyet and Carlson, 2005; Caro et al., 2006; Willbold et al., 2011; Touboul et al., 2012). (Figures 5.2 and 5.3)

One possible mechanism that could erase or reduce the expected ^{182}W and ^{142}Nd isotope heterogeneity in Earth's mantle might be the 4.5Ga-long active mantle convection as it did to the mantle heterogeneity of long-lived isotope systems. To test this hypothesis, here we developed a stochastic model for mantle mixing or stirring and basalt sampling in Earth and Mars following the principles of (Kellogg et al., 2002, 2007). Then, we explored the relative constraints that the ^{182}Hf-^{182}W isotopic system places on the convective mixing rates of an initially layered mantle structure for both Earth and Mars. Our model that leads to the observed W isotope signatures of terrestrial rocks is consistent with the mantle stirring rate that was suggested by the long-lived isotope systems; and the observed W isotope signatures of martian meteorites require the mantle stirring rate for Mars to be ≥1780 Myr, which corresponds to an at least 60 km W isotopic mantle heterogeneity in Mars. We here focus

on the application of the model to W isotopes but the general principles behind are applicable to any other extinct isotope systems (e.g. ^{142}Nd).

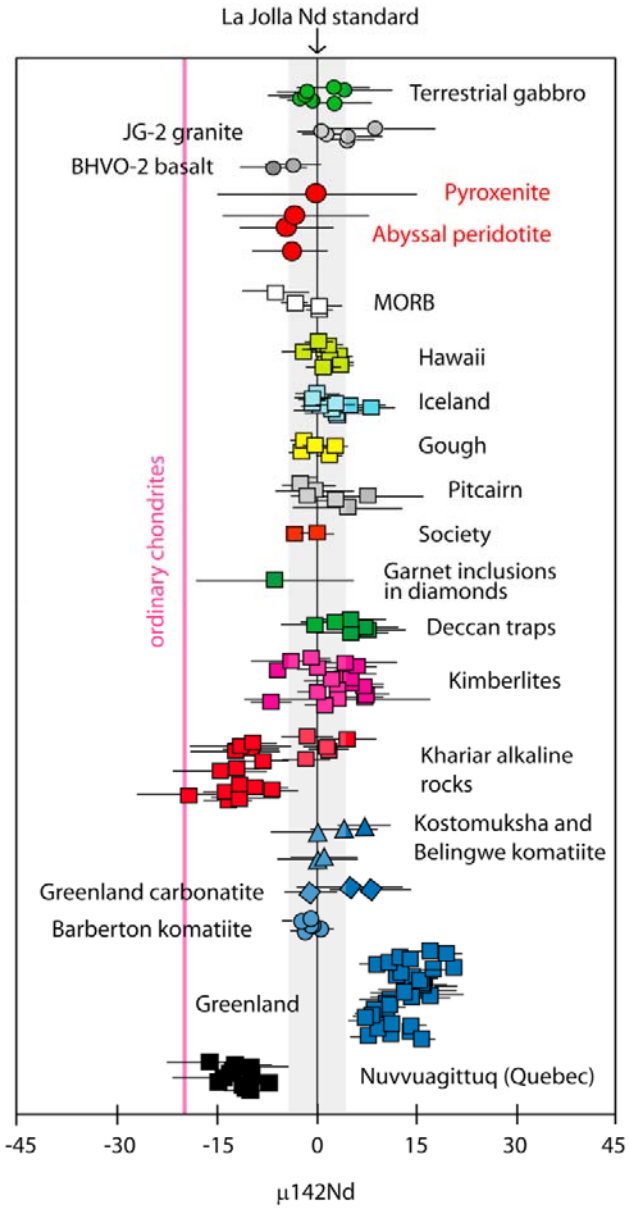

Figure 5.2 The ^{142}Nd/^{144}Nd of terrestrial rocks. The figure is from (Cipriani et al., 2011). Data are expressed as deviations in ppm (μ^{142}Nd) from the terrestrial standard. Error bars are 2 standard errors of individual measurements.

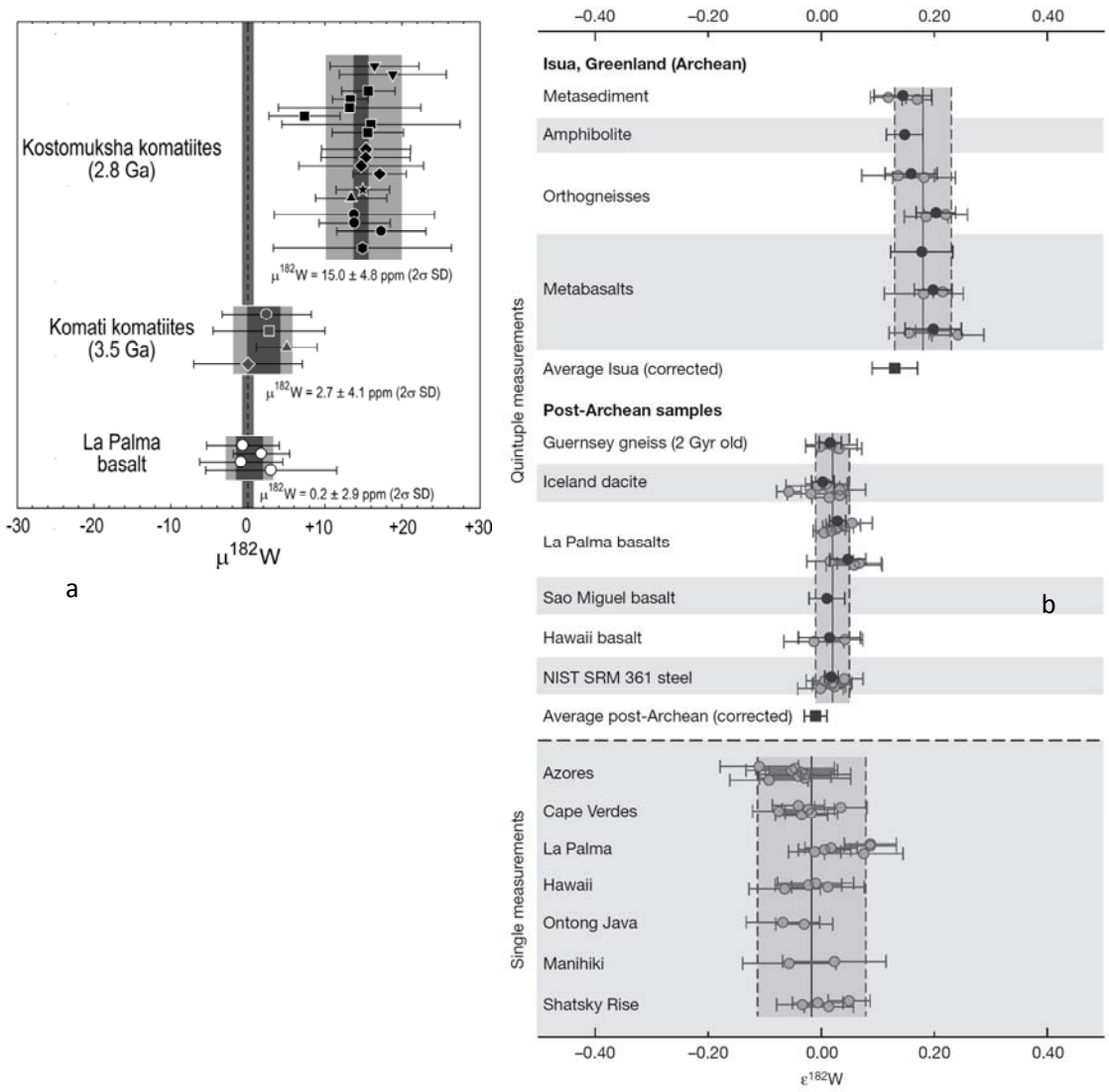

Figure 5.3 The W isotopic composition of terrestrial rocks. Figures a and b are from (Touboul et al., 2012) and (Willbold et al., 2011) respectively. Data are expressed as deviations in ppm (μ^{182}W) and in 10^{-4} (ε^{182}W) from the terrestrial standard. Error bars are 2 standard errors of individual measurements. The ε^{182}W values of young terrestrial samples agree within ~5 ppm while small ε^{182}W heterogeneities of ~15 ppm have been reported in rocks of 2.8 and 3.8 Ga old.

5.2 Model Setup

Here, we start with a simplified initial mantle structure, which is a two-layer mantle. The upper mantle (reservoir 2) and the lower mantle (reservoir 3) have different W isotopic compositions, corresponding to the situation right after the "deep magma ocean" core formation processes (Chapter 4). The simplified model can be extended to multiple-layer mantle cases following the same principles if necessary.

5.2.1 Mantle Convection Function

The evolution of an initially layered mantle structure into a heterogeneous mantle by mantle convection is modeled following the principles of (Kellogg et al., 2002). The upper and lower mantles have an initial thickness of l_{20} and l_{30} respectively. They gradually deformed due to the whole mantle convection as shown schematically in Figure 5.4a. With time, the two mantle reservoirs will become stretched, thinned, and folded, ultimately leading to a well-mixed structure. At each stage in Figure 5.4a, the long axes of the two mantles, in general, will be significantly longer than any sampling length scale of interest and therefore can be ignored. Only the short axes (l_{2t} and l_{3t}) are critical to the sampling problem.

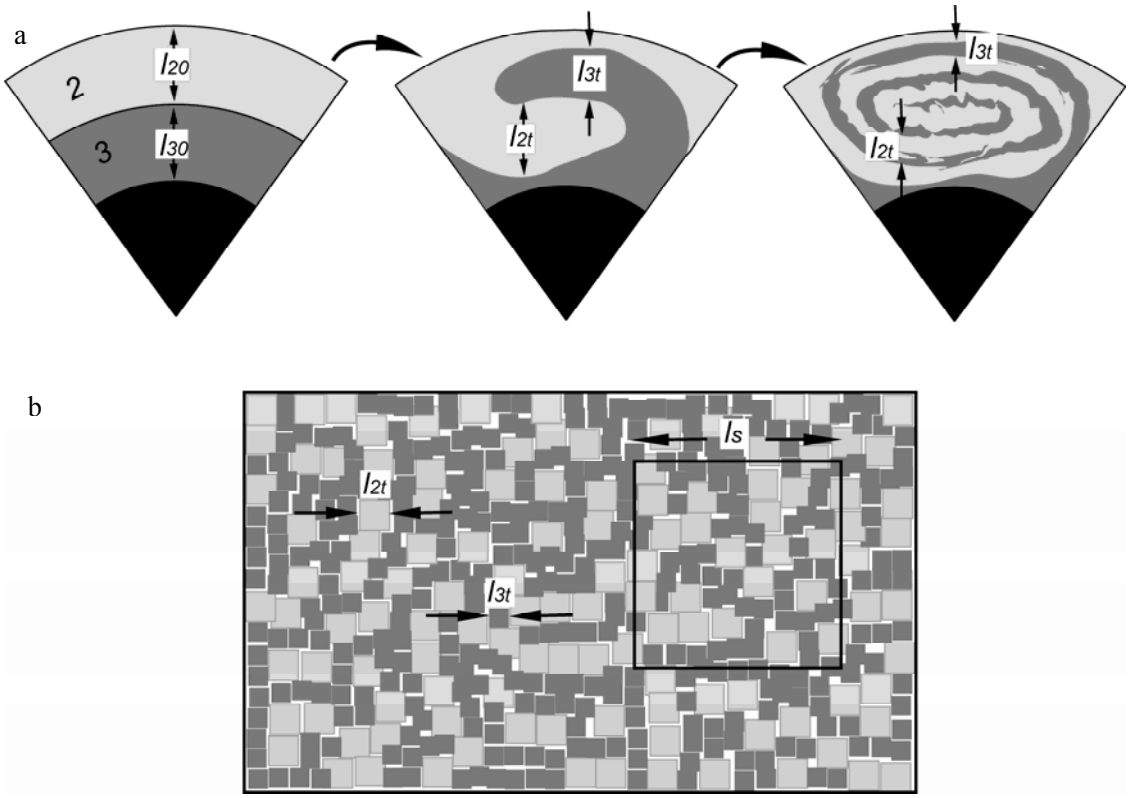

Figure 5.4 The two-dimensional version of the (a) mixing and (b) sampling models. (a) Time evolution of a two-layer mantle as it is stirring and mixing. The long axes of the deformed mantle layers are, in most cases, longer than any sampling length scale of interest and may be neglected. The lengths of the short axes (l_{2t} and l_{3t}) decrease over time. (b) Illustration of sampling in a mantle reservoir containing two isotopically distinct sub-reservoirs. We break each sub-reservoir into a number of cubes with the length of its short axis. We assume cubes to be scattered randomly throughout the mantle reservoir. We then randomly place a sampling box of volume l_s^3 in the reservoir and calculate how many cubes of each sub-reservoir are sampled and what the resulted isotopic composition of the sampling box is.

As pointed out by (Kellogg et al., 2002), this kind of three dimensions mantle convection will include toroidal motion, which can enhance mixing and place mixing in the turbulent regime even for steady state flows. Therefore, following (Kellogg et al., 2002), the short length of each mantle sub-reservoir is exponentially decreasing over time and described as:

$$l_t = l_0 e^{-\frac{t}{\tau_{stir}}} \tag{5.1}$$

where τ_{stir} is the characteristic time scale of stirring. This is due to deformation and stretching of the initial reservoir structure in the turbulent regime. Following the equation, both l_{2t} and l_{3t} are decreasing exponentially with the same rate τ_{stir}, and the ratio of l_{2t}/l_{3t} is always constant over time and equal to l_{20}/l_{30}. Since only the shortest dimensions (l_{2t} and l_{3t}) are critical to the sampling problem, we can break each sub-reservoir into a number of cubes with lengths of l_{2t} and l_{3t} in the mantles as shown in Figure 5.4b.

5.2.2 The Sampling Function

For simplification, we simulate a melting event on the Earth's surface as placing a sampling box of volume l_s randomly in the mantle. Then the sampling function would tell the composition of the sample. Since we have no information as to where in the mantle each sub-

reservoirs (cubes) resides, we therefore assume that those cubes are scattered randomly throughout the mantle. Finally, we randomly place the sampling volume within the mantle and determine the contribution of each cube as illustrated in Figure 5.4. In practice, we realized the sampling function via the following the principles of geometrical statistics.

First, we randomly choose one cube from the mantle reservoir, and then each cube could be either the $l_{2t}{}^3$ cube or the $l_{3t}{}^3$ cube. The probability (p) of each option respectively is the proportion of the total volume of each sub-reservoir over the total volume of the whole mantle reservoir:

$$\begin{cases} p_2 = \dfrac{V_2}{V_{tot}} \\ p_3 = 1 - p_2 = \dfrac{V_3}{V_{tot}} \end{cases} \tag{5.2}$$

where V_2, V_3 and V_{tot} are the volumes of the mantle reservoirs 2 and 3 and the whole mantle, respectively. They can be calculated from geometry as follows:

$$\begin{cases} V_2 = \dfrac{4}{3}\pi\left[\left(l_{20} + l_{30} + r_c\right)^3 - \left(l_{30} + r_c\right)^3\right] \\ V_3 = \dfrac{4}{3}\pi\left[\left(l_{30} + r_c\right)^3 - \left(r_c\right)^3\right] \\ V_{tot} = V_2 + V_3 \end{cases} \tag{5.3}$$

where r_c is the radius of the planet's core.

After we determine the cube sampled by the sampling box, we need to determine how much portion of the cube will be sampled. There are two different situations:

(1) when $l_s > l_{it}$ (i = 2 or 3): Given the cube is sampled, there are two cases that either the cube could be wholly sampled (lie completely within the sampling volume) or partially sampled (partially overlap with the sampling volume). The probability of each case can be derived as follows:

(Kellogg et al., 2002) gave the probability that each cube could lie completely within (p_{in}), partially overlap with (p_{edge}), or be completely outside (p_{out}) the sampling volume is, respectively:

$$\begin{cases} p_{in} = \dfrac{(l_s - l_{it})^3}{V_{tot}} \\ p_{edge} = \dfrac{(l_s + l_{it})^3}{V_{tot}} - p_{in} = \dfrac{(l_s + l_{it})^3 - (l_s - l_{it})^3}{V_{tot}} \\ p_{out} = 1 - p_{in} - p_{edge} = 1 - \dfrac{(l_s + l_{it})^3}{V_{tot}} \end{cases} \tag{5.4}$$

So the probability that each cube will be sampled is

$$p_{sampled} = p_{in} + p_{edge} = \frac{(l_s + l_{it})^3}{V_{tot}} \tag{5.5}$$

By Bayes' theorem, given a cube is sampled, the probability that the cube could be wholly sampled (p_{whole}) or partially sampled ($p_{partial}$) is derived below respectively:

$$\begin{cases} p_{whole/sampled} = \dfrac{p_{in}}{p_{sampled}} = \dfrac{(l_s - l_{it})^3}{(l_s + l_{it})^3} \\ p_{partial/sampled} = \dfrac{p_{edge}}{p_{sampled}} = \dfrac{(l_s + l_{it})^3 - (l_s - l_{it})}{(l_s + l_{it})^3} = \dfrac{2l_{it}^{\,3} + 6l_{it}l_s^{\,2}}{(l_s + l_{it})^3} \end{cases} \tag{5.6}$$

and

$$p_{whole/sampled} + p_{partial/sampled} = 1 \tag{5.7}$$

(2) when $l_s < l_{it}$ (i = 2 or 3): Given the cube is sampled, there are two cases that the sampling volume could be either filled up (the cube totally includes the sampling volume) or partially filled (the cube partially overlaps with the sampling volume) by the cube. By symmetry, the probability of each case respectively is:

$$\begin{cases} p_{fill-up} = \dfrac{(l_{it} - l_s)^3}{(l_s + l_{it})^3} \\ p_{partial} = \dfrac{2l_s^{\,3} + 6l_s l_{it}^{\,2}}{(l_s + l_{it})^3} \end{cases} \tag{5.8}$$

and

$$p_{fill-up} + p_{partial} = 1 \tag{5.9}$$

For both the partially sampled and partially filled cases described above, we need to proceed to quantify the proportion of the cube that is sampled. Since the location of each cube is random, given the cube is partially sampled, it is reasonable to assume that the likelihood that any

specific proportion of the cube will be sampled is identical. Then the proportion of the cube being sampled can be treated as a random variable x following an uniform distribution at the interval (0,1). The probability density function of x is

$$f(x)=\begin{cases}1 & 0<x<1\\ 0 & otherwise\end{cases} \tag{5.10}$$

A random number generator following the probability density function is built up in Matlab and used to determine the proportion of cube that will be sampled each time.

After calculating the volume that a given cube contributes to the sampling volume, $v_{i,\mathrm{samp}}$, we adjust the sampling volume (l_s^3), the volume of the mantle reservoir that the selected cube belongs to (V_i), and total mantle volume (V_{tot}) as

$$\begin{cases} l_s'^3 = l_s^3 - v_{i,samp} \\ V_i' = V_i - v_{i,samp} \\ V_{tot}' = V_{tot} - v_{i,samp} \end{cases} \tag{5.11}$$

where the primed variables represent the new values. As pointed out by (Kellogg et al., 2002), this adjustment takes care of the fact that the sampling of different cubes are not truly independent events.

The sampling procedure above is repeated until the sampling volume (l_s^3) is completely full. Then we move to calculating the W isotopic composition of the sample (Section 5.2.3). By running the sampling algorithm arbitrary times (usually 1000 times), we would generate a set

of synthetic W isotopic data to predict the data distribution one would expect from measuring basalt samples.

5.2.3 Calculation of Synthetic W Isotopic Data

The initial thickness of the two mantle reservoirs are calculated from the depth of the magma ocean in martian mantle during core formation as follows.

The observed abundances of siderophile elements in martian mantle suggested that the bottom pressure of the deep magma ocean during core formation is about 14 GPa (Righter and Chabot, 2011). From equation 4.43 in Chapter 4, we then can calculate the depth of the magma ocean (r_{m})

$$r_m = R\sqrt{1-\frac{P_m}{P_{CMB}}\left[1-\frac{r_c}{R}\right]^2} \tag{5.12}$$

where R is the radius of Mars, r_{c} is the radius of Mars' core, P_m is the bottom pressure of the magma ocean and P_{CMB} is the pressure at the core mantle boundary of the Mars.

After determining the initial thickness of the two mantle reservoirs, we can run the convection model and the sampling function. Let the volume proportions of the two mantle reservoirs in a sample obtained from the sampling function be x_2 and 1-x_2. Assuming the two mantle reservoirs have similar density, the mass fraction of the mantle reservoirs

in a sample are also x_2 and 1-x_2. So the W isotopic composition of the sample is

$$\varepsilon_{W(CHUR),sample} = \varepsilon_{W(CHUR),2} x_2 \frac{C_{W,2}}{C_{W,sample}} + \varepsilon_{W(CHUR),3}(1-x_2)\frac{C_{W,3}}{C_{W,sample}} \quad (5.13)$$

where $C_{W,2}$ and $C_{W,3}$ are W abundances of the two mantle reservoirs respectively. $\varepsilon_{W(CHUR),2}$ and $\varepsilon_{W(CHUR),3}$ are W isotopic compositions of the two mantle reservoir respectively. $C_{W,sample}$ is the W abundance of the sample and can be calculated by the following equation:

$$C_{W,sample} = C_{W,2} x_2 + C_{W,3}(1-x_2) \quad (5.14)$$

The primary constraint for Mars is the fact that there are two groups of martian meteorites with different W isotopic compositions: shergottites have a $\varepsilon_{W(CHUR)}$ of 2.23 ±0.21 and nakhlites + chassignites have a $\varepsilon_{W(CHUR)}$ of 5.15 ±0.50 (Foley et al., 2005). The isotope heterogeneity may represent the distinct early martian upper and lower mantles, consistent with their formation during the deep magma ocean core formation process as discussed in Chapter 4. Therefore, we employ W isotopic composition of shergottites and nakhlites + chassignites as the W isotopic composition of the upper and lower mantle reservoirs respectively in the model. All input parameters are listed in the following Table 5.1.

Table 5.1 Input parameters for Mars and Earth

	Mars	Earth
Radius (km)	3400	6371
Core's radius (km)	1800	3481
Core-mantle Boundary Pressure (GPa)	24[a]	136[a]
Bottom pressure of the magma ocean during core formation (GPa)	14[b]	44[b]
Thickness of the upper mantle reservoir (km)	790	769
Thickness of the lower mantle reservoir (km)	810	2120
W abundance in the upper mantle reservoir (ppm)	0.044[c]	0.055[e]
W abundance in the lower mantle reservoir (ppm)	0.018[c]	0.01[e]
$\varepsilon_{W(CHUR)}$ of the upper mantle reservoir	2.23[d]	1[e]
$\varepsilon_{W(CHUR)}$ of the lower mantle reservoir	5.15[d]	5[e]

(a) core-mantle boundary pressures of Mars and Earth are from (Righter, 2003). (b) bottom pressures of the magma ocean during core formation for Mars and Earth are from (Righter and Chabot, 2011) and (Wood et al., 2008) respectively. (c) W abundances in the upper and lower mantle reservoirs are from Chapter 4. (d) W isotopic compositions of the two mantle reservoirs are set to the average value of shergottites and nakhlites + chassignites (Foley et al., 2005), respectively. (e) W concentrations and isotopic compositions of the mantle reservoirs in Earth are assumed.

5.4 Results and Discussion

In this simplified case, there are only two isotopically different mantle compositions. Then we can treat the sub-reservoir with the longer short axis length scale as the matrix of the mantle and model the mantle heterogeneity as a random distribution of cubes with the shorter short axis length scale. Then the l_t = min (l_{2t}, l_{3t}) is used to indicate the mantle heterogeneity scale. For Mars, the initial thickness of the upper mantle

reservoir (l_{20}) is always less than that of the lower mantle reservoir (l_{30}) (Table 5.1). So l_{2t} is always less than l_{3t} and $l_t = l_{2t}$ for any t.

5.4.1 Outcomes of the Sampling Function

The distribution of the W isotopic composition of the 1000 randomly synthetic basalt samples is solely determined by the ratio of the sampling length scale of mantle-derived basalts (l_s) and the mantle heterogeneity scale (l_t). In order to let 95% of the synthetic basalt samples have the averaged value of W isotopic compositions of the two mantle reservoirs ($\varepsilon_{W(CHUR)} = 2.75\pm0.05$), the mantle heterogeneity scale has to be at least 10 times smaller than the sampling length scale ($l_t/l_s \leq 0.1$). In this case, the mantle heterogeneity cannot be recognized despite it may indeed exist (Figure 5.5a).

For another extreme condition that 95% of the samples show the W isotopic composition of either one of the two mantle reservoirs, which reflects the original mantle heterogeneity (Figure 5.5b), the mantle heterogeneity scale has to be at least 2 times larger than the sampling length scale ($l_t/l_s \geq 2$). Other cases between those two conditions show a mixed pattern of W isotopic compositions, where the W isotopic compositions of the 1000 synthetic samples distribute over a wide range between the W isotopic compositions of the two mantle reservoirs. For example, Figure 5.5c shows the case of $l_t/l_s = 0.5$.

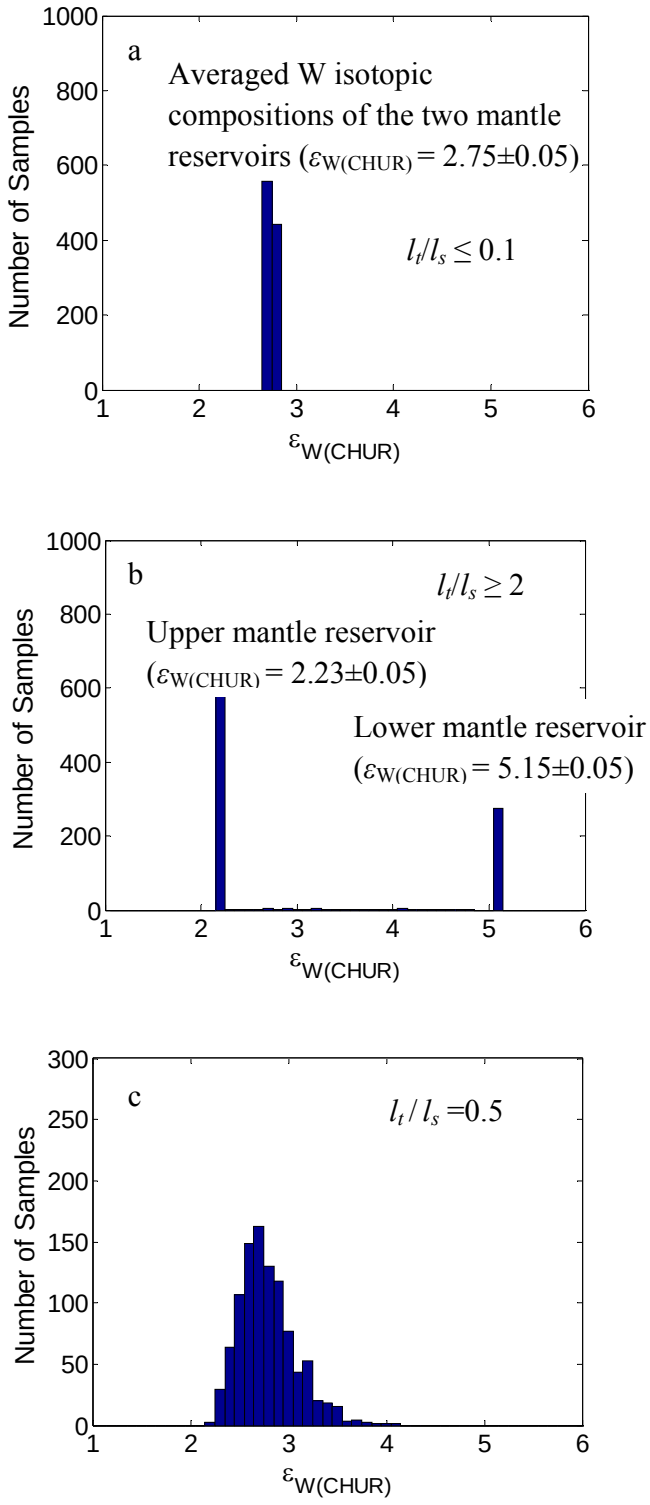

Figure 5.5 Histograms of synthetic W isotope data (binned at 0.1 ϵ unit, for various ratios of l_s/l_t).

5.4.2 Mantle Convection Rate of Mars

The mantle heterogeneity scale of Mars is decreasing exponentially over time from l_0=790 km due to the mantle convection (stirring) (Figure 5.6a). Given the sampling length scale of martian basalt is 30 km or 100 km, the l_t/l_s ratio of martian mantle is also decreasing exponentially over time from ~26.3 and ~7.9 respectively (Figure 5.6b and c). Figures 5.7-5.11 show the corresponding variation of the evolution of W isotope heterogeneity in the martian mantle over time.

In order to constrain the mantle stirring rate of Mars, we rearrange the equation (5.1) as:

$$\begin{aligned} & l_t = l_0 e^{-\frac{t}{\tau_{stir}}} \\ & \Rightarrow \ln\left(\frac{l_t}{l_0}\right) = -\frac{t}{\tau_{stir}} \\ & \Rightarrow \tau_{stir} = \frac{-t}{\ln\left(\frac{l_t}{l_0}\right)} = \frac{-t}{\ln\left(\frac{kl_s}{l_0}\right)} \end{aligned} \qquad (5.15)$$

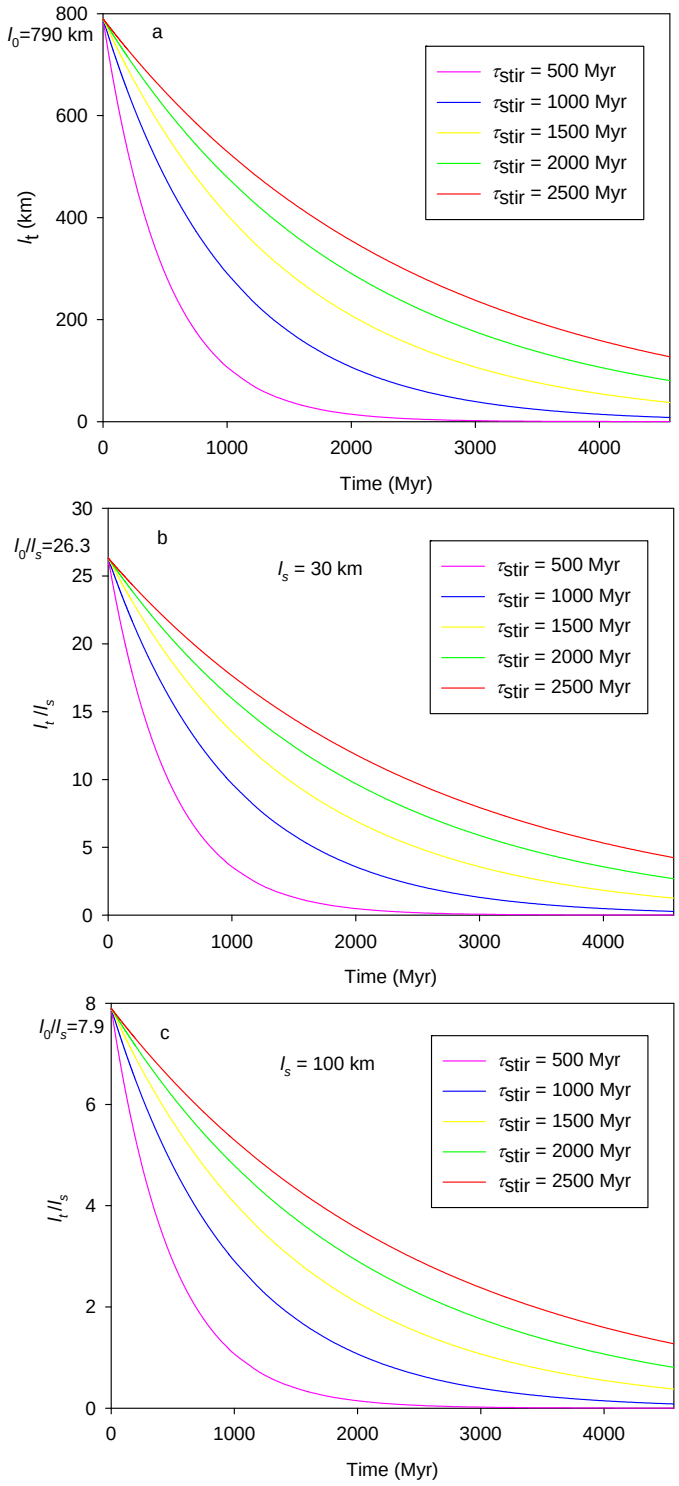

Figure 5.6 Evolution of the mantle heterogeneity scale l_t (a) and l_t/l_s ratio (b, c) of Mars over time due to the mantle stirring as a function of the mantle stirring rate. The results are calculated from equation (5.1). (b) l_s = 30 km and (c) l_s =100 km.

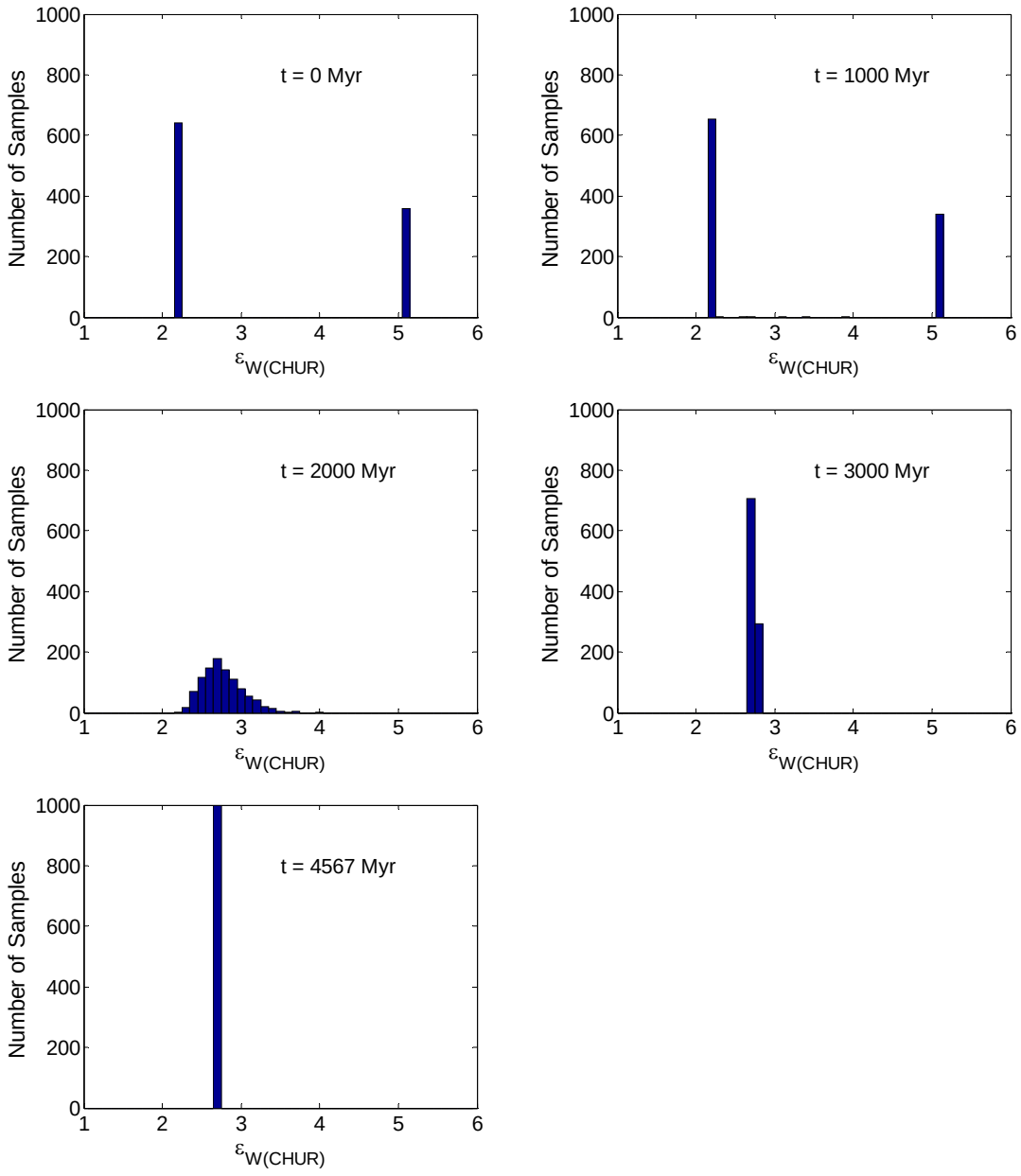

Figure 5.7 Evolution of distribution of 1000 synthetic W isotope composition of mantle derived basalts. The mantle stirring rate is τ_{stir} =500 Myr and the basaltic sampling length scale is l_s = 30 km.

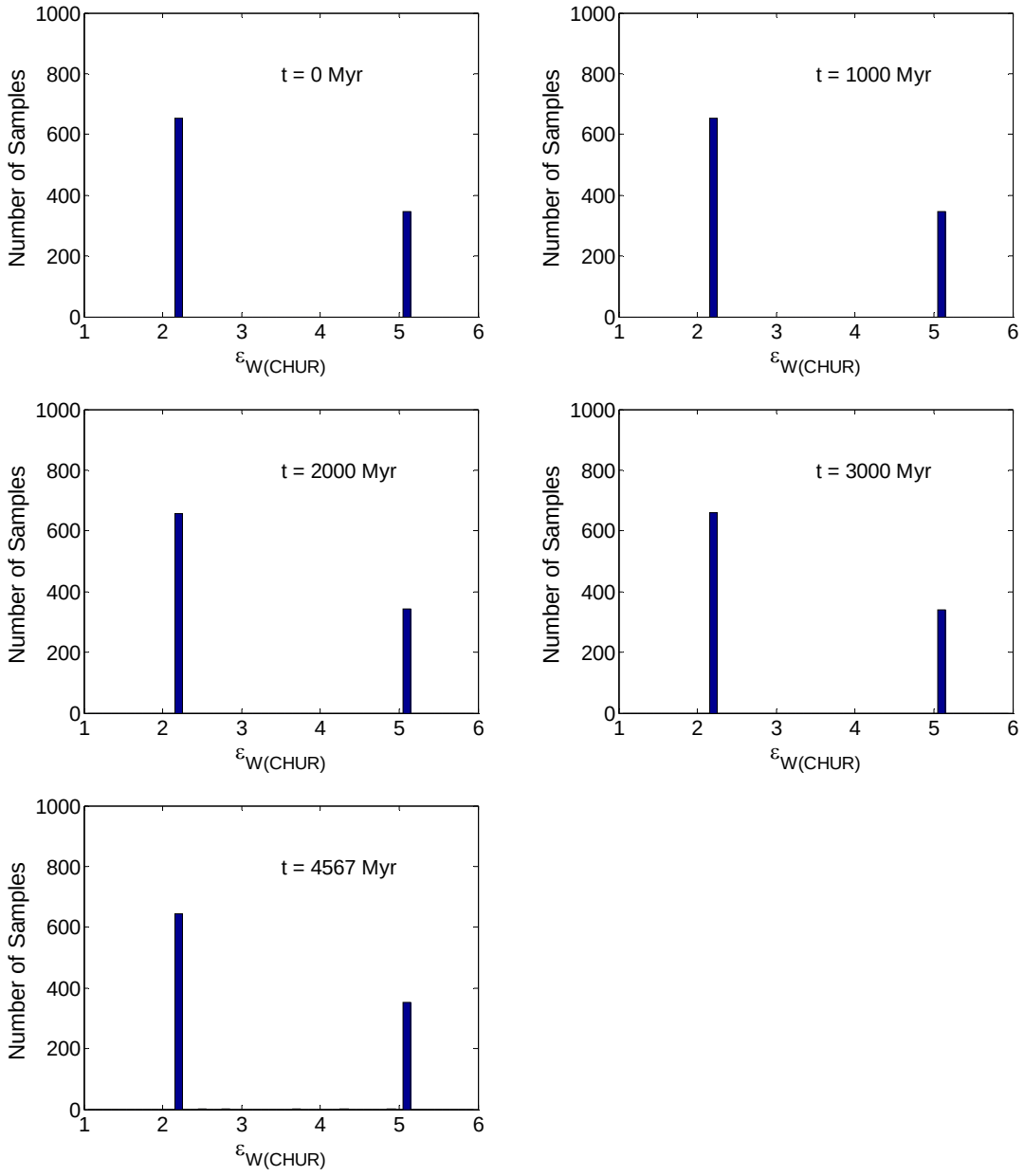

Figure 5.8 Evolution of distribution of 1000 synthetic W isotope composition of mantle derived basalts. The mantle stirring rate is τ_{stir} =2500 Myr and the basaltic sampling length scale is l_s = 30 km.

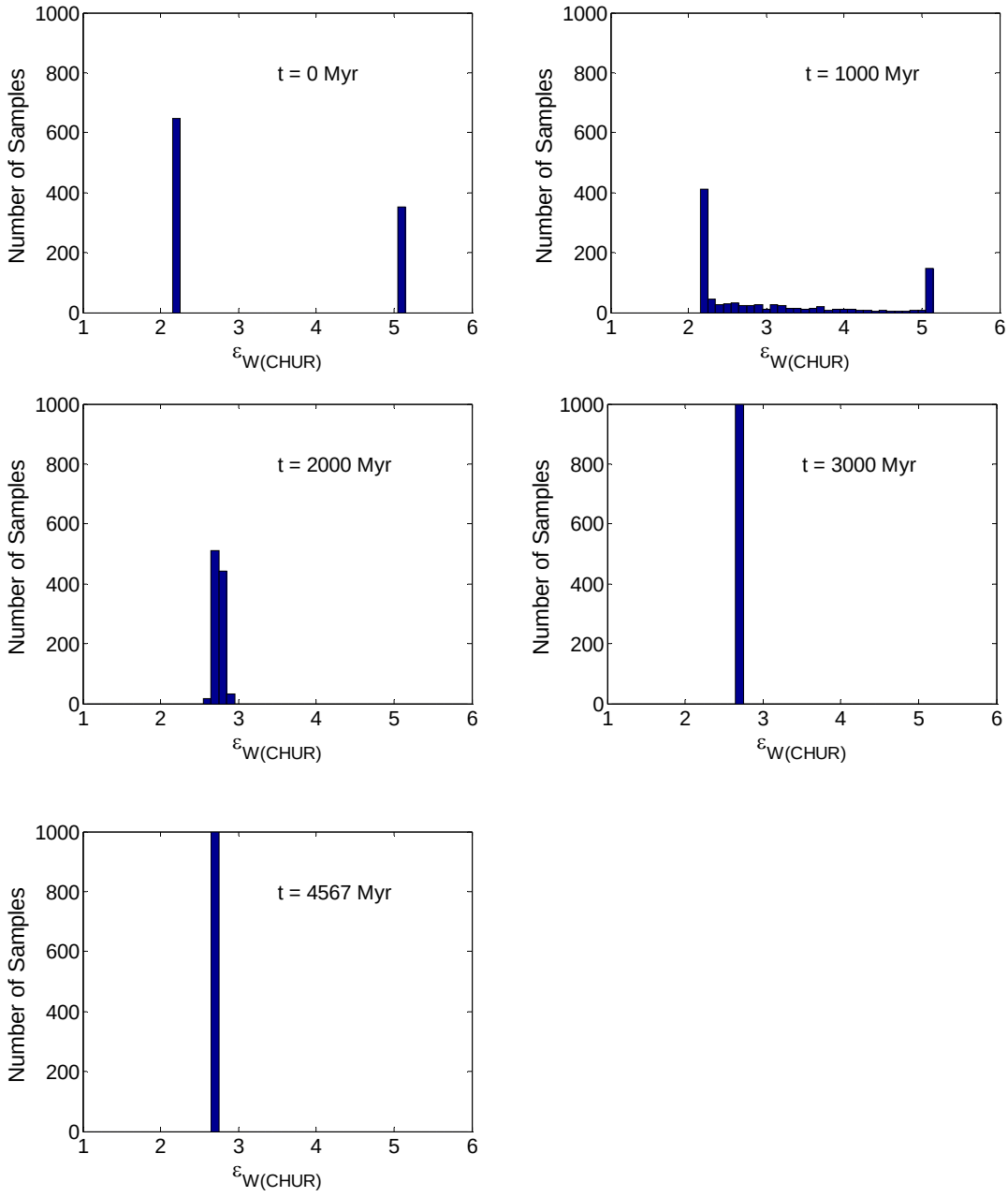

Figure 5.9 Evolution of distribution of 1000 synthetic W isotope composition of mantle derived basalts. The mantle stirring rate is τ_{stir} =500 Myr and the basaltic sampling length scale is l_s = 100 km.

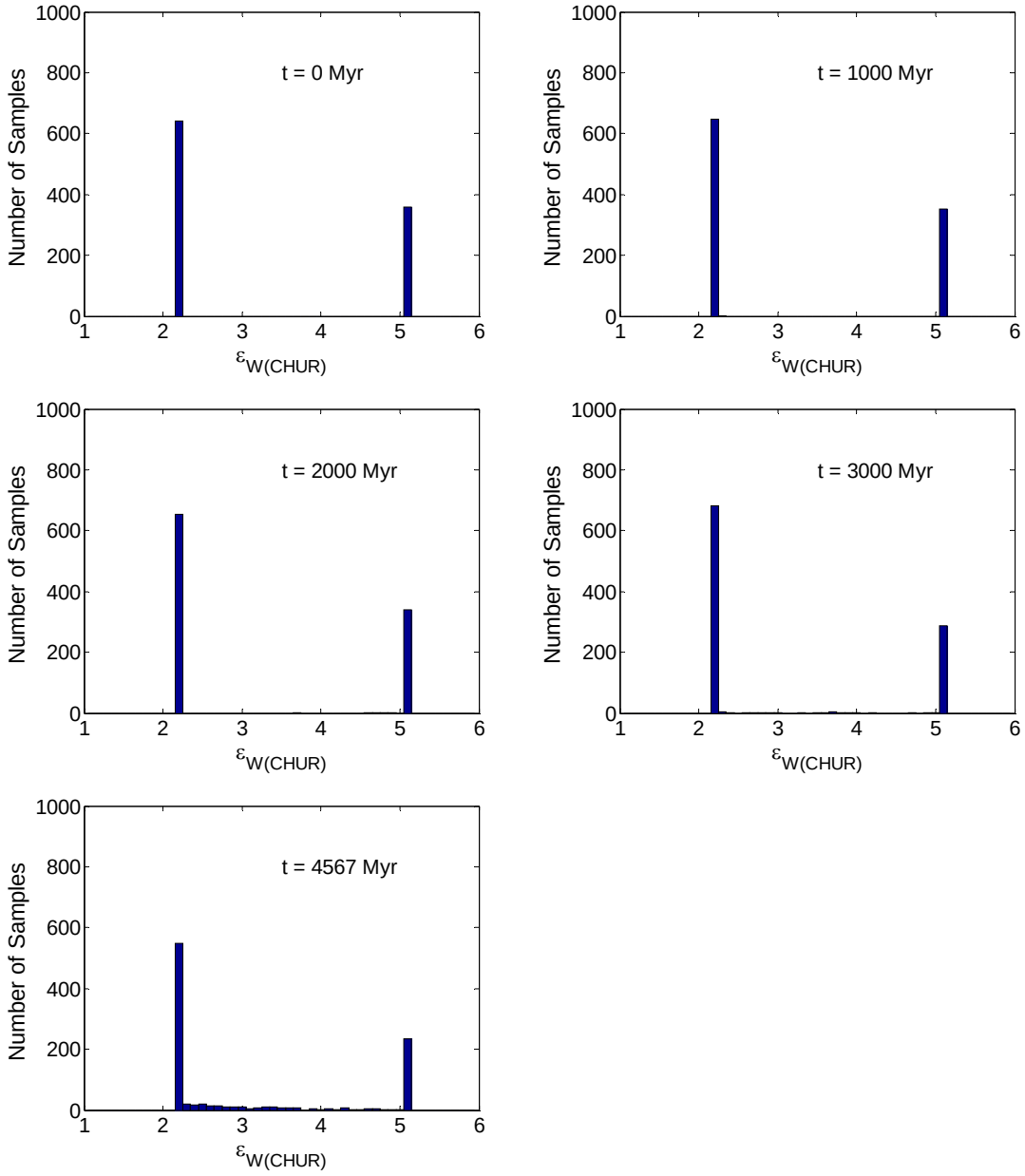

Figure 5.10 Evolution of distribution of 1000 synthetic W isotope composition of mantle derived basalts. The mantle stirring rate is τ_{stir} =2500 Myr and the basaltic sampling length scale is l_s = 100 km.

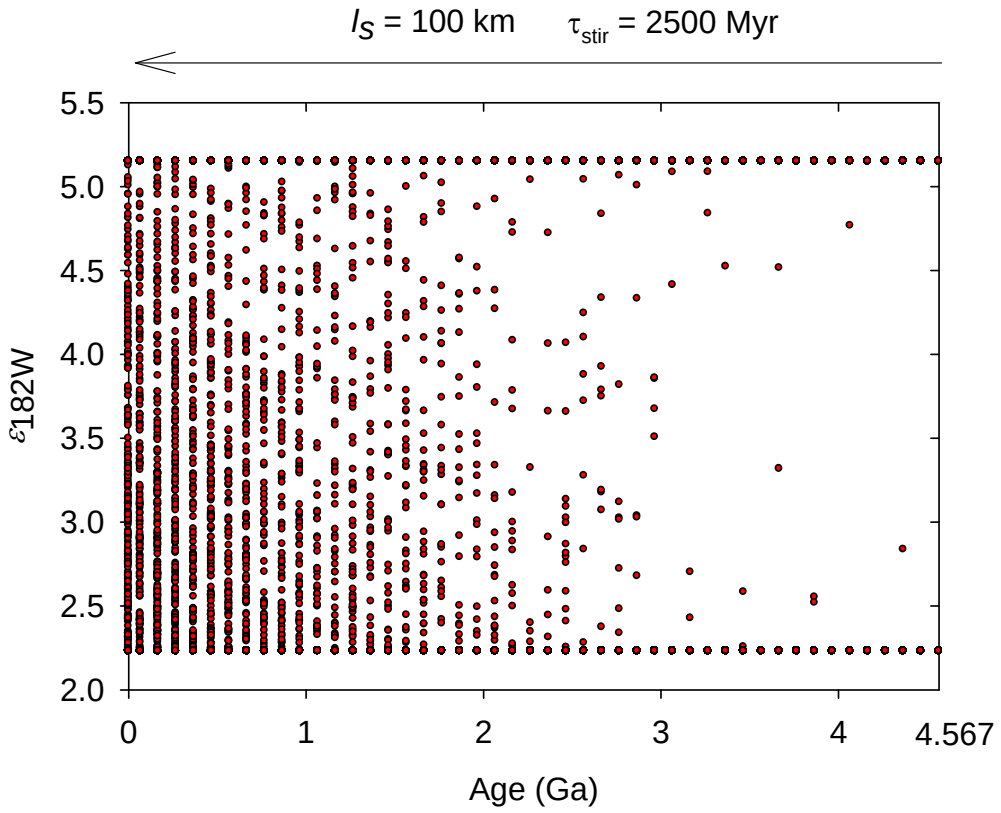

Figure 5.11 Evolution of W isotope heterogeneity in martian mantle represented by the distribution of the synthetic W isotope composition of 1000 mantle derived basalts per 100 Myr. The mantle stirring rate is τ_{stir} =2500 Myr and the basaltic sampling length scale is l_s = 100 km.

Because today (when t = 4567 Myr) we can still see the two groups of W isotopic composition from martian rocks, k has to be more than 2. Given l_0 = 790 km and l_s = 30 or 100 km, we can constrain the mantle stirring rate (τ_{stir}) for Mars to be $\geq$ 1772 Myr or 3325 Myr, which corresponds to an at least 60 or 200 km W isotopic mantle heterogeneity in Mars. The result is consistent with what was constrained by the long-lived isotopic systems (^{87}Rb-^{87}Sr and ^{147}Sm-^{143}Nd) for Mars, which

suggested a relatively consistent τ_{stir} value in the range of 2000 to 2500 Myr (James B. Kellogg's unpublished results).

5.4.3 Application to the Earth

As a neighboring planet, Earth might have experienced similar accretion and core formaiton processes with Mars. Based on the "deep magma ocean" core formation model (Wade and Wood, 2005; Wood et al., 2008), the initial mantle W isotope heterogeneity scale in Earth is comparable with that of the Mars (~769 km, Table 5.1). Since today we observe a homogeneous W isotopic composition for most terrestrial rocks, k has to be less than 0.1 when t = 4567 Myr. Given l_0 = 769 km and l_s = 30 or 100 km, we can constrain the mantle stirring rate (τ_{stir}) for Earth to be ≤823 Myr or 1052 Myr, which corresponds to an at least 3 or 10 km W isotopic mantle heterogeneity in Mars. The result is consistent with the mantle stirring rate constrained from long-lived isotopic systems (Kellogg et al., 2002) , which suggested that the present Earth mantle heterogeneities for the long-lived isotopic systems (^{87}Rb-^{87}Sr and ^{147}Sm-^{143}Nd) can be modeled with a 500 Myr stirring time and a 30-100 km sampling size. The significant difference between the stirring rates of Earth and Mars could be due to the fact that the smaller size of Mars makes it cool down faster, and then the increasing viscosity of mantle greatly lower the efficiency of stirring.

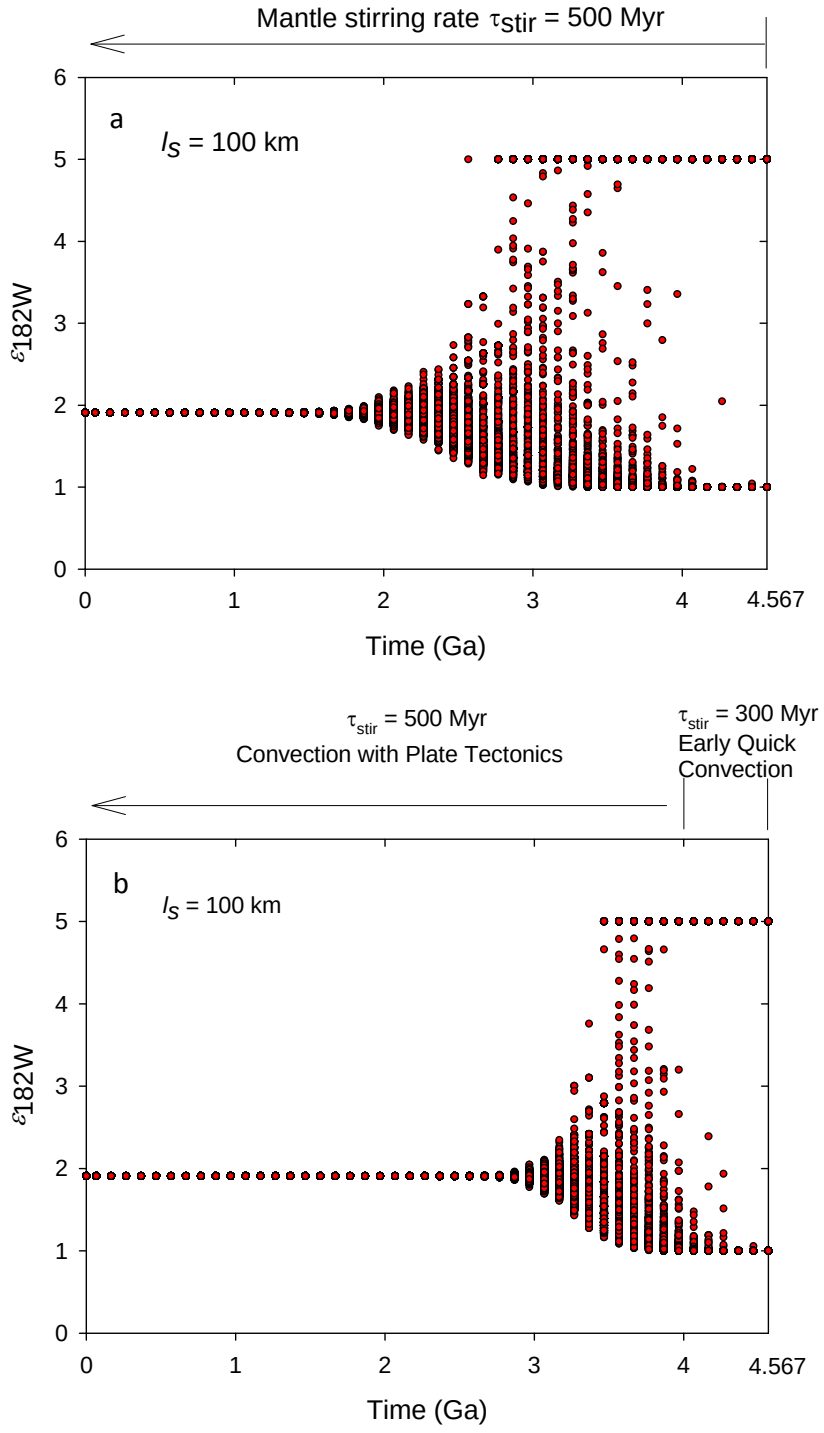

Figure 5.12 Evolution of W isotope heterogeneity in Earth's mantle represented by the distribution of the synthetic W isotope composition of 1000 mantle derived samples per 100 Myr. (a) The mantle stirring rate is τ_{stir} = 500 Myr. (b) The mantle stirring rate in the first 567 Myr is τ_{stir} = 300 Myr and later is τ_{stir} = 500 Myr in order to lead to a homogeneous W isotope signature in the Earth's mantle at ~2.8 Ga. The basalt sampling length scale is l_s = 100 km.

The parameters derived for the Earth also predict that mantle heterogeneity for extinct isotope systems (^{182}Hf-^{182}W and ^{146}Sm-^{142}Nd) at 3.8 Ga is less than 311 km, corresponding to a k less than 10 (Figure 5.9 and 5.12). So it is very likely that the isotopic heterogeneity should be present in the rocks of 3.8 Ga, which is indeed consistent with observations (Willbold et al., 2011; Touboul et al., 2012).

5.5 Conclusions

On the basis of the extinct isotope system (^{182}Hf-^{182}W), we have shown that the mantles of Earth and Mars exhibit substantially different mixing or stirring rates (Given a basalt sampling scale of 30 km, τ_{stir} is ≤823 Myr for Earth and ≥1772 Myr for Mars; Given a basalt sampling scale of 100 km, τ_{stir} is ≤1052 Myr for Earth and ≥3325 Myr for Mars). This is consistent with the expectation that the smaller Mars cooled down faster than the Earth after their formation, which leads to a lower efficient mantle convection afterwards in the martian mantle. Moreover, the mantle stirring rate is also consistent with the mantle stirring rate of ~500 Myr constrained by the long-lived isotope system in Earth (Kellogg et al., 2002).

The result also support that the “deep magma ocean” core formation model in Chapter 4 is a realistic model that can be applied to both Mars and Earth. Modern terrestrial rock does not show the W

isotopic heterogeneity suggested by the "deep magma ocean" model possibly because the very active mantle stirring reduced the W isotopic heterogeneity scale to a relatively small scale (~83 m for a mantle stirring rate of 500 Myr) compared to the common sampling scale of terrestrial basalts (~30 or 100 km).

For Earth, if it turns out that future measurements reveal more evidence for lower mantle, then it may be necessary to replace this whole mantle convection model with one with a lower viscosity and faster mixing upper mantle and a higher viscosity and slower mixing lower mantle.

This quantitative model also provides the possibility to use this new constraint (mantle stirring) to study the thermal evolutions of both planets.

Chapter 6

Core Formation Memories of Siderophile Elements in Earth and Mars

Part of this chapter has been presented at the 2012, 43rd Lunar and Planetary Science Conference.

6.1 Introduction

The siderophile elements depletion in planetary mantles is by definition due to core formation (Goldschmidt, 1923) and has long been used to constrain the conditions of formation of planetary cores (Ringwood, 1961; Drake et al., 1989; Li and Agee, 1996; Righter, 2003; Wade and Wood, 2005; Wood et al., 2008). Li and Agee (1996) demonstrated that metal-silicate partition coefficients of Ni and Co converge at high pressures (~28 GPa) by carrying out a series of experiments from 2 GPa to 20 GPa, leading to the conclusion that the similar depletion of the two elements in Earth's mantle could be caused by Fe metal segregation at 28 GPa to form the core. More recent experimental data for Ni and Co argues for metal-silicate equilibration during core formation at higher

pressures (40-55 GPa, (Wade and Wood, 2005; Kegler et al., 2008; Wood et al., 2008)). Metal-silicate partitioning experiments have also been performed on many other siderophile elements including Mo, W, Cr, Pb, P, Ge, Nb, V, Mn and Si (Wade and Wood, 2005; Corgne et al., 2008; Wood et al., 2008; Righter et al., 2011). The results have been applied to study core formation conditions for Earth, Mars and Vesta (Cottrell et al., 2008; Wood et al., 2008; Cottrell et al., 2009; Righter and Chabot, 2011; Rubie et al., 2011). However, since planetary cores are likely to form through a series of events over a long time period (1-100 million years) (Rubie et al., 2007), an important question that was not addressed in previous studies is what range of the core formation history, do the core formation conditions inferred from individual element apply to? Without this knowledge, it is very difficult to combine results from different siderophile elements to unravel the conditions of whole core formation process.

In order to answer the question, we need to quantify the capability of siderophile elements in recording core formation history.

6.2 Model Description

We employed the reservoir model for core formation as described by Jacobsen (2005) (Figure 6.1). It includes three reservoirs: (1) part of the primitive solar nebula, (2) the silicate mantle and (3) the metallic core. As accretion proceeds, the accreted material from the primitive solar

nebula adds into the planet's mantle and mixes well in a silicate magma ocean before segregating new core material. It is assumed that metal droplets reach equilibrium with the surrounding silicate melt very quickly (Rubie et al., 2003) and the magma ocean maintains homogeneity by rapid convection.

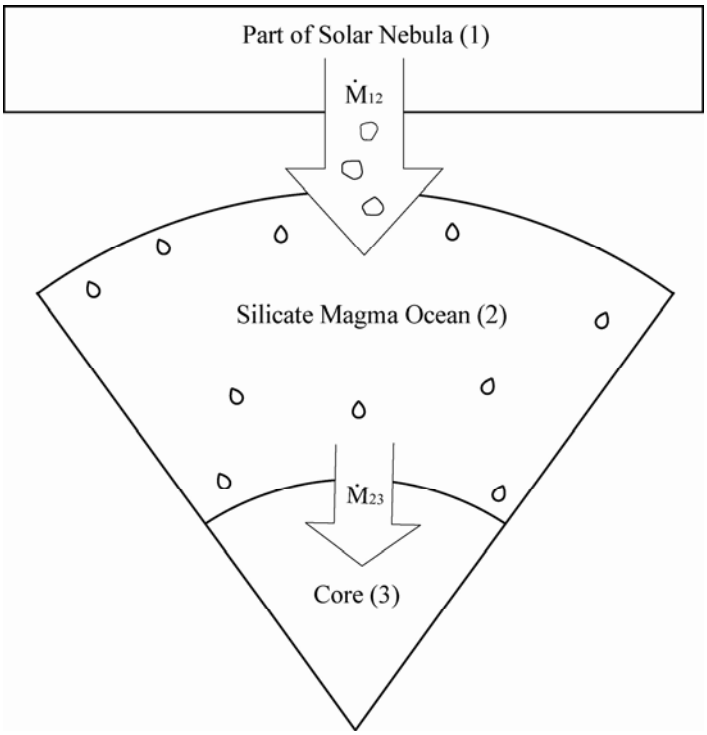

Figure 6.1 Schematic diagram of the reservoir model used to derive the expression of core formation memory. Here, $\dot{M}_{ij}$ refers to the mass fluxes between the reservoirs and are given by the time derivatives of the evolving masses.

From equation (37) in (Jacobsen, 2005), the variation of the mantle concentration of a siderophile element i in a growing planet can be expressed as a result of accretion and core formation and given as

$$dC_{i2} = \underbrace{\frac{C_{i1} - C_{i2}}{M_2} dM_{\oplus}}_{Accretion} + \underbrace{\frac{C_{i2}(1 - d_{i23})}{M_2} dM_3}_{Core\ \ Formation} \tag{6.1}$$

where $M_{\oplus}$, M_2 and M_3 are total mass of the bulk planet, its mantle and core, respectively; C_{i1} and C_{i2} represent concentrations of siderophile element i in the bulk planet and the planet's mantle; d_{i23} is the metal-silicate partition coefficient of siderophile element i. Assuming the core mass fraction (γ) is a constant, we have

$$dC_{i2} = \underbrace{\frac{C_{i1} - C_{i2}}{(1-\gamma)M_{\oplus}} dM_{\oplus}}_{Accretion} + \underbrace{\frac{C_{i2}(1 - d_{i23})\gamma}{(1-\gamma)M_{\oplus}} dM_{\oplus}}_{Core\ \ Formation} \tag{6.2}$$

Then the derivative of the mantle concentration of a siderophile element i with respect to the mass fraction of the growing planet ($M_{\oplus} \in [0, 1]$) can be obtained from equation (6.2) and given as

$$\frac{dC_{i2}}{dM_{\oplus}} = \frac{C_{i1} - (1 - \gamma + \gamma d_{i23})C_{i2}}{(1-\gamma)M_{\oplus}} \tag{6.3}$$

Considering variable metal-silicate partition coefficients (d_{i23}) in the core formation history may be more realistic, but it will incorporate uncertainties from both experimental results of metal-silicate partition coefficients and arbitrarily decision on how pressure and oxygen fugacity

varied in the core formation history. Here, for simplicity, we assume the constant metal-silicate partition coefficients for siderophile elements in the accreting planet. Moreover, let $M_{i,x}$ be a critical point on the accretion and core formation history of the planet. And the siderophile element i loses memory during the early accretion and core formation processes prior to $M_{i,x}$. Thus, we can solve the differential equation (6.3) and obtain the expression for the current mantle concentration of the element i (C_{i2}) as a function of $M_{i,x}$

$$C_{i2} = C_{i2}\left[1-\left(M_{i,x}\right)^{\frac{C_{i1}}{(1-\gamma)C_{i2}}}\right] + C_{i2}\left(M_{i,x}\right)^{\frac{C_{i1}}{(1-\gamma)C_{i2}}} \tag{6.4}$$

The contribution from the accretion and core formation processes prior $M_{i,x}$is described by the second term on the right side of the equation (6.4). As illustrated in Figure 6.2, if the contribution is smaller than the uncertainty (standard deviation) of the observed mantle concentration of element i (ΔC_{i2}), we can surely say that the siderophile element i loses its memory on the accretion and core formation history prior to $M_{i,x}$. So

$$\begin{aligned} & C_{i2}\left(M_{i,x}\right)^{\frac{C_{i1}}{(1-\gamma)C_{i2}}} \le \Delta C_{i2} \\ & \Rightarrow M_{i,x} \le \left(\frac{\Delta C_{i2}}{C_{i2}}\right)^{\frac{(1-\gamma)C_{i2}}{C_{i1}}} \end{aligned} \tag{6.5}$$

Define the depletion factor of siderophile element i in planet's mantle as $DF_i = \frac{C_{i1}/(1-\gamma) - C_{i2}}{C_{i1}/(1-\gamma)} = 1 - \frac{(1-\gamma)C_{i2}}{C_{i1}}$ and the relative standard deviation of C_{i2} as $SD_i = \frac{\Delta C_{i2}}{C_{i2}}$. This result implies:

$$M_{i,x} \le (SD_i)^{1-DF_i} \tag{6.6}$$

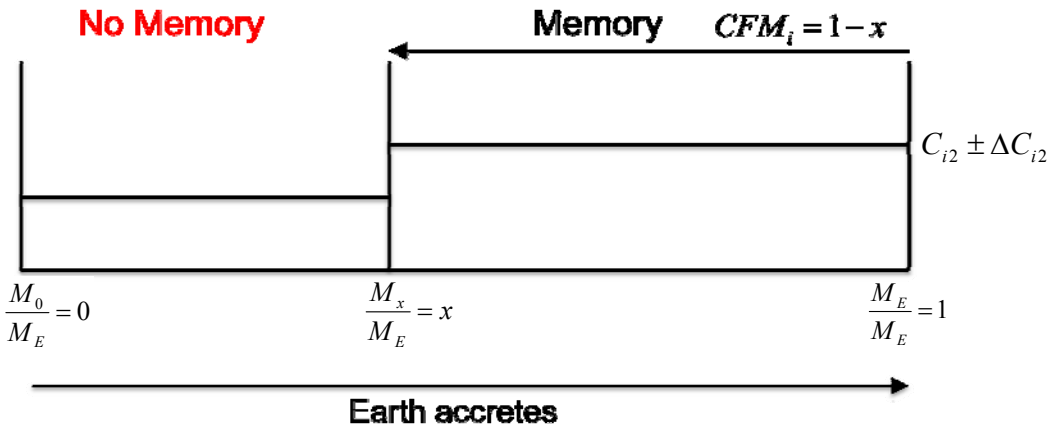

Figure 6.2 The resulting variation of the mantle concentration of siderophile element i (C_{i2}) over accretion. The contribution from the accretion and core formation before M_x/M_E = x (no memory stage) is within the bounds of observed C_{i2} (± ΔC_{i2}).

Since the siderophile element i loses its memory on accretion and core formation history prior to $M_{i,x}$, the mass fraction of planet corresponding to the accretion and core formation history memorized by element i is the core formation memory (*CFM*) of the siderophile element i , which can be written as

$$CFM_i = 1 - \max\left(M_{i,x}\right) = 1 - \left(SD_i\right)^{1-DF_i} \tag{6.7}$$

where the CFM_i technically is the mass fraction of a planet corresponding to the accretion and core formation history memorized by the element i. Thus, the core formation memory of a siderophile element is determined by both how well we know its mantle concentration and its siderophility (DF_i) and the two variables both negatively correlate with *CFM* (Figure 6.4).

It makes intuitive sense that uncertainty of the current mantle concentration of a siderophile element plays an important role in determining the *CFM* of the element. It is also clear that siderophile elements with different siderophilities would have different capabilities on recording core formation history. For instance, the most highly siderophile elements (HSEs)- Ru, Rh, Pd, Re, Os, Ir, Pt and Au have metal-silicate partition coefficients greater than 10^4 at 1 bar, which means, for these species, on the order of only 1 atom remains in the mantle for every 10^4 atoms that enter the core during core formation. Therefore, those elements have extremely low concentrations and short resident time in the mantle and can easily be totally modified by the later accretion and core formation processes. Thus, it is obvious that the present mantle concentrations of HSEs are not able to provide much information about conditions in the early core formation history and we would say that they have very short core formation memories. Correspondingly, moderately

and slightly siderophile elements would have different and longer core formation memories.

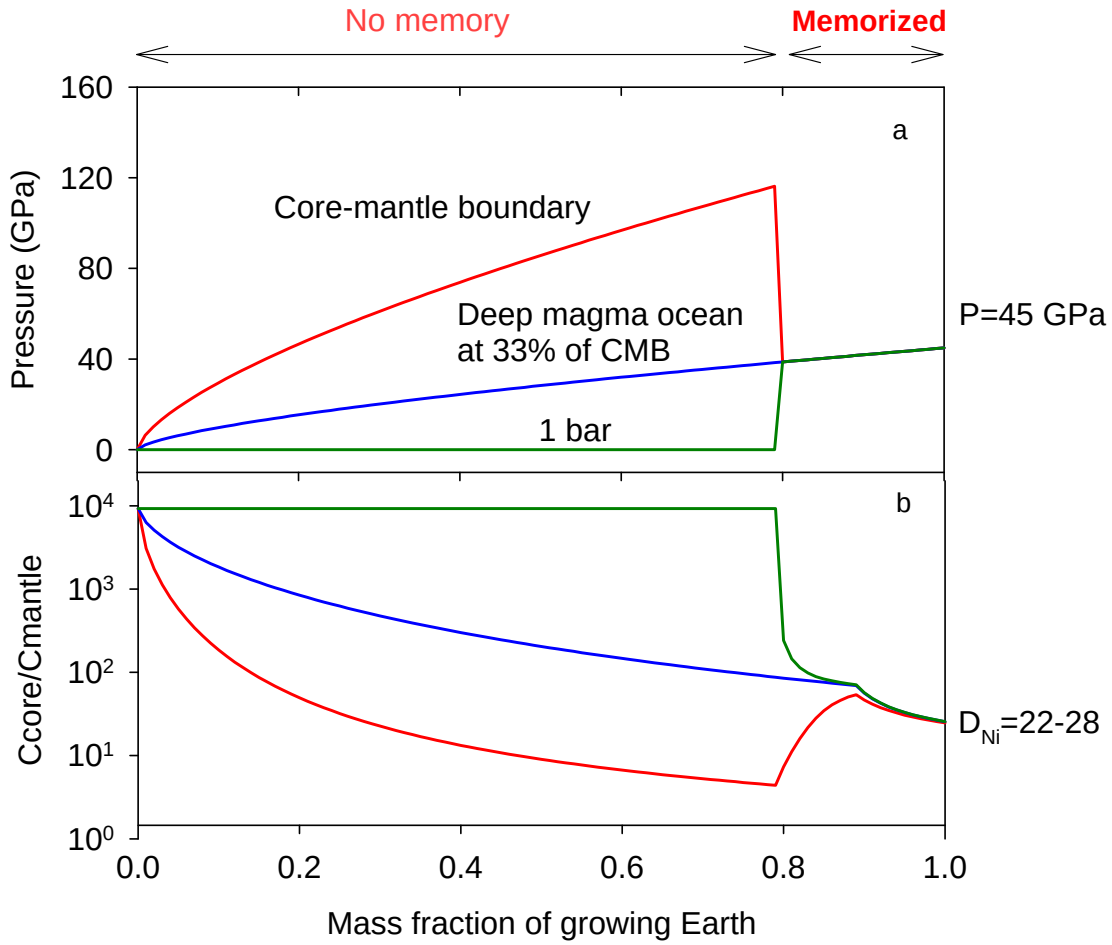

Figure 6.3 (a) Three core formation models with very different metal-silicate equilibrated pressures during the first 80% of Earth's accretion and the same metal-silicate equilibrated pressure during the last 20% of Earth's accretion. (b) Variation of the ratio of Ni concentrations in Earth's core and mantles corresponding to the three cases in (a). All three core formation models can produce a ratio match the observed ratio (D_{Ni} = 22-28). So Ni cannot record the first 80% of accretion and core formation.

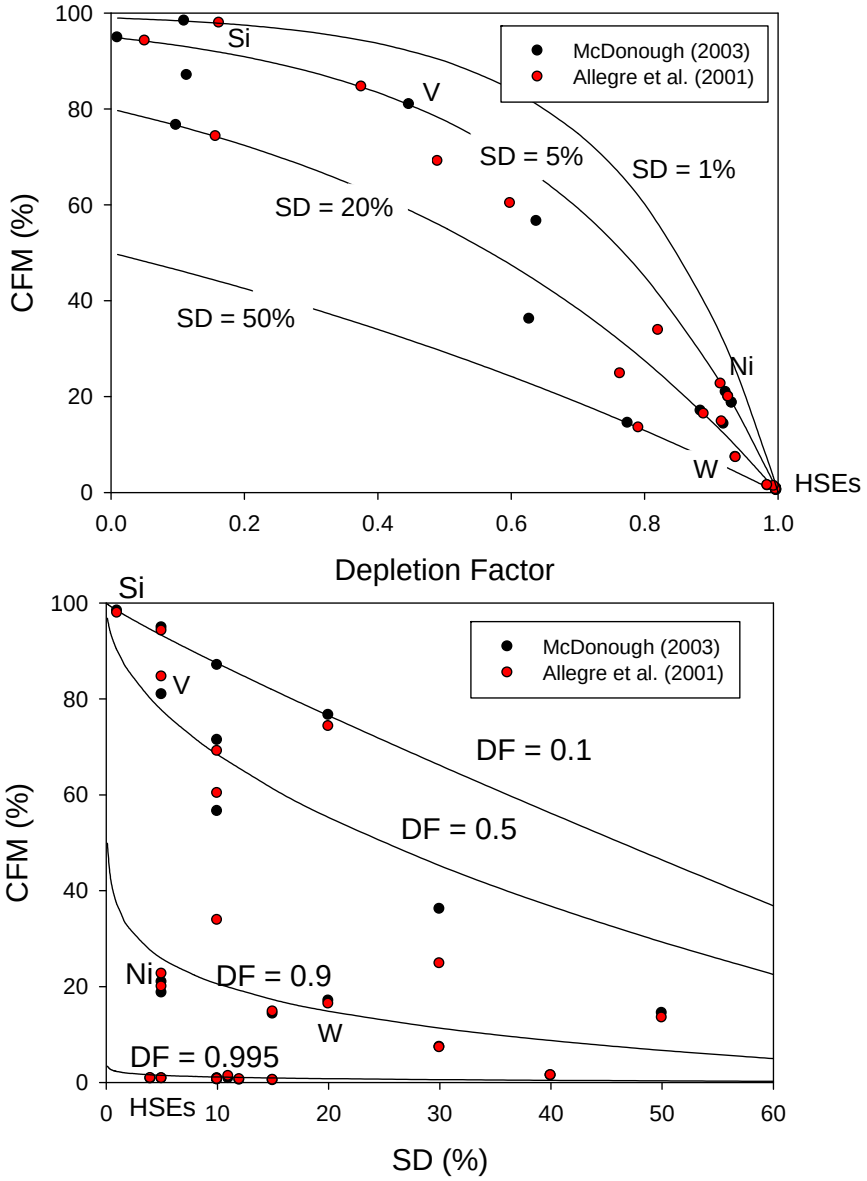

Figure 6.4 Core formation memory (*CFM*) of a siderophile element in a planetary mantle as a function of (a) the depletion factor (*DF*) of the element in the planetary mantle and (b) the relative standard deviation (*SD*) of current mantle concentration of the element. The expression is $CFM = 1 - (SD)^{1-DF}$. Ni, W, V and Si in the Earth's mantle have been shown in the figure.

6.3 Results and Discussion

6.3.1 CFMs of Siderophile Element for Earth

Memories of 23 siderophile elements on Earth's core formation history are illustrated in Figure 6.5. Memory results and modeling input parameters can be found in Table 6.1. The core mass fraction of Earth is 0.325. We chose the bulk silicate Earth (BSE) estimates from Palme and O'Neil (2003) since these are given with estimates of their uncertainties. We obtained two sets of memory results using two sets of input parameters for the bulk Earth concentrations (Allègre et al., 2001; McDonough, 2003), respectively. The offsets of the two sets of memories are relatively large only for Sn, Pb, Cr, Mn, Nb and V, which is due to the fact that McDonough (2003) and Allègre et al. (2001) corrected the volatile loss of those elements in different ways and then resulted in significantly different values for their bulk Earth concentrations.

As we expected, the highly siderophile elements (HSEs) - Ru, Rh, Pd, Re, Os, Ir, Pt and Au- have very short memories only covering the last 0.4%-1.3% of Earth's accretion and core formation. Hence those elements are not very useful for constraining the conditions of the whole core formation history due to their extremely short CFMs. Then we defined them as the ultra short-term memory group. Our model also provides a simple way to estimate the mass fraction of the late veneer required to explain the current mantle concentrations of HSEs. The "late

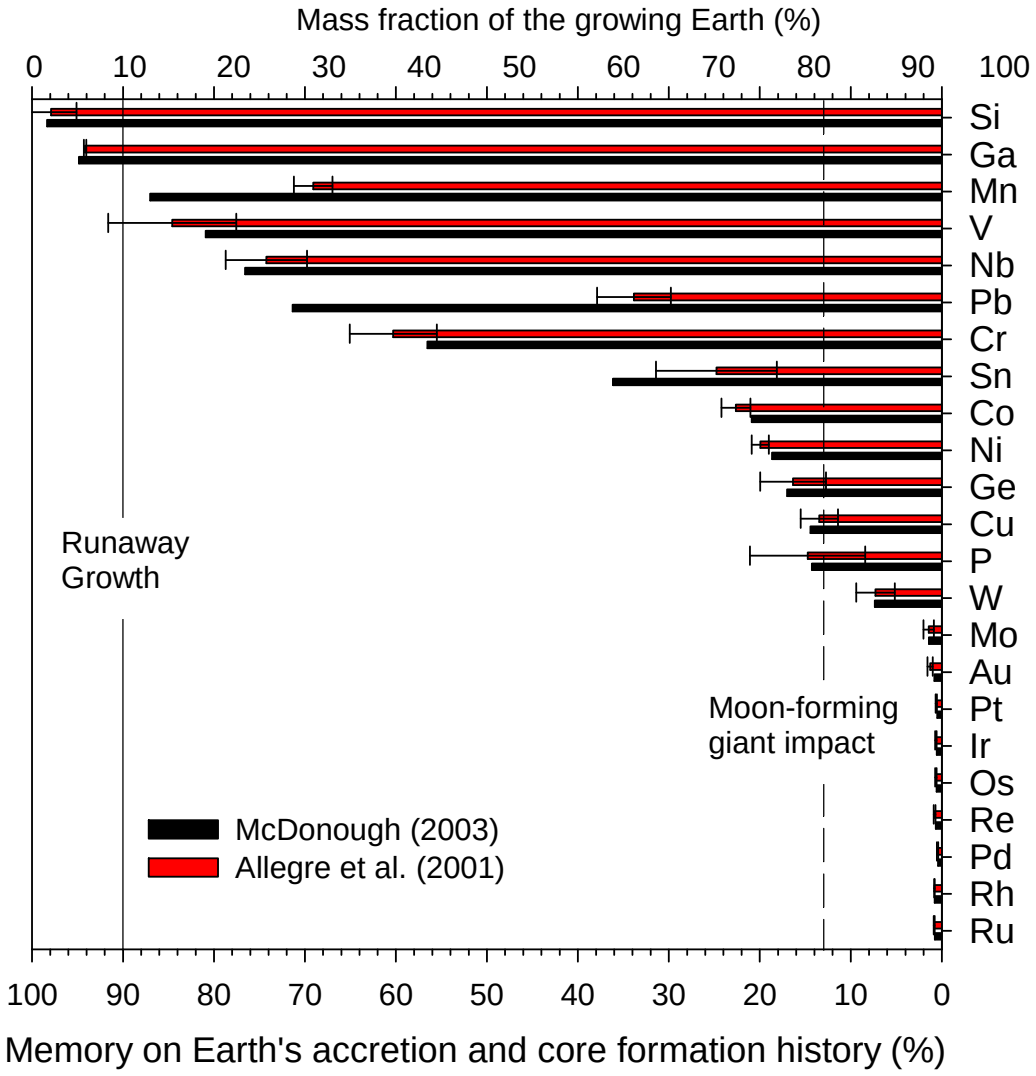

Figure 6.5 Core formation memories of 23 siderophile elements in the Earth's mantle based on mantle concentrations from Palme and O'Neil (2003). The memory technically is the mass fraction of Earth corresponding to Earth's accretion and core formation history that could be recorded by a siderophile element in the Earth's mantle. Error bars of the memories are calculated from uncertainties of estimates of bulk Earth concentrations (Allègre et al., 2001).

Table 6.1 The input parameters and results of core formation memories of 23 siderophile elements in Earth's mantle

Elements	BSE (ppm) [a]	SD(%)[a]	Bulk Earth (ppm)[b]	Depletion Factor[b]	CFM(%)[b]	Bulk Earth (ppm)[c]	±	Depletion Factor	±	CFM(%)	±[d]
Ru	0.00455	4	1.3	0.002	0.8	1.173	0.02	0.0026	0.0001	0.84	0.04
Rh	0.00093	5	0.24	0.003	0.8	0.23	0.01	0.0027	0.0002	0.81	0.05
Pd	0.00327	15	1	0.002	0.4	0.883	0.02	0.0025	0.0004	0.47	0.07
Re	0.00032	10	0.075	0.003	0.7	0.0625	0.003	0.0035	0.0004	0.79	0.09
Os	0.0034	10	0.9	0.003	0.6	0.82	0.03	0.0028	0.0003	0.64	0.07
Ir	0.0032	10	0.9	0.002	0.6	0.766	0.03	0.0028	0.0003	0.65	0.07
Pt	0.0066	12	1.9	0.002	0.5	1.562	0.04	0.0029	0.0003	0.60	0.07
Au	0.00088	11	0.16	0.004	0.8	0.102	0.02	0.006	0.001	1.3	0.3
Mo	0.039	40	1.7	0.015	1.4	1.664	0.04	0.016	0.006	1.4	0.6
W	0.016	30	0.17	0.064	7.4	0.172	0.005	0.06	0.02	7.3	2.1
P	86	15	715	0.081	14.3	690	10	0.08	0.01	14.8	2.1
Cu	20	50	60	0.23	14.4	64.7	5	0.21	0.11	13.5	6.3
Ge	1.2	20	7	0.12	17.0	7.3	1	0.11	0.03	16.4	3.6
Ni	1860	5	18200	0.069	18.7	16900	300	0.074	0.004	20.0	0.9
Co	102	5	880	0.078	20.9	804	50	0.086	0.007	22.6	1.6
Sn	0.138	30	0.25	0.37	36.1	0.394	0.03	0.24	0.07	24.8	6.6
Cr	2520	10	4700	0.36	56.5	4240	200	0.40	0.04	60.3	4.1
Pb	0.185	10	0.23	0.54	71.4	0.696	0.1	0.18	0.03	33.8	4.8
Nb	0.588	20	0.44	0.90	76.6	0.471	0.01	0.84	0.17	74.2	7.0
V	86	5	105	0.55	80.9	93	5	0.62	0.05	84.6	2.1
Mn	1050	10	800	0.89	87.0	1390	100	0.51	0.06	69.1	4.5
Ga	4.4	5	3	0.99	94.8	3.13	0.5	0.95	0.16	94.2	2.8
Si	212200	1	161000	0.89	93.0	171000	2000	0.84	0.01	97.9	0.1

a Bulk Silicate Earth (BSE) estimates and their relative standard deviations (SD) are from Palme and O'Neil (2003).

b Bulk Earth estimates are from McDonough (2003).
c Bulk Earth estimates are from Allègre et al. (2001).
d Error bars of the CFMs from the error propagation of uncertainties of estimation of bulk Earth concentrations from Allègre et al. (2001).

veneer" hypothesis proposes that some late accretions do not involve core formation process. In this case, the second term on right side of equation (6.2) disappears. Thus, by solving the equation, we obtained the result that the current mantle concentrations of HSEs require the late veneer to be less than 0.2-0.6% of the Earth's total mass.

The moderately siderophile elements – notably Mo, W, P, Cu, Ge, Ni, and Co – have memories that span the last ~1%-20% of Earth's accretion and core formation history, defining the short-term memory group. The similar depletion of Ni and Co in the current Earth's mantle has been thought to be the most convincing evidence for core formation in the Earth during metal-silicate equilibrium at high pressures (~28 or 40-55 GPa (Li and Agee, 1996; Kegler et al., 2008; Wood et al., 2008)). Our memory results imply that these high pressure conditions can apply only to the last ~19-23% of Earth's accretion and core formation (Figure 6.3).

The Earth-Moon system has been suggested to form from the last giant impact between the proto-Earth and a Mars-sized impactor (Canup, 2008). The widely accepted mass ratio of the proto-Earth and the impactor is 0.87:0.13 (Canup, 2008). Based on the memory results, the siderophile elements, which could be affected only by core formation during the Moon-forming giant impact are Mo, W, P, Cu and Ge. Other siderophile elements with longer memory (>13%) reflect the combined

effects of core formation during the Moon-forming giant impact as well as the earlier stages.

Four slightly siderophile and volatile elements Sn, Pb, Cr and Mn have memories of the last 20%-70% of Earth's accretion and core formation history and are defined as the intermediate-term memory group. Another four slightly siderophile and refractory elements V, Nb, Ga, and Si have memories that span nearly the whole accretion and core formation history of the Earth, defining the long-term memory group. Based on the depletion of Nb, V, Mn and Si in Earth's mantle, Wood et al.(2008) suggested a reduced condition for the first 20% of the accretion and core formation process of the Earth, which is supported by our memory result.

6.3.2 CFMs of Siderophile Element for Mars

Investigating the chemical signatures of core formation for other terrestrial bodies, such as Mars, could lead to important insights into Earth's core formation. Mars, only 10% of the size of Earth, would have gone through significantly different pressure and temperature regimes during core formation. Following equation (6.7), we calculate the core formation memories of siderophile elements in the martian mantle. The core mass fraction of Mars is set to 0.217 (Wänke and Dreibus, 1988). However, compared with Earth, precise estimates for the siderophile

elements concentrations in the martian mantle and bulk Mars are sparse (Lodders and Fegley, 1997; Righter and Chabot, 2011). We only obtain the memories of 8 elements for Mars (Table 6.2 and Figure 6.6). Similar to the Earth, Mo, Ni, Co and W in martian mantle have short memories of less than the last 20% of accretion and core formation history of Mars while Ga, V Cr and P have longer memories (~30%-90%).\

Table 6.2 The input parameters and results of core formation memories of 8 siderophile elements in the martian mantle

Elements	Mantle (ppm)[a]	SD (%) [a]	Bulk Mars (ppm)[b]	Depletion Factor	CFM (%)
Mo	0.34	76	1.7	0.16	4.11
Ni	400	13	15800	0.02	4.04
W	0.12	67	0.16	0.59	21.19
Co	60	8	795	0.06	13.66
P	450	33	1100	0.32	29.67
Cr	5000	40	3680	1.06	62.27
V	82.5	27	77	0.84	66.38
Ga	9.5	16	6.3	1.18	88.69

a Estimates of the martian mantle concentrations and their relative standard deviations (SD) are from Righter and Chabot (2001)
b Estimates of the bulk Mars concentrations are from Lodders and Fegley (1997)

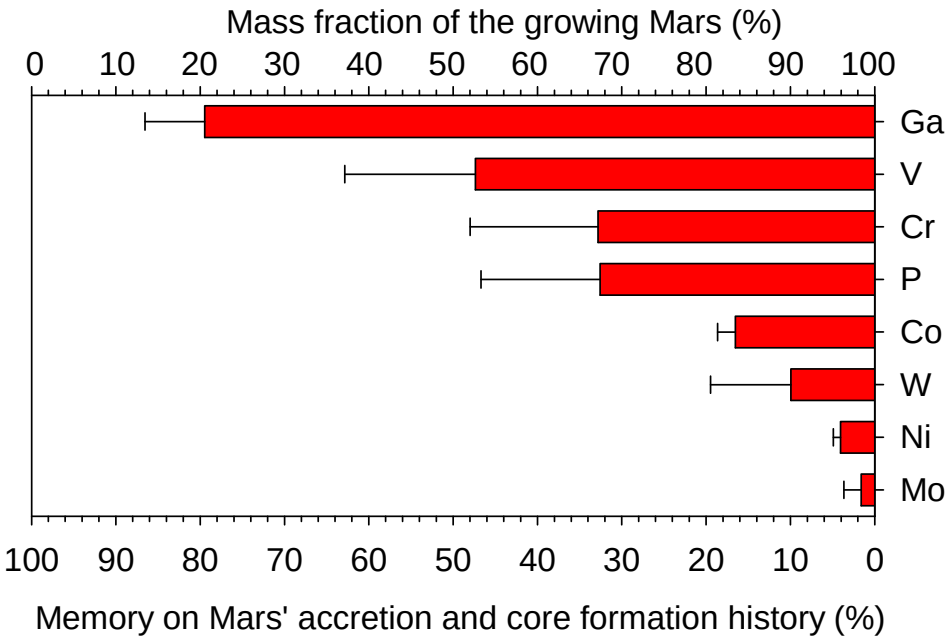

Figure 6.6 Core formation memories of 8 siderophile elements in the martian mantle. The memory technically is the mass fraction of Mars corresponding to Mars' accretion and core formation history that could be recorded by a siderophile element in the martian mantle. Error bars of the memories are calculated from uncertainties of estimates of bulk Mars concentrations.

6.3.3 Three-stage Accretion and Core Formation Model for Earth

Core formation in the Earth is widely thought to have occurred over a long time period and possibly in multiple stages with evolving physical and chemical conditions (Wade and Wood, 2005; Wood et al., 2008; Rubie et al., 2011). Our memory results also provide a substantial insight in how to reconstruct the whole process of core formation. To illustrate that, a simple three-stage core formation model for Earth divided in terms of the three groups of siderophile elements with different

memories (except the ultra short-term memory groups) was investigated (Figure 6.7). Within each stage, we model the conditions of core formation only using the siderophile elements with memory for the particular and later stages. For simplicity, we assume that pressure, temperature and oxygen fugacity within each core formation stage are constant. Temperature is fixed on the liquidus of a peridotitic silicate melt as a function of pressure (T = 28.57P + 1973). Variation of oxygen fugacity is represented by variation of Fe content in Earth's mantle, assuming Fe content in Earth's core and the activity coefficients of Fe in metal and silicate melts are constant (see (Yu and Jacobsen, 2011)). By best matching the observed current mantle contents of those siderophile elements, we can constrain the conditions of core formation processes stage by stage, from Stage III to Stage I. This modeling approach is an improvement of earlier models in two aspects: (i) the division of the stages of core formation is no longer arbitrary, but instead based upon the memories of siderophile elements; and (ii) siderophile elements with short memories are used only in the later core formation stages where the elements have significant memories.

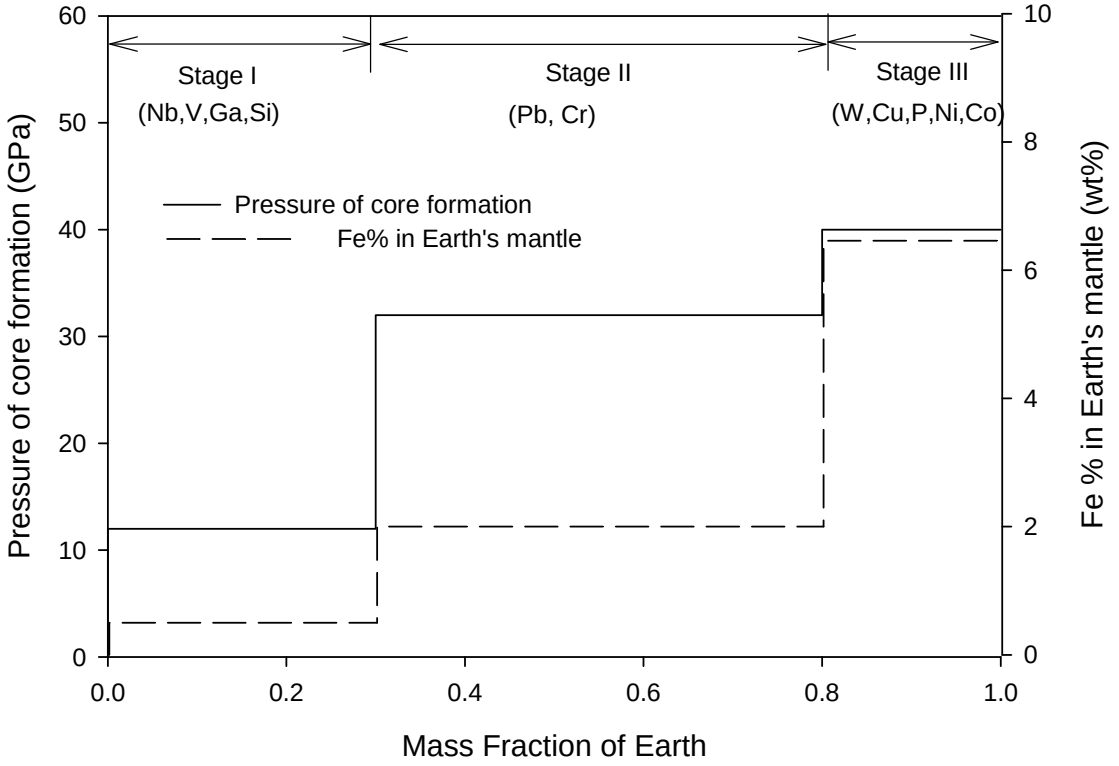

Figure 6.7 A three-stage core formation model for Earth divided in terms of the three groups of siderophile elements with different memories, except the ultra short-term memory group. Pressure, temperature and oxygen fugacity within each stage are assumed to be constant. The oxygen fugacity is represented by the Fe content in the Earth's mantle. Estimates of these parameters in each stage are obtained by best matching the observed current mantle contents of the siderophile elements, which only have memories for the particular stage and later stages. We obtain the result that core formation processes in the early Earth have increasing pressures (12→32→40 GPa), temperatures (2316→2887→3116 K) and oxygen fugacity (represented by mantle Fe content of 0.5→2→6.46 %) through stages I, II and III.

Details of three-stage accretion and core formation model for Earth

Here we assume the accretion and core formation of the Earth has three stages (n=1, 2, 3) with different core formation conditions. We define $M_j(n)$ to be the total mass of reservoir j at stage n (j=1, 2, 3; 1- part of solar nebular reservoir; 2- the Earth's silicate mantle reservoir; 3- the Earth's metal core reservoir). So $M_E(n)$ is the total mass of the growing Earth at stage n and $M_E(3)$ is the total mass of the present Earth. Then

$$\begin{cases} \dfrac{M_E(0)}{M_E(3)} = 0 \\ \dfrac{M_E(1)}{M_E(3)} = 0.3 \\ \dfrac{M_E(2)}{M_E(3)} = 0.8 \\ \dfrac{M_E(3)}{M_E(3)} = 1 \end{cases} \tag{6.8}$$

Let ΔM_E be increasing mass fraction of the growing Earth. At any time point, given the mass ratio of newly formed core ($\gamma=\Delta M_3/\Delta M_E$), then the mass change of Earth's mantle and core are:

$$\Delta M_2 = (1-\gamma)\Delta M_E \tag{6.9}$$

$$\Delta M_3 = \gamma \Delta M_E \tag{6.10}$$

We define the $N_{ij}(n)$ to be the number of atoms of species i in reservoir j at stage n and $C_{ij}(n)$ (= $N_{ij}(n)/M_j(n)$) to be the concentration of species i in reservoir j, respectively.

The concentrations of species i in the mantle ($C_{i2}(n)$) and the core ($C_{i3}(n)$) are affected by the simultaneous metal-silicate enrichment factor (d_{i23}):

$$d_{i23} = \frac{c_{i3}(n)}{C_{i2}(n)} \tag{6.11}$$

where $c_{i3}(n)$ is the concentration of species i in a new addition to the core and d_{i23} is the simultaneous metal/silicate partition coefficient for species i. For simplicity, we assume d_{i23} is constant over the history of accretion and core formation of Earth.

The increasing of the number of atoms of siderophile element i in the mantle can be written as:

$$\begin{aligned}
&\Delta N_{i2} = C_{i1}\Delta M_E - \gamma d_{i23}(n)\frac{N_{i2}(n)}{M_2(n)}\Delta M_E \\
&\Rightarrow N_{i2}(n) - N_{i2}(n-1) = C_{i1}\left[M_E(n) - M_E(n-1)\right] \\
&\qquad\qquad - \gamma d_{i23}(n)\frac{N_{i2}(n)}{M_2(n)}\left[M_E(n) - M_E(n-1)\right] \\
&\Rightarrow N_{i2}(n) = \frac{N_{i2}(n-1) + C_{i1}\left[M_E(n) - M_E(n-1)\right]}{M_E(n) - \dfrac{\gamma}{1-\gamma}d_{i23}(n)\left[M_E(n) - M_E(n-1)\right]}M_E(n) \\
&\Rightarrow C_{i2}(n) = \frac{C_{i2}(n-1)M_E(n-1) + C_{i1}\left[M_E(n) - M_E(n-1)\right]}{M_E(n) - \dfrac{\gamma}{1-\gamma}d_{i23}(n)\left[M_E(n) - M_E(n-1)\right]} \\
&\Rightarrow C_{i2}(n) = \frac{C_{i1}\dfrac{M_E(n)}{M_E(T_0)} + \left[C_{i2}(n-1) - C_{i1}\right]\dfrac{M_E(n-1)}{M_E(T_0)}}{\left[1 + \dfrac{\gamma}{1-\gamma}d_{i23}(n)\right]\dfrac{M_E(n)}{M_E(T_0)} - \dfrac{\gamma}{1-\gamma}d_{i23}(n)\dfrac{M_E(n-1)}{M_E(T_0)}}
\end{aligned} \tag{6.12}$$

By Mass balance,

$$N_{i3}(n) = N_{iE}(n) - N_{i2}(n)$$
$$C_{i3}(n) = \frac{C_{i1}M_E(n) - C_{i2}(n)M_2(n)}{M_3(n)} = \frac{C_{i1} - C_{i2}(n)(1-\gamma)}{\gamma} \quad (6.13)$$

Therefore, the metal-silicate partitioning of an element i can be obtained:

$$D_i(n) = \frac{C_{i3}(n)}{C_{i2}(n)} = \frac{\frac{C_{i1}(n)}{C_{i2}(n)} - 1 + \gamma}{\gamma} \quad (6.14)$$

The metal-silicate partitioning coefficient of a siderophile element M ($D_M^{\text{met-sil}}$) can be expressed as a function of temperature pressure and composition through the following relationship:

$$\begin{aligned}\log_{10} D_M^{met-sil} = {} & \frac{\upsilon}{2}\log_{10} D_{Fe}^{met-sil} + a + b\frac{1}{T} + c\frac{P}{T} + dN \\ & - \log_{10}\gamma_M^{metal} + \frac{\upsilon}{2}\left(\log_{10}\gamma_{Fe}^{metal} - \log_{10}\gamma_{FeO}^{silicate}\right)\end{aligned} \quad (6.15)$$

where N is 2.7 for peridotite. The activity coefficients of elements in the metal phase are assumed to depend on temperature as

$$\gamma_M^{metal}(T) = \left[\gamma_M^{metal}(T^*)\right]^{T^*/T} \quad (6.16)$$

where T^* is a reference temperature of 1873 K.

The parameters for the partition coefficients of Ni, Co, W, Cu, P, Cr, Pb, V, Nb, Ga, Si and Fe are given in Table 6.3.

Table 6.3 Parameters for the metal-silicate partition coefficients of siderophile elements in equation (6.15)

	a	*b*	*c*	*d*	ν/2	$\gamma_M^{metal}(T^*)$
Ni	0.5	3100	-78 ±5	-0.073 ±0.015	1	0.6819
Co	0.01	2511	-45 ±11	0	1	0.479
W	3.2	-1605	553 ±93	-0.85 ±0.03	2.26	0.9411
Cu	0.3	2300	-37 ±45	0.14 ±0.17	0.5	10.998
P	0.64	-1593	-74	0		4.2805
Cr	0.09	-2845 ±461	-20 ±10	0 ±0.013	1	0.7705
Pb	0.788	-2436	0	0	1	1
Nb	4.09	-15500	-166 ±31	-0.75 ±0.16	2.5	0.1107
V	0.855	-8548	-62 ±19	-0.101 ±0.029	1.5	0.1076
Ga	3.5	-4800	-126 ±36	-0.97 ±0.15	1.5	0.8762
Si	2.97	-21800	-11 ±33	-0.24 ±0.11	2	0.0077
Fe						0.8762

The partition coefficients for Ni, Co, P, Pb and V are from Wade and Wood (2005) and Wood (2008) (including corrections suggested by B. Wood). The partition coefficients for Cu, Cr, Nb, Ga, Si and Fe are from Corgne et al. (2008). The partition coefficients for W are from Cottrell et al. (2009, 2010). The γ_M^{metal} values in the table and $\gamma_{FeO}^{silicate}$ = 3 are also from Corgne et al. (2008) and Rudge et al. (2010). To evaluate the $D_{Fe}^{met\text{-}sil}$ term, the Fe content in Earth's core is fixed to 85.5% (McDonough, 2003). Modeling of metal-silicate partitioning during core formation and

related input parameters have been described in the supplementary information of Yu and Jacobsen (2011).

Results of the three-stage core formation modeling are shown in Figure 6.7. Based on observed concentrations of Nb, V, Ga, Si, Cr, Pb, Ni, Co, W, Cu and P in the Earth's mantle (Palme and O'Neill, 2003), we obtained that in the most recent 20% of core formation (Stage III), metal-silicate equilibrium occurred at a pressure of ~40 GPa and a temperature of ~3116 K with a mantle Fe content of ~6.46%. In Stage II (50% of core formation between Stage I and III), metal-silicate equilibration took place at a pressure of ~32 GPa and a temperature of ~2887 K, with a mantle Fe content of ~2%. Finally, the earliest 30% of core formation (Stage I) occurred at a pressure of ~12 GPa and a temperature of ~2316 K with an Fe content in the mantle of ~0.5%. It is worth pointing out that since Si and Ga are both volatile and slightly siderophile, it is very difficult to estimate precisely what portion of the mantle depletion (compared to CI chondrite) of these elements are due to volatile element loss during Earth's formation as opposed to their siderophile element behavior during core formation (Allègre et al., 2001; McDonough, 2003). Therefore, the results for Stage I should be treated with caution. In summary, the result shows that core formation processes in the Earth have experienced increasing pressures (12→32→40 GPa), temperatures (2316→2887→3116 K) and oxygen fugacity (represented by mantle Fe content of 0.5→2→6.46 %).

This result is consistent with previous estimates (Wade and Wood, 2005; Wood et al., 2008; Rubie et al., 2011; Yu and Jacobsen, 2011). The increasing oxidation state of Earth's mantle could be caused by heterogeneous accretion (Wänke and Gold, 1981; Ringwood, 1984; Rubie et al., 2011) or self oxidation of Earth's deep mantle (Wood et al., 2006; Wood et al., 2008).

6.4 Conclusions

We, for the first time, define and quantify a new concept – "core formation memory" for siderophile (metal-loving) elements in planetary mantles, showing the capabilities of siderophile elements for recording core formation history are decided by their siderophilicity and precisions of their determined mantle concentrations. We report CFMs of 23 and 8 siderophile elements in the mantles of Earth and Mars, respectively. The results show that (i) the moderately siderophile elements (Ni, Co and W etc.) primarily record the last 10-20 % of core formation and (ii) the slightly siderophile elements (Si and Ga) do have the capability of recording the earliest core formation history. The results provide substantial insight on how to meaningfully interpret the core formation conditions inferred from siderophile elements and reconstructing conditions of the whole core formation process.

In terms of three groups of siderophile elements with different CFM, a three stages core formation model was divided and developed to briefly illustrate how we apply the CFM results to reconstruct conditions of the whole core formation process. The model indicates that core formation processes in the Earth have experienced increasing pressures (12→32→40 GPa), temperatures (2316→2887→3116 K) and possibly also increasing oxygen fugacity (represented by mantle Fe content of 0.5→2→6.46 %). This result is consistent with previous estimates (Wade and Wood, 2005; Wood et al., 2008; Rubie et al., 2011; Yu and Jacobsen, 2011).

The "deep magma ocean" core formation model -- a continuous core formation process always has a deep magma ocean at the depth corresponding to the 35% of thickness of the whole mantle, was developed mainly based on the constraints from Ni and Co in Earth (e.g. Wood et al., 2008). So it is not necessary to be true for the early core formation stage due to the short CFMs of Ni and Co. Different core formation conditions should be obtained when the model is applied to Si and V.

Chapter 7

Conclusions

Our data of elemental abundances of three CAIs from Allende CV3 combined with the corresponding Ca isotope data on the same aliquots revealed that (1) all studied refractory inclusions have a Ca isotope composition lighter than the bulk silicate Earth; (2) variation of Rare Earth Element (REE) patterns represented by fractionation of Tm/Er ratio is correlated with the fractionation of Ca isotopes; (3) the above observations can be explained by segregation of 0.5-3 wt% of an ultra-refractory evaporation residue, characterized by relatively high $\delta^{44}Ca/^{40}Ca$ and low Tm/Er and Nd/Er, from the chondritic reservoir before condensation of CAI and other refractory inclusions or their precursors from the reservoir. Moreover, based on our new elemental abundance results for the Allende, we obtain the new effective partition coefficients (i.e. concentration ratios) of V, Cr, Mn and Si between Earth's core and mantle (D_V = 1.3 ±0.3; D_{Cr} = 2.4±0.7; D_{Mn} = 23.7±1.9 and D_{Si} = 0.39 ±0.07)

with improved precision. The results are similar to previous estimates for Cr and Si (D_{Cr} = 2.9 and D_{Si} = 0.34 from Allègre et al (1995)) and different for Mn (D_{Mn} = 5 from Allègre et al (1995))

We developed a W isotope evolution model for accretion and core formation in the Earth that is able to incorporate core formation constraints from siderophile element geochemistry and includes a parameterization allowing for a Moon-forming giant impact that could be substantially later than the main stage of Earth's accretion. We reached the following conclusions: (1) The concentrations of the refractory siderophile elements of the Earth's mantle are consistent with high-pressure metal-silicate equilibration in a terrestrial magma ocean during the Earth's accretion. This feature cannot be inherited from Mars-sized or smaller impactors. The fact that the data are consistent with equilibrium conditions that existed only in the deep Earth rather than the impactors, demonstrates that it is not necessary to introduce disequilibrium into the problem. (2) The timing of the Moon-forming giant impact is inversely correlated with the timescale of the main accretion stage of the Earth. Specifically, the earliest possible time for the Moon-forming giant impact could be at ~30 Myr, corresponding to the end of main stage accretion at ~30 Myr. A late Moon-forming giant impact (>52 Myr) requires the main stage of the Earth's accretion to complete rapidly in 10.7 ± 2.5 Myr for a giant impact at 52 Myr and 7.9±3.3 Myr for a giant impact at 100 Myr.

(3) A continuum of solutions exists between the two extreme end member solutions described in (2). (4) Only one late (>~50 Myr) giant impact with a Mars-sized body is allowed over the accretion history of the Earth, because two would completely erase the observed ε_W difference between the Earth's mantle and chondrite. (5) The apparent conflict between ^{182}Hf-^{182}W chronometry of terrestrial rocks when compared to recent estimates for a late formation of the Moon (>52 to 100 Myr) can be clearly understood from our results: a late formation of the Moon is possible, but it requires very fast formation of the Earth prior to the late Moon forming impact. (6) The late Moon-forming giant impact is a very low probability event. Specifically, the probabilities that the Moon-forming giant impact occurred later than 52 or 100 Myr are ~3×10^{-4} and ~1×10^{-10} respectively.

We measured trace element concentrations of two martian meteorites – Zagami and Nakhla from shergottite and nakhlite groups respectively. Combining other published data, the results lead to two distinct Hf/W ratios in the mantle sources of shergottites and nakhlites + chassignites during core formation as $f^{Hf/W}$ = 2.56 ± 0.46 and $f^{Hf/W}$ = 4.50 ± 0.53 respectively. The W isotope evolution in our "deep magma ocean" core formation model for Mars shows that after completion of core formation, Mars would have two mantle reservoirs with different $f^{Hf/W}$ and ε_W values, which are mainly controlled by the metal-silicate

equilibrium pressure during core formation and the fractionation of Hf and W between the upper and lower mantles. In the case where the separation of silicate minerals from the magma ocean is complete and given that the last metal-silicate equilibrium pressure is 14 ± 3 GPa, Mars would have an upper mantle reservoir with an $f^{\mathrm{Hf/W}}(\tau_0) = 3.1^{+1.3}_{-0.9}$ and a lower mantle reservoir with an $f^{\mathrm{Hf/W}}(\tau_0) = 12.8^{+3.5}_{+4}$. The Hf/W ratios are higher than the estimated mantle Hf/W ratios from shergottites and nakhlites + chassignites ($f^{\mathrm{Hf/W}}$ = 2.56 ± 0.46 and $f^{\mathrm{Hf/W}}$ = 4.50 ± 0.53 respectively). Moreover, in this case, if the observed $\varepsilon_{\mathrm{W}}(\tau_0)$ of the shergottites (2.23 ± 0.21) represents the $\varepsilon_{\mathrm{W}}(\tau_0)$ of the upper mantle reservoir of Mars, it is required for Mars to have a mean time of formation of 5.3 ± 2.4 Myr. Corresponding to this timescale, the lower mantle reservoir should develop a very high $\varepsilon_{\mathrm{W}}(\tau_0)$ of ~14-19, which has not been observed in any martian meteorites yet. In constrast, when separation of silicate crystals from silicate melt is incomplete during the solidification of the upper magma ocean and ~50% melt is trapped during the solidification of the upper magma ocean, our model can reproduce the observed Hf/W ratios and $\varepsilon_{\mathrm{W}}(\tau_0)$ of shergottites and nakhlites + chassignite in the upper and lower mantle reservoirs of Mars. This is consistent with a martian interior with a shallow shergottite mantle and a deep nakhlite mantle (Jones, 2003). In this case, the $f^{\mathrm{Hf/W}}(\tau_0)$ values of the sources of shergottites and nakhlites + chassigny are 2.6 ± 0.6 and

$4.2 \pm^{0.8}_{0.3}$, respectively. With these values, the W isotopic compositions of SNC martian meteorites provide a new mean time of accretion for Mars of 3.6 ± 0.1 Myr. (Mars finishes 63% of its accretion at 3.6 ± 0.1 Myr after the onset of the Solar System). The uncertainty is a 95% confidence interval calculated by a Monte Carlo simulation of the model. The mean accretion time of 3.6 ± 0.1 Myr is corresponding to that Mars accretes to 95% of its present mass in 10.8 ± 0.3 Myr after the formation of the Solar System. Therefore, Mars is not a planetary embryo, and Mars and proto-Earth may be formed on a similar timescale if a late Moon-forming giant impact is assumed. In contrast, if the Moon formed early at ~30 Myr then it takes about 3 times longer to form the proto-Earth compared to Mars.

Following the "deep magma ocean" core formation model, the early Earth could also develop a two-mantle-reservoir structure with different W isotopic compositions. On the basis of our stochastic mantle stirring and sampling model, the W isotope heterogeneity in Earth's mantle is very likely to be reduced to an unrecognized small scale after the 4.5 Ga-long active mantle stirring. So in practice, the core formation model with a homogeneous mantle reservoir is more suitable for the Earth as discussed in Chapter 3. Mars still keeps the W isotopic heterogeneity as indicated by non-homogeneous W isotope signature of martian meteorites, suggesting that Mars has a much slower mantle stirring rate than the

Earth. Specifically, the model shows that (1) Given a basalt sampling scale of 30 km, the mantle stirring rate is ≤823 Myr for Earth and ≥1772 Myr for Mars; (2) Given a basalt sampling scale of 100 km, the mantle stirring rate is ≤1052 Myr for Earth and ≥3325 Myr for Mars. This is consistent with the expectation that the smaller Mars cools down faster than the Earth after its formation and leads to a less efficient convective stirring of the martian mantle. The results for Earth are also consistent with the mantle stirring rate (~500 Myr) constrained by the long-lived isotope systems in Earth.

In Chapter 6, for the first time, we define and quantify a new concept – "core formation memory" (CFM) for siderophile (metal-loving) elements in planetary mantles, showing the significantly different capabilities of siderophile elements in recording core formation history. The CFMs vary among siderophile elements in the Earth and Mars' mantles ranging from only the last <1% of core formation history for highly siderophile elements to almost 100% of the core formation history for slightly siderophile elements. Specifically, for Earth, (1) highly siderophile elements (e.g. PGE) have very short CFMs, covering only the last 0.4%-1.3% of Earth's accretion and core formation history. Their CFMs would be even shorter if their mantle concentrations have contributions from the "late veneer". So they are not useful for establishing core formation history. (2) Moderately siderophile elements

(e.g. Ni, Co and W) can memorize less than ~20% of Earth's core formation history. They primarily record core formation processes in the stage of the last giant impact in the Earth's accretion. (3) Slightly siderophile elements (e.g. V, Nb, Ga, and Si) are able to remember nearly the whole accretion and core formation history of the Earth. However, uncertainty from volatility correction and other factors makes it very difficult to establish the core-formation depletions of most of these elements with sufficient accuracy to consider this information reliable. The memory results are important in establishing what constraints can and cannot be obtained from siderophile elements for core formation and will provide substantial insight into meaningfully interpreting core formation conditions inferred from siderophile elements and reconstructing conditions of the whole core formation process.

Finally, the work presented here will serve as a bridge between core formation geochemistry, formation timescale of terrestrial planets, cosmochemistry and astrophysics. Simulation of terrestrial planet formation by N-body simulations has been quite successful (Agnor et al., 1999; O'Brien et al., 2006), and combining the constraints of Hf-W chronometry here with such simulations in a realistic way is a challenge but also a promising field that is worthy of more attention and efforts in future.

References

Agnor, C.B., Canup, R.M., Levison, H.F., 1999. On the character and consequences of large impacts in the late stage of terrestrial planet formation. *Icarus* 142, 219-237.

Allègre, C., Manhès, G., Lewin, É., 2001. Chemical composition of the Earth and the volatility control on planetary genetics. *Earth and Planetary Science Letters* 185, 49-69.

Allègre, C., Poirier, J., Humler, E., Hofmann, A., 1995. The chemical composition of the Earth. *Earth and Planetary Science Letters* 134, 515-526.

Amelin, Y., Kaltenbach, A., Iizuka, T., Stirling, C.H., Ireland, T.R., Petaev, M., Jacobsen, S.B., 2010. U-Pb chronology of the Solar System's oldest solids with variable $^{238}U/^{235}U$. *Earth and Planetary Science Letters* 300, 343-350.

Amelin, Y., Krot, A.N., Hutcheon, I.D., Ulyanov, A.A., 2002. Lead isotopic ages of chondrules and calcium-aluminum-rich inclusions, pp. 1678-1683.

Anand, M., James, S., Greenwood, R.C., Johnson, D., Franchi, I.A., Grady, M.M., 2008. Mineralogy and geochemistry of shergottite RBT 04262, 39th Lunar & Planetary Science Conference, League City, Texas, USA, p. 2173.

Anders, E., Grevesse, N., 1989. Abundances of the elements: Meteoritic and solar. *Geochimica et Cosmochimica Acta* 53, 197-214.

Arevalo, R., McDonough, W.F., 2008. Tungsten geochemistry and implications for understanding the Earth's interior. *Earth and Planetary Science Letters* 272, 656-665.

Barrat, J.A., Benoit, M., Cotten, J., 2006. Bulk chemistry of the nakhlite Miller Range 03346 (MIL 03346), 37th Lunar & Planetary Science Conference, p. 1569.

Barrat, J.A., Blichert-toft, J., Nesbitt, R.W., Keller, F., 2001. Bulk chemistry of Saharan shergottite Dar al Gani 476. *Meteoritics & Planetary Science* 36, 23-29.

Barrat, J.A., Gillet, P., Sautter, V., Jambon, A., Javoy, M., Göpel, C., Lesourd, M., Keller, F., Petit, E., 2002. Petrology and chemistry of the basaltic shergottite North West Africa 480. *Meteoritics & Planetary Science* 37, 487-499.

Barrat, J.A., Zanda, B., Moynier, F., Bollinger, C., Liorzou, C., Bayon, G., 2012. Geochemistry of CI chondrites: Major and trace elements, and Cu and Zn isotopes. *Geochemica et Cosmochimica Acta,* (In presse).

Beck, P., Barrat, J.A., Gillet, P., Wadhwa, M., Franchi, I.A., Greenwood, R.C., Bohn, M., Cotten, J., van de Moortčle, B., Reynard, B., 2006. Petrography and geochemistry of the chassignite Northwest Africa 2737 (NWA 2737). *Geochimica et Cosmochimica Acta* 70, 2127-2139.

Beckett, J.R., Connolly, H.C., Ebel, D.S., 2006. Chemical processes in igneous calcium-aluminum-rich inclusions: A mostly CMAS view of melting and crystallization, *Meteorites and the Early Solar System II*. Univ of Arizona Pr, pp. 399-429.

Bertka, C.M., Fei, Y., 1997. Mineralogy of the martian interior up to core-mantle boundary pressures. *Journal of Geophysical Research* 102, 5251-5264.

Bouvier, A., Blichert-Toft, J., Albarède, F., 2009. Martian meteorite chronology and the evolution of the interior of Mars. *Earth and Planetary Science Letters* 280, 285-295.

Boyet, M., Carlson, R.W., 2005. ^{142}Nd evidence for early (> 4.53 Ga) global differentiation of the silicate Earth. *Science* 309, 576-581.

Boynton, W.V., 1975. Fractionation in the solar nebula: Condensation of yttrium and the rare earth elements. *Geochimica et Cosmochimica Acta* 39, 569-584.

Boynton, W.V., Frazier, R.M., Macdougall, J.D., 1980. Identification of an ultra-refractory component in the Murchison meteorite, Lunar and Planetary Science Conference, pp. 103-105.

Brandon, A.D., Lapen, T.J., Debaille, V., Beard, B.L., Rankenburg, K., Neal, C., 2009. Re-evaluating ^{142}Nd/^{144}Nd in lunar mare basalts with

implications for the early evolution and bulk Sm/Nd of the Moon. *Geochimica et Cosmochimica Acta* 73, 6421-6445.

Cameron, A.G.W., 2000. Higher-resolution simulations of the giant impact, in: Canup, R.M., Righter, K. (Eds.), *Origin of the earth and moon*. University of Arizona Press, Tucson, pp. 133-144.

Canup, R.M., 2004. Simulations of a late lunar-forming impact. *Icarus* 168, 433-456.

Canup, R.M., 2008. Accretion of the Earth. *Philosophical Transactions of the Royal Society A: Mathematical, Physical and Engineering Sciences* 366, 4061-4075.

Canup, R.M., Agnor, C.B., 2000. Accretion of the terrestrial planets and the Earth-Moon system, in: Canup, R.M., Righter, K. (Eds.), *Origin of the earth and moon*, pp. 113-129.

Canup, R.M., Asphaug, E., 2001. Origin of the Moon in a giant impact near the end of the Earth's formation. *Nature* 412, 708-712.

Carlson, R.W., Irving, A.J., 2004. Pb-Hf-Sr-Nd isotopic systematics and age of nakhlite NWA 998, Lunar and Planetary Science Conference XXXV, p. 1442.

Caro, G., Bourdon, B., Birck, J.L., Moorbath, S., 2006. High-precision $^{142}Nd/^{144}Nd$ measurements in terrestrial rocks: constraints on the early differentiation of the Earth's mantle. *Geochimica et Cosmochimica Acta* 70, 164-191.

Chabot, N.L., Agee, C.B., 2003. Core formation in the Earth and Moon: new experimental constraints from V, Cr, and Mn. *Geochimica et Cosmochimica Acta* 67, 2077-2091.

Chambers, J.E., 2004. Planetary accretion in the inner Solar System. *Earth and Planetary Science Letters* 223, 241-252.

Cipriani, A., Bonatti, E., Carlson, R.W., 2011. Nonchondritic ^{142}Nd in suboceanic mantle peridotites. *Geochemistry Geophysics Geosystems* 12, Q03006.

Clayton, R.N., Grossman, L., Mayeda, T.K., 1973. A component of primitive nuclear composition in carbonaceous meteorites. *Science* 182, 485-488.

Clayton, R.N., Hinton, R.W., Davis, A.M., 1988. Isotopic variations in the rock-forming elements in meteorites. *Philosophical Transactions of the Royal Society of London. Series A, Mathematical and Physical Sciences* 325, 483-501.

Corgne, A., Keshav, S., Wood, B.J., McDonough, W.F., Fei, Y., 2008. Metal-silicate partitioning and constraints on core composition and oxygen fugacity during earth accretion. *Geochimica et Cosmochimica Acta* 72, 574-589.

Cottrell, E., Walter, M., Walker, D., 2008. W Partitioning Between Liquid Metal and Liquid Silicate as a Function of P, T, fO 2, X carbon, and Melt Structure: Implications for the Earth, Moon, Mars, and Vesta. *39th Lunar and Planetary Science Conference* p. 2238

Cottrell, E., Walter, M.J., Walker, D., 2009. Metal-silicate partitioning of tungsten at high pressure and temperature: Implications for equilibrium core formation in Earth. *Earth and Planetary Science Letters* 281, 275-287.

Cottrell, E., Walter, M.J., Walker, D., 2010. Erratum to``Metal--silicate partitioning of tungsten at high pressure and temperature: Implications for equilibrium core formation in Earth"[Earth and Planetary Science Letters 281 (2009) 275--287]. *Earth and Planetary Science Letters* 289, 631-634.

Dauphas, N., Pourmand, A., 2011. Hf-W-Th evidence for rapid growth of Mars and its status as a planetary embryo. *Nature* 473, 489-492.

Davis, A.M., Grossman, L., 1979. Condensation and fractionation of rare earths in the solar nebula. *Geochimica et Cosmochimica Acta* 43, 1611-1632.

Davis, A.M., Tanaka, T., Grossman, L., Lee, T., Wasserburg, G.J., Chicago Univ, I.L., 1982. Chemical composition of HAL, an isotopically-unusual Allende inclusion. *Geochimica et Cosmochimica Acta* 46, 1627-1651.

Debaille, V., Brandon, A., O'Neill, C., Yin, Q.Z., Jacobsen, B., 2009. Early martian mantle overturn inferred from isotopic composition of nakhlite meteorites. *Nature Geoscience* 2, 548-552.

Debaille, V., Brandon, A., Yin, Q., Jacobsen, B., 2007. Coupled ^{142}Nd–^{143}Nd evidence for a protracted magma ocean in Mars. *Nature* 450, 525-528.

Drake, M., Capobianco, C., Newsom, H., 1989. V, Cr, and Mn in the earth, moon, EPB, and SPB and the origin of the moon- Experimental studies. *Geochimica et Cosmochimica Acta* 53, 2101-2111.

Drake, M.J., Righter, K., 2002. Determining the composition of the Earth. *Nature* 416, 39-44.

El Goresy, A., Zinner, E., Matsunami, S., Palme, H., Spettel, B., Lin, Y., Nazarov, M., 2002. Efremovka 101.1: A CAI with ultrarefractory REE patterns and enormous enrichments of Sc, Zr, and Y in fassaite and perovskite. *Geochimica et Cosmochimica Acta* 66, 1459-1491.

Foley, C.N., Wadhwa, M., Borg, L.E., Janney, P.E., Hines, R., Grove, T.L., 2005. The early differentiation history of Mars from ^{182}W-^{142}Nd isotope systematics in the SNC meteorites. *Geochimica et Cosmochimica Acta* 69, 4557-4571.

Gillet, P., Barrat, J.A., Beck, P., Marty, B., Greenwood, R.C., Franchi, I.A., Bohn, M., Cotten, J., 2005. Petrology, geochemistry, and cosmic-ray exposure age of lherzolitic shergottite Northwest Africa 1950. *Meteoritics and Planetary Science* 40, 1175-1184.

Goldschmidt, V.M., 1923. Geochemische verteilungsgesetze der elemente (I). *Videnskapsselskapets skrifter, I. Mat.-naturv. klasse* 3, 1-18.

Goldschmidt, V.M., 1937. The principles of distribution of chemical elements in minerals and rocks. The seventh Hugo Müller Lecture, delivered before the Chemical Society on March 17th, 1937. *J. Chem. Soc.*, 655-673.

Gray, C., Papanastassiou, D., Wasserburg, G., 1973. The identification of early condensates from the solar nebula. *Icarus* 20, 213-239.

Grossman, L., Simon, S.B., Rai, V.K., Thiemens, M.H., Hutcheon, I.D., Williams, R.W., Galy, A., Ding, T., Fedkin, A.V., Clayton, R.N., 2008. Primordial compositions of refractory inclusions. *Geochimica et Cosmochimica Acta* 72, 3001-3021.

Haisch, K.E., E.A., L., C.J., L., 2001. Disk frequencies and lifetimes in young clusters. *The Astrophysical Journal* 553, L153-L156.

Halliday, A.N., 2008. A young Moon-forming giant impact at 70-110 million years accompanied by late-stage mixing, core formation and degassing of the Earth. *Philosophical Transactions A* 366, 4163-4181.

Harper, C.L., Jacobsen, S.B., 1996. Evidence for ^{182}Hf in the early Solar System and constraints on the timescale of terrestrial accretion and core formation. *Geochimica et Cosmochimica Acta* 60, 1131-1153.

Harper, C.L., Nyquist, L.E., Bansal, B., Wiesmann, H., Shih, C.Y., 1995. Rapid accretion and early differentiation of Mars indicated by ^{142}Nd/^{144}Nd in SNC meteorites. *Science* 267, 213-217.

Hinton, R.W., Davis, A.M., Scatena-Wachel, D.E., Grossman, L., Draus, R.J., 1988. A chemical and isotopic study of hibonite-rich refractory inclusions in primitive meteorites. *Geochimica et Cosmochimica Acta* 52, 2573-2598.

Hiyagon, H., Hashimoto, A., Kimura, M., Ushikubo, T., 2003. First discovery of an ultra-refractory nodule in an Allende fine-grained inclusion, 34th Lunar and Planetary Science Conference, p. 1552.

Huang, S., Farkaİ, J., Jacobsen, S.B., 2010. Calcium isotopic fractionation between clinopyroxene and orthopyroxene from mantle peridotites. *Earth and Planetary Science Letters* 292, 337-344.

Huang, S., Farkaİ, J., Yu, G., Petaev, M.I., Jacobsen, S.B., 2012. Calcium Isotopic Ratios and Rare Earth Element Abundances in Refractory Inclusions from Allende CV3 Chondrite. *Geochimica et Cosmochimica Acta* 77, 252-265.

Ireland, T.R., Fahey, A.J., Zinner, E.K., 1988. Trace-element abundances in hibonites from the Murchison carbonaceous chondrite: Constraints on high-temperature processes in the solar nebula. *Geochimica et Cosmochimica Acta* 52, 2841-2854.

Ireland, T.R., Fegley, J.B., 2000. The solar system's earliest chemistry: Systematics of refractory inclusions. *International Geology Review* 42, 865-894.

Ireland, T.R., Zinner, E.K., Fahey, A.J., Esat, T.M., 1992. Evidence for distillation in the formation of HAL and related hibonite inclusions. *Geochimica et Cosmochimica Acta* 56, 2503-2520.

Jacobsen, S., Chakrabarti, R., Bogdanovski, O., Ranen, M., Petaev, M., 2007. High Resolution ^{26}Al-^{26}Mg Chronometry of CAIs from the Allende Meteorite, Workshop on the Chronology of Meteorites and the Early Solar System, Kauai, Hawaii, pp. 82-83.

Jacobsen, S., Chakrabarti, R., Ranen, M., Petaev, M., 2008. High Resolution ^{26}Al-^{26}Mg Chronometry of CAIs from the Allende Meteorite, Lunar and Planetary Science 39th, p. 1999.

Jacobsen, S.B., 2005. The Hf-W Isotopic System and the Origin of the Earth and Moon. *Annual Review of Earth and Planetary Sciences* 33, 531-570.

Jacobsen, S.B., Harper, C.L., 1996. Accretion and early differentiation history of the earth based on extinct radionuclides, in: Basu, A., Hart, S. (Eds.), *In Earth Processes. Reading the Isotope Code*. AGU, Washington, DC, pp. 47-74.

Jambon, A., Barrat, J.A., Sautter, V., Gillet, P., Göpel, C., Javoy, M., Joron, J.L., Lesourd, M., 2002. The basaltic shergottite Northwest Africa 856: Petrology and chemistry. *Meteoritics & Planetary Science* 37, 1147-1164.

Jones, J., 2003. Constraints on the structure of the martian interior determined from the chemical and isotopic systematics of SNC meteorites. *Meteoritics & Planetary Science* 38, 1807-1814.

Jones, J.H., Drake, M.J., 1986. Geochemical constraints on core formation in the Earth. *Nature* 322, 221-228.

Jungck, M.H.A., Shimamura, T., Lugmair, G.W., 1984. Ca isotope variations in Allende. *Geochimica et Cosmochimica Acta* 48, 2651-2658.

Kegler, P., Holzheid, A., Frost, D., Rubie, D., Dohmen, R., Palme, H., 2008. New Ni and Co metal-silicate partitioning data and their relevance for an early terrestrial magma ocean. *Earth and Planetary Science Letters* 268, 28-40.

Kellogg, J.B., Jacobsen, S.B., O'Connell, R.J., 2002. Modeling the distribution of isotopic ratios in geochemical reservoirs. *Earth and Planetary Science Letters* 204, 183-202.

Kellogg, J.B., Jacobsen, S.B., O'Connell, R.J., 2007. Modeling lead isotopic heterogeneity in mid-ocean ridge basalts. *Earth and Planetary Science Letters* 262, 328-342.

Kinoshita, N., Paul, M., Kashiv, Y., Alcorta, M., Collon, P., Deibel, C., DiGiovine, B., Greene, J., Henderson, D., Jiang, C., Marley, S., Nakanishi, T., Pardo, R., Rehm, K.E., Robertson, D., Scott, R., Schmitt, C., Tang, X.,

Ugalde, C., Vondrasek, R.C., 2011. Geocosmochronometer ^{146}Sm: A Revised Half-Life Value, Goldschmidt2011, Prague, Czech Republic, p. 1191.

Kleine, T., Mezger, K., Münker, C., Palme, H., Bischoff, A., 2004. ^{182}Hf-^{182}W isotope systematics of chondrites, eucrites, and martian meteorites: Chronology of core formation and early mantle differentiation in Vesta and Mars. *Geochimica et Cosmochimica Acta* 68, 2935-2946.

Kleine, T., Müker, C., Mezger, K., Palme, H., 2002. Rapid accretion and early core formation on asteroids and the terrestrial planets from Hf-W chronometry. *Nature* 418, 952-955.

Kleine, T., Touboul, M., Bourdon, B., Nimmo, F., Mezger, K., Palme, H., Jacobsen, S.B., Yin, Q.Z., Halliday, A.N., 2009. Hf-W chronology of the accretion and early evolution of asteroids and terrestrial planets. *Geochimica et Cosmochimica Acta* 73, 5150-5188.

Klemme, S., Gunther, D., Hametner, K., Prowatke, S., Zack, T., 2006. The partitioning of trace elements between ilmenite, ulvospinel, armalcolite and silicate melts with implications for the early differentiation of the moon. *Chemical Geology* 234, 251-263.

König, S., Münker, C., Hohl, S., Paulick, H., Barth, A., Lagos, M., Pfander, J., Büchl, A., 2011. The Earth's tungsten budget during mantle melting and crust formation. *Geochimica et Cosmochimica Acta* 75, 2119-2136.

Kortenkamp, S.J., Kokubo, E., Weidenschilling, S.J., 2000. Formation of planetary embryos, in: Canup, R.M., Righter, K. (Eds.), *Origin of the earth and moon*. University of Arizona, Tucson, TX, pp. 85-100.

Krot, A.N., Keil, K., Goodrich, C.A., Scott, E.R.D., Weisberg, M.K., 2003. Classification of Meteorites, in: Holland, H.D., Turekian, K.K. (Eds.), *Treatise on Geochemistry*. Elsevier Ltd, pp. 83-128.

Krot, A.N., Nagashima, K., Hutcheon, I.D., Davis, A.M., Thrane, K., Bizzarro, M., Huss, G.R., Papanastassiou, D.A., Wasserburg, G.J., 2008. Oxygen isotopic compositions of individual minerals from FUN CAIs, 39th Lunar and Planetary Science Conference, p. 2162.

Lee, D.C., Halliday, A.N., 1996. Hf-W isotopic evidence for rapid accretion and differentiation in the early solar system. *Science* 274, 1876-1879.

Lee, T., Chen, W.H., Chen, J.C., 2011. Ca-43 Isotopic Anomaly in CAI and the Astrophysical Origin of Ca Isotopes, 42nd Lunar and Planetary Science Conference, p. 1828.

Lee, T., Russell, W.A., Wasserburg, G.J., 1979. Calcium isotopic anomalies and the lack of aluminum-26 in an unusual Allende inclusion. *The Astrophysical Journal* 228, L93-L98.

Lejeune, A.M., Richet, P., 1995. Rheology of crystal-bearing silicate melts: an experimental study at high viscosities. *Journal of Geophysical Research* 100, 4215-4229.

Li, J., Agee, C.B., 1996. Geochemistry of mantle-core differentiation at high pressure. *Nature* 381, 686-689.

Li, J., Chen, B., Leinenweber, K., Wang, Y., 2011. Rapid Core Formation through Diapirism from High-Pressure X-Ray Radiography, 42nd Lunar & Planetary Science Conference, p. 2219.

Lodders, K., Fegley, B., 1997. An oxygen isotope model for the composition of Mars. *Icarus* 126, 373-394.

Longhi, J., Knittle, E., Holloway, J.R., Wa¨nke, H., 1992. The bulk composition, mineralogy and internal structure of Mars, in: Kieffer, H.H., Jakosky, B.M., Snyder, C.W., Matthews, M.S. (Eds.), *Mars*. University of Arizona Press, Tucson, pp. 184-208.

Lu, Y., Makishima, A., Nakamura, E., 2007. Coprecipitation of Ti, Mo, Sn and Sb with fluorides and application to determination of B, Ti, Zr, Nb, Mo, Sn, Sb, Hf and Ta by ICP-MS. *Chemical Geology* 236, 13-26.

MacPherson, G.J., 2003. Calcium-aluminum-rich inclusions in chondritic meteorites, in: Holland, H.D., Turekian, K.K. (Eds.), *Treatise on Geochemistry*. Elsevier, pp. 201-246.

MacPherson, G.J., Davis, A.M., 1994. Refractory inclusions in the prototypical CM chondrite, Mighei. *Geochimica et Cosmochimica Acta* 58, 5599-5625.

MacPherson, G.J., Nagashima, K., Bullock, E.S., Krot, A.N., 2008. Mass-dependent oxygen isotopic fractionation in non-FUN forsterite-bearing Type B CAIs, 39th Lunar and Planetary Science Conference, League City, p. 2039.

Makishima, A., Nakamura, E., 2006. Determination of Major/Minor and Trace Elements in Silicate Samples by ICP-QMS and ICP-SFMS Applying Isotope Dilution-Internal Standardisation (ID-IS) and Multi-Stage Internal Standardisation. *Geostandards and Geoanalytical Research* 30, 245-271.

Mason, B., Taylor, S.R., 1982. Inclusions in the Allende meteorite. *Smithsonian Contributions to the Earth Sciences* 25, 1-30.

McDonough, W., 2003. Compositional model for the Earth's core, in: Holland, H.D., Turekian, K.K. (Eds.), *Treatise on Geochemistry*. Elsevier, pp. 547-568.

McDonough, W.F., Sun, S., 1995. The composition of the Earth. *Chemical Geology* 120, 223-253.

McSween, J.H.Y., 2003. Mars, in: Holland, H.D., Turekian, K.K. (Eds.), *Treatise on Geochemistry*.

Nakamura, N., Unruh, D.M., Tatsumoto, M., Hutchison, R., 1982. Origin and evolution of the Nakhla meteorite inferred from the Sm-Nd and U-Pb systematics and REE, Ba, Sr, Rb and K abundances. *Geochimica et Cosmochimica Acta* 46, 1555-1573.

Neal, C., Taylor, L., Ely, J., Jain, J., Nazarov, M., 2001. Detailed geochemistry of new shergottite, Dhofar 019, 32nd Lunar and Planetary Science, Houston, TX, p. 1671.

Niederer, F.R., Papanastassiou, D.A., 1984. Ca isotopes in refractory inclusions. *Geochimica et Cosmochimica Acta* 48, 1279-1293.

Nimmo, F., Kleine, T., 2007. How rapidly did Mars accrete? Uncertainties in the Hf-W timing of core formation. *Icarus* 191, 497-504.

O'Brien, D.P., Morbidelli, A., Levison, H.F., 2006. Terrestrial planet formation with strong dynamical friction. *Icarus* 184, 39-58.

O'Neill, H.S.C., 1991. The origin of the Moon and the early history of the Earth-A chemical model. Part 2: The Earth. *Geochim. Cosmochim. Acta* 55.

Palme, H., O'Neill, H.S.C., 2003. Cosmochemical estimates of mantle composition, in: Holland, H.D., Turekian, K.K. (Eds.), *Treatise on Geochemistry*. Elsevier, pp. 1-38.

Petaev, M.I., Jacobsen, S.B., 2009. Petrologic study of SJ101, a new forsterite-bearing CAI from the Allende CV3 chondrite. *Geochimica et Cosmochimica Acta* 73, 5100-5114.

Pourmand, A., Dauphas, N., Ireland, T.J., 2012. A novel extraction chromatography and MC-ICP-MS technique for rapid analysis of REE, Sc and Y: Revising CI-chondrite and Post-Archean Australian Shale (PAAS) abundances. *Chemical Geology* 291, 38-54.

Raymond, S.N., O'Brien, D.P., Morbidelli, A., Kaib, N.A., 2009. Building the terrestrial planets: Constrained accretion in the inner Solar System. *Icarus* 203, 644-662.

Richter, F.M., 2004. Timescales determining the degree of kinetic isotope fractionation by evaporation and condensation. *Geochimica et Cosmochimica Acta* 68, 4971-4992.

Richter, F.M., Davis, A.M., Ebel, D.S., Hashimoto, A., 2002. Elemental and isotopic fractionation of Type B calcium-, aluminum-rich inclusions: experiments, theoretical considerations, and constraints on their thermal evolution. *Geochimica et Cosmochimica Acta* 66, 521-540.

Righter, K., 2003. Metal-Silicate Partitioning of Siderophile Elements and Core Formation in the Early Earth. *Annual Review of Earth and Planetary Sciences* 31, 135-174.

Righter, K., Chabot, N.L., 2011. Moderately and slightly siderophile element constraints on the depth and extent of melting in early Mars. *Meteoritics & Planetary Science* 46, 157-176.

Righter, K., Drake, M.J., 1997. Metal-silicate equilibrium in a homogeneously accreting earth: new results for Re. *Earth and Planetary Science Letters* 146, 541-553.

Righter, K., Drake, M.J., Scott, E.R.D., 2006. Compositional relationships between meteorites and terrestrial planets, in: Lauretta, D.S., McSween, H.Y. (Eds.), *Meteorites and the Early Solar System II*. University of Arizona Press, Tucson, pp. 803-828.

Righter, K., King, C., Danielson, L., Pando, K., Lee, C., 2011. Experimental determination of the metal/silicate partition coefficient of Germanium: Implications for core and mantle differentiation. *Earth and Planetary Science Letters* 304, 379–388.

Righter, K., Shearer, C.K., 2003. Magmatic fractionation of Hf and W: constraints on the timing of core formation and differentiation in the Moon and Mars. *Geochimica et Cosmochimica Acta* 67, 2497-2507.

Ringwood, A., 1961. Silicon in the metal phase of enstatite chondrites and some geochemical implications. *Geochimica et Cosmochimica Acta* 25, 1-13.

Ringwood, A.E., 1984. The Bakerian Lecture, 1983: the Earth's core: its composition, formation and bearing upon the origin of the Earth. *Proceedings of the Royal Society of London. A. Mathematical and Physical Sciences* 395, 1.

Rubie, D.C., Frost, D.J., Mann, U., Asahara, Y., Nimmo, F., Tsuno, K., Kegler, P., Holzheid, A., Palme, H., 2011. Heterogeneous accretion, composition and core-mantle differentiation of the Earth. *Earth and Planetary Science Letters* 301, 31-42.

Rubie, D.C., Melosh, H.J., Reid, J.E., Liebske, C., Righter, K., 2003. Mechanisms of metal-silicate equilibration in the terrestrial magma ocean. *Earth and Planetary Science Letters* 205, 239-255.

Rubie, D.C., Nimmo, F., Melosh, H.J., 2007. Formation of Earth's core, in: Schubert, G. (Ed.), *Treatise on Geophysics*. Elsevier, pp. 51-90.

Rudge, J., Kleine, T., Bourdon, B., 2010. Broad bounds on Earth's accretion and core formation constrained by geochemical models. *Nature Geoscience* 3, 439-443.

Sautter, V., Barrat, J.A., Jambon, A., Lorand, J.P., Gillet, P., Javoy, M., Joron, J.L., Lesourd, M., 2002. A new Martian meteorite from Morocco: the nakhlite North West Africa 817. *Earth and Planetary Science Letters* 195, 223-238.

Schersten, A., Elliott, T., Hawkesworth, C., Norman, M., 2004. Tungsten isotope evidence that mantle plumes contain no contribution from the Earth's core. *Nature* 427, 234-237.

Schoenberg, R., Kamber, B.S., Collerson, K.D., Eugster, O., 2002a. New W-isotope evidence for rapid terrestrial accretion and very early core formation. *Geochimica et Cosmochimica Acta* 66, 3151-3160.

Schoenberg, R., Kamber, B.S., Collerson, K.D., Moorbath, S., 2002b. Tungsten isotope evidence from~ 3.8-Gyr metamorphosed sediments for early meteorite bombardment of the Earth. *Nature* 418, 403-405.

Shinotsuka, K., Hidaka, H., Ebihara, M., 1995. Detailed abundances of rare earth elements, thorium and uranium in chondritic meteorites: An ICP-MS study. *Meteoritics* 30, 694-699.

Simon, J.I., DePaolo, D.J., 2010. Stable calcium isotopic composition of meteorites and rocky planets. *Earth and Planetary Science Letters* 289, 457-466.

Simon, S.B., Davis, A.M., Grossman, L., 1996. A unique ultrarefractory inclusion from the Murchison meteorite. *Meteoritics & Planetary Science* 31, 106-115.

Simon, S.B., Davis, A.M., Grossman, L., McKeegan, K.D., 2002. A hibonite-corundum inclusion from Murchison: A first-generation condensate from the solar nebula. *Meteoritics & Planetary Science* 37, 533-548.

Stevenson, D.J., 1990. Fluid dynamics of core formation, in: Newsom, H.E., Jones, J.H. (Eds.), *Origin of the Earth*. Oxford University Press, London, pp. 231-249.

Tanaka, T., Masuda, A., 1973. Rare-earth elements in matrix, inclusions, and chondrules of the Allende meteorite. *Icarus* 19, 523-530.

Taylor, L.A., Nazarov, M.A., Shearer, C.K., McSween, H.Y., Cahill, J., Neal, C.R., Ivanova, M.A., Barsukova, L.D., Lentz, R.C., Clayton, R.N., 2002. Martian meteorite Dhofar 019: A new shergottite. *Meteoritics and Planetary Science* 37, 1107-1128.

Taylor, S.R., McLennan, S.M., 2009. Planetary crusts: their composition, origin and evolution. Cambridge University Press, New York.

Touboul, M., Kleine, T., Bourdon, B., Palme, H., Wieler, R., 2007. Late formation and prolonged differentiation of the Moon inferred from W isotopes in lunar metals. *Nature* 450, 1206-1209.

Touboul, M., Puchtel, I.S., Walker, R.J., 2012. ^{182}W Evidence for Long-Term Preservation of Early Mantle Differentiation Products. *Science* 335, 1065-1069.

Urey, H.C., 1947. The thermodynamic properties of isotopic substances. *Journal of the Chemical Society (Resumed)* 1947, 562-581.

Vockenhuber, C., Oberli, F., Bichler, M., Ahmad, I., Quitt, G., Meier, M., Halliday, A.N., Lee, D.C., Kutschera, W., Steier, P., 2004. New Half-Life Measurement of ^{182}Hf: Improved Chronometer for the Early Solar System. *Physical Review Letters* 93, 172501.

Wade, J., Wood, B.J., 2005. Core formation and the oxidation state of the Earth. *Earth and Planetary Science Letters* 236, 78-95.

Wänke, H., Dreibus, G., 1988. Chemical composition and accretion history of terrestrial planets. *Philosophical Transactions of the Royal Society of London. Series A, Mathematical and Physical Sciences* 325, 545-557.

Wänke, H., Gold, T., 1981. Constitution of Terrestrial Planets [and Discussion]. *Philosophical Transactions of the Royal Society of London. Series A, Mathematical and Physical Sciences* 303, 287-302.

Wetherill, G.W., 1985. Occurrence of giant impacts during the growth of the terrestrial planets. *Science* 228, 877-879.

Wetherill, G.W., 1986. Accumulation of the terrestrial planets and implications concerning lunar origin, in: Hartmann, W.K., Phillips, R.J., Taylor, G.J. (Eds.), *Origin of the Moon*. Lunar and Planetary Institue, Houston, pp. 519-550.

Wetherill, G.W., 1991. Why Isn't Mars as Big as Earth?, Lunar and Planetary Science Conference, p. 1495.

Willbold, M., Elliott, T., Moorbath, S., 2011. The tungsten isotopic composition of the Earth/'s mantle before the terminal bombardment. *Nature* 477, 195-198.

Wood, B.J., 2008. Accretion and core formation: constraints from metal-silicate partitioning. *Phil. Trans. R. Soc. A* 366, 4339-4355.

Wood, B.J., Wade, J., Kilburn, M.R., 2008. Core formation and the oxidation state of the Earth: Additional constraints from Nb, V and Cr partitioning. *Geochimica et Cosmochimica Acta* 72, 1415-1426.

Wood, B.J., Walter, M.J., Wade, J., 2006. Accretion of the Earth and segregation of its core. *Nature* 441, 825-833.

Yin, Q., Jacobsen, S.B., Yamashita, K., Blichert-Toft, J., Telouk, P., Albarede, F., 2002. A short timescale for terrestrial planet formation from Hf-W chronometry of meteorites. *Nature* 418, 949-952.

Yu, G., Jacobsen, S.B., 2008. A W-Isotope Evolution Model with a Deep Magma Ocean and a Solid Lower Mantle: Application to Mars and Earth, 39th Lunar and Planetary Science Conference, League City, Texas., p. 1847.

Yu, G., Jacobsen, S.B., 2011. Fast accretion of the Earth with a late Moon-forming giant impact. *Proceedings of the National Academy of Sciences* 108, 17604-17609.